The University of Melbourne

Department of Mechanical and Manufacturing Engineering

Developments In Smooth Wall Turbulent Duct Flows

by

Jason Patrick Monty

Submitted in total fulfilment of the requirements

of the degree of Doctor of Philosophy

2005

Delcaration

This is to certify that:

i. *the thesis comprises only my original work;*

ii. *due acknowledgement has been made in the text to all other material used;*

iii. *the thesis is less than 100,000 words in length, exclusive of tables, maps, bibliographies and appendices.*

Jason Patrick Monty

Abstract

An experimental investigation into the fully developed, turbulent flow in circular pipes and high aspect ratio rectangular ducts (channels) was undertaken. A review of the literature revealed that there is a need for more accurate duct flow measurements, despite the large number of studies already completed. Thus, a new, high quality channel flow apparatus has been carefully designed and constructed. For the fully developed flow, all measureable turbulence statistics at the centre of the channel are presented. Measurements are recorded using hot-wire and pitot tube anemometry, with an insistence on the highest accuracy. All results are analysed with the intention of providing a better physical understanding of turbulent flows.

An existing pipe flow apparatus — most recently employed by Henbest (1983) — is used to check the applicability of common pitot corrections by comparison with hot-wire data. It is found that applying the MacMillan (1956) and turbulence intensity corrections gives good agreement between measurements. Velocity profiles measured at the centre of the channel display the expected logarithmic scaling. These also highlight a significant difference between pipe and channel flow velocity profiles; that is, pipe flow has a much larger wake. This observation has been observed, but not explained in the literature. It was postulated that the difference is due to an increased number of eddies contributing to the outer flow in the pipe. Evidence supporting this claim is found from the attached eddy hypothesis.

Recent literature has provided predictions of the turbulence intensities in boundary layers, based on the attached eddy hypothesis. These predictions are compared and extended to channel flow measurements for the first time. In the analysis of flow structure, the auto-correlation of streamwise velocity fluctuations is an often neglected statistic. It is shown here that channel flow auto-correlation measurements

indicate the existence of streamwise 'packets' of attached eddies. The packets appear to persist well into the outer flow region, in contrast to packet behaviour observed in boundary layers.

Accurate measurements of flow quantities in the vicinity of the channel side-walls are also uncommon in the literature. An investigation is undertaken to learn more about the flow in this part of the channel. Perimetric wall shear stress distributions are presented. These attest to the two-dimensionality of the central flow and the Reynolds number independence of side-wall effects. Side-wall velocity profiles confirm the above trends. Finally, the channel length required to permit full flow development is investigated. Side-wall and central flow velocity profiles, measured at various streamwise stations, suggest a length of no less than 130 channel heights is necessary for fully developed turbulent flow.

Acknowledgements

Prof. M. S. Chong as my principal supervisor, was a constant source of advice, motivation and above all, friendship. His hard-working, yet down-to-earth attitude to research, and indeed life, was an inspiration and encouragement to me throughout my candidature. Our many discussions — both work related and football related — will be fondly remembered.

Thanks to the late Prof. A. E. Perry as my secondary supervisor. I feel honoured to have worked with such a brilliant mind. His inspirational guidance was the reason I embarked on this PhD adventure. He will forever be remembered for his incredible understanding, thought-provoking discussion and dedication to students.

Thanks to Dr. M. B. Jones, who has been my mentor throughout my candidature. His broad knowledge, experimental experience and research skill made this thesis possible. Our daily academic and social conversations over coffee were the highlight of many a frustrating day!

Without the technical experience of Mr. D. Jacquest, the practical side of this project would have been impossible. No doubt the same applies to countless students who have drawn on his experience and knowledge over the last 40 years. It was great to learn from such a friendly, caring and helpful personality — thanks mate.

Thanks also to Dr. A. Ooi who provided invaluable encouragement, advice and support throughout the project.

I would also like to thank my fellow students and friends in the Walter Bassett Aerodynaamics laboratory: Dr.'s A. K. Hellstedt, S. Hafez and K. Higgins, Messr's N. Nishizawa, M. Giacobello, P. Gregory, K. Moinmuddin, J. M. Wettenhall, R. Widjaja, K. Lien, R. Cohen and T. Mattner.

Thanks to my family for their constant support and encouragement not only during my PhD, but throughout my life.

I would like to thank Christine for her wonderful love and support and for preserving my sanity, especially in my final year.

Finally, all this work would be impossible without the grace of God. The amazing complexity and intricacy of nature, which He provided for us, will never cease to intrigue and fascinate my mind.

Dedicated to my father,

Patrick Lewis Antoine Monty

Contents

List of Figures

Nomenclature

A	Universal constant in the logarithmic law of the wall
A_1	Universal constant in the logarithmic $\overline{u'^2}$ formulation
A_2	Universal constant in the $\overline{w'^2}$ formulation
A_3	Universal constant in the $\overline{v'^2}$ formulation
A_s	Aspect ratio of rectangular duct
a_0	Universal constant in the mean velocity formulation of Nickels (2001)
a_2	Characteristic constant in the mean velocity formulation of Nickels (2001)
B	Large scale characteristic constant in the velocity defect log law
B_1	Characteristic constant in the logarithmic $\overline{u'^2}$ formulation
B_2	Characteristic constant in the $\overline{w'^2}$ formulation
B_3	Characteristic constant in the $\overline{v'^2}$ formulation
B_d	Constant in the function W_g, equal to the normalised streamwise turbulence intensity at the duct centreline
C	Universal constant in the viscous correction term of the $\overline{u'^2}$ formulation
C_1	Constant in Prandtl's smooth wall resistance law for pipes
C_2	Constant in Prandtl's smooth wall resistance law for pipes
C_3	Constant in channel flow logarithmic skin friction law
C_4	Constant in channel flow logarithmic skin friction law
C_f	Local skin friction in a rectangular duct
D	Pipe diameter
D_e	Hydraulic diameter
d_p	Pitot tube outer diameter
d_s	Wall mounted static pressure tap diameter

E_1	Hot-wire output voltage
E_2	Hot-wire output voltage
E_{A1}	Matching circuit offset voltage
E_{A2}	Matching circuit offset voltage
E_u	Matching circuit output voltage
E_v	Matching circuit output voltage
F	Constant in the channel flow resistance law of Dean (1978)
h	Channel height
I_{ij}	Townsend's eddy intensity function
K_1	Matching circuit gain
K_2	Matching circuit gain
K_2'	Matching circuit gain
K_2''	Matching circuit gain
K_τ	Karman number; $K_\tau = \Delta U_\tau/\nu$
k_1	Streamwise wavenumber
L	Distance from duct inlet to measuring station
l	Length of hot-wire filament
M	Universal constant in the attached eddy hypothesis
M_d	Constant in the AEH; $M_d = M/\Delta_E$
P	Duct perimeter
p	Static pressure
p_H	p.d.f. of attached eddy hierarchy scales
p'	Pressure fluctuation
Q	Mean component of velocity tangential to a streamline
q	Velocity tangential to a streamline
q'	Fluctuating component of velocity tangential to a streamline
R	Circular pipe radius
Re	Reynolds number based on bulk velocity and pipe diameter/channel height; i.e. $Re = U_b D/\nu$ or $Re = U_b h/\nu$
R_{11}	Normalised auto-correlation coefficient
Re_c	Reynolds number based on centreline, rather than bulk, velocity
Re_θ	Reynolds number based on free-stream velocity and momentum

	thickness, θ
r_0	Attached eddy core radius
T	Weighting function in the attached eddy hypothesis
t	Time
t'	Time delay/lag
t'_m	Peak time lag
U	Mean streamwise velocity
U_{CL}	Centreline velocity (duct flows)
U_D	Mean streamwise velocity defect; $U_D = U_{CL} - U$
U_b	Bulk velocity (duct flows)
U_c	Convection velocity
U_m	Measured streamwise velocity
U_{max}	Maximum streamwise velocity
U_τ	Friction velocity
u	Streamwise velocity
u'	Streamwise velocity fluctuation
$\overline{u'^2}$	Streamwise turbulence intensity
$\overline{u'v'}$	Reynolds shear stress
$\overline{u'w'}$	Reynolds shear stress
V	Chapter 2: Mean velocity tangential to a streamline
	Chapter 6: Viscous correction for turbulence intensity predictions
V_g	Extended viscous correction for turb. intensity predictions
v	Wall-normal velocity
v'	Normalwise velocity fluctuation
$\overline{v'^2}$	Normalwise turbulence intensity
W	Weighting function in the attached eddy hypothesis
W_g	Outer flow component of $\overline{u'^2}$ formulation
w	Channel width; spanwise velocity
w'	Spanwise velocity fluctuation
$\overline{w'^2}$	Spanwise turbulence intensity
x	Streamwise coordinate
x_0	Streamwise spacing associated with time delay, t'

y	Wall-normal coordinate, also referred to as *wall-distance*
z	Spanwise coordinate
z_s	Offset spanwise coordinate; $z_s = z + 0.585$
$\mathcal{L}$	Integral length scale
$\mathcal{O}$	Indicates 'of the order'
$\mathcal{R}_{11}$	Auto-correlation coefficient
$\mathcal{T}$	Integral time scale
α	Coefficient of the mean velocity power law
	Note that α is also the shear parameter in Chue's pitot correction
β	Exponent of the mean velocity power law
$\Delta(y)$	Wall-distance correction
Δ	Outer flow length scale
Δ_E	Largest height scale of attached eddies
Δp	Static pressure error
δ	Characteristic height scale of hierarchy of attached eddies
δ_1	Smallest height scale of attached eddies
ϵ	Chapter 2 & 4: aspect ratio dependent, three-dimensionality factor;
	Chapter 7: viscous dissipation rate
Φ_{11}	Streamwise velocity spectra
η	Wall-distance scaled with outer flow variables; $\eta = y/\Delta$
Γ	Mean velocity power law diagnostic function
κ	Universal constant in the logarithmic law of the wall
λ	Chapters 2 & 5: An intermediate variable defined as $\ln(\delta/y)$;
	Chapter 7: Taylor microscale
λ_1	Defined as $\ln(\delta_1/y)$
λ_E	Defined as $\ln(\delta_E/y)$
λ_p	The Darcy friction factor
λ_t	Total friction factor
ν	Kinematic viscosity
Π	Wake factor determined from Jones' wake formulation
Π_c	Coles wake factor
Π_m	Non-dimensional static pressure error

Θ	Mean velocity log law diagnostic function
θ	Momentum thickness
ρ	Fluid density
τ_w	Wall shear stress
$\overline{\tau_w}$	Perimeter-averaged wall shear stress
ξ	Spanwise (azimuthal for pipe flow) vorticity
ξ_H	Spanwise or azimuthal vorticity contribution from a hierarchy of attached eddies
ψ_{ii}	Pre-multiplied hierarchy spectral function
$+$	When used as superscript, indicates scaling with inner flow variables; e.g. $y^+ = yU_\tau/\nu$ and $U^+ = U/U_\tau$

Chapter 1

Introduction

For centuries the behaviour of fluid flows has captured the attention of some of history's most esteemed minds. Indeed, almost all of us have been captivated at times by the intriguing patterns observed in smoke rising from a fire or in the wakes of ships or boats, or even in water simply draining out of a basin. It is perhaps not surprising to learn then, that those responsible for some of the earliest known scientific activities were similarly captivated by these phenomena. Respected intellectuals such as Aristotle and Archimedes — whose thoughts on a remarkable array of other complex processes are well documented — raised questions concerning the mechanisms behind fluid flows, centuries before the birth of Christ. Over 1500 years later, Leonardo's astonishing portfolio of scientific observations included various aspects of fluid mechanics. In fact, it was Leonardo who first discovered the principle of continuity. However, as centuries passed, further questions were raised concerning the mechanics of fluid flow, with few adequate answers provided. Even those who are now considered history's greatest mathematicians would find themselves challenged by the complexity of fluid motions: Newton, Euler, Lagrange, L'Hopital, Bernoulli, Stokes and d'Alembert are examples. All these men are famous for their monumental contributions to other sciences, however all encountered many obstacles in contributing to fluid mechanics theory. Thus, progress in fluid mechanics was relatively slow in a period of history when solutions to other classical physics problems were appearing at a rapid rate.

Even into the 18th and early 19th centuries, fluid mechanics remained poorly understood, although these times did see moderate success in the formulation of equations of fluid motion, most notably evidenced by the work of Euler, d'Alembert, Bernoulli and Navier. The fact that all theories at this time were limited by their exclusion of undiscovered viscous effects, proved to be the major hinderance. A technical exception to this shortcoming was Navier's equations — now known as the Navier-Stokes equations — which contain all mathematical information of any fluid flow. These equations included terms related to the intermolecular forces in the fluid which we now know should be replaced by viscosity. Navier was a French engineer and graduate of the *École des Ponts et Chaussées* (School of Roads and Bridges) who is often mistakenly identified as a pure mathematician due to his exceptional mathematical abilities. Navier's work was indeed an impressive achievement for his time, although even he could not have contemplated the significance his equations would have to future fluid mechanics research.

Although theories were developing, experimental studies were much further behind. Prior to the 19th Century, one of the few experimental events of historical significance was the discovery of the Pitot tube by the French engineer, Henri Pitot in 1732. Indeed, it was Pitot's countrymen who led the way in experimental research at this time. The École des Ponts et Chaussées (EPC) was established in 1747, becoming the first institution dedicated to the education of engineers. The EPC produced a number of famous engineers including Coriolis, Cauchy and Navier and the school still exists today, although it is now known as the École *Nationale* des Ponts et Chaussées. In a more direct effort to improve scientific experimental research, the *Learned Committee* was set up in the late 18th Century, headed by d'Alembert. The committee's aim was to understand fluid flow through careful experimental studies in order to improve navigation of ships. d'Alembert soon realised that past experiments in fluid mechanics had been of no interest to science due

Figure 1.1: Jean Le Rond d'Alembert [1717 – 1783].

to experimentalists ignorance of new developments in fluid flow theory:

> "The whole business of experimental investigations is so delicate a matter, however, that it requires a very special attention, while in actual fact it often appears to be accidental. Information and data collected by many superficial investigators often appear to be unrelated to each other. In many cases, it is difficult to understand the causes and the sources of the data. Some forget the purpose of science... It is necessary to be careful with the information presented by an experimentor who lacks theoretical principles; such an experimentor lacks vision and reasoning, and therefore often presents one and the same fact in different guises, without realizing it himself. Or he gathers at random several facts and presents them as proofs, without being able to explain them. It must be understood that scientific knowledge without reasoning — that is, without theory — does not exist." *Nouvelles experiences sur la resistance des fluides.* Jombert, Paris (1777); from Rouse & Ince (1957), p91.

With recently discovered theories at its foundation, the Learned Committee proceeded to build on their understanding with experimental observations. Bossut — a member of the Learned Committee — and his contemporaries, Borda and Du Buat produced the earliest of these truly scientific experimental studies in fluid mechanics. It should be noted that the work of the Learned Committee spawned many experiments that warrant inclusion in an historical discussion, however considering the contention of this thesis, the focus will be on those experiments concerning duct flows. Since most experimentalists were military or civil engineers, almost all of the ducts constructed for studies before the 20th Century were either circular in cross section (pipe flow) or open channels (simulating rivers); the military engineer Du Buat is an example. Du Buat published the first scientific study of pipe flow resistance in 1779, noting the retardation of the fluid by the pipe walls and that the effects of this extended through the flow away from the wall. Although he was unaware that viscous effects were the cause of this phenomena, Du Buat had made

the first steps leading to the discovery of the boundary layer. Du Buat observed many interesting flow features during his extensive research endeavours, however he still struggled to gain an understanding of the complex fluid processes involved. He soon realised he was not alone in this struggle, commenting on his colleagues similar experiences:

> "Everybody reasons about Hydraulics, but there are few people who understand it... For lack of pinciples, one adopts projects of which the cost is only too real but of which the success is ephemeral." *George Du Buat [1739–1804].*

Du Buat's efforts would prove valuable to future workers, however fluid flow experimentation would continue into the 19th century with little more success — due in part to the aforementioned slow progress of fluid mechanics theory.

In Germany in 1839, Hagen noticed that saw-dust particles in heated pipe flow moved in straight lines when the temperature was low. As the temperature increased, particles began to swirl around randomly. This would indicate that Hagen was the first to discover laminar to turbulent pipe flow transition. However, Hagen is not credited for this discovery because he related his findings to temperature changes rather than viscosity variation. No more than a few years after Hagen conducted his measurements, a French physician named Poiseulle also experimented with laminar pipe flow. The two experimentalists were unknown to each other, both knew little about the mathematics behind their work and both documented a parabolic velocity profile for laminar flow. This velocity profile, analytically confirmed in 1858, is now commonly known as the Hagen-Poiseuille profile.

A largely forgotten figure in fluid mechanics was the next to contribute to pipe flow research. Henry Darcy (another French engineer) published many papers discussing his experimental work between 1850 and 1858. Arguably the most influential of Darcy's contributions to experimental fluid mechanics was his modifications to the Pitot tube. Since its discovery in 1732, the Pitot tube was no more than a scientists toy; an inaccurate and awkward device. For over 130 years it remained as such, until Darcy's improvements. The new Pitot tube was an experimental breakthrough since,

for the first time, accurate measurements of velocity in fluid flows could be recorded. Darcy proceeded to use the device to measure velocity fields of pipe and open channel flows with reasonable accuracy. Among other outstanding achievements, Darcy contributed to the development of the Darcy-Weisbach equation (still used today for calculating head loss through a pipe), he made further steps toward the discovery of the boundary layer and his name is given to the well known Darcy friction factor.

One Professor who took a keen interest in Darcy's work is now familiar to all students of fluid mechanics due to his 1883 paper on the characterisation of laminar to turbulent flow transition. Osborne Reynolds, an Englishman and graduate of Cambridge University, became only the second Professor of engineering in England at Owen's college, Manchester in 1868. Reynolds work included significant contributions to many other fields, however his most famous discoveries were in fluid mechanics. The 1883 paper is acclaimed for its introduction of a non-dimensional quantity later given the title of *Reynolds number*. Although Reynolds was able to correctly characterise laminar to turbulent transition, he remarked that the mechanism of transition needed further study. Today, studies into flow transition are common and there remains a need for futher study on this phenomenon. It should also be noted that a large section of Reynolds (1883) is devoted to a comparison of Reynolds' pipe flow resistance results with those of Darcy and Poiseulle, emphasising the importance of their respective studies.

A second ouststanding paper by Osborne Reynolds was presented to the Royal Society in 1894. This analytical paper included the derivation of what we now know as the Reynolds Averaged Navier-Stokes (RANS) equations. Reynolds was the first to consider fluid flow velocities as the sum of a mean velocity and a fluctuating velocity component. Substituting velocity in the Navier-Stokes equations for the two velocity components and time averaging the resulting equation, results in the RANS equation used by almost all commercial numerical simulation software packages today. Due to the widespread use of RANS, it is often forgotten that Reynolds (1894) also includes an analytical study of the equations of motion of flow between parallel plates — a flow which has received much attention since the advent of the computerised numerical simulation. Reynolds analytically determined the laminar

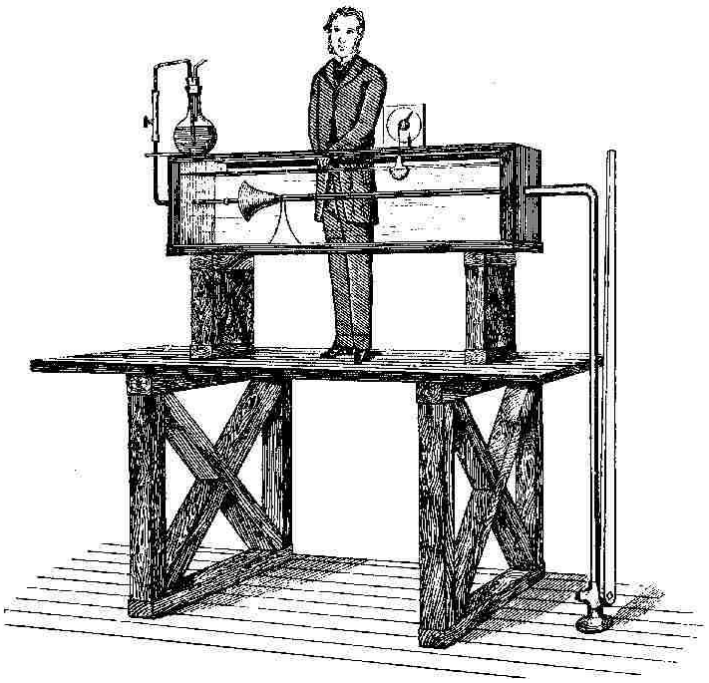

Figure 1.2: Osborne Reynolds [1842–1912] stands beside his famous pipe flow apparatus. Sketch taken from Reynolds (1883).

to turbulent transition Reynolds number of this flow to be 517. Since there were no high aspect ratio rectangular duct studies prior to 1894, Reynolds could make no comparison with experiment. However it has more recently been determined that transition occurs around Reynolds number of 1000, impressively close to Reynolds calculations.

Shortly after Reynolds milestone publications, arguably the single most important discovery in the history of fluid mechanics was made. Ludwig Prandtl of Göttingen, Germany published a paper in 1904 suggesting that flow over a solid boundary may be thought of in two parts. Firstly, a region of fluid very close to the boundary where velocity is significantly influenced by viscosity called the *boundary layer*, and secondly, the rest of the flow (i.e. outside the boundary layer) which may be considered inviscid. The rapid progress of aerodynamics immediately following this discovery is plain to see. Finally, d'Alembert's 250 year old potential flow paradox — that fluid mechanics theory predicts zero drag on any object moving through a fluid, contrary to reality — was explained. The concept of the boundary layer also led to an explanation of duct flows which were, without an understanding of viscous effects, poorly understood.

Prandtl continued to present outstanding theories in fluid mechanics, heat transfer and physics throughout his career, however it should be noted that Prandtl was not simply a theoretician, he was an experimentalist also. In fact, it was Prandtl who made further modifications to Darcy's improved Pitot tube to obtain much higher accuracy velocity measurements. This new anemometer was essential to experimental studies conducted by Prandtl's students, and indeed many other researchers throughout the 20th Century. This brings us to yet another remarkable aspect of Prandtl's career: his teaching ability. He is frequently described as someone who was capable of making the difficult concepts seem simple. Whatever his methods were, Prandtl's students are some of the most highly respected names in fluid mechanics: Blasius, Schlichting, Nikuradse, Ackeret and von Kármán are just a few examples. This astonishing group of researchers were responsible for many benchmark studies in fluid dynamics. Johann Nikuradse conducted extensive pipe flow experiments including investigations into rough wall pipe flow. His paper, Nikuradse (1933), is one of the most frequently cited publications in circulation. Unfortunately, it is reported that Nikuradse's success drove him to challenge his mentor's leadership at Göttingen. Failure to effect Prandtl's demotion led to the premature end of a promising research career — Nikuradse never published again. Shortly after Nikuradse's pipe flow work, Herman Schlichting studied turbulent rectangular duct flow with great attention to detail, using highly accurate experimental techniques. Results of the smooth and rough wall studies are presented in Schlichting (1936) — yet another frequently cited publication from Göttingen. Schlichting was also the first to publish a textbook on his teachers' boundary layer theory (*Boundary Layer Theory*, 1951); a highlight of an impressive research career.

Figure 1.3: Ludwig Prandtl [1875 – 1953].

Prandtl's theories opened the floodgates holding back experimental investigations. The new theory combined with rapid advances in measurement technologies during

the 20th Century resulted in a surge of studies into all kinds of flows. A selection of the most important literature of the 20th Century relevant to this thesis will be reviewed in the following chapter.

1.1 The 20th century and beyond

Over the past 100 years, a large amount of experimental pipe flow data has been published. New technology has allowed measurement of flow properties that were previously immeasurable. However, much of the more recent mean flow and friction factor data is ignored or only briefly discussed as researchers and practical engineers frequently refer to the benchmark results of Nikuradse, despite considerable concerns raised about the quality of the data. Firstly, the experiments were conducted in 1936 while measurement techniques were still in the relatively early stages of development. Secondly, Nikuradse's analysis techniques have been questioned; some researchers even accusing him of selecting favorable results from the data collected. The reliance on Nikuradse's work led to the decline of dedicated mean flow studies in pipes through the latter half of the 20th century. Although these studies are important, it is clear that turbulent pipe flow is not yet fully understood. The lack of understanding was distinctly revealed through the Princeton University 'superpipe' controversy in 1996 (analysed in detail in chapter 2). While unanswered questions concerning even the simplest quantities in turbulent pipe flow remain, further experimental pipe flow studies will be required.

Recent turbulent channel flow history is almost identical to that of pipe flow. Laufer (1950) is the benchmark study in the case of smooth wall channel flow. Laufer was the first to use the now common *hot-wire* anemometry to record the first detailed turbulence measurements in a channel. As with Nikuradse's data, this study has its serious faults which, in the author's opinion — are given insufficient consideration by engineers and many researchers. In the later years of the 20th Century, channel flow received even less attention than pipe flow for two reasons: firstly, there is uncertainty in two-dimensionality of the flow due to corner effects, and secondly, great success of numerical simulations in channel flow was achieved in this period.

After 1980 there are very few channel flow experimental results in the literature. Only recently, Zanoun *et al.* (2002) and the author have conducted experimental studies into the fluid mechanics of fully developed channel flow at moderate—high Reynolds numbers. It is likely that numerical simulations of channel flows will dominate experimental studies in the foreseeable future as computational power increases. However, until numerical simulations can reach high Reynolds numbers, there is still much to learn about turbulent channel flow through experiment.

In summary, centuries after the great mathematicians and experimentalists struggled to make progress in fluid mechanics, we find ourselves in a similar position today. Turbulent fluid motion remains the last unsolved problem in classical physics. Du Buat's statement that experimentalists of his time adopted "projects of which the cost is only too real but of which the success is ephemeral", still applies today. Often the most elaborate and innovative experiments raise as many questions as answers (e.g. the Princeton Superpipe). However, these difficulties need not discourage the experimentalist, rather, he should be inspired to journey into the unknown; to make a valuable contribution to an intriguing, developing science.

1.2 Aims of this investigation

This thesis intends to build on the foundations of duct flow knowledge established over centuries, particularly the 20th century, as discussed above. The overall aim of the investigation is to further our understanding of the behaviour and development of turbulent duct flows. The specific aims are as follows:

1. To develop new and more efficient hot-wire anemometry techniques. Current measurement techniques have typically remained unchanged for many years. It has been suggested that some of these techniques could be improved. This study aims to determine which modifications are beneficial and to implement the necessary changes so that the techniques used for experiment are most accurate and efficient.

2. To record accurate mean streamwise velocity profiles in a fully developed tur-

bulent pipe flow using pitot tube and hot-wire anemometry. At the time of writing, hot-wire measured mean velocity profiles in a circular pipe had not been published. Comparison of data recorded using the two measurement techniques will help to answer questions regarding the validity of the log law and appropriate pitot tube corrections.

3. To carefully construct a large, high aspect ratio, rectangular duct (channel) facility in the Walter Bassett Aerodynamics Laboratory. The ultimate purpose of this channel will be to study the effect of wall roughness. As such, the apparatus must be designed to facilitate frequent substitution of roughness types.

4. The smooth wall channel flow case: measurements of mean streamwise velocity, turbulence intensities, the measurable Reynolds shear stresses and autocorrelation and spectra of velocity fluctuations will be recorded. Measurements are to be taken using both hot-wires and pitot tubes with the highest accuracy and care.

5. To analyse the flow development through the channel. Two sets of streamwise velocity profiles measured at various longitudinal stations in the channel will be required: firstly, a set of profiles will be measured laterally from the sidewall; a second set will be recorded normal to the wall at the centre of the channel bed.

6. There is currently an observed anomaly in the mean velocity profiles of turbulent pipe flow and channel flow. That is, pipe flow has a much larger wake than channel flow, which is counter-intuitive. An explanation of this phenomenon based on the attached eddy hypothesis of Perry & Chong (1982) will be explored.

Chapter 2

Literature review and background theory

In the interest of making a meaningful contribution to the future of fluid dynamics research, it is imperative that past work in the field is reviewed and analysed carefully. In the following chapter, a selection of important publications are reviewed. However, reviewing the literature without an explanation of some basic theories of duct flows would only confuse the reader. Therefore a number of sections in this chapter will be devoted to the background theory relevant to the succeeding publication reviews.

There have been a large number of pipe flow studies conducted over the last century that could justifiably be reviewed here; the author has selected only those studies having most relevance to the current investigation. For turbulent channel flow, Dean (1978) compiled a comprehensive review of rectangular duct flow experimental results up to 1978. This reference will be discussed in the following pages along with more recent developments in turbulent channel flow.

Following these discussions will be a review of pitot tube corrections. Although the pitot tube is now a common laboratory tool, there remains some doubt about its correct application to wall-bounded shear flows. Also included is a discussion of a physical model for wall-bounded turbulent flows — a rather poorly understood, though very promising, branch of turbulence research. Finally, the chapter will

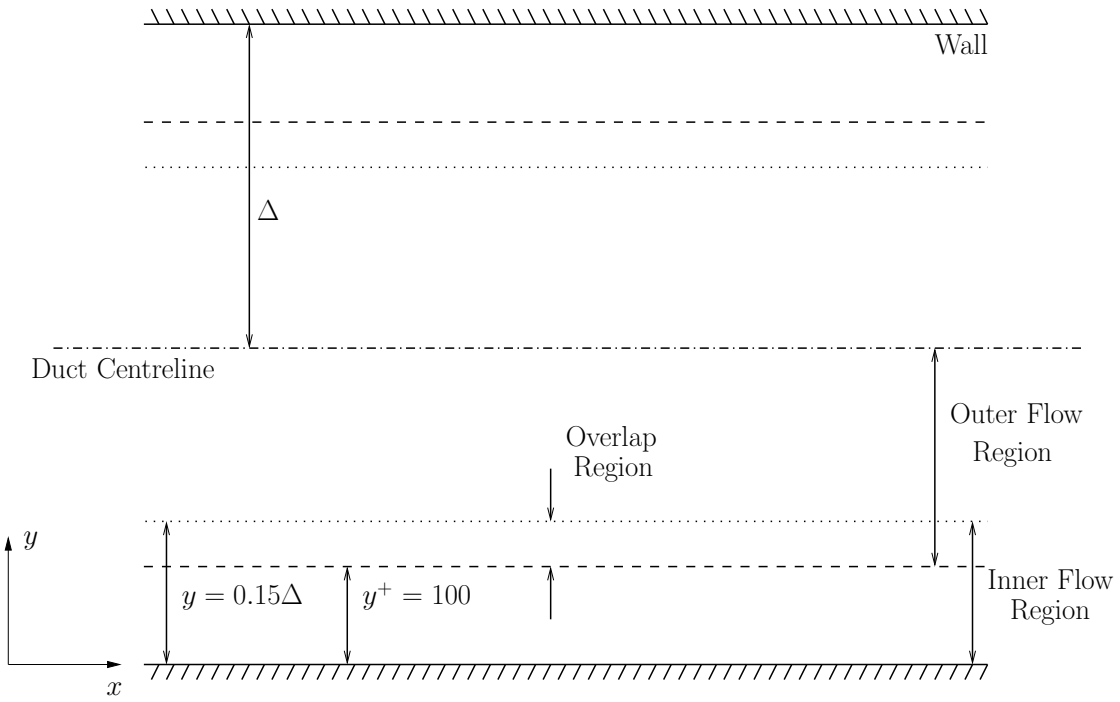

Figure 2.1: Definition of various flow regions in turbulent duct flow.

conclude with the author's overview of the literature and thoughts on the current status of turbulent duct flow research.

2.1 Mean flow

Wall bounded shear flows can be divided into two flow regions; an *inner flow* layer close to the wall, and an *outer flow* region further away from the wall, which extends to the edge of the shear layer. In turbulent duct flow there is no 'edge' of the shear layer, so the outer flow region is the entire flow between the inner flow region and the centreline. Therefore in ducts, the outer flow region is commonly known as the *core* flow region. These regions in a fully developed duct flow are illustrated schematically in figure 2.1. The distinction between the two regions is explained in the following paragraphs.

In the inner flow region, the important variables affecting the mean streamwise velocity, U, are wall-distance, y, friction velocity, U_τ, and kinematic viscosity, ν. Note that $U_\tau = \sqrt{\tau_w/\rho}$ is a velocity scale based on local shear stress at the wall, τ_w and fluid density, ρ. The large scale geometry of the flow is unimportant close

to the wall. Therefore, flow through a circular pipe will have the same inner flow behaviour as that over a flat plate or channel bed. The following result is obtained from a dimensional analysis of the inner flow variables:

$$\frac{U}{U_\tau} = f\left(\frac{yU_\tau}{\nu}\right). \tag{2.1}$$

Prandtl (1925) was the first to propose this relationship, hence it is commonly referred to as *Prandtl's law of the wall*. In the outer or core flow region the viscosity is no longer an important parameter; however the large scale geometry of the duct (diameter or height) is important. Applying dimensional analysis to the important variables in the core region gives a relationship for local velocity relative to centreline velocity, U_{CL}:

$$\frac{U_{CL} - U}{U_\tau} = g\left(\frac{y}{\Delta}\right). \tag{2.2}$$

Here, Δ is an outer flow length scale which, depending on the duct, is either the pipe radius, R, or channel half-height, $h/2$. Equation (2.2) is known as the *von Kármán velocity defect law* since von Kármán (1930) first derived this formulation. Note that the arguments of f and g are usually written as $y^+ = yU_\tau/\nu$ and $\eta = y/\Delta$ respectively.

Now, it is assumed that the inner and outer flow regions are not distinct; that is, there must exist a region of overlap between the two regions. This region is commonly referred to as the *overlap* or *turbulent wall* region, and equations (2.1) & (2.2) must hold simultaneously in this region. Equating the derivatives of these two equations gives

$$\frac{\partial}{\partial y}\left(\frac{U}{U_\tau}\right) = \frac{U_\tau}{\nu} f'\left(\frac{yU_\tau}{\nu}\right) = -\frac{1}{\Delta} g'\left(\frac{y}{\Delta}\right), \tag{2.3}$$

for which there is only one solution: f' and g' are inversely proportional to their respective arguments, y^+ and η. Integration then yields the following explicit forms for the scaled velocity and velocity defect in the turbulent wall region:

$$\frac{U}{U_\tau} = \frac{1}{\kappa} \ln\left(\frac{yU_\tau}{\nu}\right) + A, \tag{2.4}$$

$$\frac{U_{CL} - U}{U_\tau} = -\frac{1}{\kappa} \ln\left(\frac{y}{\Delta}\right) + B. \tag{2.5}$$

Where κ and A are universal constants and B depends only on large scale geometry. Coles (1962) suggested κ and A should be 0.41 and 5.0 respectively, based on a

survey of data† available at the time, including that of Nikuradse (1933). From this time onward, Coles' log law constants have been widely adopted by the fluid dynamics community — indeed, Coles (1962) states: "these [log law constants] ought to be both satisfactory and non-controversial".

It should be noted that the derivation detailed above is not the only method of arriving at the classical equations (2.4) & (2.5). In fact, Prandtl (1925) first derived the equations using his mixing length argument, while the more common approach used above, was proposed over 10 years later by Millikan (1938). It would be expected that these very different methods arriving at the same logarithmic laws would instill a degree of confidence in the equations. This has been the case for most wall turbulence analysts throughout the 20^{th} century, with a wealth of experimental evidence in support. However, in recent years the validity of the logarithmic laws has come into question. Although equation (2.1) is almost universally accepted, the velocity scale used in von Kármán's defect law has been challenged — especially at low to moderate‡ Reynolds number. Changing the outer flow velocity scale invalidates the above derivation, leaving no universal scaling law for the mean flow. Those who dispute the logarithmic law (2.4) usually give their support to a power law relationship for inner flow scaled velocity,

$$\frac{U}{U_\tau} = \alpha(y^+)^\beta, \tag{2.6}$$

where α and β are Reynolds number dependent coefficients. Originally, the power law was no more than an empirical curve fit since it was not analytically justified. Following the simple, analytical derivation of the log law by Millikan, the power law curve fit was almost completely discarded. Today, the list of power law proponents is growing and already includes many prominent researchers such as Barenblatt (1993), George, Castillo & Knecht (1993)¶ and Zagarola & Smits (1998). The first two of these references also give new, analytical justifications for the power law, thus providing a much stronger case for this alternative to the log law.

† Coles (1962) acknowledges the substantial scatter observed in this data set.

‡ That is, flow Reynolds numbers commonly attained in laboratory facilities of the order 10^5.

¶It should be noted that George *et al.* (1993) relates only to turbulent boundary layers — not pipes or channels.

It is not the intention of this thesis to prove which scaling is correct, although experimental data will be presented in later chapters to provide further evidence in this ongoing argument. However, the importance of the power law versus log law debate to this study cannot be understated. Indeed, it was the controversial results of Zagarola & Smits (1998) in support of the power law that provided much of the motivation for the experimental investigation of this thesis. The milestone work of Zagarola & Smits (1998) is the topic of the following section.

2.2 The Princeton 'Superpipe'

In 1996 the first results of the Princeton high Reynolds number pipe flow facility (the *Superpipe*) were released in the PhD thesis of Zagarola (1996). A paper on the findings was also published: Zagarola & Smits (1998). The Superpipe is a unique apparatus in that pressurised air is used as the working fluid. Pressures in the pipe can reach up to $230atm$, drastically reducing the kinematic viscosity of the air and thereby increasing Reynolds number (based on bulk velocity and pipe diameter) to an unprecedented 35 million. The Superpipe also has a diameter, D of $129.4mm$ and development length of $L \approx 160D$, where L is the distance from the pipe inlet to the measurement location. These dimensions are quite large in magnitude compared with other laboratory pipe flow facilities. Many turbulence analysts were eagerly anticipating the outcomes of Zagarola's study; however, the Superpipe, instead of resolving some controversial issues, created more uncertainty. Some of the controversial Superpipe results and their impact are discussed in this section.

2.2.1 Controversial results

Firstly, Zagarola found that the superpipe data disagreed with the well-known and generally accepted smooth wall friction factor formulation proposed by Prandtl (1935),

$$\frac{1}{\sqrt{\lambda_p}} = C_1 \log_{10}(Re\sqrt{\lambda_p}) + C_2 \tag{2.7}$$

where the constants C_1 and C_2 are 2.0 and -0.8 respectively. These constants were determined empirically from the data of Nikuradse (1933). In equation (2.7), λ_p is the Darcy friction factor defined as:

$$\lambda_p = \frac{4\tau_w}{\frac{1}{2}\rho U_b^2} = 8\left(\frac{U_\tau}{U_b}\right)^2. \tag{2.8}$$

Note that very similar values of C_1 and C_2 (2.035 and -0.91) can be found through Prandtl's analytical derivation of equation (2.7). This is not overly surprising, however, since the derivation begins with the log law (2.4) having constants of $\kappa = 0.4$ and $A = 5.5$, which were themselves found from the data of Nikuradse (1933). This derivation will be further discussed in §2.4.3 and is given in full in Appendix A.

For the Superpipe results, it was shown that values of $C_1 = 1.889$ and $C_2 = -0.3577$ gave best agreement with Prandtl's smooth wall law (2.7) at high Reynolds number ($Re = U_b D/\nu = 10^5$ – 35×10^6). To cover the entire Re range, Zagarola found that a second Re dependent term was needed in (2.7). Therefore,

$$\frac{1}{\sqrt{\lambda_p}} = 1.872\log_{10}(Re\sqrt{\lambda_p}) - 0.2555 - \frac{228}{(Re\sqrt{\lambda_p})^{0.89}} \tag{2.9}$$

was proposed. This equation is significantly different to Prandtl's smooth wall formula, as illustrated in figure 2.2. Furthermore, the result contradicts the data of Nikuradse (1933) which displays excellent collapse onto (2.7) with Prandtl's constants for all Reynolds numbers up to 3.4×10^6. However, Nikuradse (1933) is often criticised in the experimental fluid dynamics community for reasons ranging from insufficient flow development, to suggestions of unjustified selectivity of the data. Unfortunately such opinions raise doubts which signify that one cannot discount the Superpipe data on the basis of disagreement with that of Nikuradse (1933).

In regards to the deviation of the Superpipe data from equation (2.7), it must be noted that Prandtl's law relies on the logarithmic behaviour of the inner flow scaled mean velocity profile† , which — even the most avid opponents of the log law agree — must hold as $Re \to \infty$. Therefore, if the Superpipe data is different to Prandtl's smooth wall law at high Reynolds number, it is implied that the mean velocity

† Throughout this thesis, unless otherwise stated, the *mean velocity profile* refers to the wall-normal distribution of mean streamwise velocity with inner flow scaling.

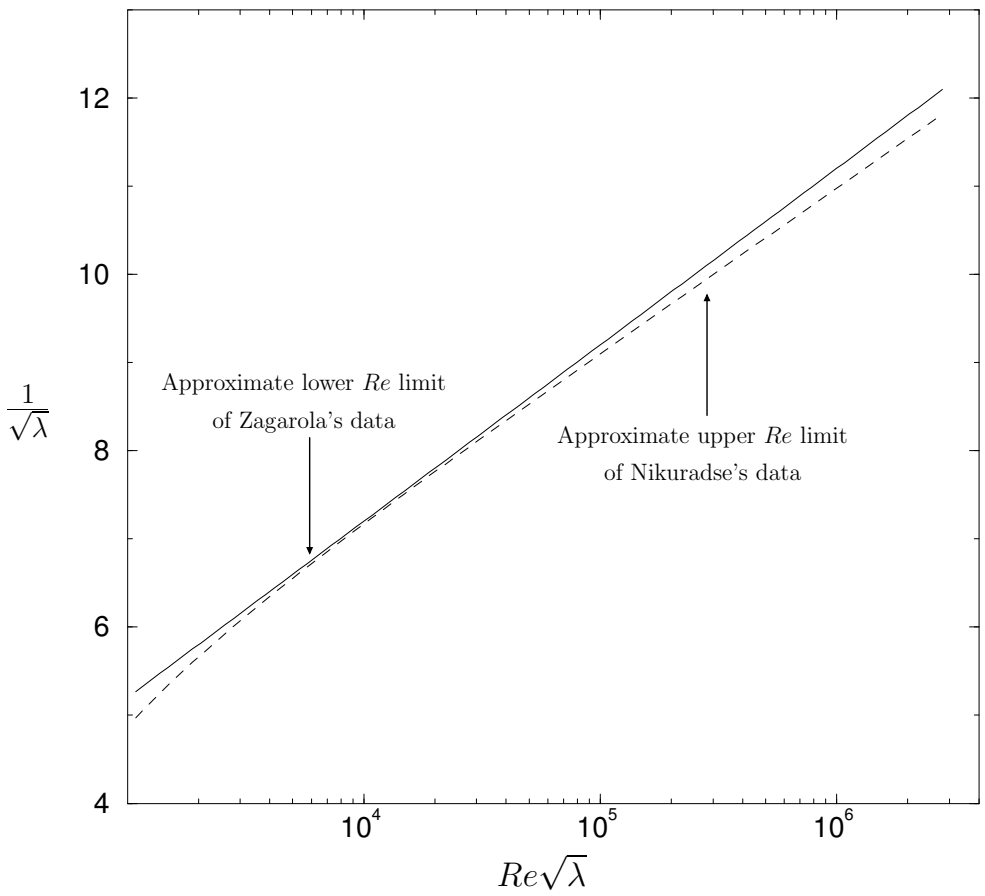

Figure 2.2: Comparison of friction factor relations: ——— , Prandtl's smooth wall law (2.7); ---- , Zagarola (2.9).

profiles in the pipe at high Re must have different log law constants, κ and A, when compared to those used by Prandtl.

This leads to the highly controversial Superpipe mean velocity profiles and their variation over the Reynolds number range. Some of these velocity profiles will be presented in Chapter 5 for comparison with results of the present study. Zagarola's analysis of the profiles yielded a power law relationship of the inner flow scaled velocity in the turbulent wall region for low Reynolds number. That is, for $Re < 230 \times 10^3$ the mean velocity scales as

$$U^+ = 8.7(y^+)^{0.137}. \tag{2.10}$$

For all higher Reynolds numbers, Zagarola found a combination of both the log and power laws was applicable. The classical log law was found to hold from $y^+ = 500$ to $y/R = 0.1$ with

$$U^+ = \frac{1}{0.436}\ln(y^+) + 6.13, \tag{2.11}$$

although the constants are obviously quite different to the traditional $\kappa = 0.41$, $A = 5.0$. For the region $50 < y^+ < 500$, the power law (2.10) was found to more suitably fit the data. In analysing these results, some researchers have postulated that the pitot tube measured profiles may have inappropriate corrections and roughness effects at high Reynolds numbers. Both potential criticisms are documented in Perry, Hafez & Chong (2001) which presents evidence of a shift in inner flow scaled velocity profiles at high Reynolds number — a characteristic roughness effect. A plot taken from Perry *et al.* (2001) is shown in figure 2.3 to illustrate this shift in velocity profiles and the clear effects of applying different pitot tube corrections (note that pitot corrections will be discussed further in §2.7). However, two important observations must be stated at this point:

i. Wall roughness effects on turbulence are poorly understood, especially at high Reynolds number.

ii. The Superpipe reaches Reynolds numbers that are an order of magnitude higher than any other study, and more than two orders of magnitude higher than most studies. Hence, without further high Reynolds number studies, it will always be difficult to argue that conclusions drawn from results at low Re will be applicable at the maximum Superpipe Reynolds number.

Unfortunately it was beyond the scope of this thesis to contribute to (i); however, pipe flow data recorded here will hopefully provide insights into pitot tube corrections with (ii) in mind.

In summary, the above results have stirred the fluid dynamics community because they challenge the classical laws that were once, without doubt, thought to extend to infinite Reynolds number. The repurcussions are evident in the literature: there have been numerous debates over high Reynolds number scaling of turbulent pipe flow and boundary layer flow since the publication of Zagarola & Smits (1998). See, for example, Perry *et al.* (2001), Österlund *et al.* (2000b), Barenblatt, Chorin & Protoskishin (2000), Österlund, Johansson & Nagib (2000a) and Panton (2002). These debates will undoubtedly continue until further high Reynolds number pipe flow data is available.

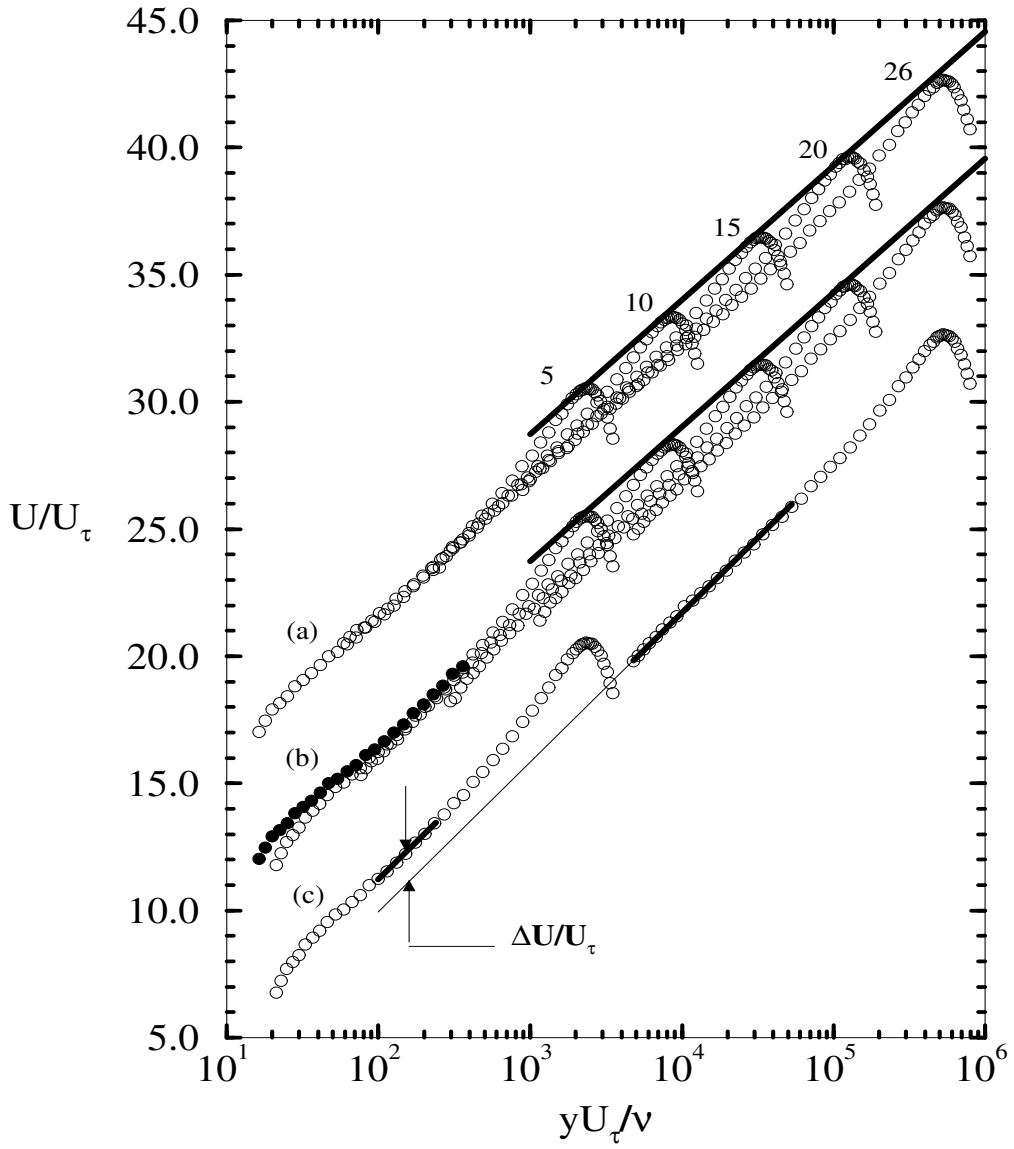

Figure 2.3: Reanalysed Superpipe data from Perry *et al.* (2001). (a) Uncorrected Superpipe data shifted up vertically by 5 ordinate units. Profiles 5, 10, 15, 20 and 26 correspond to Karman number $= K_\tau = 2.344\times10^3, 8.486\times10^3, 3.288\times10^4, 1.273\times10^5$, and 5.286×10^5 respectively. (b) Corrected Superpipe data, $\circ$, with uncorrected data, $\bullet$, superimposed for comparison. (c) Profile 5 is compared with profile 26; Both profiles are shifted down by 5 ordinate units. The slope of heavy logarithmic lines in (a) and (b) is $\kappa = 0.436$, while in (c) it is 0.39.

2.2.2 Recent results

More recently, McKeon & Smits (2002) used the superpipe to quantify errors and provide corrections for wall mounted static pressure tappings at high Reynolds number. Previous studies by Shaw (1960) and Franklin & Wallace (1970) have shown that for small hole diameter, d_s, the calculated error in pressure measurement tends to a universal constant as $d_s^+ = d_s U_\tau/\nu$ increased (that is, as Reynolds number increased). Interestingly, measured pressure was found to be higher than the true static pressure in all cases. However, both the Shaw (1960) and Franklin & Wallace (1970) studies were at much lower Reynolds number than the Superpipe study of McKeon & Smits (2002).

McKeon's careful experiments (detailed in the PhD thesis of McKeon, 2003) conclusively showed that the static pressure error does not asymptote to a constant value with rising d_s^+, nor does her pressure error data collapse onto a universal curve. The results of McKeon & Smits (2002) are summarised by an empirical correction for non-dimensional measured mean velocity, U_m^+, given by

$$U^+ = U_m^+ \sqrt{1 + \frac{2\Pi_m}{(U_m^+)^2}}. \tag{2.12}$$

Here, Π_m is the non-dimensional pressure error ($\Pi_m = \Delta p/\tau_w$, where Δp is the pressure error and τ_w is the wall shear stress) which may be interpolated from McKeon's data. Of importance to this thesis is that $\Pi_m \to 0$ as $d_s^+ \to 0$. Since static pressure measurements presented in this thesis are measured with tappings of $d_s^+ < 100$ (due to the relatively low Reynolds number), the maximum error in velocity measurements according to equation (2.12) is 0.084% — certainly an insignificant fraction for any experiment.

A second paper by McKeon concerning total pitot tube corrections was published in 2003. Note that further discussion of the methods and results of McKeon *et al.* (2003a) can be found in §2.7 which will cover pitot tube corrections in detail. To summarise, McKeon *et al.* (2003a) found a new displacement and wall correction that collapsed their data well. The authors also found that the MacMillan (1956) corrections gave almost identical results. However, the important finding was that the corrections proposed by Chue (1975) and adopted by Zagarola & Smits (1998)

performed poorly. McKeon *et al.* (2003a) concluded that the Chue (1975) correction should be discarded in favour of their new correction or that of MacMillan (1956).

McKeon's findings may have only a minor direct impact on the results of this thesis, however her studies did lead to an important reanalysis of Zagarola's data. Correcting the original static and total pressure measurements gave new constants for the log law ($\kappa = 0.421$ and $A = 5.6$, from McKeon *et al.*, 2003b) and friction factor relation,

$$\frac{1}{\sqrt{\lambda_p}} = 1.920 \log(Re\sqrt{\lambda_p}) - 0.475 - \frac{7.04}{(Re\sqrt{\lambda_p})^{0.55}}. \tag{2.13}$$

Furthermore, from data presented in McKeon (2003) it is evident that (2.13) is not noticeably dissimilar to Prandtl's traditional friction law (2.7) in the range of Reynolds numbers ($\sim 30 \times 10^3$ – 200×10^3) studied in this thesis. Therefore, it is not expected that data presented here will contribute to the argument over friction factor laws. However, it is important that the Superpipe results are discussed in detail here as they provided motivation for this study, as mentioned earlier, and will be frequently cited in subsequent chapters.

2.3 Further analytical forms of the velocity profile

In §2.1 the form of the velocity profile in the overlap region was introduced. While the significance of this region increases as Reynolds number increases, most of the velocity profile lies outside this region for the Re range of common studies. To describe the velocity profile in the inner or outer flow regions, one must resort to empirical relationships. In determining such relationships, the velocity profile is often broken down into three regions: the *sublayer* extending from the wall to the near edge of the outer layer, the overlap region, and the *wake* which spans the edge of the overlap region to the duct centreline.

Coles (1956) was the first to propose the concept of the law of the wall, law of the wake formulation:

$$U^+ = \frac{1}{\kappa} \ln(y^+) + A + \frac{\Pi}{\kappa} W_c(\eta), \tag{2.14}$$

where Π is commonly known as the Coles wake factor and W_c the Coles wake function. Π is a non-universal, free parameter to be determined from measured

velocity profiles. Coles (1968) suggested a possible wake function,

$$W_c(\eta) = 1 - \cos(\pi\eta), \tag{2.15}$$

which may be sufficient. For analytical work, however, a polynomial form of (2.15) is more convenient:

$$W_c(\eta) = 2\eta^2(3 - 2\eta), \tag{2.16}$$

as given by Jones (1998). Further, Jones, Marusic & Perry (2001a) points out that for 'pure wall flow' (i.e., flow having almost no wake†) these wake descriptions are inadequate since they assert that the log law continues until the shear layer edge. To solve this problem Jones *et al.* (2001a) introduce a *corner function*, $-\eta^3/(3\kappa)$, so that the law of the wall, law of the wake becomes:

$$U^+ = \frac{1}{\kappa}\ln(y^+) + A - \frac{1}{3\kappa}\eta^3 + \frac{2\Pi}{\kappa}\eta^2(3 - 2\eta). \tag{2.17}$$

It should be noted that the inclusion of the corner function will require different values of Π to fit the data as compared with (2.14) using either form of W_c. Defining Π_c as the value of Π determined from the result of including (2.15) in equation (2.14), it can be shown that, theoretically,

$$\Pi = \Pi_c + \frac{1}{6}, \tag{2.18}$$

where Π_c is Coles' original wake factor. Throughout the remainder of this thesis, values of Π will be determined from equation (2.17). Therefore Π is expected be higher than previously published values (of $\Pi = \Pi_c$) by roughly 1/6.

Prandtl's law of the wall (2.1) tells us that inner flow scaled velocity should follow a universal curve in the sublayer. Experiments confirm this behaviour and a number of authors have proposed curve-fits to the data. Two popular examples are referred to here. Firstly, Reichardt (1951) gives one equation to describe the complete inner flow velocity profile:

$$U^+ = \frac{1}{\kappa}\ln(1 + \kappa y^+) + \left(A - \frac{ln(\kappa)}{\kappa}\right)\left(1 - e^{-\frac{y^+}{11}} - \frac{y^+}{11}e^{-0.33y^+}\right). \tag{2.19}$$

This formulation has the correct asymptotic behaviour as illustrated in figure 2.4. It

† 'No wake' implies the velocity profile does not deviate above the log law and $\Pi \to 0$.

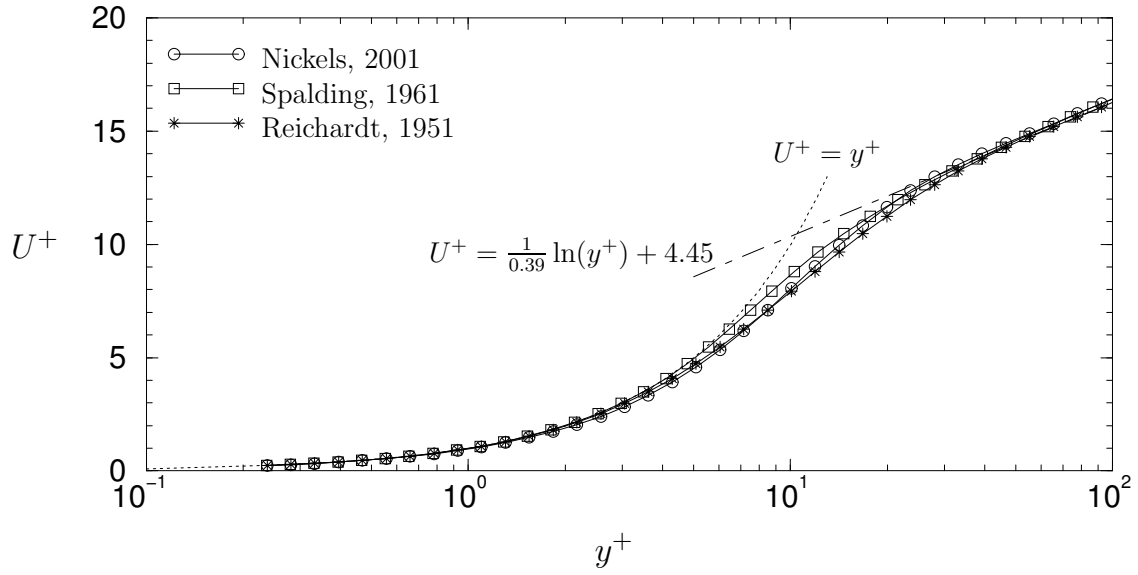

Figure 2.4: Sublayer velocity profile formulations given by Nickels (2001), Spalding (1961) and Reichardt (1951).

is observed that Reichardt's formula smoothly joins the log law (2.4) in the overlap region with the well-known linear relationship, $U^+ = y^+$, describing the viscous sublayer velocity profile. Secondly, the curve of Spalding (1961), who saw no reason why one should rigidly require U^+ as a function of y^+, is given as:

$$y^+ = U^+ + e^{-\kappa A}\left(e^{\kappa U^+} - 1 - \kappa U^+ - \frac{(\kappa U^+)^2}{2!} - \frac{(\kappa U^+)^3}{3!} - \frac{(\kappa U^+)^4}{4!}\right). \qquad (2.20)$$

This equation is also plotted in figure 2.4 which shows that (2.20) has the same asymptotic behaviour as (2.19); however, between the viscous sublayer and the overlap region, there is a noticeable difference between the two formulations. Unfortunately, for analyses appropriate to this study, Spalding's function was inconvenient, as U^+ was always required as a function of y^+.

The two formulations just described are appropriate for zero pressure gradient boundary layer or high Reynolds number duct flows. For wall-bounded flows where the non-dimensional streamwise pressure gradient,

$$p^+ = \frac{\nu}{U_\tau^3}\frac{dp}{dx}, \qquad (2.21)$$

is large enough, the sublayer velocity profile will deviate from (2.19) & (2.20). Nickels (2001) accounts for p^+ effects with the following functional form applicable to the

sublayer only:

$$U^+ = \frac{1}{a_0}(1 - [1 + 2a_0 y^+ + \frac{1}{2}(3a_0^2 - a_0 p^+){y^+}^2 - \frac{3}{2}a_0^2 p^+ {y^+}^3]e^{-3a_0 y^+}). \qquad (2.22)$$

If p^+ is negligible (i.e., $|p^+| < 0.002$) then a_0 is a universal constant. Nickels (2001) gives $a_0 = 0.0829 + 0.75p^+$ based on a number of experimental data analyses. Nickels' formulation is shown in figure 2.4 for comparison with (2.19) & (2.20). This formulation is important in duct flows where p^+ becomes significant for low Re. Although accurate experimental measurements in this Re range are rare, numerical simulation Reynolds numbers are typically in the range where pressure gradient effects are evident. Thus, when analysing duct flow DNS data, one must not expect collapse onto the inner flow formulations of Spalding and Reichardt; or for that matter, any high Re measurements.

2.4 Wall shear stress

The wall shear stress, τ_w, in fully developed duct flow is one of three parameters required to determine the Darcy friction factor, λ_p (U_b and ρ are the others), the behaviour of which was discussed in the previous section (§2.2). λ_p is a very important quantity in practical duct flows since it can be related to the head loss due to friction through the duct. For the purposes of this thesis, τ_w takes on further significance because almost all analyses of turbulence quantities require knowledge of wall shear stress at the measurement location. In fact, turbulence analyses for *any* wall-bounded turbulent shear flow require τ_w, because it is used to calculate the important velocity scale $U_\tau = \sqrt{\tau_w/\rho}$, introduced earlier as the *friction velocity*. Determining wall shear stress presents a serious obstacle for boundary layer researchers who have no reliable non-intrusive method for determining skin friction† . The most common methods employed are the Clauser (1954) method and the Preston tube (Patel, 1965); however, both rely on the assumption of Reynolds number similarity near the wall — a rather severe limitation, especially if one is interested in analysing the extent of this similarity. Numerous physical devices to intrusively measure shear

† The exception to this is the equilibrium boundary layer where a momentum balance gives U_τ, see Rotta (1962).

stress have been implemented, with varying degrees of accuracy. Examples are oil-film interferometry (Tanner & Blows, 1976) and Micro-Electro-Mechanical Machines (MEMS) employing hot-film devices (Österlund, 1999). Generally, these are expensive, complex devices that struggle to give better than 1% accuracy. Herein lies a significant advantage for duct flow experimentalists who have a simple, accurate and indirect method for determining τ_w, as will be explained in the following sections.

2.4.1 Pipe flow

A simple momentum balance of turbulent pipe flow gives the following equation relating wall shear stress to streamwise static pressure gradient, dp/dx:

$$\tau_w = \frac{D}{4}\left|\frac{dp}{dx}\right|. \tag{2.23}$$

Measurements confirm that the pressure gradient is constant if the flow is fully developed. Furthermore, dp/dx is easily measurable; experimentalists often only measure static pressure at two streamwise locations to determine dp/dx. Equation (2.23) has been well-known for many years, with measurements of friction factor based on τ_w dating back to the late 18th century as discussed in Chapter 1. Hence, determining wall shear stress in pipe flow is a simple and highly accurate exercise which requires no further validation or correction. When working with rectangular ducts, however, a complication emerges.

2.4.2 Rectangular duct flow

Experimentalists working with high aspect ratio rectangular ducts are generally interested in simulating true channel flow; that is, flow between infinitely wide parallel plates. One reason for this is that true channel flow is often studied not only by analytical and experimental researchers, but also by computational fluid dynamicists. Firstly, any turbulence analyst may be attracted by the similarities of channel flows with pipe flows and zero-pressure-gradient boundary layer flows. Second, fully developed channel flow is favourable to numerical simulation due to the simple geometry and applicability of the Cartesian coordinate system (cf. complications arising in

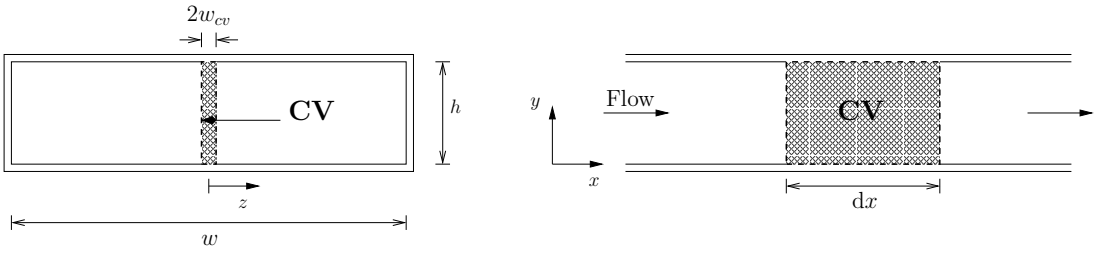

a) Front **b) Side**

Figure 2.5: Thin control volume (CV) containing only fully-developed two-dimensional flow.

pipe flow simulations in cylindrical coordinates, particularly at the pipe centreline). Moreover, an important advantage for computationalists and experimentalists alike, is that flow properties between parallel plates are independent of spanwise location. In other words, *true* channel flow is truly two-dimensional. In relation to wall shear stress (also invariant over the span), two-dimensionality ensures τ_w can again be determined from a simple momentum balance, similar to that which produced equation (2.23) for pipe flow. This momentum balance gives

$$\tau_w = \frac{h}{2}\left|\frac{dp}{dx}\right|, \tag{2.24}$$

where h is the channel height, at any location on the wall.

Obviously, in reality, the experimentalist has a finite aspect ratio rectangular duct in which τ_w will not be constant over the perimeter. If the aspect ratio is high enough, however, there may exist a section of the flow toward the centre of the duct which can be considered *nominally two-dimensional*. This means there is no measurable spanwise variation in mean streamwise velocity and the quotient of mean spanwise velocity and mean streamwise velocity is less than ± 0.005. In this case, the relationship for wall shear stress may be given by equation (2.24) — although not necessarily: the relationship depends on the choice of control volume over which the momentum balance is applied. If the control volume chosen encloses only a thin slice of the duct (as shown in figure 2.5) where the flow is known to be nominally two-dimensional, the momentum balance will return the result of equation (2.24). This is because the shear stress on the walls is the only shear stress at the control volume boundaries; shear on the sides of the control volume is zero in two-dimensional flow. Therefore, equation (2.24) will give accurate τ_w anywhere on the wall within $\pm w_{cv}$

of the centre. It must be noted that it is τ_w obtained in this way that should be used to calculate the important velocity scale, U_τ. Now, it is often argued that shear stress on the side walls of a rectangular duct affects the centre τ_w. However, *if* the flow is two-dimensional for $-w_{cv} < z < w_{cv}$ it is clear that there is no reason for side wall shear to enter the argument presented above.

Alternatively, if the control volume selected encloses the entire cross section of the channel (i.e., $-w/2 < z < w/2$), then the momentum balance gives a wall shear stress averaged over the perimeter (P) of the duct, $\overline{\tau_w}$.

$$\overline{\tau_w} = \frac{1}{P}\oint_P \tau_w(s)ds = \frac{wh}{2(w+h)}\left|\frac{dp}{dx}\right|, \tag{2.25}$$

where w is the channel width and s is a coordinate around the perimeter of the duct. The wall shear stress equation (2.25) now includes the shear stress on the side walls. However, $\overline{\tau_w}$ is obviously a different quantity to wall shear stress in the centre of the channel, τ_w. In fact, the perimeter-averaged shear stress is *only* useful for calculating total skin friction loss through the duct; $\overline{\tau_w}$ is not a useful quantity in turbulence scaling arguments. Furthermore, the definition of local skin friction in a channel,

$$C_f = \frac{\tau_w}{\frac{1}{2}\rho U_b^2}, \tag{2.26}$$

(cf. Darcy friction factor for a pipe) should not have τ_w replaced with $\overline{\tau_w}$ to account for side wall shear as suggested by Coleman *et al.* (1984).

It is critical then, to have some region of two-dimensionality in the duct flow in order to calculate τ_w accurately from the pressure gradient using equation (2.24) alone. As mentioned above, duct flow can never be truly two-dimensional unless the aspect ratio is infinite, a fact which implies an overestimation of centre wall shear stress determined by (2.24). This error in calculation of τ_w must depend on aspect ratio, A_s since it is this parameter that specifies the extent of two-dimensionality. Such an error term could simply be included in (2.24) so that:

$$\tau_w = \epsilon\frac{h}{2}\left|\frac{dp}{dx}\right|. \tag{2.27}$$

The *three-dimensionality factor*, $\epsilon(A_s)$ will be unity provided A_s is large enough that the flow is nominally two-dimensional near the centre. It would diverge from the

aims of this thesis to experimentally analyse this function and, moreover, such an analysis would require a variable aspect ratio rectangular duct facility. However, the aims of this thesis stated in Chapter 1 do require two-dimensional duct flow. Further, two-dimensional flow is necessary to assume $\epsilon(A_s) \approx 1$. In Chapter 4, exit velocity profiles, shear stress distributions and crossed hot-wire measurements will be presented, from which the extent of two-dimensional flow may be judged. At this point it is postulated that τ_w may be reliably calculated from streamwise pressure gradient through equation (2.24) for ducts with *large* aspect ratio (§2.5.2 discusses the criteria for 'large' A_s). τ_w calculated as such will be used throughout this thesis unless otherwise stated.

An important note concerning the above argument justifying equation (2.24), is that it does not suggest side wall shear stress is negligible. In fact, shear stress distribution plots show that the side walls make an appreciable contribution to the perimeter-averaged shear stress. However, the essential point made here is that the secondary flows in the vicinity of side walls have a negligible effect on the central flow region of a high aspect ratio duct.

2.4.3 Skin friction in rectangular ducts

From the previous section (§2.4.2) there are two wall shear stress definitions that may be of interest, depending on the motivation of the researcher. For example, Dean (1978), Schlichting (1936) and Laufer (1950) all required centreline wall shear stress, τ_w for turbulence scaling arguments; whereas Jones (1976) and Hartnett, Koh & McComas (1962) used $\overline{\tau_w}$ in studies motivated by practical engineering interests concerning total frictional loss through rectangular ducts of arbitrary aspect ratio. Therefore, when perusing the literature concerning skin friction in duct flow, the reader must ensure that the authors' field of interest is clearly understood . To reinforce this point, an example of confusion in the literature concerning the definitions of wall shear stress is discussed. Following this short discussion will be a review of the literature regarding the relationship of pipe flow friction factor to rectangular duct flow skin friction.

Coleman *et al.* (1984)

In this reference, the results of Schlichting (1936) are reanalysed by essentially substituting τ_w with $\overline{\tau_w}$. Coleman *et al.* (1984) argue that Schlichting ignored the side wall shear stress contribution on the assumption that it was negligible. It is correctly pointed out that studies have since shown side wall shear does make a significant contribution to $\overline{\tau_w}$ (e.g. Leutheusser, 1963, and results presented in Chapter 4). Coleman *et al.* (1984) conclude that Schlicting's skin friction results were significantly higher than they should be due to this 'mistake'. This is not a surprising conclusion since dividing equation (2.24) by (2.25) gives

$$\frac{\tau_w}{\overline{\tau_w}} = 1 + \frac{1}{A_s}, \tag{2.28}$$

which stipulates that $\overline{\tau_w}$ must always be less than centre ${\tau_w}^{\dagger}$. However, the criticism by Coleman *et al.* (1984) of Schlicting's work is inappropriate for the simple reason that Schlichting required τ_w to determine U_τ. That is, Schlichting (1936) was interested in studying turbulent flow behaviour, not total friction loss in the duct. Therefore Schlichting had no need to calculate the average wall shear stress. Although Schlichting's use of τ_w is acceptable, he did make a false assumption concerning the two-dimensionality of the duct flow. As discussed earlier, a large aspect ratio duct is required for two-dimensional flow in the centre of the duct; for Schlichting's duct, $A_s = 4.25$. It has been conclusively shown (see Chapter 4) that duct flows with an aspect ratio of less than 6 cannot be considered two-dimensional at the centre. Thus, referring to equation (2.27), the error factor, $\epsilon(A_s)$ would not be unity for an $A_s = 4.25$ duct.

Pipe-channel 'similarity'

The Darcy friction factor for pipe flow gives a measure of total frictional loss through the pipe. For rectangular duct flows a similar friction factor, λ_t, can be defined (hereafter referred to as *total friction factor*):

$$\lambda_t = \frac{4\overline{\tau_w}}{\frac{1}{2}\rho {U_b}^2}. \tag{2.29}$$

† This is because side-wall shear stress makes a smaller contribution to $\overline{\tau_w}$ than channel centre shear stress.

The total friction factor should not be confused with local skin friction, C_f, which is defined by (2.26) and requires centre wall shear stress rather than the perimeter-averaged value, $\overline{\tau_w}$. Studies of total friction factor in rectangular ducts are common and are often found in civil engineering journals. An excellent source is Jones (1976) who compiled total friction factor data from a number of other sources in addition to his own experimental results. The studies surveyed in this reference utilised rectangular ducts of various aspect ratio ranging from 1:1 to 39:1. It should be noted that throughout Jones (1976), Reynolds number is based on hydraulic diameter $D_e = 4A/P$ (A is the duct cross-sectional area) rather than the conventional channel height or pipe diameter, while $\lambda_t = \lambda_p$ and $D_e = D$ for pipe flow. Plots of total friction factor versus Reynolds number found in Jones (1976), unsurprisingly, show no collapse of the data for turbulent flow Reynolds numbers. Jones asserts that there must be some way to collapse this duct flow data onto Prandtl's smooth wall friction formula for circular pipes given in equation (2.7).

At this point the reader is reminded of the Prandtl smooth wall law (2.7) derivation† : the radial mean velocity profile through the pipe is integrated to determine the quantity, U_b/U_τ. This quantity defines λ_p for circular pipes (as given in equation 2.8) at any point on the pipe surface. To extend this to rectangular ducts is not physically sensible since τ_w values and mean velocity profiles vary with position on the duct perimeter. Moreover, the Prandtl smooth wall law derivation requires that the mean velocity profile normal to the surface of the duct is invariant over the perimeter, which *only* occurs with infinite aspect ratio ducts (true channel flows). However, even for true channel flows, the mean velocity profiles are not identical to pipe flow profiles. This is a well-known fact, although reasons for this are not yet understood. The wake strength of pipe flow velocity profiles is considerably larger than that of channel flow profiles, resulting in different values of the constant, C_2 of equation (2.7) for channel and pipe flows. This was not considered by Jones (1976).

Now, Jones proposed a modified Reynolds number,

$$Re^* = \frac{U_b \phi^*(A_s) D_e}{\nu}, \tag{2.30}$$

† See Appendix A for full details of this derivation.

where $\phi^*(A_s)$ was determined from the data of Cornish (1928) and is given here in approximate form as

$$\phi^*(A_s) \approx \frac{2}{3} + \frac{11}{24}\frac{1}{A_s}\left(2 - \frac{1}{A_s}\right). \tag{2.31}$$

Re^* was found to collapse λ_t for laminar rectangular duct flow onto the well-known laminar flow solution for pipe flow† ,

$$\lambda_p = \lambda_t = \frac{64}{Re^*}. \tag{2.32}$$

The highlight of Jones (1976) is the finding that simply replacing Re in Prandtl's formula with Re^* collapses the data with only $\pm 5\%$ scatter. Since there is no physial reasoning for this result, the generalised Prandtl smooth wall formula found by Jones (1976),

$$\frac{1}{\sqrt{\lambda_t}} = 2.0 \log_{10}(Re^* \sqrt{\lambda_t}) - 0.8, \tag{2.33}$$

can best be described as an empirical curve fit to the available data rather than the so-claimed "similarity between circular and rectangular geometries". Furthermore, whilst this is a neat and clever solution, it is suggested that other curve-fits could be investigated, such as a power law, which may give better collapse of the data. The only other criticism of the above analysis is that very little experimental data was considered; most data came from ducts with very small height and low Reynolds number (less than 100,000 based on D_e).

2.5 Recent developments in turbulent channel flow

The single most widely cited turbulent, smooth wall, high aspect ratio, rectangular duct flow study is that of Laufer (1950). For almost 30 years after Laufer's work, many investigations into this particular flow were conducted and a review of these was published by Dean (1978). Since 1978, experiment became overtaken by numerical simulation with the pioneering work of Moin & Kim (1982) leading to many more numerical investigations (e.g. Kim, 1987 and Kuroda *et al.*, 1993). Today there appears to be more effort directed toward the achievement of higher Reynolds number (and more geometrically complex) numerical simulations than experiments.

† For pipe flow: $\phi^* = 1$ so that $Re^* = Re$.

However, numerical channel flow studies must be validated by comparison with experimental data. In many cases concerning smooth wall flow, this is achieved through the data of Laufer (1950), underlining the reliance of current research on that data.

2.5.1 The benchmark study

The experimental results of Laufer (1950) are often accepted without question due to their frequent citation in the literature. Regardless of popularity however, the complexity and sensitivity of turbulent fluid flows obligate the researcher to look carefully at the flow condition and historical setting of any publication — Laufer (1950) is no exception. Firstly, it is important to note that only mean flow and skin friction data had been studied in channel flow prior to 1950, and even those studies were rare — Davies & White (1928) is among the few published. Laufer intended to take a rather large leap forward by measuring turbulent velocity fluctuations in a channel for the first time. Such measurements require high frequency response anemometers, necessitating the use of hot-wire anemometry technology which was still in its infancy in 1950. Indeed, Laufer was one of the first to use hot-wires for scientific experimentation and, since the superior constant temperature hot-wire anemometer was not discovered until the early 1960's, the only option was to employ the less reliable constant current anemometer.

The channel flow apparatus studied by Laufer (1950) was located at GALCIT† and had good spatial resolution with a height of $5''$ ($127mm$) and aspect ratio of 12:1. A single test was also carried out with the height reduced to $1''$ for comparison. As discussed later in this section, an aspect ratio of 12:1 should be more than sufficient to provide two-dimensional flow in the centre of the channel. The major criticism of the experimental apparatus of Laufer (1950) was that the overall length of the channel was only $23'$ ($7m$) and of this, the first $7'$ ($2.13m$) weakly diffused the flow as the channel height grew from $3''$ to $5''$. Therefore the development length, L/h of the channel was at best, 55 and if the diffusing section is excluded, $L/h = 38$

† Graduate Aeronautical Laboratories of the California Institute of Technology (Caltech), USA.

(values are for the 5″ height case). Although little is known about flow development, most experimentalists would now agree that these lengths are insufficient for fully developed flow.

As a pioneering work, Laufer (1950) is an impressive and important reference. Based on the above criticisms however, the data is not of sufficient accuracy to be used for validation of high accuracy numerical simulations or turbulence theories. That is, more accurate, truly fully developed flow data is presented in this thesis and is recommended for these purposes.

2.5.2 Literature review of mean flow results

Dean (1978) provides a comprehensive review of mean flow and skin friction variation in turbulent channel flow. Dean consulted a total of 42 references, of which he found only 27 could be considered 'channel' flow; that is, only 27 had sufficiently high aspect ratio. Based on his observations, Dean postulated that the minimum aspect ratio to ensure two-dimensional flow in the duct was 7:1. Thus, only references with ducts exceeding this aspect ratio were considered.

An important note about the collection of references cited in Dean (1978) is that flow development was not completely taken into account. Dean provides a table detailing the aspect ratio, method of determining τ_w, date and development length. He states that the reader should bear in mind that the channel development lengths range from $L/h = 23 - 500$; although he also states the minimum length required was unknown at the time of writing. Even to this day there has been no further advancement in knowledge of development length. This unknown property leads to the construction of possibly over-sized facilities, wasting time, valuable laboratory space and money. Hence an important aim of this study is to determine the required length of duct for full flow development (discussion of this topic is continued in Chapter 4).

The main aim of Dean (1978) was to determine suitable functions describing the behaviour of skin friction, C_f, with Reynolds number variation. Firstly, a simple power law curve-fit (cf. Blasius' pipe flow friction factor relation given in Appendix B) was

applied to the data in the turbulent Re regime. The result was

$$C_f = 0.073 Re^{-0.25}. \tag{2.34}$$

Dean continues, deriving a skin friction logarithmic law by integration of the mean velocity profile at the centre of the channel, similar to that of Prandtl (1935) for pipe flow. This law was written as

$$\sqrt{\frac{2}{C_f}} = \frac{1}{\kappa} \ln \left(\frac{Re}{2} \sqrt{\frac{C_f}{2}} \right) + F, \tag{2.35}$$

where

$$F = A + \frac{2\Pi_c}{\kappa} - \frac{U_{CL} - U_b}{U_\tau}.$$

The equation differs from Prandtl's law in that the wake component of the velocity profile is included in the derivation (appearing in the constant F). Through a comprehensive analysis of the mean velocity data, Dean finds $\kappa = 0.41$, $A = 5.17$ and $F = 3.2$. It is shown that κ and A are indeed universal as they have no dependence on Reynolds number. The reader should note, however, that the value of κ found was not representative of all data sets; Dean (1978) selected only a few data sets which he considered to be fully developed (i.e. the long channel flow data) to include in this analysis. This leads the reader to question why the short channel data sets are included in other analyses, especially in the determination of the other log law constant, A.

Dean's comparison of equations (2.34) and (2.35) with the skin friction data from the literature shows that both are a good fit — although equation (2.34) is, unsurprisingly, the better of the two since it is a curve-fit to the data. These formulations will be compared with data from the current investigation and discussed in more detail in Chapter 4.

2.6 Previous pipe flow studies at Melbourne

The investigation into pipe flow of this thesis was in fact the third experimental investigation involving the pipe apparatus at the University of Melbourne. Henbest

and Abell (independently) were the researchers involved with the previous studies, although the most recent of these (Henbest, 1983) commenced over 20 years prior to the current study. Both Henbest and Abell have been, and continue to be widely cited in the literature and their important results are summarised below.

2.6.1 Abell (1974)

The pipe flow facility was first constructed by Abell around 1970. At this time the pipe was relatively short with the measurment station being only $84.7D$ from the inlet. Thus the results presented in the thesis of Abell (1974) are questionable due to the potentially underdeveloped flow condition. The criticism may be regarded as harsh since Abell conducted many tests to ensure the flow was fully developed. These included comparing local mean velocity, turbulence intensity and centreline velocity spectra at two streamwise locations ($71.9D$, $84.9D$). After completing these tests and therefore having confidence that the flow was fully developed, Abell proceeded to measure all streamwise turbulence statistics and power spectral density (spectra) for both smooth and rough wall cases. Unfortunately for the current investigation, Abell used the Clauser chart with traditional log law constants ($\kappa = 0.41$, $A = 5.0$) to determine the friction velocity, U_τ. Since the values of U_τ determined as such were consistently lower than those given by the more appropriate pressure drop formula (2.23) (up to 3% lower according to Abell, 1974), it is difficult to draw meaningful comparisons between data collected during the current investigation and that presented in Abell (1974).

Among the most notable of Abell's experimental observations was the inverse power law ('-1 law') describing the power spectral density of streamwise velocity fluctuations. The power law relationship had previously been analytically deduced from dimensional arguments, while Abell's findings (also recorded in Perry & Abell, 1975) provided the supporting experimental evidence. Shortly after Abell (1974), it was shown that the -1 law was also predicted by the Perry & Chong (1982) attached eddy model for wall turbulence (see §2.9).

Another important result which was not documented until Perry & Abell (1977)

was a scaling law for streamwise turbulence intensity in the turbulent wall region:

$$\frac{\overline{u'^2}}{U_\tau^2} = B_1 - A_1 \ln[\eta] - C\left(\frac{yU_\tau}{\nu}\right)^{-\frac{1}{2}}, \tag{2.36}$$

where the constants A_1 and C are universal and B_1 is large scale characteristic. An extended form of equation (2.36) will be compared with new experimental data presented in Chapter 6. However, the reader is reminded of the aforementioned Clauser—U_τ issue, which should ensure that the constants of Perry & Abell ($A_1 = 0.80$, $B_1 = 3.53$ and $C = 9.54$) will not be reproduced here.

Finally, Abell found support for the inner flow scaling law (2.4) for mean velocity profiles, and the turbulent wall region was observed to extend from the traditional $y^+ \approx 100$ to $y/R \approx 0.1$. Constants in the log law (2.4) were effectively forced to be $\kappa = 0.41$ and $A = 5.0$ by application of the Clauser method for finding U_τ. Outer flow similarity was also observed, although the extent of collapse onto von Kármán's velocity defect law was not a consideration in Abell (1974).

It must be finally noted that after completion, Abell himself acknowledges the length of pipe used for his experiment was likely to be insufficient for full flow development (see Perry & Abell, 1977). Hence, the contribution of the Walter Bassett Aerodynamics Laboratory to turbulent pipe flow research was not to cease after Abell (1974)...

2.6.2 Henbest (1983)

Due to this speculation concerning development length, Henbest left nothing to chance as a further $315D$ in length was added to the pipe, bringing the total working section length to an extraordinary $398.5D$ or $39.77m$. This apparatus (detailed in Chapter 3) is one of the longest pipe flow facilities with such a large diameter, $D = 0.0998m$, used for the study of turbulence. Henbest, like Abell, experimented with both smooth and rough wall pipe flow and also repeated the same measurements: mean velocity profiles, friction factor, all turbulence statistics and spectra. Results found in the thesis of Henbest (1983) may be more suitable for comparison with the current study (than Abell, 1974) since the friction velocity appears to have

been correctly determined from pressure drop. It should be noted that Henbest is not clear on this point, however no mention of the Clauser chart is made, nor any other method of friction velocity determination other than the pressure drop method.

The two most important aims of Henbest (1983) were: i) to provide accurate data for a very long pipe flow free of development effects; ii) to experimentally validate the attached eddy model for wall-bounded turbulent flow proposed by Perry & Chong (1982). Results agreed well with model predictions and once again the -1 law was found in the inner flow scaled power spectral density. Many of Henbest's important results were also published in Perry, Henbest & Chong (1986). In Chapter 5, the smooth wall data of Henbest (1983) will be presented and compared with results of the present study.

Perhaps of most relevance to this study is that both Abell and Henbest chose not to measure mean streamwise velocity profiles with a hot-wire anemometer. A pitot tube was used for both investigations, despite the employment of hot-wires for most other measurements (e.g., turbulence intensity, Reynolds stress and spectra). This preference for pitot tubes is common in the literature — in fact, there are no pipe flow studies known to the author that provide accurate hot-wire measured mean velocity. Such measurements would be useful for comparison with pitot tube results which require corrections for known errors. The validity of these corrections is an often debated topic that will receive further attention in §2.7 below. Hence, an initial aim of this project was to record hot-wire measured mean velocity profiles in a turbulent pipe flow for comparison with pitot tube measurements.

2.7 Pitot tube corrections

The frequently used pitot tube anemometer is known to provide simple and accurate velocity measurements in non-turbulent, low-shear flows. Unfortunately, the same accuracy is not available when using the anemometer for measuring mean velocities in turbulent wall-bounded shear flows. In such flows the pitot tube is affected by various phenomena including shear, viscosity, wall proximity and turbulence.

Importantly, these effects vary throughout the shear layer and generally become more pronounced as the wall is approached. Errors due to most of these effects have been known for many years and so a variety of corrections for pitot tube measurements may be found in the literature; Young & Maas (1936), MacMillan (1956) and Chue (1975) are examples.

2.7.1 MacMillan's correction

Most popular among pitot tube experimentalists is the correction proposed by MacMillan (1956) (usually referred to as the MacMillan correction). The MacMillan correction provides a correction for the over-reading of pitot tube measured velocity, U_m, caused by the effects of shear. This is a very important correction since, in most cases, shear effects dominate other effects on the pitot tube. To determine the correction, MacMillan conducted a number of experiments in a turbulent pipe flow and boundary layer with circular, square-ended, pitot tubes of different outer diameter, d_p. Five tubes in total were used, with outer diameters of $d_p = 0.607, 0.74, 1.38, 2.30$ and $3.08mm$. The internal diameter of the pipe facility used by MacMillan was $50.8mm$ ($2''$). The procedure followed was to measure velocity profiles through the shear flow with all pitot tubes, ensuring wall-normal position was measured accurately. Then, at a given distance from the wall, the measured velocity, U_m of each pitot tube was plotted against d_p. From each U_m versus d_p plot, MacMillan extrapolated the data to $d_p = 0$, at which point U_m should be the true velocity, U (or at least U should be the velocity free from shear effects). Thus, MacMillan was able to determine the error in U_m as a function of d_p.

Now, MacMillan was aware of a study conducted many years earlier (Young & Mass, 1936) that proposed the error in pitot tube measured velocity may be more conveniently expressed as an error in wall-normal position, y; although the study of Young & Maas (1936) concerned free-shear flows, not wall-bounded flows. So, knowing the 'true' velocity profiles from extrapolation, MacMillan reinterpreted the

U_m error, producing the surprisingly simple displacement correction† :

$$\frac{\Delta y}{d_p} = 0.15, \tag{2.37}$$

where Δy is the necessary adjustment to probe position. This correction is favorable to the experimentalist since all that is required is an addition of $0.15d_p$ to each y-coordinate of the mean velocity profile. There exists published experimental data in support of MacMillan's correction and further evidence is presented in Chapter 5. Conversely, the author is unaware of any experimental evidence in the literature that reveals any serious limitations of the MacMillan correction. In support of the correction are, for example, Jones *et al.* (2001a) and McKeon *et al.* (2003a). Both references have very different approaches with Jones *et al.* (2001a) showing MacMillan corrected (pitot tube) turbulent boundary layer profiles collapse onto profiles measured with a hot-wire anemometer. McKeon *et al.* (2003a), on the other hand, compares corrected turbulent pipe flow velocity profiles measured with different diameter pitot tubes (cf. experiments of MacMillan, 1956). The latter, more recent study addresses some important questions and therefore warrants further discussion in this section.

Recent experimental support for the MacMillan correction

McKeon *et al.* (2003a) gives results of a recent Superpipe study into pitot tube corrections at high Reynolds number as briefly mentioned in §2.2.2. Following MacMillan's work, this investigation involved mean velocity profile measurement with four different diameter pitot tubes at two relatively low Reynolds numbers: 75×10^3 and 146×10^3. The smallest tube with outer diamter, $d_p = 0.3mm$ was also used for 21 velocity profile measurements over the Reynolds number range, $Re = 75 \times 10^3$ – 35×10^6. The latter data set was used for comparison with the original Superpipe data found in Zagarola & Smits (1998) (this original study utilised a larger pitot tube with $d_p = 0.9mm$). MacMillan's extrapolation to zero pitot tube diameter was not followed by McKeon *et al.* (2003a). Instead, the suitability of correction methods was judged by the extent of collapse of corrected velocity profiles measured

† Young & Maas (1936) proposed a very similar relationship for free-shear flows: $\Delta y/d_p = 0.18$.

with the different diameter pitot tubes. Note that this analysis only has the capacity to point out failure of a correction method since corrected measurements are not compared to 'true' values. So, although complete collapse of the data on to *one* velocity profile may be observed, the question of whether or not this is the 'true' profile is not addressed† .

Careful and accurate experimental techniques used by McKeon *et al.* (2003a) ensure that the data produced provides useful evidence in the ongoing debate over which pitot tube corrections are appropriate. Importantly, it was made quite obvious in McKeon *et al.* (2003a) that the correction of Chue (1975) was inadequate since it failed to collapse the different diameter pitot tube measurements onto a single curve. This is an important discovery since Zagarola & Smits (1998) applied Chue's correction represented by

$$\frac{\Delta y}{d_p} = 0.18\alpha(1 - 0.17\alpha^2), \tag{2.38}$$

where

$$\alpha = \frac{d_p}{2U}\frac{dU}{dy},$$

to all pitot tube measurements. Note that in the definition of the shear parameter, α, U and its gradient must be evaluated at the geometric centre of the pitot probe. In light of McKeon *et al.* (2003a), the results of Zagarola & Smits (1998) were reanalysed (as discussed in §2.2.2) and new conclusions were drawn concerning mean flow behaviour in wall-bounded shear flows.

While Chue's correction was dismissed, McKeon *et al.* (2003a) show that the MacMillan correction collapsed all pitot tube data effectively. Even so, the authors propose a new, alternative correction that includes the shear parameter, α:

$$\frac{\Delta y}{d_p} = 0.15\tanh(4\sqrt{\alpha}), \tag{2.39}$$

Although (2.39) is shown to perform very well, no quantified evidence was presented that would suggest this far more complex correction should take preference over

† This is not a criticism of McKeon *et al.* (2003a); the author is aware that a 'true' reference velocity cannot be determined beyond doubt at this time. However, hot-wire data is commonly accepted as sufficient for comparison.

the MacMillan correction. Theoretically, (2.39) is more correct than MacMillan's correction because $\Delta y \to 0$ as the edge of the shear layer (or centreline of a duct) is approached, whereas this will obviously not occur with the MacMillan correction. However, in support of MacMillan's correction, $\Delta y = 0.15 d_p$ becomes a negligible quantity near the edge of the shear layer.

From the reliable experimental data presented by McKeon *et al.* (2003a), private communications with other experimentalists and data presented later in this thesis, the author holds the view that the correction for shear effects on pitot tube measurements is no longer in debate for any Reynolds number up to 35×10^6. Furthermore, there appears no reason that the corrections should become inappropriate at even higher Reynolds numbers. Finally, while the correction proposed by McKeon *et al.* (2003a) is technically more appropriate, the simple MacMillan displacement correction has been proven to be adequate. Hence, MacMillan's correction has been applied to all velocity profiles measured with a pitot tube in both the circular pipe flow and channel flow investigations of this thesis.

2.7.2 The effects of turbulence

When taking pitot tube measurements in any turbulent flow, a correction for the effects of turbulent velocity fluctuations is required. This is due to the fact that, when using a pitot tube, static pressure[†] is subtracted from pitot measured total pressure to give dynamic pressure; that is, velocity is not measured directly. This can be shown analytically[‡] by examination of the equation of motion of a fluid element moving along a streamline (*Euler's* equation):

$$-\frac{1}{\rho}\frac{\partial p}{\partial s} = q\frac{\partial q}{\partial s} + \frac{\partial q}{\partial t}, \tag{2.40}$$

where s is a coordinate along the streamline, q is the velocity in the s direction, t is time and p is pressure. Note that viscosity and external body forces are insignificant in this analysis and so have been neglected in equation (2.40). Integrating along the

[†] Usually measured with a static pressure tube or wall tapping.

[‡] After Goldstein (1936).

streamline gives

$$\frac{p}{\rho} = -\frac{1}{2}q^2 - \int \frac{\partial q}{\partial t} ds + f(t), \tag{2.41}$$

where $f(t)$ is a time varying constant of spatial integration. For wall-bounded turbulent shear flows, q may be decomposed into mean and fluctuating components, Q and q' respectively. Applying the same decomposition to pressure, substituting into equation (2.41) and time-averaging the result gives

$$\frac{\overline{P + p'}}{\rho} = -\frac{1}{2}\overline{(Q + q')^2} - \int \frac{\partial \overline{(Q + q')}}{\partial t} ds + constant. \tag{2.42}$$

By definition, $\partial Q/\partial t = 0$ and $\overline{p'} = \overline{q'} = \overline{Q \cdot q'} = 0$ so that (2.42) may be simplified to

$$\frac{P}{\rho} + \frac{1}{2}(Q^2 + \overline{q'^2}) = constant, \tag{2.43}$$

which differs from the classical Bernoulli equation only by the turbulence intensity term, $\overline{q'^2}$. Assuming a pitot tube is aligned with the flow direction, then $Q = U$. It can also be shown that the resultant mean square of fluctuating velocity, $\overline{q'^2} = \overline{u'^2} + \overline{v'^2} + \overline{w'^2}$. Finally, with reference to the local static pressure, (2.43) can be used to determine the following relationship:

$$\Delta P = \frac{1}{2}\rho(U^2 + \overline{u'^2} + \overline{v'^2} + \overline{w'^2}). \tag{2.44}$$

However, due to the relatively small magnitudes of $\overline{v'^2}$ and $\overline{w'^2}$, it will be assumed acceptable to neglect these components, leaving

$$\Delta P = \frac{1}{2}\rho(U^2 + \overline{u'^2}). \tag{2.45}$$

Now, the pitot tube measures — relative to static pressure — ΔP, the mean dynamic pressure. Therefore, the calculated velocity without turbulence correction, U_m is not the true velocity — in fact,

$$U_m = U^2 + \overline{u'^2}. \tag{2.46}$$

This applies to any pitot tube, regardless of diameter, for the simple reason that there is a non-linear relationship between velocity and dynamic pressure.

MacMillan (1956) is quite clear in stating that his correction for shear did not account for the effects of turbulence, which implies that a turbulence correction

should be applied in addition to the MacMillan correction. However, it is argued in McKeon *et al.* (2003a) that applying both corrections is inappropriate because MacMillan's correction was derived from experiments conducted in turbulent shear flows and therefore implicitly accounts for turbulence effects. Now, in summary of the above explanation of MacMillan's experiment: the correction deduced effectively calibrates a pitot tube of arbitrary diameter against one of zero diameter; that is, a tube that provides no interference to the flow and is unaffected by velocity gradient. This infinitely small pitot probe *still measures pressure*, however. Therefore the $d_p = 0$ reference velocity, which MacMillan determined by extrapolation, is itself affected by turbulence due to equation (2.45). Put simply, the MacMillan correction is essentially a spatial correction whereas the effect of turbulence on pitot tubes is temporal in nature.

McKeon *et al.* (2003a) extend their argument against a turbulence correction by providing experimental evidence showing that application of the correction, in addition to MacMillan's, over-corrects the data. This conclusion is based on the pipe flow data of McKeon *et al.* (2003b), with correction for turbulence applied, failing to blend on to the well-known $U^+ = y^+$ curve which holds in the viscous sublayer of the flow (i.e., below $y^+ \approx 5$). There are many reasons why this misalignment might be observed, not the least of which is experimental error. For example, a simple calculation reveals that a wall-normal position error of only $18\mu m$ would completely account for the observed deviation in the viscous sublayer region (based on $d_p = 0.3mm$ and $U_\tau = 0.42$, estimated from data published in McKeon *et al.*, 2003a). However, the trends in experimental data are irrelevant to this argument. There is no doubt that the effects of turbulence *must* be accounted for by virtue of (2.45) — notwithstanding the fact that the turbulence correction has a small impact on the data relative to the MacMillan correction for common pitot tube diameters.

An explicit turbulence correction

The turbulence correction can easily be determined by inspection of equation (2.45) and is written in full as:

$$U^+ = \frac{U}{U_\tau} = \sqrt{\left(\frac{U_m}{U_\tau}\right)^2 - \frac{\overline{u'^2}}{U_\tau^2}}, \tag{2.47}$$

where U_τ is the friction velocity. Clearly, to apply this correction requires knowledge of the scaled $\overline{u'^2}$ profile of the flow. Empirical relationships for turbulence intensity are available (equation (2.36) from Perry & Abell (1977) is commonly cited for example) although the accuracy of such relationships is questionable due to experimental error in $\overline{u'^2}$ data in the inner flow region. One source of this error is that high response anemometers (e.g. hot-wires) used to measure turbulent velocity fluctuations are now known to suffer from the effects of inadequate spatial resolution at low to moderate Re. Further work is required to understand these problems which limit the accuracy of the turbulence correction near the wall. Note however, that the turbulence correction is relatively small in magnitude, particularly as the wall is approached. Therefore, errors in — or assumptions about — turbulence intensity profiles are likely to have little noticeable effect on the corrected velocity profile.

All MacMillan corrected velocity profiles measured with a pitot tube presented in this thesis will have the additional turbulence correction (2.47) applied; turbulence intensity is determined from normal hot-wire measurements.

2.7.3 Wall proximity correction

In addition to his correction for shear, MacMillan (1956) proposed a *wall proximity* correction. This correction accounts for the effect of the pitot tube when it is very close to the wall. The criteria to determine whether a tube was 'close to the wall' was found to depend on pitot tube outer diameter only; that is, for $y < 2d_p$ a wall proximity correction was found necessary. Now, MacMillan had already determined the true velocity profile for $y > 2d_p$, as described in §2.7.1, down to $y^+ = 30$. It was therefore possible to compare non-dimensional velocity measurements at a given y^+ made with pitot tubes of various outer diameter with the 'true' velocity

profile. With this method it was found that the wall proximity correction was most conveniently represented by a single curve relating the quotient of velocity correction and measured velocity ($\Delta U/U_m$) to y/d_p. MacMillan (1956) provides a graph of $\Delta U/U_m$ versus y/d_p from which the author has extracted and tabulated data points; this table is included for reference in Appendix C. An interesting observation of the wall correction is that it shows the velocity is *under-read* by the pitot tube for $y < 2d_p$ — so the wall proximity effect is in opposition to the effect of shear (which causes over-reading of velocity).

It is acknowledged here that MacMillan's wall proximity correction was shown to be inaccurate by McKeon *et al.* (2003a). However, due to the simplicity of the correction, the small magnitude of error highlighted by McKeon *et al.* (2003a) and the inconsequence of this error to the velocity profile regions of interest here, MacMillan's correction for wall effects is applied to all pitot tube measurements in the range $y < 2d_p$ presented in this thesis.

2.8 Numerical simulation

The field of numerical simulation is a promising and rapidly advancing one. Unfortunately, at this point in time computational power is insufficient to simulate duct flows at the Reynolds numbers easily obtained in the laboratory. As discussed earlier, the pioneering numerical investigation into channel flow simulation was that of Moin & Kim (1982). This study introduced the *Large Eddy Simulation* (LES) approach which requires the input of a turbulence model for the fine scales; that is, only the large scale motions are numerically computed. This allows the simulation of higher Reynolds number flows by sacrificing spatial resolution. At the time of writing, Karman numbers in the vicinity of 1000 (corresponding to $Re \approx 30 \times 10^3$ for the channel flow of this study) are possible with LES.

Direct Numerical Simulation (DNS) does not suffer from the limitation of LES since all scales are resolved by numerical solution of the Navier-Stokes equations — the governing equations of fluid flow. The Reynolds numbers attainable are much lower using DNS than LES. Kim *et al.* (1987) was one of the first DNS studies into

fully developed channel flow. For their study $Re_c = 3300$, where Re_c is Reynolds number based on centreline velocity. This is an order of magnitude lower than the lowest Re of this study. For constant pressure turbulent boundary layers, Spalart (1990) conducted a DNS study reaching a Reynolds number based on momentum thickness of $Re_\theta = 1410$. This corresponds to a Karman number, $K_\tau = \Delta U_\tau/\nu$ of approximately 750 which may be compared with the lowest K_τ studied in this thesis of $K_\tau \approx 1000$. Spalart (1990) is a useful reference since, although the Reynolds number is low, the behaviour in the inner flow region of the boundary layer should be the same as that at higher Re, as discussed earlier. This highlights a problem with low Reynolds number duct flow simulations — the pressure is not constant. Thus the pressure gradient parameter, p^+, will affect the flow as discussed in §2.3. This makes comparisons of most experimental duct flow data with most DNS data impossible. In fact, comparisons of experimental data with Spalart (1990) would be more useful than with simulations of duct flow.

While DNS algorithms continue to progress and computational power increases, current technology does not allow the fully resolved simulation of even moderate Re duct flows. Thus, in this thesis only the data of Spalart (1990) will be compared with experimental results. Further, the LES method requires knowledge of fine scale behaviour and it is suggested that data acquired in this experimental project may be useful for the validation of fine scale models.

2.9 The mechanism of wall turbulence

At this point it may be observed from the literature that most studies present statistical wall-bounded turbulence data which implies a certain degree of randomness of the turbulence. Conceptual models that aim to provide a physical understanding of the mechanism of wall turbulence are comparatively much more difficult to find. One such concept is the *Attached Eddy Hypothesis* of Townsend (1976) which considers turbulence as a field of organised eddies or structures with an important property:

> "The velocity fields of the main eddies, regarded as persistent, organised flow patterns, extend to the wall and, in a sense, they are *attached* to the wall." *Townsend (1976), p152.*

This hypothesis allowed Townsend (1976) to model the complex turbulent flow with reasonable success. More pertinent to this thesis, however, is that the above hypothesis formed the basis for a detailed turbulence model established by Perry & Chong (1982).

2.9.1 The hierarchy of structures

The proposition that wall-bounded turbulent flow contains hairpin-type vortex loops is well supported in the literature. The famous boundary layer flow visualisations of Head & Bandyopadhyay (1981) and the annual review of Robinson (1991) are two of the earlier publications. More recently, substantial evidence has arisen from both numerical simulation of channel flow, Liu & Adrian (1999), and Particle Image Velocimetry (PIV) measurements in a boundary layer, Adrian, Meinhardt & Tomkins (2000) and Ganapathisubramani, Longmire & Marusic (2003).

After observation of the flow visualisations of Head & Bandyopadhyay (1981), Perry & Chong (1982) proposed the model of boundary layer turbulence consisting of a random array of characteristic hairpin vortices. These vortices grow out of the viscous sublayer 'material', then undergo a period of stretching until their ultimate 'death' by viscous dissipation and vorticity cancellation; the characteristic vortices were all considered to be inclined at 45^o. For simplicity, Perry & Chong (1982) considered only the $\wedge$-shaped vortex, as shown in figure 2.6a, rather than the more complex hairpin or horseshoe vortices. It was shown that an array of such vortices, all at different stages of stretching, does not give the required mean velocity distribution. That is, the model resulted in a limit on the extent of the overlap region, where the log law is valid, as Re increases. It is commonly accepted that the overlap region continues to increase as $Re \rightarrow \infty$. To overcome this problem Perry & Chong (1982) proposed the *hierarchy* of geometrically similar eddies as shown in figure 2.6. The eddies shown are in the final stages of stretching and the characteristic height

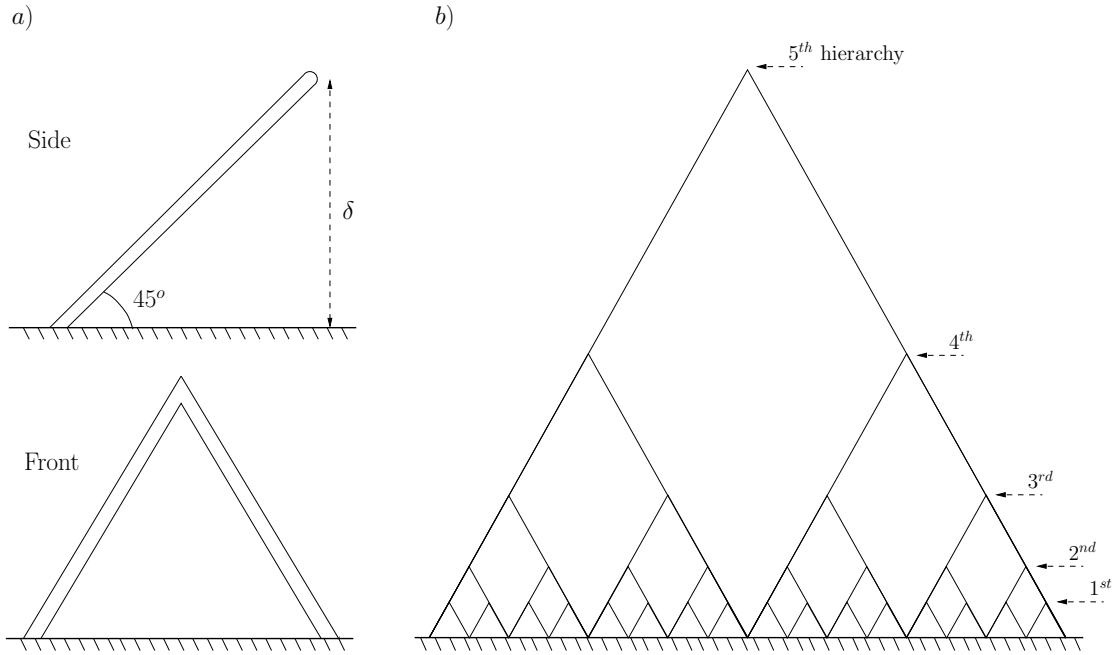

Figure 2.6: a) Schematic of a simple ∧-vortex; b) The discrete hierarchy of eddies proposed by Perry & Chong (1982).

scale of eddies at such a stage is δ. For a discrete system of hierarchies this height scale increases by a factor of 2 for each hierarchy. The introduction of this system of eddies gave the desired mean velocity behaviour as $Re \to \infty$. Perry & Chong (1982) concede that the mechanism for the formation of hierarchies remains a mystery. Although it was conjectured that a vortex in a given hierarchy may be formed by the pairing of two vortices from the hierarchy below. Finally, the hierarchy concept was further extended to the more realistic continuous distribution of scales. It was shown that, to achieve the same mean velocity behaviour as the discrete hierarchy system, the required p.d.f. (probability density function) of scales was:

$$p_H(\delta) = \frac{M}{\delta}, \tag{2.48}$$

where M is a constant.

Having conceptually developed the array of attached eddies in a turbulent flow, Perry & Chong (1982) show that second order statistics can be calculated through

$$\frac{\overline{u_i u_j}}{U_\tau^2} = \int_{\delta_1}^{\Delta_E} I_{ij} p_H(\delta) d\delta; \tag{2.49}$$

a result also derived by Townsend (1976). Townsend referred to I_{ij} as the eddy-intensity function and δ_1 is the smallest hierarchy scale, assumed to be of the Kline

et al. (1967) scaling order (i.e., $\delta_1 \sim 100\nu/U_\tau$). Δ_E is the height scale of the largest hierarchy. Incorporating the proposed functional forms of I_{ij} given in Townsend (1976), equation (2.49) predicts a constant Reynolds shear stress and wall-normal turbulence intensity, while logarithmic distributions of streamwise and spanwise turbulence intensity are given. Perry & Chong (1982) finally calculate the spectra of streamwise velocity Φ_{11}, showing that a -1 power law in the moderate $k_1 y$ range (where k_1 is streamwise wavenumber) is predicted, provided enough hierarchies are included. That is,

$$\frac{\Phi_{11}(k_1 y)}{U_\tau^2} = \frac{C}{k_1 y}, \tag{2.50}$$

where C is a universal constant. It is interesting to note that dimensional arguments presented in Perry & Abell (1975) led to the same result as (2.50). Additionally, the attached eddy prediction of logarithmic streamwise turbulence intensity was also deduced by Perry & Abell (1977) from the spectral similarity law (2.50). Some limited experimental pipe flow spectra (from Abell, 1974) was supplied by Perry & Chong (1982) which roughly supports (2.50). However, figure 24 of this reference implies that *at least* 10 hierarchies of eddies (using the discrete system of hierarchies) are required before a -1 slope appears in the predicted spectra. Assuming $\delta_1^+ = \delta_1 U_\tau/\nu = \mathcal{O}(100)$ (after Kline *et al.*, 1967) the Karman number, K_τ, of the flow required for the streamwise spectra to exhibit the -1 law is $K_\tau = \Delta_E^+ = \mathcal{O}(10^5)$. For the study of Abell (1974): $K_\tau = \mathcal{O}(10^3)$; indeed, this order is typical of most laboratory flows including those of the present study.

2.9.2 Modifications to the attached eddy model

The foundational study of Perry & Chong (1982) provided an interesting and useful explanation of the turbulent flow in the overlap region. The behaviour of the outer flow region, however, remained unexplained. That was until the publication of Perry, Henbest & Chong (1986). By considering a variety of different shapes of eddies, Perry *et al.* (1986) showed that simply changing eddy shape could never satisfactorily describe the wake behaviour of the mean velocity. It is worth noting that the most promising characteristic eddy shapes found were the previously tested $\wedge$-vortex and the $\sqcap$-vortex which is featured in figure 2.9. It was eventually found that simply

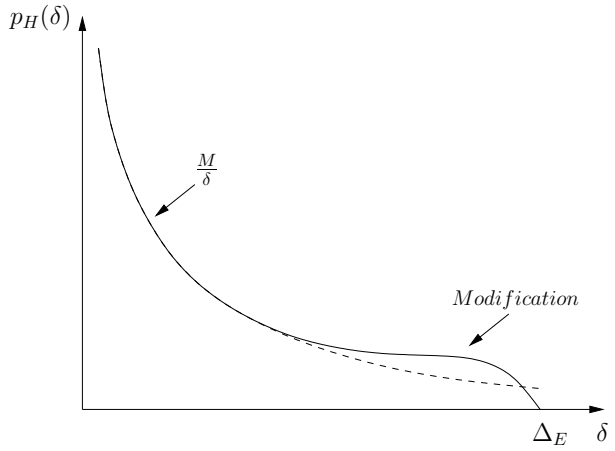

Figure 2.7: An illustration of the original and modified p.d.f. of hierarchy scales. Δ_E is the scale of the largest hierarchy.

modifying the p.d.f. of hierarchy scales could account for the known streamwise mean velocity deviation from a log law in the outer flow region. The modification involved an increase in p.d.f. (above $1/\delta$) for the larger scales as illustrated in figure 2.7. Now, since the new p.d.f. was not physically justified, any model using an arbitrarily modified p.d.f. requires the prescription of the mean velocity field. That is, the mean velocity is not *given* by the model; rather it is an *input* to the model.

Another major change by Perry *et al.* (1986) to the original model was a new method of calculating spectra. By introducing the variable $\lambda = \ln(\delta/y)$ the p.d.f. of scales can be written as

$$p_H(\delta) = \frac{M}{\delta} W(\lambda - \lambda_E). \tag{2.51}$$

W will be referred to hereafter as the *weighting function* for hierarchy scales† and $\lambda_E = \ln(\Delta_E/y)$. It was shown that the spectra of any velocity component is simply given by:

$$\frac{\Phi_{ii}}{U_\tau^2} = \frac{1}{k_1 y} \int_{\lambda_1}^{\lambda_E} M \frac{\psi_{ii}(k_1\delta, \lambda)}{U_\tau^2} W(\lambda - \lambda_E) \bigg|_{k_1 y \,=\, \text{const}} d\lambda. \tag{2.52}$$

ψ_{ii} is termed the *pre-multiplied hierarchy spectral function*; it is the contibution to the pre-multiplied spectra from one hierarchy of eddies and it may be determined as follows:

† It should be noted that Perry *et al.* (1986) label the weighting function w; to avoid confusion with the spanwise component of velocity and channel width definitions in this thesis, however, W was deemed a more appropriate variable.

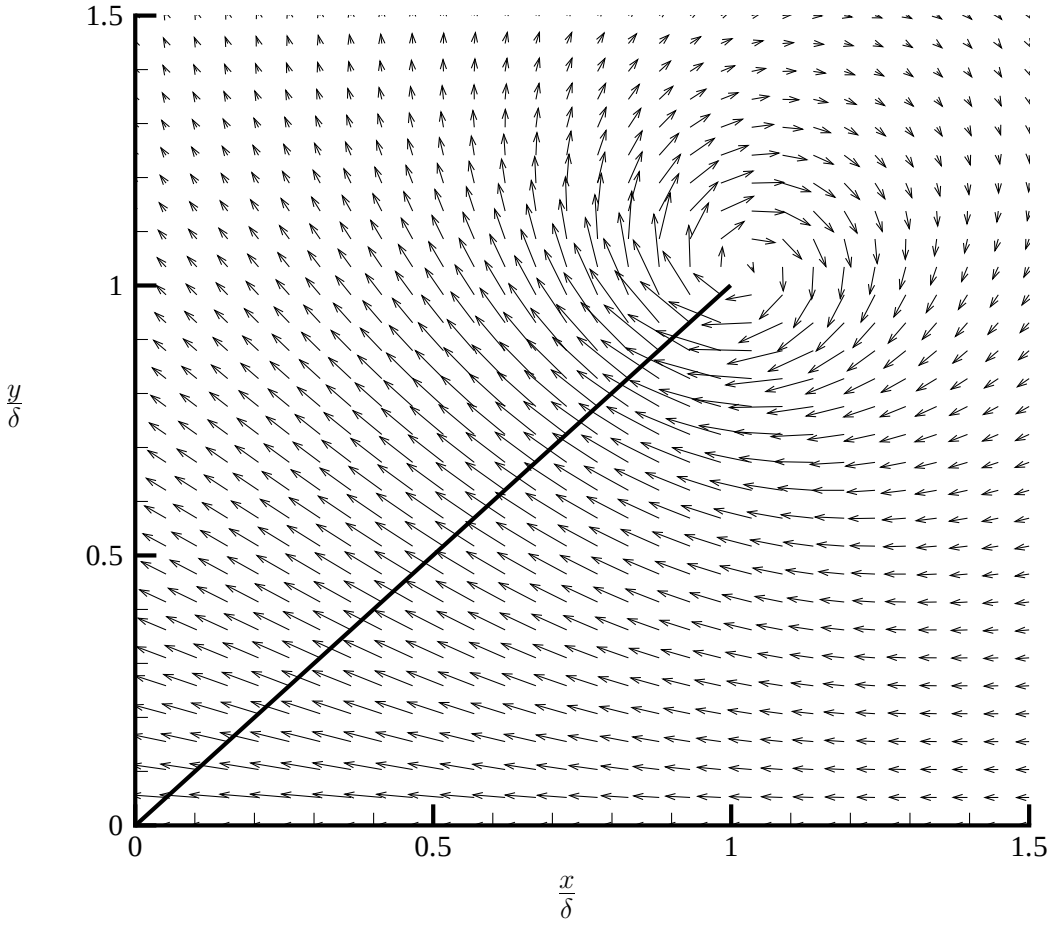

Figure 2.8: Velocity field in the $x-y$ (symmetry) plane of an attached $\sqcap$-eddy. A solid line is drawn through the centre of one 'leg' of the eddy. Note the rapid decay in velocity magnitude beyond $y/\delta \approx 1$.

1. The velocity field generated by an isolated attached eddy of height scale δ and its image in the wall is calculated from the Biot-Savart law. An example of such a field is shown in figure 2.8 which presents velocity vectors in the $x-y$ plane of a $\sqcap$-shaped eddy. A three-dimensional illustration is provided in figure 2.9. In this figure, streamlines in the vicinity of an isolated $\sqcap$-vortex are shown for the $x-z$ and $x-y$ planes. The vortex rods have a core radius of 0.1δ.

2. The power spectral density (PSD) of velocity signatures in a given y/δ plane along a line of constant z/δ (i.e., a streamwise 'cut') is calculated. The PSD for each streamwise cut will be a function of non-dimensionalised streamwise wavenumber, $k_1\delta$.

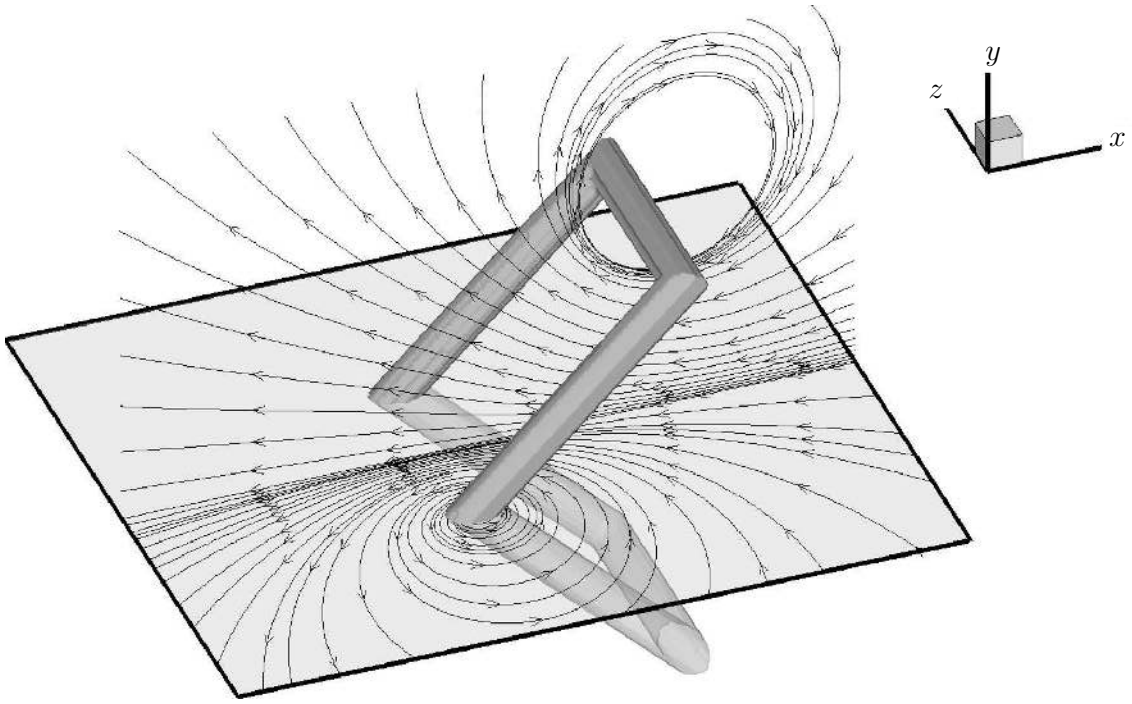

Figure 2.9: Streamlines in the $x-z$ and $x-y$ planes around an attached $\sqcap$-eddy. The shaded plane is the wall; the lower, translucent 'eddy' represents the attached eddy's image in the wall.

3. An ensemble average of the PSD for all streamwise cuts is formed for a given y/δ (i.e., wall-normal distance). Pre-multiplying this ensemble average by $k_1 y$ gives ψ_{ii} as a function of $k_1\delta$ at a given y/δ.

The final step is to perform the integration of (2.52) to determine the PSD (spectra) for all hierarchies. This integration is not straightforward and the reader is encouraged to consult Perry *et al.* (1986), Li (1989) or Marusic (1991) for more details on this. Whereas the Perry & Chong (1982) method was used to calculate u spectra only, this new method clearly allows the calculation of the spectra of any velocity component. Further, any desired modification to the p.d.f. is easily implemented by simply altering W (this is a useful feature if wall-bounded flows with various geometries or pressure gradients are of interest).

2.9.3 Recent extensions to the attached eddy model

Since Perry *et al.* (1986), the attached eddy model has been successfully extended to rough wall flows (see Perry *et al.*, 1987, and Perry & Li, 1990) and non-zero pressure gradient boundary layers (see Perry & Marusic, 1995, and Marusic & Perry, 1995). Even turbulent jet characteristics have been modelled using arrays of haripin vortices (see Nickels & Perry, 1996, and Nickels & Marusic, 2001).

The pressure gradient studies show that any model incorporating only one shape of eddy, regardless of weighting function or geometry, cannot predict the correct behaviour of Reynolds shear or normal stresses for strongly adverse pressure gradient boundary layers. This problem was very successfully removed by adding an array of a second type of eddies that are not *attached* to the wall. These were named 'type-B' eddies; the attached $\sqcap$-eddies were termed 'type-A' and their arrangement and individual properties remain as described above. No further discussion of 'type-B' eddies is warranted here as they are unnecessary for modelling of constant area turbulent duct flows. Perry & Marusic (1995) also introduce the additional weighting function, $T(\lambda-\lambda_E)$, to account for changes in the velocity scale between hierarchies of eddies (e.g. changes in circulation). Implementation simply involves multiplying $T(\lambda-\lambda_E)$ into the integrand of equation (2.52). Introducing this new weighting function, equation (2.51) and the variable λ into equation (2.49) gives:

$$\frac{\overline{u_i u_j}}{U_\tau^2} = \int_{\lambda_1}^{\lambda_E} I_{ij}(\lambda) T^2(\lambda-\lambda_E) W(\lambda-\lambda_E) d\lambda. \tag{2.53}$$

This equation is simply a convolution of $I_{ij}(\lambda)$ and $T^2W(\lambda)$. Therefore, if one knows or can deduce the formulation of $I_{13}(\lambda)$, T^2W may be determined by a deconvolution of the expected/measured $\overline{u_1 u_3}$ (Reynolds shear stress,also referred to as $\overline{u'v'}$ in this thesis) distribution. T can be extracted from T^2W since the known mean flow behaviour dictates W. The remaining second order turbulence statistics may be found from equation (2.53) once T^2W is known. Perry & Marusic (1995) and Marusic & Perry (1995) show that this method results in excellent agreement between predicted and experimental streamwise turbulence intensity. Now, for fully developed turbulent channel flow it can be shown that

$$-\frac{\overline{u_1 u_3}}{U_\tau^2} = 1-\eta-\frac{dU^+}{dy^+}, \tag{2.54}$$

where the velocity gradient, dU^+/dy^+, is negligible away from the wall. Marusic (1991) showed that using a suitable weighting function $W^\dagger$, $T = 1$ and $I_{13} = -\kappa e^{-\lambda}$ in (2.53) agreed with the theoretical distribution of $\overline{u_1 u_3}$ given by (2.54). That is, changes in eddy velocity scale may be considered negligible across all scales for channel flow ($T = 1$) — in so far as the attached eddy model is concerned.

The most recent extension to the Perry & Chong model, which is also of most relevance to this thesis, was that of Marusic (2001). In this reference the auto-correlation of streamwise velocity fluctuations was analysed and compared with attached eddy model results. The agreement was shown to be poor requiring further amendments to the attached eddy model. Details of the modifications proposed by Marusic (2001) will be revealed and discussed in depth in Chapter 7 where auto-correlation measurements are presented.

In summary, the application of the attached eddy hypothesis has been largely successful over the past two decades. As the model has evolved, however, it has become apparent that it is not a predictive model as such. In its current stage the model provides a simple, physical explanation for the statistical properties of turbulence that are readily measureable and available in the literature. Due to the complexity of even the simplest (geometrically) turbulent flows, such physical understanding may prove invaluable as more complex flows are studied in the future (e.g. rough wall-bounded flows).

2.10 Auto-correlation

Most experiments in turbulent flows aiming to determine higher-order turbulence stastics involve the use of a single hot-wire probe. These probes are usually only capable of wall-normal movement during an experiment. Certainly probes used in the current study are of this type. Clearly, measurements of velocity components as a function of streamwise coordinate are not possible with such a probe (unless multiple probes are employed). This prevents direct calculation of the longitudinal spatial correlation of streamwise velocity. Thus, it is the Eulerian streamwise ve-

† A detailed discussion of W for channel flow will be given in Chapter 5.

locity correlation with respect to time that is generally the favoured correlation of the practical researcher† . This correlation is more commonly known as the *auto-correlation* with respect to time, $\mathcal{R}_{11}(t')$, and is simply the mean of the product of velocity fluctuations at time t with those fluctuations at time $t = t - t'$. That is,

$$\mathcal{R}_{11}(t') = \overline{u'(t)u'(t-t')}, \tag{2.55}$$

where t' is the *time difference* or *time lag*. The auto-correlation coefficient, $R_{11}(t')$, or normalised auto-correlation can also be defined:

$$R_{11}(t') = \frac{\overline{u'(t)u'(t-t')}}{\overline{u'^2}}. \tag{2.56}$$

The auto-correlation coefficient is of some use in the analysis of vortical structures in turbulent shear flows as will be evident in Chapter 7. However, if structure identification is the motivation of the investigation of R_{11}, then the auto-correlation with respect to streamwise coordinate would have more direct application than the correlation with respect to time. To move out of the temporal and into the spatial domain, Taylor's hypothesis of frozen turbulence is invoked. This hypothesis permits the transformation $x_0 = U_c t'$, so that

$$R_{11}(x_0) = R_{11}(U_c t'), \tag{2.57}$$

where U_c is a convection velocity. While this transformation appears simple, the convection velocity is a quantity that is difficult to determine and one that has received extensive attention in the literature.

2.10.1 Taylor's hypothesis and convection velocity

Taylor (1938) in his highly regarded paper: "The spectrum of turbulence", first hypothesised the concept of *stationary* or *frozen* turbulence. The now commonly cited Taylor hypothesis states that the structure of turbulence remains statistically unchanged as the flow moves downstream. That is, flow structures are convected downstream, without significant modification or breakdown, with some convection

† The rapid and promising emergence of Particle Image Velocimetry (PIV) technology is an exception, since the instantaneous spatial variation of velocity is available using this technique.

velocity, U_c. This means that information gleaned from a turbulent flow snapshot (e.g. PIV measurements), which gives spatial distributions of flow quantities, is the same information that can be recorded by a stationary probe as the flow passes by.

This hypothesis is very useful to experimentalists, if indeed it is accurate. Thus, much research has been devoted to verification of Taylor's hypothesis. Taylor himself conducted grid turbulence measurements which gave support to his argument. Clearly though, the hypothesis cannot hold either for the finer scales in the flow or very near to a wall. This is because the small scales are dissipated by viscosity on very small time scales. In fact, the Taylor hypothesis will always have a time scale associated with its applicability. Eventually the structures will change even for low wavenumber motions; although the time scales of structure change will become too large to be of consequence if the wavenumber is low enough.

In support of the above restrictions, Hussein, Jeong & Kim (1987) have shown that the Taylor hypothesis is accurate everywhere in a channel flow except very near the wall. Kim & Hussein (1993) explain that errors near the wall can be numerically accounted for by modification of the convection velocity, however, this would seem physically intractable due to the aforementioned viscous dissipation of fine scales. Away from the wall, both of the above references agree that the convection velocity should be the local mean, U. This conclusion is questionable given the significant amount of literature suggesting a constant convection velocity throughout the shear flow.

The pioneering work of Favre, Gaviglio & Dumas (1958) who took extensive space-time correlation measurements in a boundary layer with two normal hot-wire probes, clearly shows that the convection velocity is not equal to the local mean velocity. Plots of the auto-correlation calculated both with varying spatial separation of the hot-wires and using Taylor's hypothesis illustrate that the convection velocity is only equal to the local mean at $y/\delta = 0.24$. Measurements were also taken at $y/\delta = 0.03$, $y/\delta = 0.15$ and $y/\delta = 0.77$. It is shown that for $y/\delta < 0.24$, U underestimates U_c and for $y/\delta = 0.77$, U overestimates U_c. Sternberg (1967) presents a physical argument based on convection of point vorticity sources which agrees with the above findings. Sternberg concludes: "Thus in the outer portion of a boundary layer, the

large scale disturbances should be convected more slowly than the mean velocity, and in the inner portions more rapidly than the local mean velocity".

In this author's view, perhaps the most convincing of all arguments is given by the experimental investigation of Uddin (1994). Uddin (1994) rigorously tested Taylor's hypothesis in a similar study to that of Favre *et al.* (1958) in a constant pressure boundary layer. Uddin gathered space-time correlation data with two hot-wire probes that had the capacity to vary the wall-normal and streamwise spacing between them. Uddin took care to avoid the problems Favre *et al.* (1958) encountered due to probe intereference. The study showed that the true longitudinal space-time correlation, obtained by varying the streamwise spacing of the wires, was almost indistinguishable from that determined using Taylor's hypothesis (for small, fixed wall-normal spacing). Importantly, Uddin uses a constant convection velocity, $U_c = 0.82U_1$, where U_1 is the free-stream velocity of the boundary layer flow. While this test is interesting, plots of peak time lag, t'_m versus streamwise spacing, Δx are truly convincing† . *Peak time lag* is defined as the time lag, t', at which the auto-correlation peaks for a given physical probe spacing, Δx, Δy. It can be shown that

$$U_c t'_m = \Delta x - g(\Delta y), \tag{2.58}$$

where g is a known function of wall-normal spacing of the probes, Δy. Therefore, plots of t'_m against Δx should reveal a slope of $1/U_c$. Further, this slope should not change for any fixed wall-normal spacing if the convection velocity is invariant through the shear layer. The plots given in Uddin (1994) are remarkably linear for all streamwise and wall-normal spacing. The slope in all cases is consistent and reveals $U_c \approx 0.8U_1$.

Based on the described extensive work of Uddin (1994), the convection velocity will be assumed constant throughout the flow and across all turbulent scales in this thesis. While it is acknowledged that this assumption may introduce errors at high wavenumbers and that the author's duct flows are different to that studied by Uddin, $U_c = 0.82U_{CL}$ is judged to be the best choice for convection velocity at this time.

† Note that Uddin (1994) actually plots non-dimensional t'_m against non-dimensional Δx. See this reference for further details.

In the future, it is anticipated that high accuracy, higher Reynolds number PIV measurements will be able to shed further light on the issue of convection velocity.

2.11 A final observation on channel flow literature

Although there is definitely no shortage of rectangular duct flow studies in the literature, there does appear to be limited comprehensive data of all measurable turbulence quantities in long ducts with high aspect ratio and large height. This is undoubtedly due to the limited laboratory space for such large facilities available to researchers. Often studies that have some or all of these elements are found in civil or practical engineering journals and as such, have different aims and motives to those of this study. As stated earlier, numerical simulation is making steady progress in channel flows. However, there is still significant ground to cover before experiments can be effectively replaced with simulations. Furthermore, the lack of quality experimental data in high aspect ratio ducts inhibits the accurate validation of simulations. Hence, it is this author's view that, although duct flows appear to be well studied and numerical simulation rapidly advances, there is a need for further experimental research into channel flows.

Chapter 3

Experimental apparatus and techniques

Despite increasing efforts to improve the understanding of even the simplest wall-bounded turbulent flows, it appears that a lack of consensus with published results has developed. Although poor experimental techniques or technological limitations may be partly responsible, these do not provide a complete explanation of the discrepancies observed in the literature. It has become apparent to the author that a large number of studies claiming to investigate *simple* wall-bounded flows are, in fact, investigating much more complex flows. Complications may arise, for example, in the form of: pressure gradient effects in purportedly zero pressure gradient boundary layers; insufficient length of pipe/channel; inadequate aspect ratio (of a rectangular duct); roughness effects; or poor inlet flow quality. Such complications do not necessarily invalidate a study, however, they must be realised and taken into account by the researcher. Thus, the author believes it is of great importance to allow the reader to judge the flow condition by plainly providing full details of the facilities employed.

A complete and detailed explanation of the apparatus and techniques used for this study is presented here. By taking great care and thoroughly examining the literature, the components constructed for this project were expected to provide the high quality, *simple* duct flows that the aims of this study require. It is hoped that the

details given in this chapter will convincingly attest to this claim and to the quality of the measurements recorded.

3.1 Pipe flow facility

Perhaps the most important characteristic of this experimental apparatus is the length of the pipe. The distance between the inlet and the test location is close to 400 diameters ($L/D = 393.4$). This is significant since the length of pipe required for full flow development has not been definitely determined at this time. A commonly accepted figure is around 150 diameters, however, even results from facilities of this size have been questioned. The extraordinary length-to-diameter ratio of the pipe studied here should ensure fully developed turbulent flow well before the measuring station. The pipe length has added significance since most researchers are forced to compromise L/D for spatial resolution (large diameter) due to laboratory space constraints. The result is that experiments with extremely large L/D pipes are uncommon. Fortunately, spatial constraints in this investigation were not so restrictive, with the Walter Bassett Laboratory being nearly $50m$ in length.

3.1.1 General layout of the measurement apparatus

The pipe setup for fully developed flow measurements is schematically presented in figure 3.1a. Most of the apparatus was orignally used by Henbest (1983) and further details can be found in this reference. The fan at the pipe exit sucks air through a settling chamber containing honeycomb and mesh screens. The flow then accelerates through a circular contraction (I) of area ratio 5.2:1. At the working section entrance, a $60grit$ sand paper trip ($150mm$ long) had been glued around the entire circumference.

The working section was constructed from six lengths of precision drawn brass tubing with internal diameter, $D = 0.0988m$. Tubes were joined with custom made collars designed to produce minimal gap or step and all joints were sealed before experiments began. The six pipe lengths, contraction, settling chamber and fan were originally assembled by Henbest (1983). A new removable measuring section

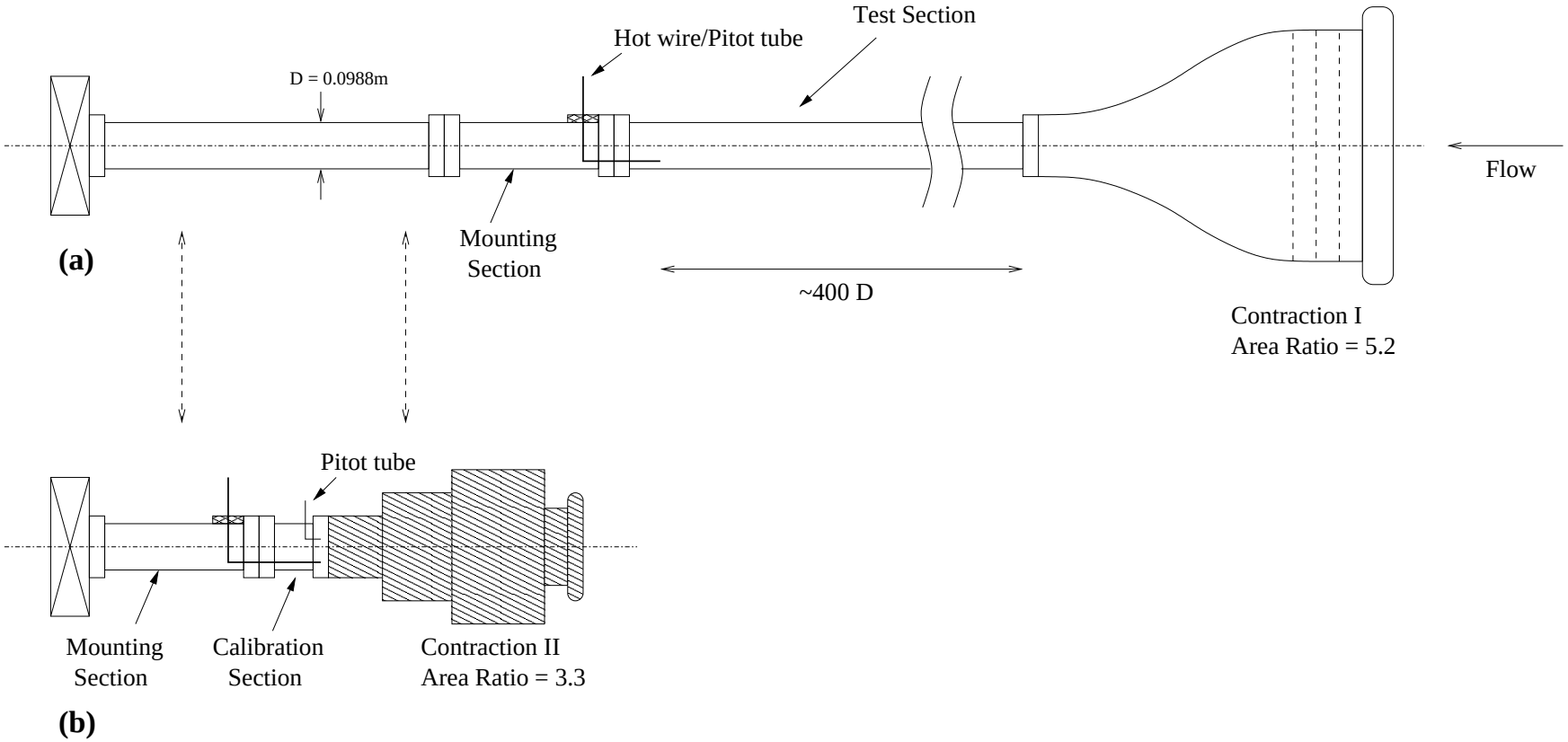

Figure 3.1: Schematic diagram of pipe flow apparatus.

was built to house the anemometer and traverse. This section was bolted between the sixth length of pipe and the final pipe length. The final pipe was attached to the fan inlet through a flexible rubber coupling.

Other modifications to the Henbest (1983) pipe included installation of a new DC motor controller along with disassmebly of the whole working section for checking. All tubes were then carefully polished, reassembled and realigned† .

Measurements were taken at a distance of $L = 38.87m$ from the working section inlet and $2.46m$ from the exit. When flow is sucked rather than blown through the pipe, the fan will have a swirling effect on the flow upstream of the exit. Thus, it is important to take measurements at a location well upstream of the exit. The chosen distance of $2.46m$ was thought to be sufficiently upstream of any exit effects.

There are a total of six static pressure taps inserted along the length of the pipe, at roughly $6m$ intervals, used to calculate the static pressure gradient.

3.1.2 Calibration section

Figure 3.1b shows the hot-wire anemometry (HWA) static calibration setup. During calibration, the measuring section is detached from the measurement setup (shown in figure 3.1a) and attached to a new contraction (II) with area ratio 3.3:1 via a short extension tube. This extension has a fixed reference pitot-static tube inserted to measure mean velocity. The downstream end of the test section is connected to the fan inlet through the flexible rubber coupling. The purpose of this setup is to produce a uniform flow in which to calibrate. It was thought that calibrating in the uniform flow was preferable to in-situ calibration. For in-situ calibrations, both the hot-wire and reference pitot-static tubes must be closely aligned due to the radial velocity profile. Furthermore, turbulence effects on the pitot-static tube must be neglected. After the investigation was concluded, it was found that these problems are not insurmountable. It can be shown that a large error in probe alignment is allowable if the anemometers are placed near the pipe centreline. This is because

† The author would like to acknowledge the invaluable contribution of Dr. S. Hafez to this stage of the investigation.

the mean velocity profile has a very weak gradient in this region. Also, turbulence effects can be neglected in the centre of the pipe since turbulence intensity, $\overline{u'^2}$, is less than 0.1% of the square of mean velocity.

In hindsight, in-situ calibration in this facility would have been preferable for two reasons:

i Simplicity — clearly an in-situ method would be much simpler to implement as the setup shown in 3.1b is not required and the hot-wire need not be handled between calibration and measurement.

ii Temperature stability — this is a serious issue which is often given insufficient consideration during the design of experiments involving hot-wire measurements.

Due to the length of the pipe and temperature distribution in the laboratory, the flow temperature during calibration was often significantly higher than that during measurements. This problem would not exist if calibration had been performed in the fully developed flow. Further discussion of temperature variation will be included in §3.3.

3.2 Channel flow facility

A schematic diagram of the entire channel flow facility is presented in figure 3.2. The fan, diffusing section and settling chamber were part of an existing boundary layer wind tunnel facility (see Saddoughi, 1988). The working section and contraction were constructed for this investigation. Further details of the apparatus are provided in the following sections.

3.2.1 Fan, settling chamber and contraction

The fan, motor and DC controller were well chosen by previous researchers. At the controller output limit, the motor speed was close to its limit of $1700RPM$. The belt drive was setup with a gear ratio of 4:3, driving the fan near to its limit of

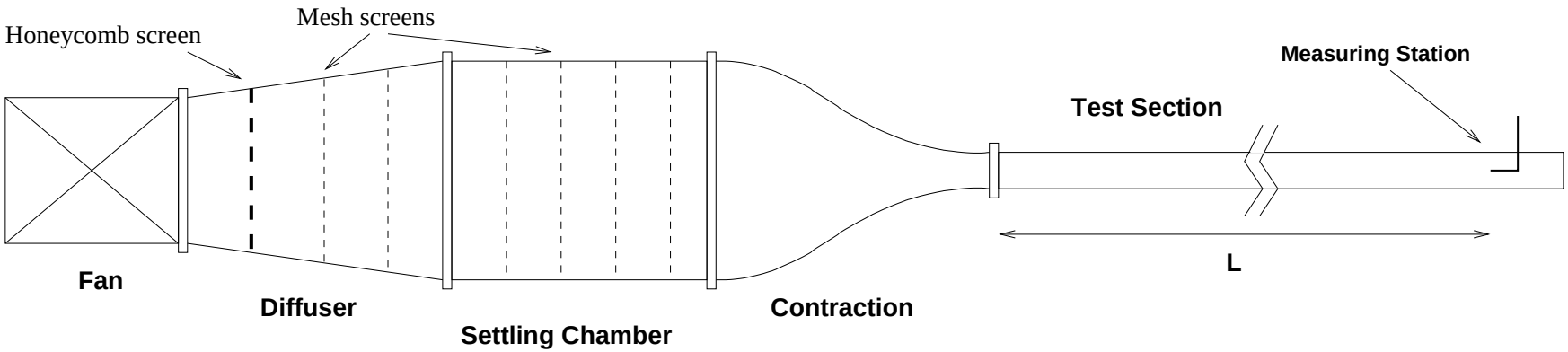

Figure 3.2: Schematic diagram of channel flow facility.

$2232RPM$ for a volume flow rate of approximately $3.6m^3/s$ (corresponding to a bulk velocity of approximately $30m/s$ through the working section).

After leaving the fan, the flow passes through a honeycomb screen for straightening. A fine-mesh screen is inserted at each join in the diffuser and settling chamber. This gives a total of 11 screens, ensuring the flow is uniform with minimal turbulence at the contraction inlet.

Fortunately, the settling chamber width was equivalent to the desired width of the channel working section. Hence, only a two-dimensional contraction between the two sections was required, with an area ratio of 9:1. Mathematically, the contraction shape was defined by a cubic curve leading to a parabolic curve near the exit. A 1:3 scale model of the contraction was built to check for flow separation. This model was tested in a small model-testing wind tunnel. No separation could be detected at any inlet velocity during testing. The shape was accepted and the contraction constructed, with the finished surface varnished and sanded repeatedly until smooth.

With considerable care in design and construction of the contraction — combined with the high quality flow conditioning before the contraction — the inlet flow to the working section was expected to be uniform with low turbulence intensity. The extent of flow uniformity will be shown later in this section.

3.2.2 Working section

The channel flow working section was originally designed with the intention to conduct a parametric study of wall roughness effects on the flow. The large number of roughness types of interest, combined with time limitations, meant the interior walls of the channel were required to be easily accessible. A simple design shown in figure 3.3 was chosen and proved successful.

The full channel consists of eighteen, $18 \times 1220 \times 2440mm$ MDF (Medium Density Fibreboard) walls. The interior faces of each were varnished and sanded back multiple times before assembly of the working section. After varnishing, a coat of wax was applied to achieve the required smoothness.

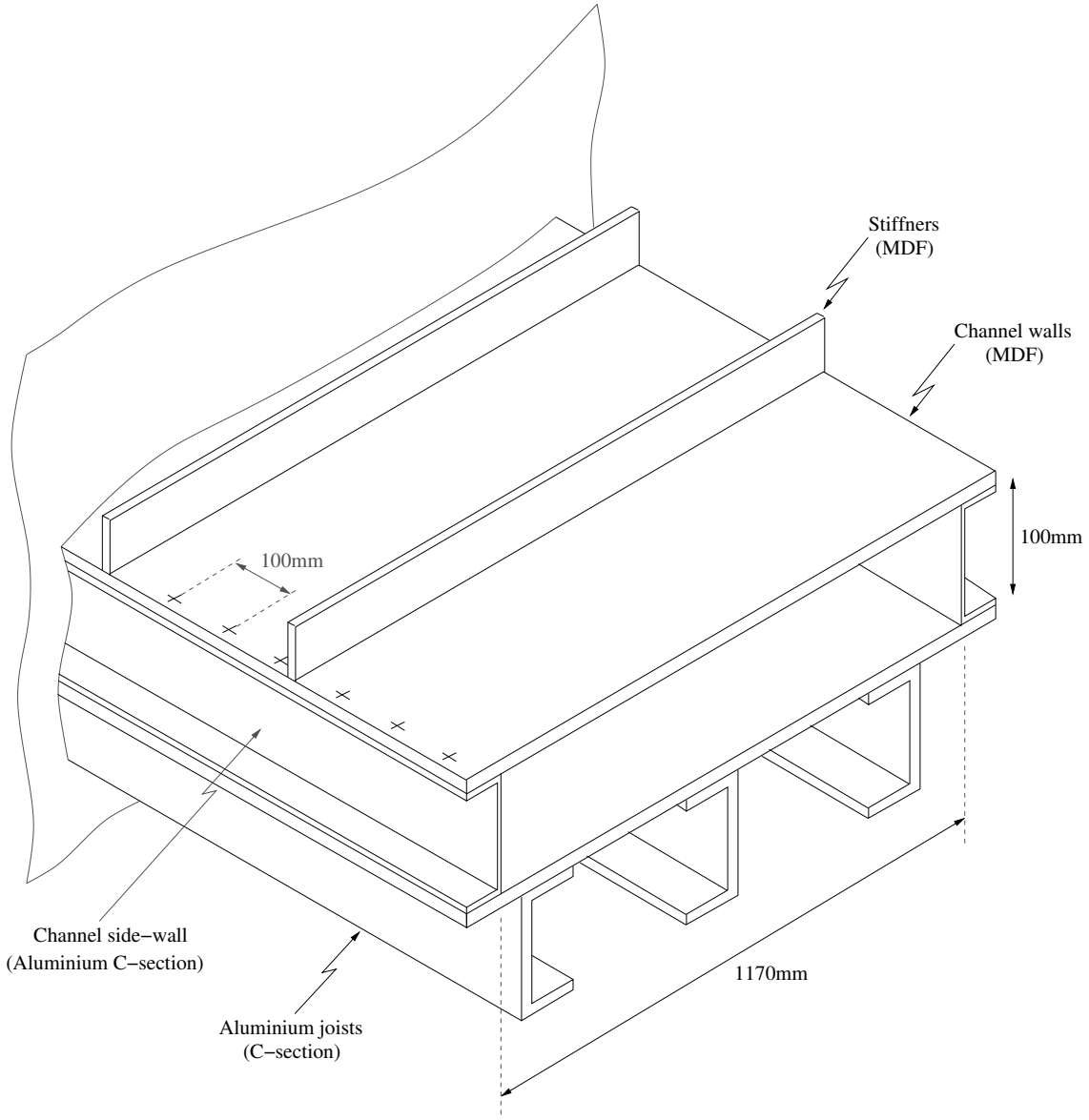

Figure 3.3: Isometric view of a short section of the channel, illustrating the main features of its design. The crosses on the channel edges represent bolt locations, evenly spaced $100mm$ apart over the entire channel length. The diagram is not drawn to scale.

The channel floor (bed) was laid on longitudinally oriented aliminium joists — one close to each side and one through the centre as shown in figure 3.3. The joists were $6mm$ thick C-section aluminium, providing sufficient support to deter deflection of the floor. The channel ceiling was braced laterally with $75mm$ high MDF stiffeners. These stiffeners proved to have inadequate stiffness and deflection of the ceiling resulted. The amount of deflection depended on flow rate and longitudinal position, since a higher pressure at the inlet is required for higher flow rates and pressure decreases as the exit is approached. The deflection problem was solved by building adjustable supports at 35 longitudinal locations along the channel (not shown in figure 3.3). Before any measurement, the supports were checked/adjusted to ensure less than $\pm 0.5mm$ lateral deflection was present in the channel ceiling at any point along the channel.

During construction of the tunnel, a laser level was used to align the channel vertically. The supporting frames under the working section were adjustable in height. Longitudinal alignment was achieved using a simple string line. These procedures ensured there was less than $\pm 0.5mm$ in lateral or longitudinal waviness along the entire length of the channel.

At the working section inlet, 100mm wide strips of $80grit$ sand paper were glued around the entire perimeter. This tripping device ensured the laminar boundary layers formed in the contraction would become turbulent at the inlet. Without the tripping device, the flow would require a far greater length to reach full development.

A pitot-static tube was inserted at the centre of the channel over the roughness trip to measure the inlet velocity of the flow. Since the boundary layers are so thin at the end of the contraction, the velocity measured at the inlet should be very close to the bulk velocity of the fully developed flow (measurements confirmed this).

A measuring station was set up $20.55m$ from the trip, $1.40m$ from the exit. This location was chosen in the hope that the flow would be fully developed (development length of $205h$) and uncontaminated by exit effects. At the measurement location, a pressure tap was inserted to measure static pressure during experiments.

Upstream of the measuring station, a further six wall mounted pressure taps were

inserted in the channel ceiling. Their locations were 7.29, 9.73, 12,17, 14.61, 17.04 and 19.48m from the inlet trip. The stainless steel pressure taps were 1.6mm in diameter and upon microscopic inspection, were found to be free from burrs or other defects. All pressure taps were tested against a removable static pressure probe before use.

3.2.3 Flow Condition

Before any useful measurements could be taken, establishment of the flow quality was imperative. Many procedures involving various tests and checks were involved in this process. The two most important checks, inlet flow condition and two-dimensionality, are discussed here.

Uniform flow at inlet

After construction of the two-dimensional contraction, measurements of mean streamwise velocity at the contraction exit were taken. These consisted of wall-normal velocity profiles at seven spanwise locations measured with a pitot tube. Results were taken with a centerline velocity of $U_{CL} = 17m/s$ and are presented in figure 3.4. This figure clearly indicates that the flow is uniform almost throughout the entire inlet cross-section. In fact, the mean velocity is within $\pm 0.5\%$ of U_{CL} for $y \gtrsim 0.02h = 2mm$. These results indicate excellent contraction design and construction as well as effective flow conditioning in the diffuser and settling chamber.

Two-dimensionality

To check that the flow was *nominally two-dimensional*, centreline mean streamwise velocity and the quotient of spanwise and streamwise velocity, W/U, were measured at various spanwise locations at the channel exit. Experiments were not taken at the station used for final measurements, since no spanwise traverse was available at that location. Nominal two-dimensionality requires all mean flow quantities to be independent of spanwise coordinate and $-0.005U < W < 0.005U$. Measurements of the quantities of interest were recorded with a pitot-static tube and a crossed

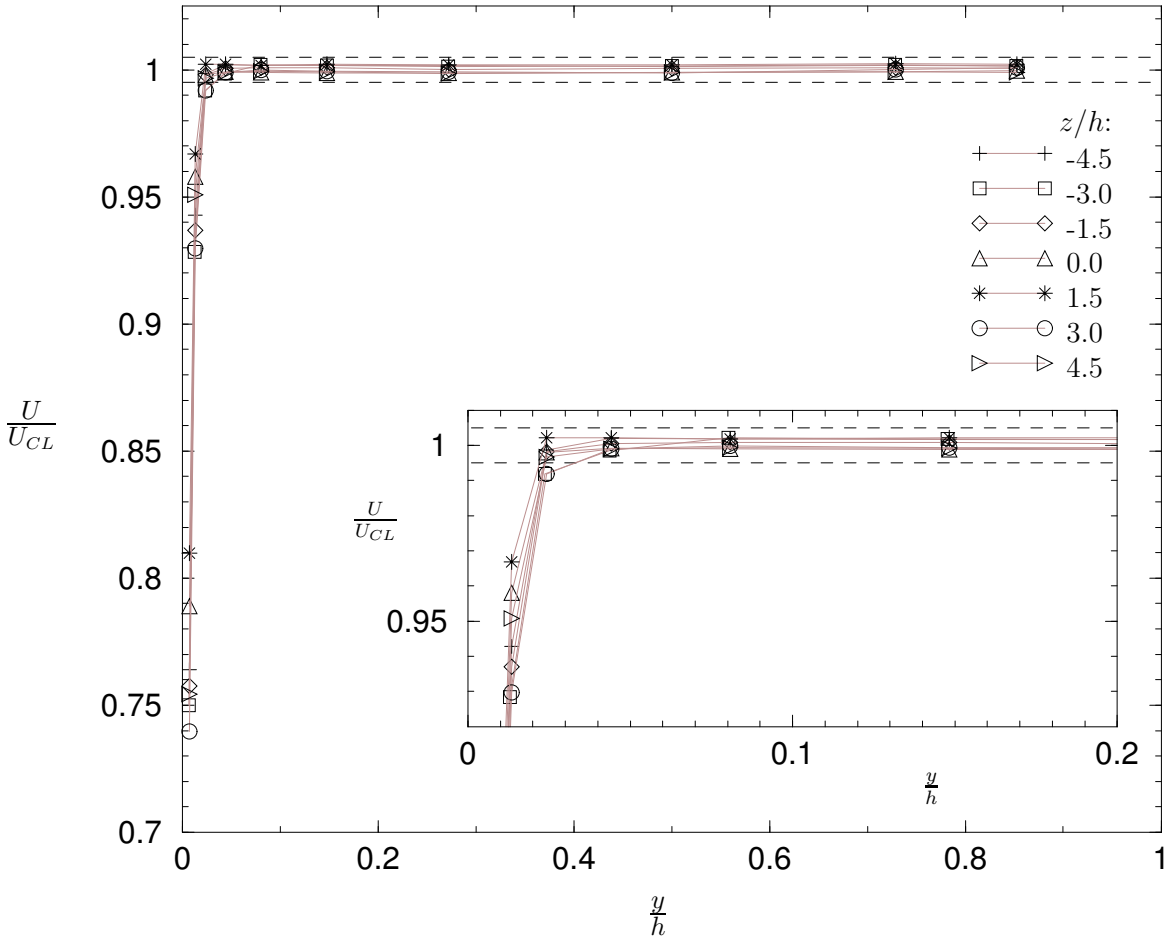

Figure 3.4: Inlet velocity profiles at seven z/h (spanwise) locations for a constant $U_{CL} = 17m/s$. The inset plot is a magnification of the main plot for small wall-distance, y/h. Broken lines represent $\pm 0.5\%$ deviation from unity.

hot-wire (X-wire). The results are shown in figures 3.5 and 3.6. Both figures clearly indicate the flow is nominally two-dimensional. Further experimental support for two-dimensionality will be shown in Chapter 4, using measurements of spanwise wall shear stress (see §4.1.3). Also in Chapter 4, more detailed spanwise distributions of streamwise velocity along the centre of the channel are presented (see §4.2).

One of the most frustrating problems in experimental turbulence research using hot-wire anemometery (HWA), is temperature variation. The calibration of a hot-wire becomes inaccurate if the temperature variation of the flow exceeds 0.5^oC according to Perry (1982). When statically calibrating a normal hot-wire in the turbulent flow at the channel centreline, this problem is avoided (provided that measurements are taken without excessive delay). However, when calibrating in an apparatus

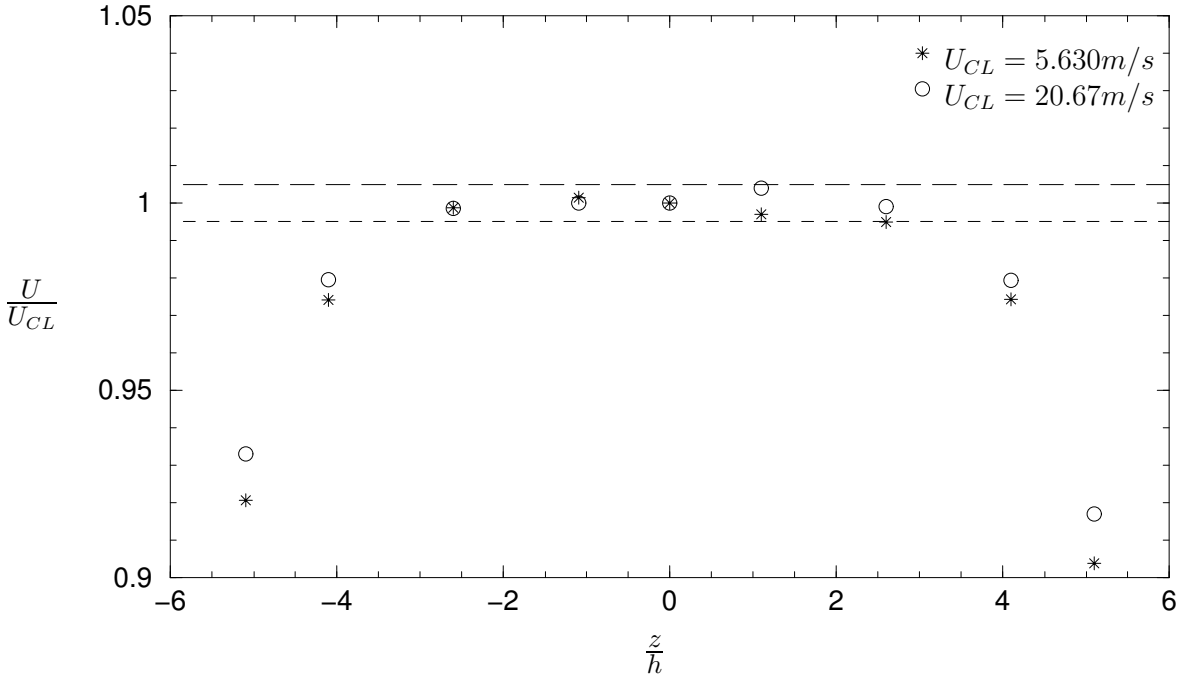

Figure 3.5: Mean streamwise velocity distribution across the span of the channel exit ($y = h/2$). Broken lines represent $\pm 0.5\%$ deviation from unity.

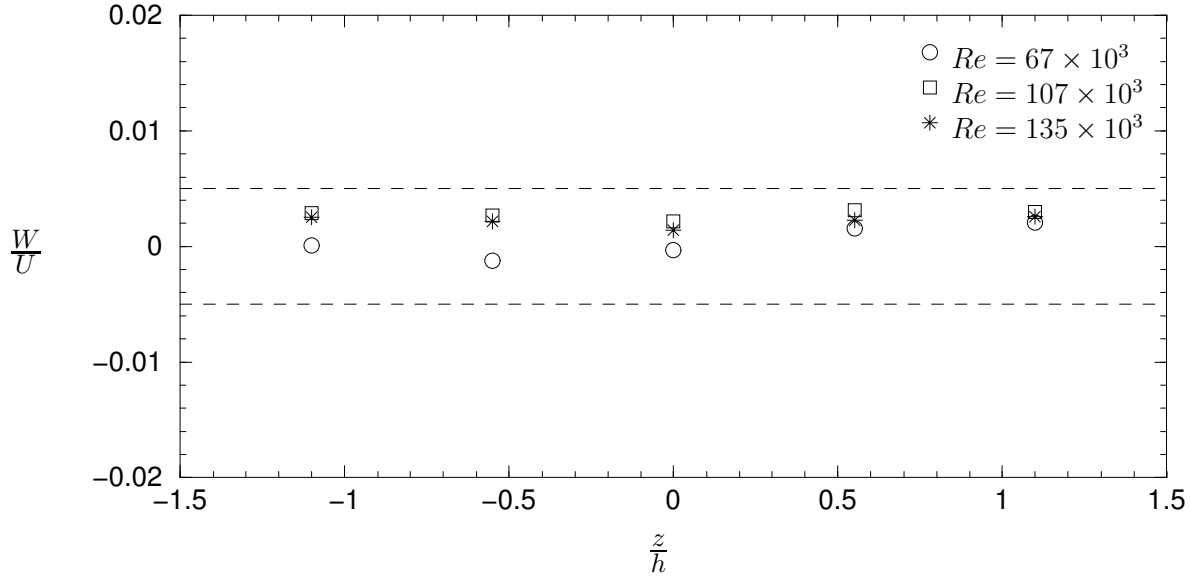

Figure 3.6: W/U distribution across the span of the channel exit ($y = h/2$). Broken lines represent $\pm 0.5\%$ deviation from unity.

external to the channel, temperature changes are more likely and less avoidable. This is because of the physical separation of the channel and calibration tunnel, and the ambient temperature variation throughout the laboratory. Unfortunately, for the crossed hot-wire (X-wire) calibration technique used, it was not possible to calibrate inside the channel. Hence, an external wind tunnel was necessarily employed for calibration, requiring resolution of the problems resulting from ambient temperature change.

3.3 Temperature controlled calibration tunnel

Although corrections may be applied to hot-wire results to account for temperature variation (see Perry, 1982), it would obviously be more desirable to eliminate the problem rather than correct for it. This view led to the installation of a heating element into the settling chamber of the external calibration tunnel. The element was inserted upstream of the flow conditioning screens to improve heat distribution and maintain flow uniformity at the test section. The power output of the element, and therefore, the temperature in the tunnel was manually controlled with a variable voltage AC power supply. No cooling was required since the calibration tunnel was fortuitously situated in the coolest area of the laboratory. At any velocity range, temperature variation in the working section of the calibration tunnel could be accurately controlled to within $\pm 0.1^{o}C$ of the desired operating temperature.

Figure 3.7 displays a schematic diagram of the calibration tunnel showing the location of the heating element. This tunnel was originially constructed by Jones (1998) and further details may be found in this reference. Figure 3.7 also shows a rough sketch of the dynamic calibrator used to calibrate X-wires. The setup allows the accurate oscillatory shaking of the X-wire in the horizontal and vertical (x and y) directions required for the dynamic calibration technique of Perry (1982). Further discussion of this calibration method will be included later in this Chapter (§3.8).

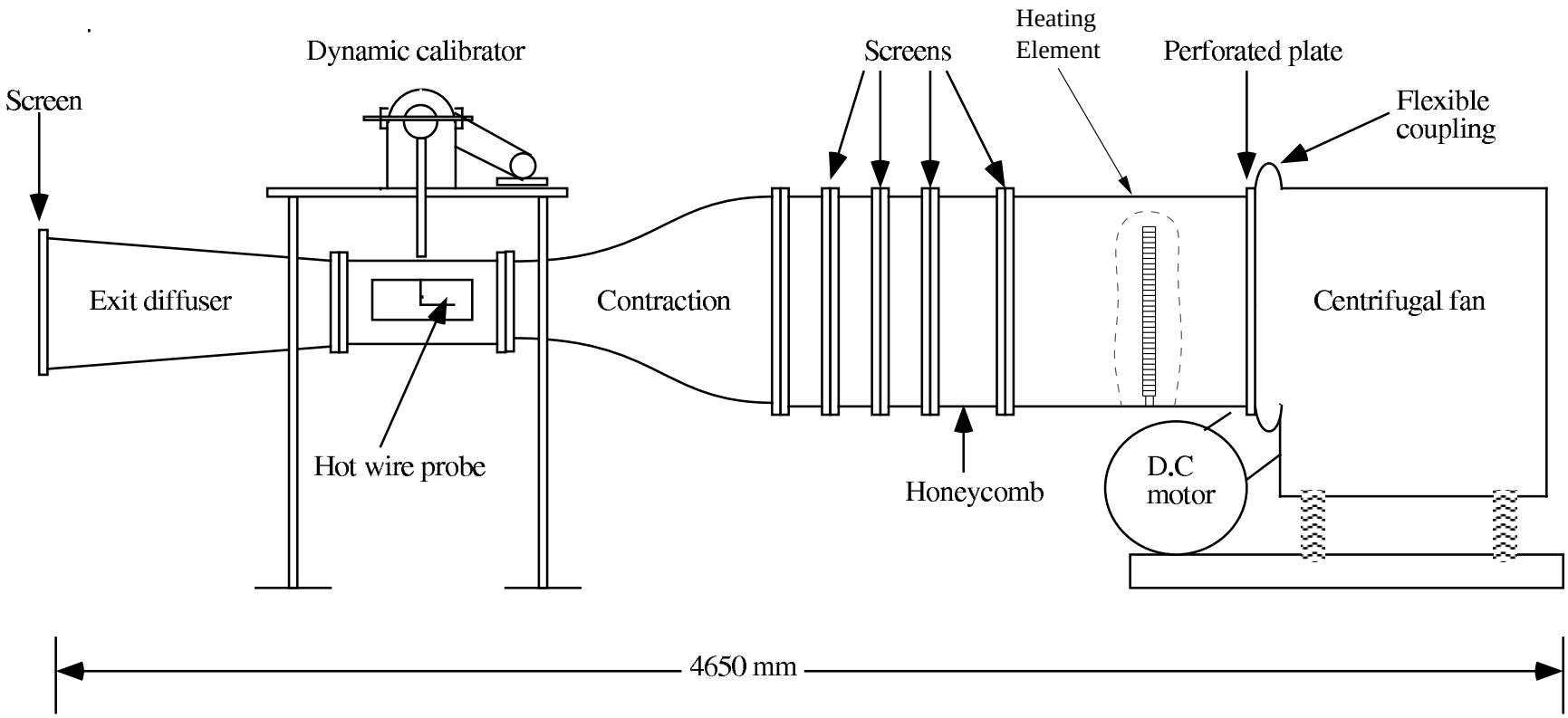

Figure 3.7: Schematic diagram of the temperature controlled calibration wind tunnel.

3.4 Data acquisition and automation

For all experiments, a PC with a *Microstar dap 4000a* data acquisition processor (DAP) interface was used to record measurements. The DAP had 16-bit digital resolution and maximum sampling rate of 80kHz. The input/output voltage range of the board was set to $\pm 5V$ so that the acquisition resolution was $\pm 0.15mV$. Sixteen analog input channels were available for simultaneous sampling with negligible time delay during switching of channels.

The DAP had 2 analog output channels. The first was used to control the anemometer traversing mechanism. The traversing mechanism consisted of a stepper-motor capable of 0.9^o rotation increments, attached to a threaded rod of $1.25mm$ pitch. The threaded rod rotates through a tapped hole in a carriage which grips the anemometer sting. The minimum distance traversable was $3.125\mu m$. No measurable backlash was observed, despite repeated testing to detect this unavoidable phenomenon. It was concluded that the careful design and construction of the traverse effectively reduced the backlash to an insignificant quantity.

During hot-wire measurements, it was found that the stepper motor control circuit transmitted a significant noise signal to the HWA output. Unsuccessful attempts to completely remove the noise resulted in the decision to switch off the stepper motor between measurements. Automation was maintained by incorporating a $240VAC$ relay on the stepper motor control circuit power source. The motor controller could then be software activated by sending a $5V$ impulse to the relay through the second analog output channel of the DAP.

3.5 Pressure measurement and filtering

Two different pressure transducers were employed during the investigations. For low pressure measurement in the pipe, a *HALSTRUP TYPE PU* pressure transducer was used. The maximum pressure difference measurable with this transducer was $250Pa$. In the channel, and for high pressure measurement in the pipe, an *MKS Baratron* pressure transducer was employed. This transducer was able to measure

much larger pressure differences, up to $1300Pa$ ($10mmHg$). All pressure measurements, including pitot-static tube measurements, were low pass filtered at $10Hz$.

A *Krohn-Hite 3321* filter with cut-off frequency range of $0.01Hz - 100kHz$ was used for pipe flow measurements. This versatile single-channel filter could be set to either high or low pass filtering modes. For channel flow measurements a *Frequency Devices 9002* low pass filter with cut-off frequency range of $0.1Hz - 100kHz$ was employed. Software remote control of this device was possible through a serial port connection, allowing automated filter adjustment. A separate *Frequency Devices 9002* high pass filter with $0.1Hz - 100kHz$ cut-off frequency range was required for energy spectra measurements. Both *Frequency Devices* filters were dual-channel instruments.

3.6 Anemometer details

For measurement of turbulence statistics, two types of anemometers were employed: the pitot tube and the hot-wire. Within these two categories, there exists many different types of each device so that a discussion of the full details of the anemometers used is imperative.

3.6.1 Pitot-static tubes

The geometry of the stainless steel pitot-static tubes used is shown in figure 3.8. For pipe flow experiments, the outer diameter of the pitot tube, d_p, was $1.44mm$, while for central channel flow measurements, $d_p = 1.0mm$. For channel measurements, a wall-mounted static pressure tap was inserted at the point of measurement ($x/h \approx 205$) for comparison with the static tube shown in figure 3.8a — no significant difference was found between the two readings during testing. Also shown in figure 3.8 is a sketch of the pitot-static tube used for side-wall mean velocity measurements. This tube was of the 'inverted' type, such that measurements could be taken very close to the wall on which the traverse was mounted.

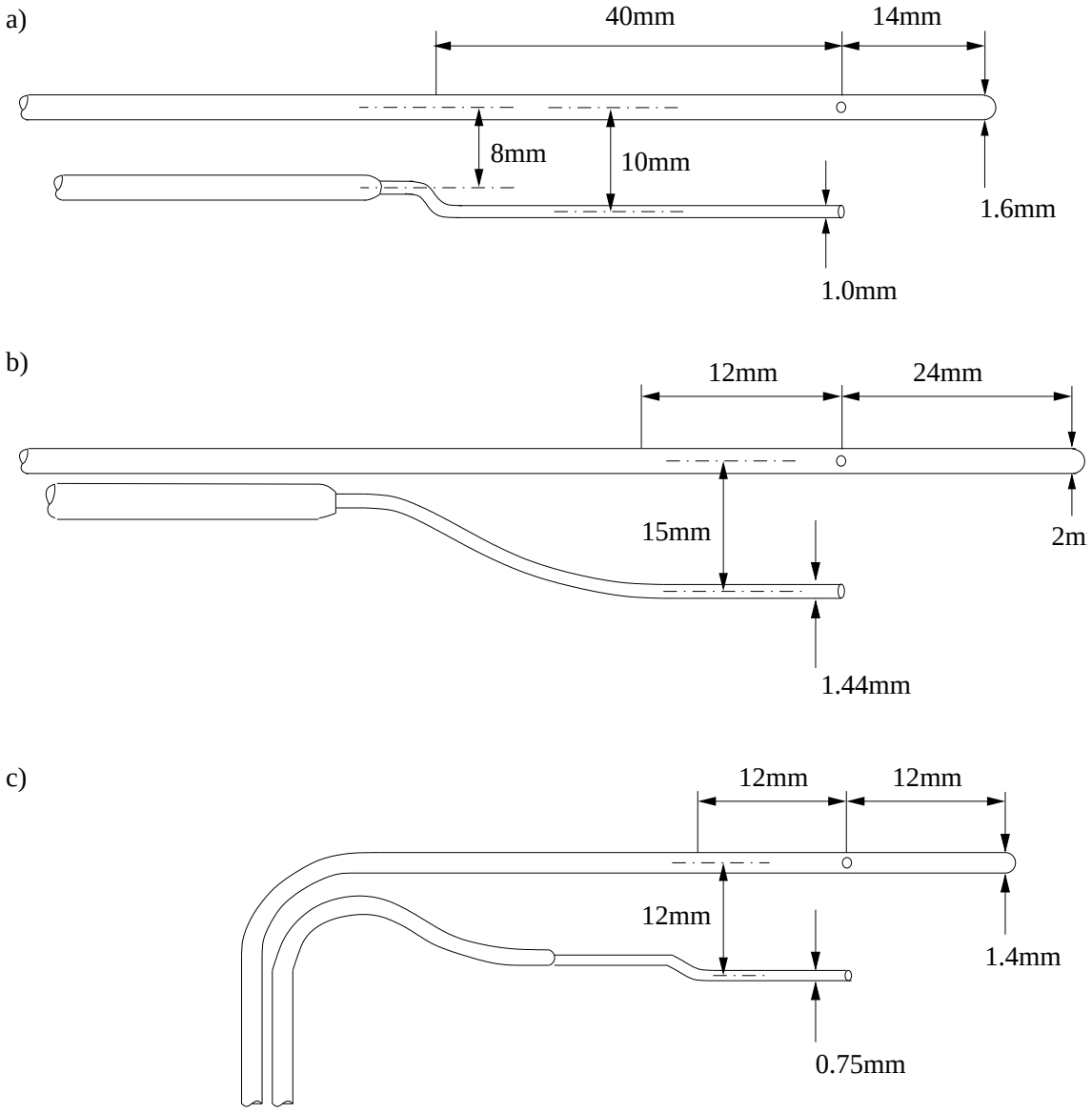

Figure 3.8: Diagrams of pitot-static tubes used for: a) central channel flow; b) pipe flow and; c) channel side-wall flow.

3.6.2 Hot-wire anemometry

Commercial *DANTEC* normal hot-wire and crossed hot-wire (X-wire) probes were used for turbulence measurements. The probe tip spacing was approximately $3mm$ for all tips. $5\mu m$ platinum Wollaston wire was manually soldered between the tips, with $1mm$ of the silver coating etched with nitric acid. Thus, the exposed platinum wire had length to diameter ratio of 200. The geometries of the hot-wires are given in figure 3.9. For the X-wire probe, the distance between the two wires was approximately $1mm$.

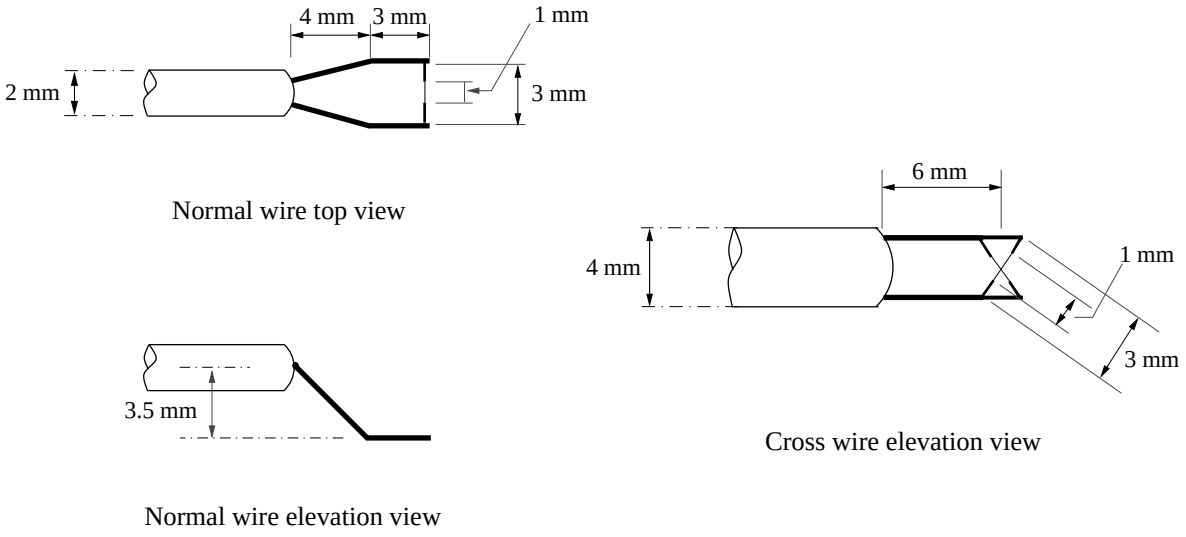

Figure 3.9: Hot-wire anemometer tips.

After etching, hot-wires were connected to custom made constant temperature HWA control circuits with a frequency response range up to approximately 35kHz. More details of the HWA circuit are given in Perry (1982). The resistance ratio of each HWA was set to 2.0. All hot-wire filaments were allowed to anneal for 12 hours (min.) after etching, before use. The outputs of the HWA circuits were offset and amplified appropriately to fit into the input voltage window of the DAP. The response of each HWA to a step input was set to second-order with a minimum frequency response of 25kHz for all velocities in the range to be measured.

3.6.3 Determination of hot-wire wall-distance

Before hot-wire measurement of any flow quantity, the distance of the wire from the wall must be accurately known. This is a common problem with wall turbulence measurements close to the wall, which is further complicated in duct flows where the probe is generally not visible.

Various solutions have been proposed in the literature and, after considerable thought, it was decided to use an electrical contact method. This method is usually implemented through a microswitch attached to the hot-wire probe body. On contact with the wall, the geometry of the probe gives the wall-distance. Clearly, knowing the

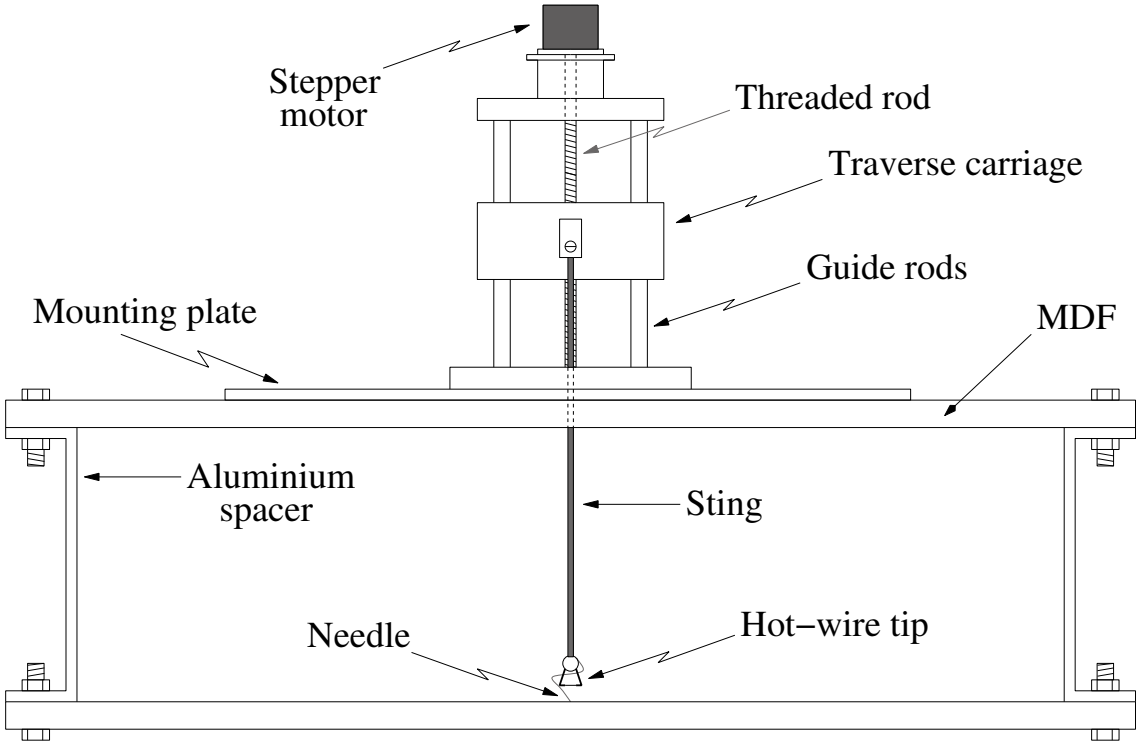

Figure 3.10: Schematic diagram of 'dummy' duct section required for wall-distance determination in the channel. The traverse mechanism is also illustrated. Note that the traverse was mounted to the same mounting plate for measurements in the channel.

geometry of the probe and its orientation accurately is crucial for this method. To avoid the reliance on probe geometry, it was decided that the best implementation of the electrical contact method required the use of a 'dummy' duct section. The dummy section was a small, portable model of the duct that holds the probe and traverse. For the channel, the dummy section is illustrated in detail in figure 3.10. Note that the dummy pipe section was essentially the same only circular in shape. The dummy duct was constructed so that the probe was in line with the end of the duct (when looking down on the wire). A microscope could then be focused on the edge of the duct and the hot-wire simultaneously. The needle shown in figure 3.10 is attached to the probe body and acts as a switch in a trivial electrical circuit. This circuit simply illuminates an LED when the switch is activated. To determine the height of the probe from the wall at contact, the probe is first traversed toward the lower wall until the needle is sufficiently deflected to complete the circuit. At this point, the distance of the hot-wire from the wall could be determined with the aid

of the microscope. The microscope employed was equipped with an eyepiece ruler, having divisions of $0.038mm$ at a magnification of 26x. The probe and traverse are then transferred to the duct test section where the probe is no longer visible. No pitching or yawing of the probe resulted when moving from the dummy section to the test section, even with flow present. This was checked in the channel through use of a CCD camera. For the pipe, the 'dummy' section was, in fact, the mounting section shown in figure 3.1 with the small extension pipe attached to the end. Since the whole mounting section was inserted into the pipe for measurement, no change in probe orientation was possible.

To begin a measurement, the probe was traversed toward the wall until the aforementioned electrical circuit was completed. The wall-distance was then accurately known from the 'dummy' duct procedure. This method was repeatedly checked by traversing the probe into the wall until the hot-wire broke. In the pipe the method exceeded expectations with accuracy of $\pm 0.02mm$. However, in the channel the method was consistently inaccurate. It was found that the wall-distance predicted was approximately $0.1mm$ larger than the true value. Due to insufficient time, it was not possible to correct this error, so channel flow measurements with a normal hot-wire were conducted by traversing the probe into the wall until breakpoint. For X-wires, the error was deemed negligible so the procedure described above was followed.

It is suggested that the wall-distance error in the channel may be attributed to the surface of the channel. The wooden surface of the channel appears less suitable for this method than the brass surface of the pipe. This may be because it is more difficult to produce a high quality sharp edge in wood compared to brass. If the edge is rounded, the distance between the wall and the hot-wire becomes ambiguous because the exact location of the wall cannot be seen clearly through the microscope. Despite the problems encountered in the channel, pipe flow results suggest this method for determining wall-distance is superior to many other popular methods.

3.7 Static calibration of normal hot-wires

Two different methods of statically calibrating normal hot-wires were employed for the pipe and channel flow experiments. The two methods are described in the following sections.

3.7.1 Pipe flow: calibration in uniform flow

A separate calibration section, as illustrated in figure 3.1, was constructed in order to remove the effect of turbulence on the mean velocity measured during calibration. This approach proved successful although exceedingly troublesome due to the difference in temperature between the flow through the calibration section and measurement section. The calibration section was simply a very short version of the main measurement section of the pipe. Since the flow has no length over which to develop, the bulk of the flow through the pipe has uniform velocity with negligible turbulence.

The calibration procedure simply involved taking simultaneous measurements from the hot-wire and a pitot-static tube inserted in the flow. The hot-wire signal was low pass filtered at 10Hz and no less than eight velocity measurements were taken over the appropriate velocity range. A further three measurements across the range were recorded in order to check the calibration. A polynomial of desired degree (usually third degree) was then fitted to the data and the three checkpoints were compared with this polynomial. The calibration was only accepted if all checkpoints lay within $\pm 0.5\%$ of the fitted polynomial.

3.7.2 Channel flow: in-situ normal hot-wire calibration

Calibration of normal hot-wires was performed on the centreline of the turbulent channel flow at the measurement location (i.e., $205h$ from the inlet). At the centreline, turbulence intensity is less than $\pm 0.1\%$ of the square of mean velocity. Therefore, a calibrated normal hot-wire and a pitot-static tube should give almost identical velocity measurements at the centreline (see equation 2.47). That is, even though

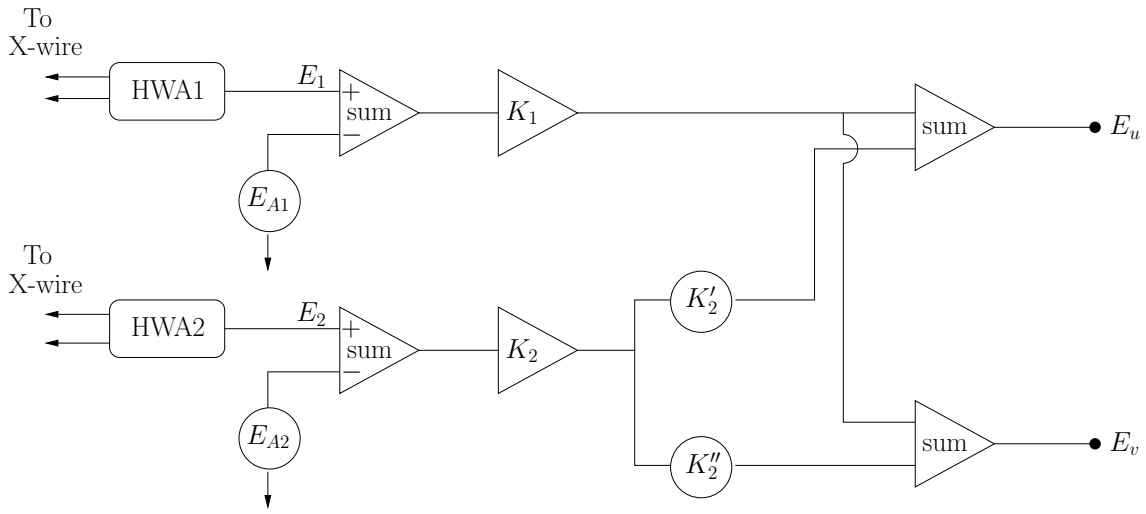

Figure 3.11: Basic diagram of the electrical circuit used to match X-wires.

the flow is turbulent, the turbulence is low enough to permit accurate calibration of the normal hot-wire.

To perform this calibration, the hot-wire and the pitot-static tube were firstly traversed to the centreline. This was achieved easily by mounting both anemometers on separate traverse mechanisms. After this, the same procedure as that described in the previous section for pipe flow calibration was employed.

3.8 Dynamic calibration of X-wires

Dynamic calibration of X-wires was performed in the Temperature Controlled Calibration Tunnel external to the channel as detailed in §3.3. Note that X-wires were used in the channel flow experiments only. The calibration procedure and the apparatus used are identical to those used by Jones (1998). For a more detailed explanation of the procedure, the reader is referred to Perry (1982).

3.8.1 Matching circuit

Before calibration, a method of extracting the voltages E_u and E_v (sensitive to the streamwise and normal velocities, respectively) from the individual X-wire signals is required. Traditionally, this has been accomplished through an electronic matching circuit shown in figure 3.11. This simply adds the amplified and offset outputs of

each of the X-wire HWA circuits and its function can be written mathematically as:

$$E_u = K_1(E_1 - E_{A1}) + K_2K_2'(E_2 - E_{A2}) \quad (3.1)$$

$$E_v = K_1(E_1 - E_{A1}) - K_2K_2''(E_2 - E_{A2}). \quad (3.2)$$

See figure 3.11 for the definitions of E_1, E_2, E_{A1} and E_{A2}. In order to determine the appropriate gains, K_1, K_2, K_2' and K_2'', the X-wire probe is shaken sinusoidally in the streamwise direction (horizontally) and then in the normal direction (vertically). Accurate sinusoidal shaking is imperative and is achieved by attaching the X-wire probe to a Murray cycloidal drive unit. Further details of the matching method are provided in Perry (1982). The X-wires are deemed to be matched when $E_v < 0.05E_u$ during horizontal shaking and $E_u < 0.1E_v$ during vertical shaking.

This circuit has been successfully implemented by many researchers, although it has been unneccesarily complicated. A signal analysis of the matching circuit with two HWA's having sinusoidal outputs (E_1, E_2) that are slightly out of phase is given in Appendix D. It is shown that optimum matching is achieved when

$$K_2K_2' = K_2K_2'' = \frac{|E_1 - E_{A1}|}{|E_2 - E_{A2}|}. \quad (3.3)$$

Practically, $|E_1 - E_{A1}|$ can easily be set very close to $|E_2 - E_{A2}|$ and the HWA outputs are not perfectly sinusoidal. Thus, if $K_2K_2' \approx K_2K_2'' \approx 1$, optimum matching is achieved. If so, it is also shown in Appendix D that E_u and E_v will be out of phase by 90^o.

Until now, matching has been achieved by observing the matching box output during shaking on an oscilloscope, then adjusting potentiometers through trial and error. The above result (3.3) gives a guide to the approximate amplifier gains required. However, the matching circuit is a redundant electronic device. This is because its function can be easily replicated through computational manipulation of HWA signals sampled by the DAP during shaking. A simple program was written to numerically apply equations (3.1) & (3.2) to the sampled data and optimise the constants, K_2K_2' and K_2K_2'' (with $K_1 = K_2 = 1$), based on the criteria stated above. This simple method gives more accurate matching and eliminates the relatively complex, potentially noise infected electronic matching circuit from the system.

3.8.2 Dynamic calibration procedure

During calibration, the X-wire was shaken in one direction and then in the other at no less than eight free-stream velocities, U, spanning the desired range. U was measured with a Pitot-static tube. The Murray cycloidal drive is fitted with an *HEDS–5640A06* optical rotary encoder. This allows measurement of the shaking frequency and phase sampling of E_u and E_v at 500 locations per cycle. The HWA outputs were low pass filtered at $10Hz$. Data sampled at $200Hz$ was phase-averaged over 25 shaking cycles. From these measurements, mean voltages $\overline{E_u}$, $\overline{E_v}$ and sensitivities $\partial U/\partial E_u$, $\partial V/\partial E_v$ were calculated. From these quantities, all constants in the calibration equations,

$$U = a_0 + a_1 E_u + a_2 E_u^2 + a_3 E_u^3 \tag{3.4}$$

$$W = b_0 + b_1 E_u + b_2 E_v + b_3 E_u^2 + b_4 E_u E_v + b_5 E_u^2 E_v, \tag{3.5}$$

derived by Perry (1982)[†], may be found. At three representative velocities during calibration, large samples of E_u, E_v and U were recorded at $200Hz$ (typically 6000 samples). After the calibration curve was determined, it was applied to these data sets, giving $U_m, \overline{u_m'^2}$ and $\overline{v_m'^2}$ (where subscript m denotes X-wire measured quantities). The true values of the stresses, $\overline{u'^2}$ and $\overline{v'^2}$, depending on the shaking direction, are related to the shaking frequency, f_{sh}, by:

$$2(\pi A_{sh} f_{sh})^2 = \begin{cases} \overline{u'^2}, & \text{horizontal shaking,} \\ \overline{v'^2}, & \text{vertical shaking.} \end{cases} \tag{3.6}$$

$A_{sh} = 37.95mm$ is the amplitude of sinusoidal shaking. A calibration was accepted provided U_m is within $\pm 0.5\%$ of U and measured stresses were within $\pm 2\%$ of that predicted by (3.6).

3.9 Central flow mean velocity measurements

For both the pipe and channel flow facilities, the same methods were applied for measuring streamwise mean velocity profiles normal to the wall. Both pitot-static

[†] Perry omitted the E_u^2 term. This omission seems unjustified, hence, the term is included in all calibrations performed in this study.

tubes and normal hot-wires were traversed from as near to the wall as possible, to the duct centreline (and beyond in cases where flow symmetry was checked).

3.9.1 Pitot-static tube

The pitot-static tubes used in the pipe and channel flow are shown in figure 3.8. The tubes were connected to the pressure transducer and the output sampled by the DAP at 200Hz. It was found that 18000 samples were sufficient for convergence.

To begin a streamwise mean velocity profile measurement, the probe is traversed toward the wall until the pitot tube hits the wall. The probe is then traversed away from the wall in $0.05mm$ increments until a significant change in mean velocity is detected (typically a 2 – 5% change). The mean velocity at this point ($y = 0.05 + 0.5d_p$) becomes the first measured value. There is clearly a spatial error of $\pm 0.025mm$ involved with this method. However, this is insignificant for the Reynolds number flows encountered in this study. The estimated experimental error of pitot tube velocity measurements was $\pm 0.3\%$. This estimate includes errors introduced by the static pressure tubes, pitot manufacturing flaws (i.e., pitot tube reading deviations from true velocity) and the pressure transducer which has a known accuracy of $\pm 0.1\%$.

3.9.2 Normal hot-wire

After wall-distance was determined and the HWA was calibrated, a mean velocity profile (and streamwise turbulence intensity profile) could be measured. During measurement, the hot-wire probe was traversed normal to the channel bed-wall with logarithmic spacing in wall-distance. For this measurement, the HWA output was passed through the low pass filter with a cut-off frequency of 20kHz and then input to the DAP. Three bursts of 4000 samples were taken at a frequency of 200Hz. Convergence tests prove that this relatively short sampling time was sufficient (see Appendix E). Data recorded was processed and graphically plotted on-the-fly during a traverse for monitoring purposes.

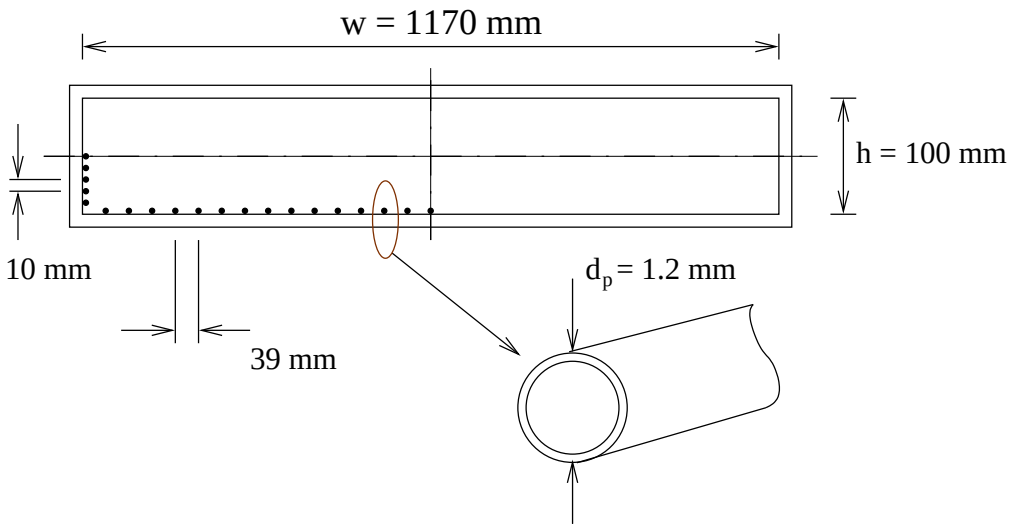

Figure 3.12: Channel cross section displaying Preston tube locations.

Following a measurement, the HWA is re-calibrated to ensure the calibration did not drift during measurement. Unfortunately, in cases where the hot-wire was traversed into the wall (channel flow), this check was clearly not possible. However, all measurements were repeated at least once before acceptance. The estimated experimental error of hot-wire velocity measurements was at most $\pm 0.5\%$. This error is necessarily higher than pitot error since the hot-wire was calibrated using a pitot tube and hot-wire drift was deemed acceptable if within $\pm 0.5\%$.

3.10 Spanwise measurements

Wall shear stress

Measurements of wall shear stress were taken using a total of 21 circular, square ended pitot tubes of $1.2mm$ outer diameter placed on the wall (Preston tubes). The calibration curves given by Patel (1965) were used to convert the preston pressure reading to shear stress. Each tube end was cleaned and examined carefully under a microscope to ensure no burrs or other irregularities were present. The tubes were evenly spaced along the measurement wall and side wall of one quadrant of the channel as shown in figure 3.12. Measurements were recorded at $L/h = 205$ only. The Preston tube pressures were sampled sequentially by the DAP at a frequency of $200Hz$, with 18000 samples recorded and ensemble-averaged.

Spanwise distributions of centreline velocity

The pitot-static tube shown in figure 3.8c was used for all spanwise distributions of streamwise velocity at the centreline ($y = h/2$). The aim of these measurements was to analyse the development of the side-wall flow. Therefore, a total of six streamwise stations were investigated. These stations were at the locations, $L/h = 50, 100, 125, 150, 176$ and 205. At each station, a small hole ($3/4''$ in diameter) was drilled in the side-wall of the channel to allow insertion of the pitot-static tube. The anemometer was attached to the same traverse as used for the central flow measurements as illustrated in figure 3.10. Extended sliding and threaded rods replaced those shown in figure 3.10 to allow a traverse distance of up to $400mm$. An extended circular sting, housed in a tube of aerofoil cross-section, connected the anemometer to the traverse.

The pitot-static tubes were connected to the pressure transducer and the same procedures as those used for central flow pitot measurements was followed.

3.11 Second-order turbulence statistics

Streamwise turbulence intensity, $\overline{u'^2}$, was calculated from data recorded during mean velocity profile measurements with a normal hot-wire in the central flow at $L/h = 205$. Reynolds stresses ($\overline{u'v'}, \overline{u'w'}$), normal stresses ($\overline{u'^2}, \overline{v'^2}, \overline{w'^2}$) and mean velocities in all directions are measured with a calibrated X-wire during a normal traverse. For all measurements, the sampling and filtering settings are as stated in §3.9.2 above. The X-wires were also re-calibrated after a measurement to check for drift.

3.12 Auto-correlation coefficient

The auto-correlation coefficient, $R_{11}(\tau)$, was introduced in §2.10. The auto-correlation is simply determined from the correlation of hot-wire measured streamwise velocity fluctuations as described by equation (2.56). However, high frequency sampling is required for adequate temporal resolution so that data recorded during a mean

velocity profile measurement is not suitable for calculation of auto-correlation. It is often assumed that the difference between auto-correlation coefficient of velocity fluctuations and that of HWA output voltage fluctuations is negligible. Since insufficient evidence is available to justify this assumption, calibrated hot-wires were used in all cases. In Chapter 7, the validity of this assumption will be further discussed in light of the measurements recorded during this study.

Auto-correlation measurements were taken with a normal hot-wire at various wall-normal coordinates up to, and including, the channel centreline in the central flow region at $L/h = 205$. The HWA output was low pass filtered with a cut-off frequency of $20kHz$. The filtered signal was then sampled at $15kHz$ in 20 bursts of 60000 samples. 20 bursts proved to be sufficient for convergence of the correlation data.

Chapter 4

Boundary shear and flow development

While certain aspects of rectangular duct flow are strongly represented in the literature (as discussed in Chapter 2), other important and interesting features of such flows receive far less attention. Perhaps it is the concentration on the two-dimensional, fully developed central flow that gives the impression that all aspects of channel flow have been studied. This is especially true of high aspect ratio ducts where most studies focus on one 'fully developed' measurement location at the centre of the channel bed, measuring such quantities as skin friction and wall-normal profiles of turbulence statistics.

Thus, the following chapter provides a detailed discussion of two features of channel flows that the author believes are under-represented in the literature. First, wall shear stress measurements are presented, of which the distributions around the rectangular duct perimeter are most interesting. Secondly, and most importantly, a study of streamwise flow development is presented. This study is considered long overdue as almost all duct flow experimentalists either assume full development in a relatively short apparatus, acknowledging the possibility of a resultant error, or build excessively large facilities to ensure full flow development. It is hoped that the analysis presented here will not only provide an interesting insight into flow development, but also a guide to the length of duct required for future experiments.

4.1 Wall shear stress

While it is the wall shear stress, τ_w, distribution around the rectangular duct perimeter that will receive most attention in this section, measurements of τ_w in the fully developed pipe and at the centre of the channel bed were also recorded. These important measurements were required to determine the friction velocity U_τ for velocity scaling. The variation of channel centre and pipe τ_w (determined from streamwise pressure gradient), with Reynolds number will be included in this section for completeness. The investigation of perimetric τ_w distribution in the channel will follow these analyses.

4.1.1 Pipe flow

The friction factor, λ_p, values were determined for each of the five Reynolds numbers studied in the pipe flow facility and the results are presented in figure 4.1. In this figure, $1/\sqrt{\lambda_p}$ is plotted against $Re\sqrt{\lambda_p}$ on semi-logarithmic axes for comparison with Prandtl's smooth wall equation (2.7). It is immediately obvious that further data is requried to make a substantial statement concerning the variation of λ_p with Re. Unfortunately, only a small range of Reynolds number was achievable in the existing apparatus. Nevertheless, comparison of measurements with the formulations of Prandtl and Zagarola (1996), given by equations (2.7) and (2.9) respectively, are shown. Furthermore, a curve-fit of Prandtl's smooth wall friction factor relation (2.7) to the data of figure 4.1 gives the constants: $C_1 = 2.114$ and $C_2 = -1.323$. It can be shown by derivation of Prandtl's law (2.7) (see Appendix A) that the log law constant κ is simply related to C_1 by

$$\kappa = \frac{\ln(10)}{C_1\sqrt{8}}. \tag{4.1}$$

Hence, if $C_1 = 2.114$, then $\kappa = 0.385$. It is therefore expected that the value of κ determined from mean velocity profiles in the pipe will be close to 0.385. Further discussion of log law constants will be included in Chapter 5, although at this point it will be noted that $\kappa = 0.386$ has been found to fit the pitot tube measured mean velocity profiles. The agreement of κ determined by these two very different methods is encouraging and is an important finding in relation to the work of Zagarola (1996).

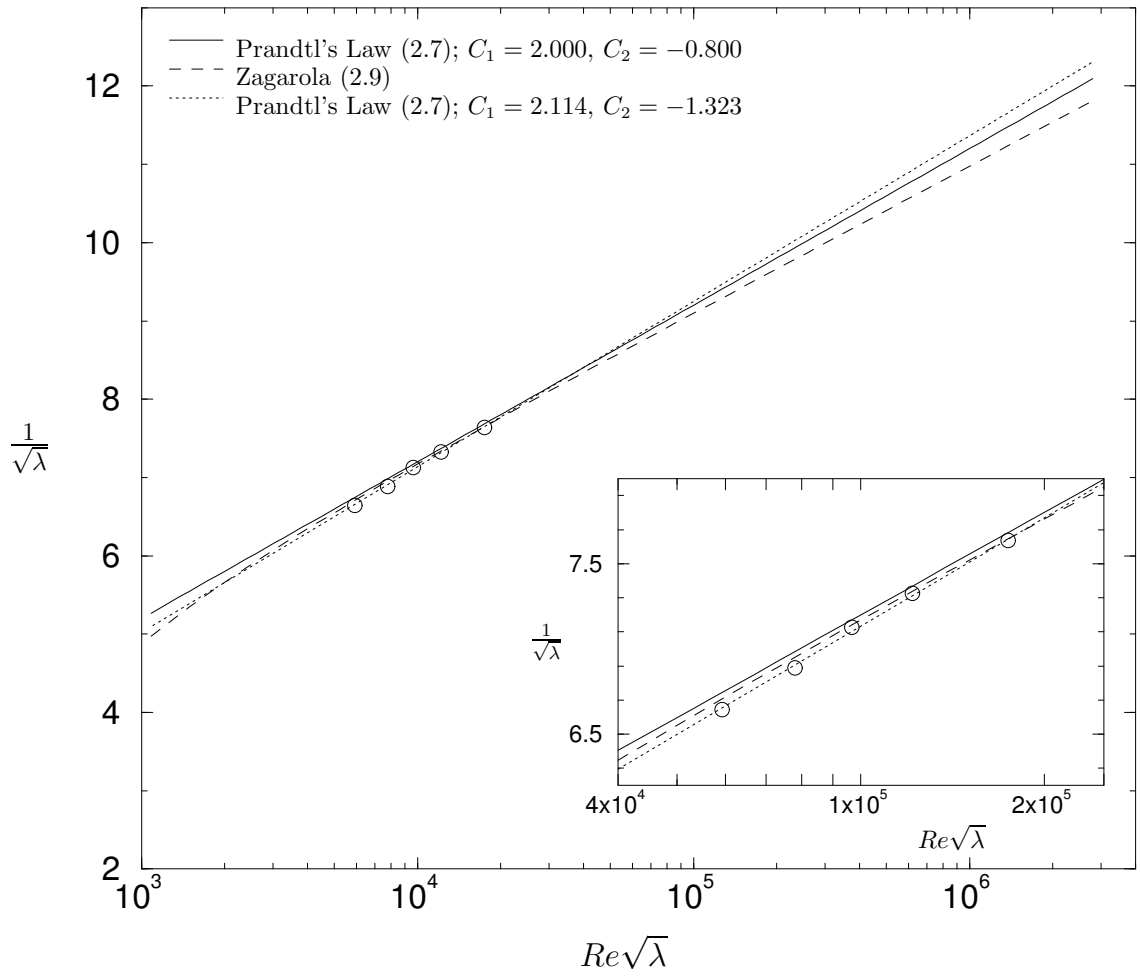

Figure 4.1: Friction factor measurements presented to best provide comparisons between the data and Prandtl's smooth wall formula (2.7). The inset plot is simply a magnification of the main plot in the $Re\sqrt{\lambda_p}$ range studied here.

In his analysis of the Superpipe data, Zagarola (1996) uses curve-fits to the friction factor data to determine κ. Zagarola states that this is more accurate than curve-fitting the mean velocity profiles. While this statement is true, it must be expected that both methods would return similar results as found in the current investigation. If the methods consistently give different results, as found by Zagarola (1996), no conclusions about the true logarithmic behaviour in the overlap region can be drawn without justification for the difference† .

Returning to figure 4.1: the inset plot focuses on the Reynolds number range of the current pipe flow investigation. In this plot it can be seen that the data increasingly

† Random error associated with curve-fitting mean velocity profiles cannot justify *consistent* differences.

deviate from Prandtl's law with original constants as $Re\sqrt{\lambda_p}$ decreases. The relationship proposed by Zagarola (1996) provides a better fit than Prandtl's original law, although it must be noted that all three curves are similar over the limited Re range studied. The main plot illustrates how much more the curves differ at higher Reynolds number. It is conceded that the limited number of data points and Re range prevent solid conclusions concerning the friction factor behaviour. However, the measurements do provide useful evidence in support of the log law constant κ to be determined in subsequent analyses.

4.1.2 Channel flow: central wall shear stress

Skin friction, C_f, at the most downstream measurement location was calculated from a large number of measurements of streamwise pressure gradient, over the possible range of Reynolds number. The variation of C_f with Re is presented in figure 4.2. Also included in this plot are the power law curve-fits of Dean (1978) and Zanoun *et al.* (2003), along with a relationship analagous to Prandtl's smooth wall formula (2.7). The latter relationship is derived in the same way as Prandtl's formula (i.e., integration of the logarithmic velocity profile) with the result:

$$\sqrt{\frac{1}{C_f}} = C_3 \log_{10}(Re\sqrt{C_f}) + C_4, \tag{4.2}$$

where $C_3\sqrt{2} = \ln 10/\kappa$ (See Appendix A for this derivation). From a curve-fit to the data for $Re \gtrsim 40 \times 10^3$ the values of the constants in (4.2) were found to be $C_3 = 4.175$ and $C_4 = -0.416$. The value of C_3 gives $\kappa = 0.390$ which will again be shown to compare well with the central flow mean velocity profile analysis in Chapter 5. For $Re < 40 \times 10^3$ the log law no longer represents an appreciable portion of the flow, therefore, by definition, equation (4.2) is not expected to hold in this Re regime. Figure 4.2 shows that the smooth wall law (4.2) provides a good fit to the data for all $Re \gtrsim 40 \times 10^3$. The expected deviation of the data from this curve for lower Re is also clear. The sharpness of this deviation, however, is surprising. It is suggested that experimental error due to the small pressure differences and velocities measured at low Re may be the reason for this observation.

The power law curve-fits found in the literature appear to agree well with the data

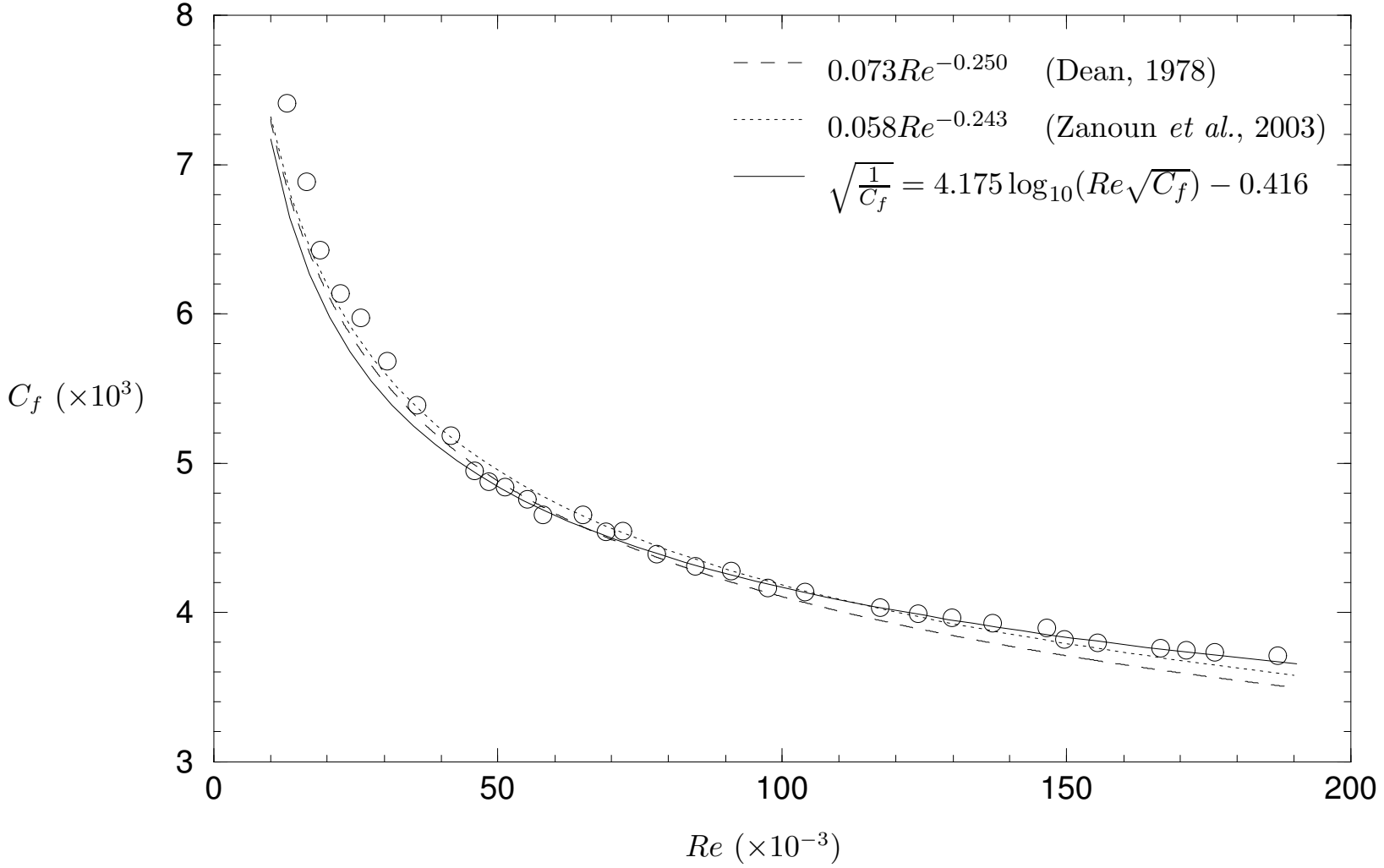

Figure 4.2: Channel flow skin friction measurements over a broad Reynolds number range. The curve-fits of Dean (1978) and Zanoun *et al.* (2003) are included for comparison. A third curve, similar to Prandtl's smooth wall formula, is also plotted with constants determined by curve-fitting.

at low to moderate Re. At higher Re, the curve-fit of Dean (1978) drops well below the data. This is most likely due to the lack of quality high Re data available; in fact, above $Re = 150 \times 10^3$ Dean (1978) presents only four data points, of which three were extracted from almost certainly underdeveloped channel flow facilities (the fourth lies above the curve-fit). The curve-fit of Zanoun *et al.* (2003) provides a better fit to the data presented here across the Re range; this power law is therefore recommended by the author, if indeed a power law relationship is of interest. It should be noted that the power law relationship is bound to the assumption of a power law mean velocity distribution (see Appendix B for more details on the relationship between the resistance and velocity power laws). It can also be shown that the Re index of 0.25 assumes the Blasius $1/7^{th}$ mean velocity power law. Since the $1/7^{th}$ power law has not received experimental support, particularly at high Re, a power law relationship will become less accurate than (4.2) as Re increases. This statement is, of course, based on the experimentally supported assumption of a logarithmic mean velocity profile in the overlap region.

4.1.3 Channel flow: perimetric wall shear stress

Distributions of τ_w around the perimeter of a duct are often used to determine the average wall shear stress, $\overline{\tau_w}$, which is required to determine the total friction factor, λ_t (defined in §2.4.3). This property is useful for calculating frictional losses through rectangular ducts (in air conditioning systems, for example). Therefore λ_t is of most interest to researchers in the field of civil engineering, and publications concerning its behaviour are available in the according journals. However, the author has noticed from these studies that, while the experimental facilities used are often well designed, error tolerance is much higher than that of common turbulence studies† and, more specifically, of this investigation. Hence the need for more accurate perimetric wall shear stress distributions as measured during this project and presented in figures 4.3 & 4.4.

The first of the two figures displays the normalised τ_w variation (normalised with

† This is a generalisation only and should not be regarded as applicable to all publications.

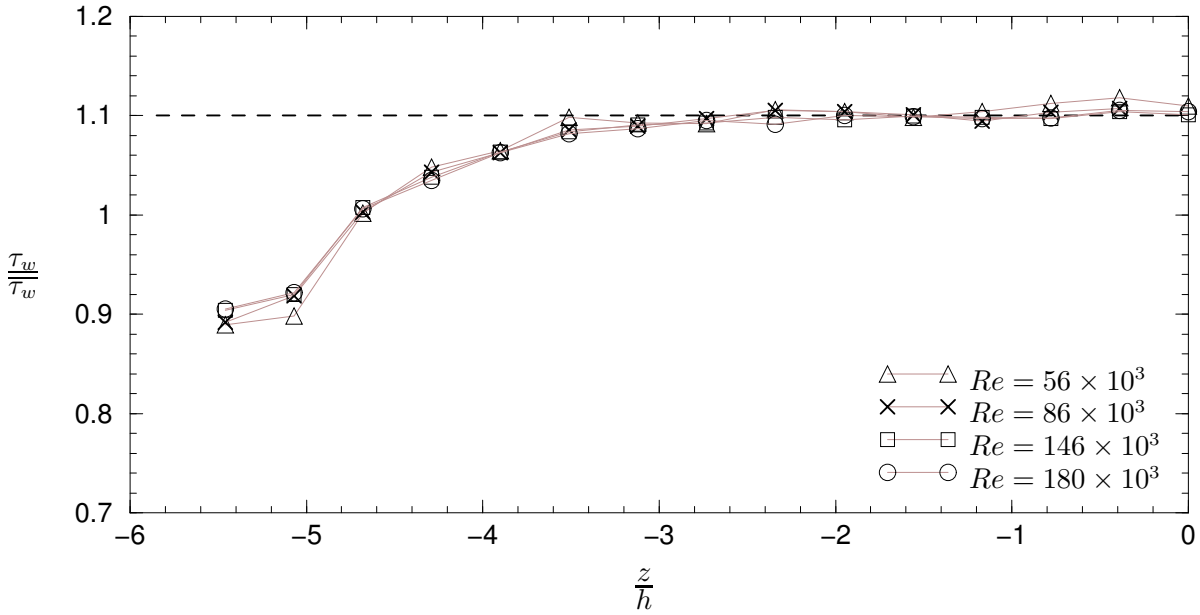

Figure 4.3: Spanwise variation of channel bed shear stress normalised with perimeter-averaged wall shear stress $\overline{\tau_w}$.

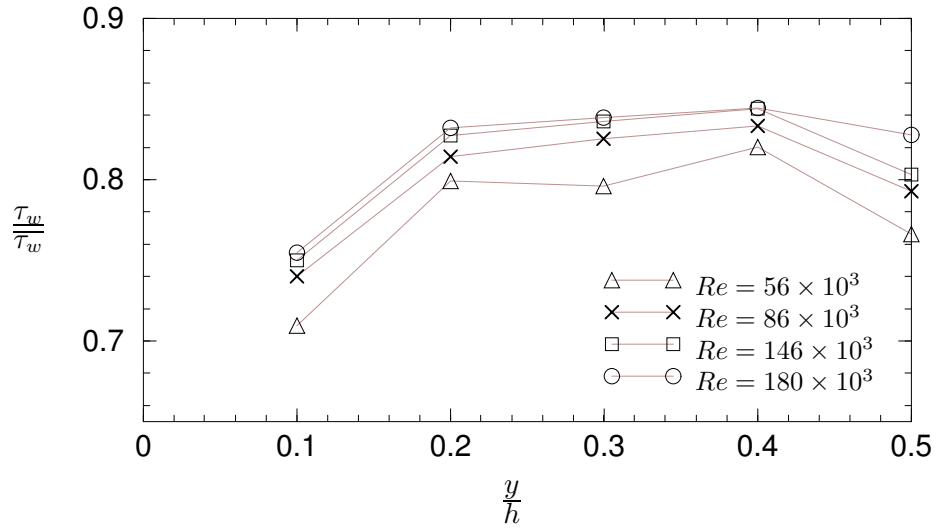

Figure 4.4: Variation of channel side-wall shear stress normalised with perimeter-averaged wall shear stress $\overline{\tau_w}$.

the perimeter-averaged shear stress $\overline{\tau_w}$) with non-dimensional spanwise coordinate. Here it is seen that the normalised wall shear stress maintains a constant level from $z \approx -3.5h$ to the channel bed centre within Preston tube error limits. It is stated in Patel (1965), from which the Preston tube calibration curves employed may be found, that the Preston tube method can be considered accurate to within $\pm 3\%$. Thus, as $z = 0$ is approached, the variations observed about $\tau_w = 1.1\overline{\tau_w}$ are attributed to experimental error. The constancy of $\tau_w/\overline{\tau_w}$ would suggest that any side-wall effects on the wall shear stress are negligible beyond a distance of $2.4h$ from the side-wall (more on side-wall effects will be discussed in the following section, §4.2). Another interesting observation from figure 4.3 is the absence of Reynolds number dependence in normalised τ_w away from the side-wall (i.e., beyond $z = -3.5h$). This is interesting because τ_w in the vicinity of the side-wall ($z \approx -5h$) appears to increase with Re for low Re. For higher Reynolds number, $\tau_w/\overline{\tau_w}$ appears to reach a constant at *any* given perimetric point. Further, the side-wall shear stress distributions, shown in figure 4.4, show similar Re dependence. The behaviour of the side-wall shear stress implies that the functional relationship between $\overline{\tau_w}$ and Re is different to that of the centreline τ_w—Re relation. This should result in a Reynolds number dependence of normalised centreline τ_w, at least for low Re. The reason such a result is not realised in the data is simply that, due to the high aspect ratio of the duct, the side-wall shear stress makes only a small contribution to the perimetric average. That is, the Re variation of side-wall shear stress is not strong enough to make an impact on the normalised centreline τ_w. Now, the Re independence is a useful practical result as it means that, for any Re, an engineer may accurately calculate the more useful quantity, $\overline{\tau_w}$, from the practically less important, but easily measured, channel centre τ_w.

The above observation is in contrast to the results of Leutheusser (1963). In this reference, the perimetric wall shear stress distribution around ducts of aspect ratio 1 and 3 were studied in the same manner as the author's study. Due to the low aspect ratio, a noticeable Re dependence of the normalised centre τ_w was observed in the $A_s = 3$ case. This indicates that the $\tau_w/\overline{\tau_w}$—Re relation is aspect ratio dependent. This is hardly surprising since dividing equation (2.27) by (2.25) gives,

at the channel bed centre,

$$\frac{\tau_w}{\overline{\tau_w}} = \epsilon(A_s)\left(1 + \frac{1}{A_s}\right). \tag{4.3}$$

From a practical standpoint it would be useful to know how the normalised τ_w varies with A_s so that $\overline{\tau_w}$ could be determined from centre τ_w for *any* aspect ratio duct; that is, it would be useful to know the behaviour ϵ. In the following section §4.1.4, a graphical form of $\epsilon(A_s)$ will be postulated.

Leutheusser (1963) also presents side-wall shear stress distributions for his two ducts. The results show similar trends to that of figure 4.4 in that the normalised shear reaches a peak below, and a trough at, the side-wall centreline. This behaviour is due to the well-known presence of secondary flow cells in the channel corner as discovered by Gessner & Jones (1965) and sketched in figure 4.8.

According to equation (4.3), the normalised wall shear stress at the channel centre should be $1 + 1/A_s = 1.085$ for the duct studied here — assuming $\epsilon(A_s) = 1$. From figure 4.3 it is evident that this prediction underestimates the measured ratio by around 1.5%. Although this is within experimental error, the trend in the channel bed shear stress is undeniably $\tau_w \approx 1.1\overline{\tau_w}$ in the central flow region. Since there is no reason that equation (4.3) should not hold, consistent error in Preston tube readings must be present. The only region where such (consistent) error could be introduced is in the side-wall region where the flow has significant secondary motions. Under-reading in this region would not have to be excessive; it is unlikely that the error would be greater than 3.0% given the $\overline{\tau_w}$ error is only 1.5%. A possible problem with the Preston tube near the duct corner is that the true line of action of wall shear stress is not aligned with the streamwise direction. Gessner & Jones (1965) have shown that this misalignment does not exceed 4^o for flow near a corner. This amount would appear too small to account for the errors observed. In the context of this thesis, however, it is sufficient only to acknowledge the presence of Preston tube error in secondary flow regions. Further research, beyond the scope of this investigation, would definitely be required to quantify this error.

4.1.4 The three-dimensionality factor

In Chapter 2, the issue of determining channel centre wall shear stress from pressure gradient was discussed. It was shown that, for high aspect ratios, a region of two-dimensional flow should exist, which permits the use of the τ_w—dp/dx relationship (2.24). For low aspect ratio ducts, however, the three-dimensionality factor, $\epsilon(A_s)$ was introduced into (2.24):

$$\tau_w = \epsilon \frac{h}{2} \left| \frac{dp}{dx} \right| .$$

Now, the form of $\epsilon(A_s)$, as illustrated in figure 4.5, has been roughly estimated from the following sources:

i. Leutheusser (1963), as discussed in the previous section, provides wall shear stress distributions of square and $A_s = 3$ ducts. The experimental procedures and facilities employed by Leutheusser (1963) were impressive; the $3''$ high ducts had a development length of $L/h \approx 280$ and wall shear stress was measured with $0.82mm$ diameter Preston tubes. The wall shear stress measurements were checked by comparison with $1.6mm$ Preston tubes and two flow Reynolds numbers were studied. As stated, Leutheusser observed a weak Re dependence of normalised centre τ_w, which might imply a similar Re dependence of ϵ.

ii. Wall shear stress distributions from the present study indicate that a duct of $A_s > 7$ will have two-dimensional flow at its centre. This is confirmed by channel exit velocity profiles, crossed hot-wire measurements (presented in Chapter 3) and the channel flow literature review of Dean (1978). Therefore the $\epsilon(A_s)$ curve should be very close to unity at $A_s = 7$. From the current investigation, only one data point is contributed to figure 4.5 since only one aspect ratio was studied. Recall that no Re dependence was observed in figure 4.3 and therefore, the Reynolds number effect on ϵ remains uncertain.

It is obvious that the $\epsilon(A_s)$ curve, displayed in figure 4.5, is only a crude approximation; it is designed to give the reader a rough idea of aspect ratio effects. Unfortunately there is insufficient accurate experimental data in the literature to construct

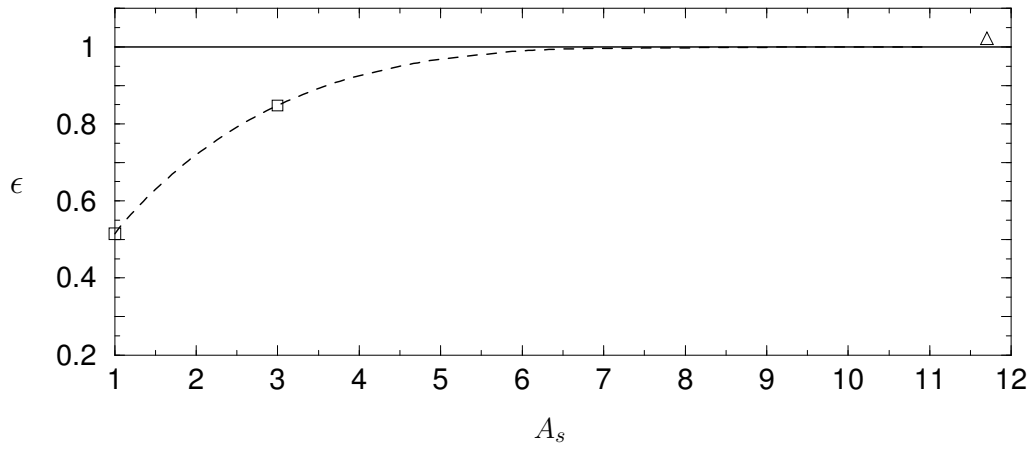

Figure 4.5: Approximate form of the three-dimensionality factor, ϵ; ▫ , estimated from Leutheusser (1963) and △ , present study.

a more accurate $\epsilon(A_s)$. Obviously a variable aspect ratio duct would be required for further experimental analysis of this function; a feature which was not available on the facility built for this project.

4.2 Spanwise mean velocity measurements

To the author's knowledge, no detailed investigation into the streamwise development of the flow near the sides of a high aspect ratio rectangular duct has been published in the literature. The question was posed to the author by colleagues during private communications: does the *side-wall boundary layer*, by which is meant the region of flow affected by the presence of the side boundaries, develop indefinitely in the streamwise sense? Or does this layer reach a state where no further growth toward the centre of the channel occurs? The author argued that, if the flow is fully developed, the protrusion of the side-wall effect must cease at a spanwise location which is invariant with x, for large enough x. If this is not the case, that is, if the thickness of the side-wall boundary layer, Δ, increases with x, then truly fully developed flow does not exist; or *may* exist asymptotically if Δ is only asymptotically constant. Others argued that the side-wall boundary layer will evolve in a manner similar to any other boundary layer, since its growth is not restricted by the relatively distant opposing wall. Both arguments were merely conjectures, however, requiring measurements of the side-wall boundary layer to provide evidence in

support.

The measurements were taken at six streamwise locations, $L/h = 50$, 100, 125, 150, 176 and 210, with a pitot tube as detailed in Chapter 3. The results shown in figure 4.6 are scaled and plotted in such a way as to provide evidence pertaining to the aforementioned argument. The velocity scale used is the velocity at the end of the traverse, U_{CL}, while the length scale is the channel height, h. Note that the offset, non-dimensionalised spanwise distance from the channel side-wall is denoted as

$$\frac{z_s}{h} = \frac{z}{h} + \frac{w}{2h},$$

where w is the channel width.

The first plot in figure 4.6 clearly indicates that the mean velocity on the horizontal plane of symmetry of the channel is invariant with z_s after approximately $3h$ from the side-wall. Thus, at the measuring station, $L/h = 205$, the central flow region is unaffected by the side-wall presence. Futhermore, from the upstream measurements shown in figure 4.6, there appears to be negligible difference in the protrusion of the side-wall layer up to $L/h = 125$. At $L/h = 100$, very slight changes are noticeable in the profile. For example, in the vicinity of $z_s/h = 1$, the velocity remains closer to the centre value than at previous stations; slight waviness in the velocity away from the wall is evident; and Δ is reduced to $2.35h$. The observed values of Δ are highlighted by the dotted grey lines indicating the approximate thickness of the side-wall layer. It is acknowledged that the positions of the dotted lines are somewhat subjective, especially considering the abscissa resolution is only 0.15 units, however the trends in the data are unmistakable. At the most upstream measuring station, $L/h = 50$, the side-wall layer thickness is dramatically decreased with $\Delta \approx 1.5h$. In figure 4.7, a larger plot of the side-wall profile for $L/h = 50$ is shown to more clearly illustrate the underdeveloped flow features. The most distinctive of the features observed is the strength of the intermittency in mean velocity toward the channel centre. Interestingly, this 'intermittency' appears to have consistent trends at all Reynolds numbers, that is, peaks and troughs in the mean velocity occur at identical spanwise wall-distances regardless of Re. This consistency has been observed in other channel flow studies presented in the literature. Knight & Patel (1985),

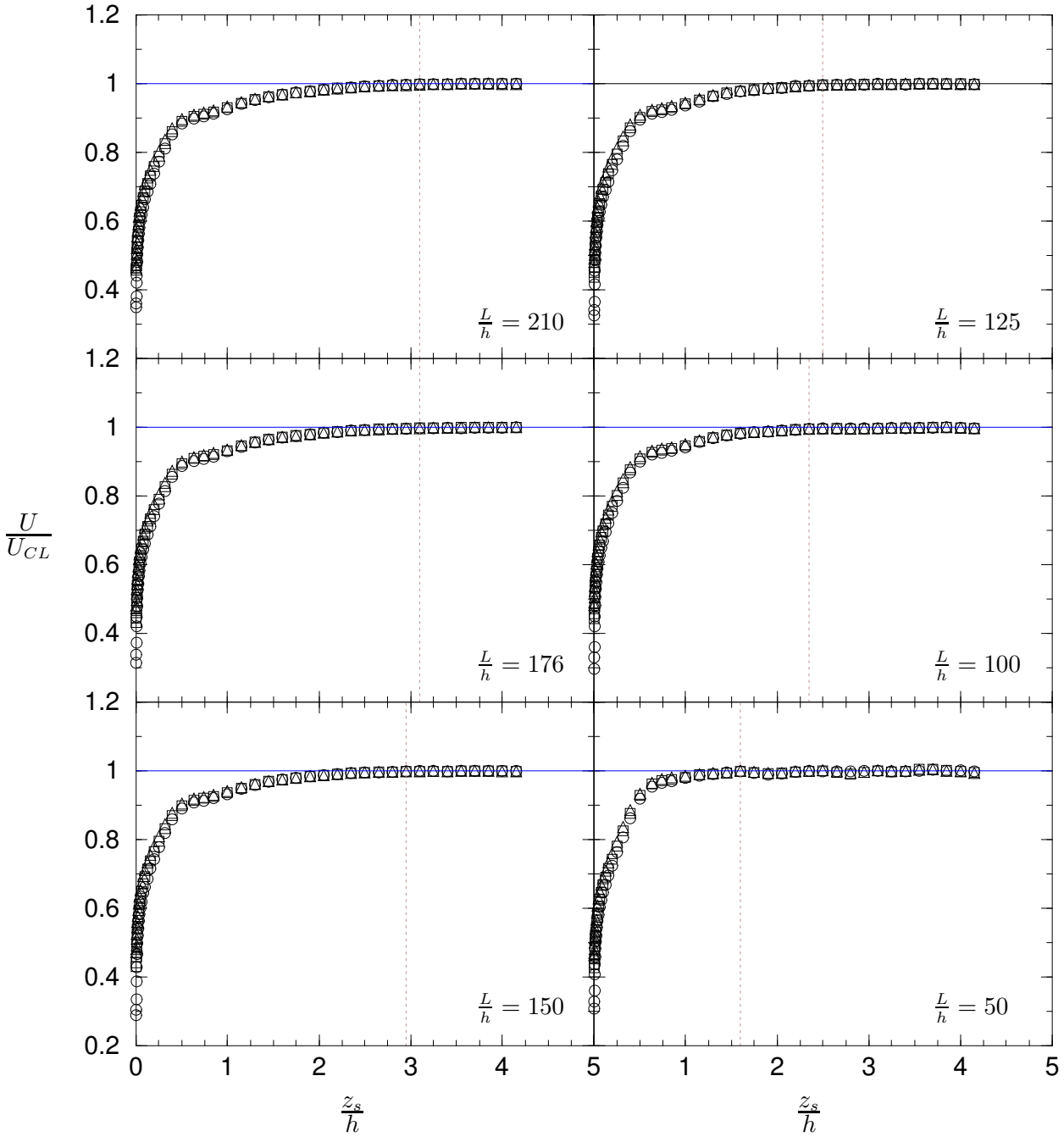

Figure 4.6: Spanwise distribution of streamwise mean velocity measured along the plane of symmetry. Three Reynolds numbers are shown: $Re = 40 \times 10^3$, $\circ$; $Re = 106 \times 10^3$, $\square$; $Re = 186 \times 10^3$, $\triangle$.

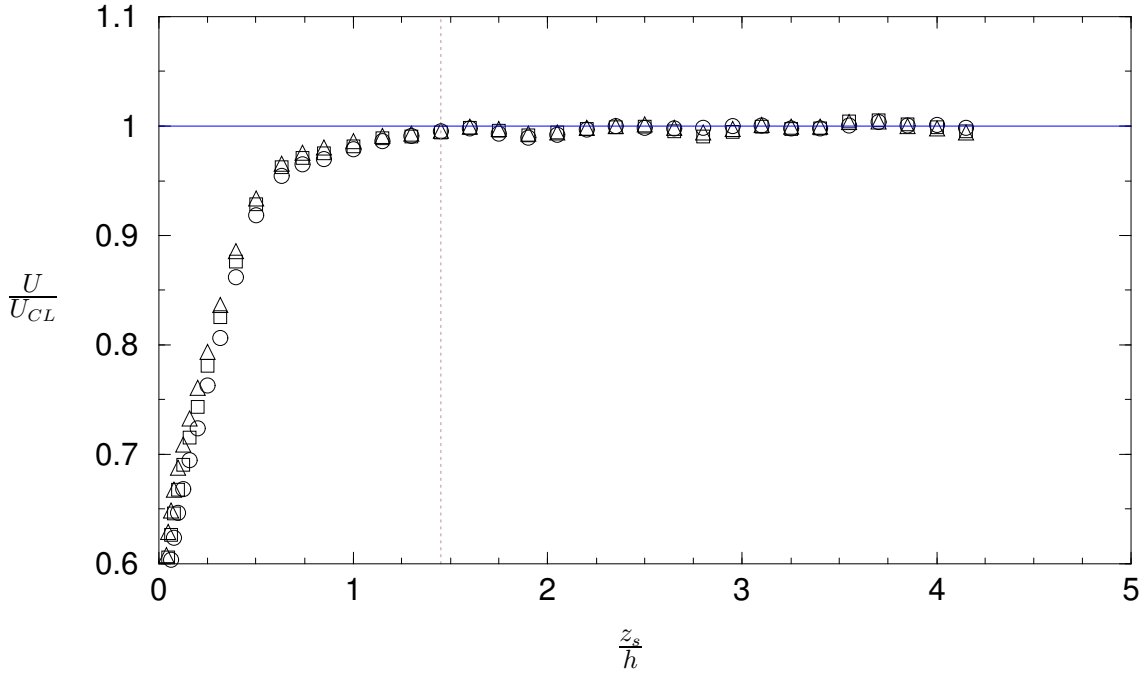

Figure 4.7: Expanded view of the spanwise distribution of streamwise mean velocity for $L/h = 50$. Symbols as in figure 4.6.

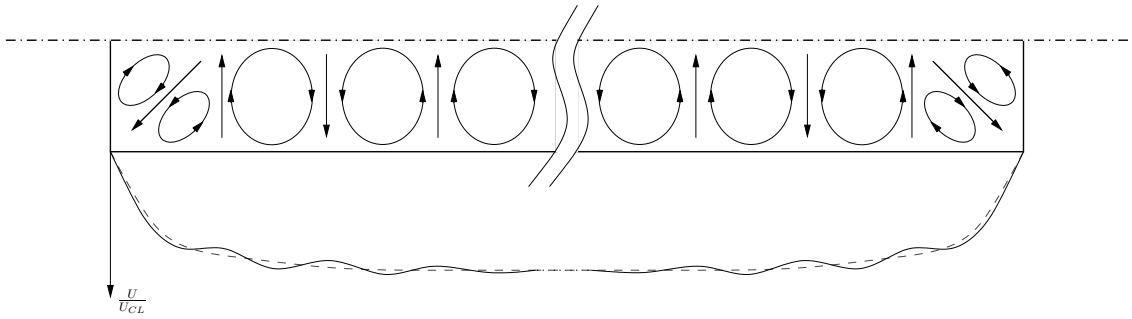

Figure 4.8: Sketch of hypothetical secondary flow cells in the underdeveloped channel flow. Also included is a rough sketch of the mean velocity profile resulting from such a flow pattern.

for example, suggest that there exists secondary flow cells across the channel† as sketched in figure 4.8. Note, however, that the experimental evidence presented in figure 4.6 does not support the presence of such cells for fully developed flow as suggested by Knight & Patel (1985). The cells only appear noticeably at $L/h = 50$ and may be distinguishable as far as $L/h = 100$.

† This suggestion is made based on wall shear stress distributions in fully developed channel flow, rather than mean velocity profiles.

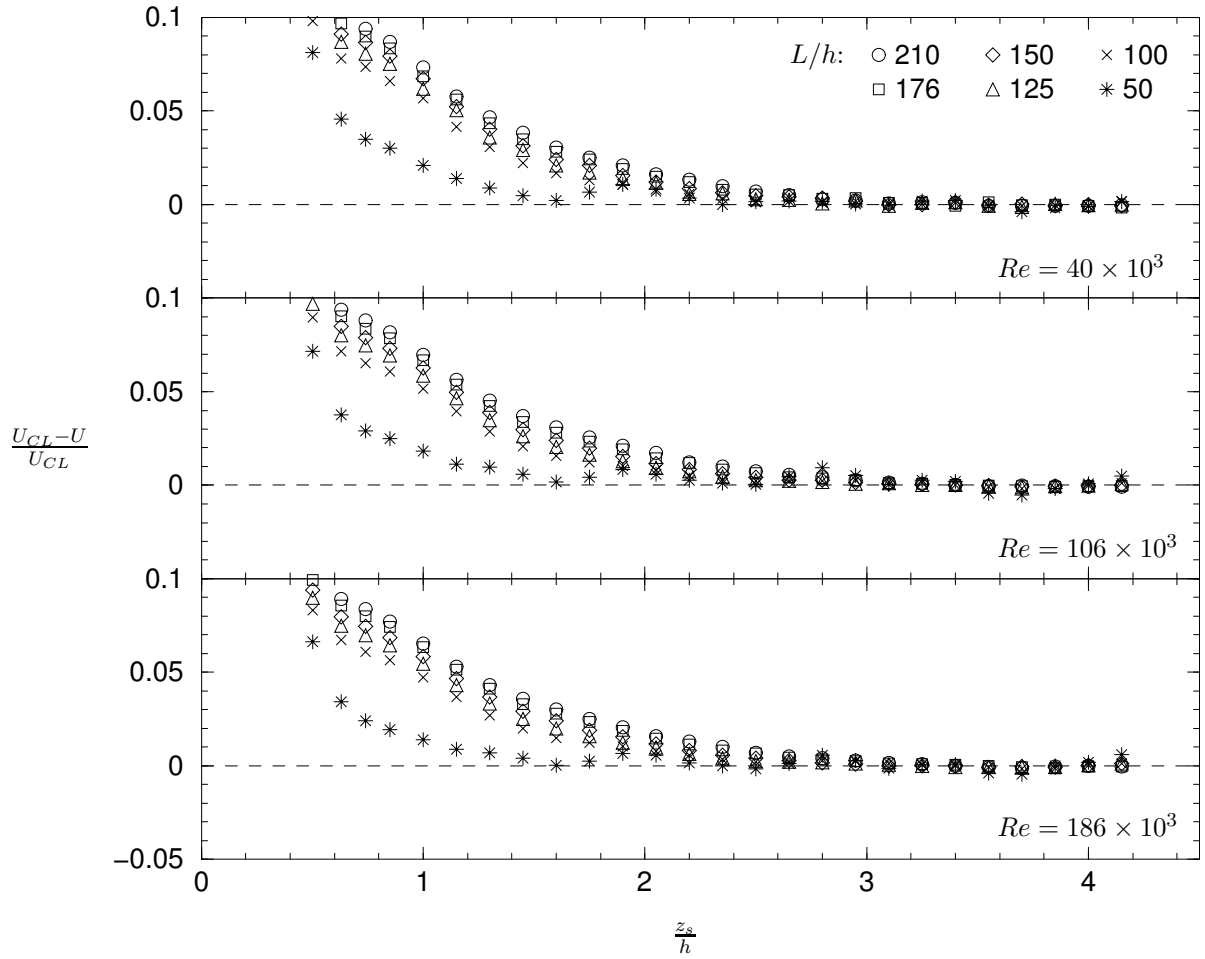

Figure 4.9: Side-wall velocity defect profiles at each measuring station. Outer flow scaling applied.

To further investigate the side-wall flow development, it is useful to plot data from all stations at a given Reynolds number together. Since three Reynolds numbers were studied across the possible range, three subplots are provided in figure 4.9, each displaying velocity defect profiles for all streamwise stations. Reynolds numbers for each downstream location were matched to within 1% for $L/h > 50$ and 2% for $L/h \geqslant 50$. It is once again immediately obvious that the $L/h = 50$ flow case for all Reynolds numbers is underdeveloped. All subplots of 4.9 consistently show that, with increasing streamwise distance from the inlet, the velocity defect level decreases for $z_s/h < 2$; that is, in the vicinity of the side-wall layer edge. Acknowledging experimental error, the two most downstream profiles are almost indistinguishable for all Re (admittedly, the $L/h = 176$ profile lies marginally below the $L/h = 210$ profile), while all other profiles display a noticeable vertical shift for $z_s/h < 2$. This undeniable trend indicates that the side-wall flow is still under devel-

opment at least as far as $L/h = 125$ and arguably up to $L/h = 150$. In fact, it could be argued that the side-wall boundary layer growth is indeed asymptotic, owing to the slight discrepancies between the $L/h = 150, 176$ and 210 profiles. This would imply that the central flow development is also asymptotic, although from the measurements presented so far, changes in the flow beyond $L/h = 176$ are undoubtedly insignificant.

In this section so far, only the details of side-wall flow behaviour far from the side-wall have received attention. The flow in the immediate vicinity of the wall was also studied, however, and the results are presented in the six subplots of figure 4.10. The measurements shown are scaled with inner flow variables and plotted on semi-logarithmic axes to more clearly observe the inner flow behaviour. The data show excellent collapse in the inner flow region, even in the underdeveloped flow stations, although it must be noted that the friction velocity, U_τ, at the centre of the channel side-wall was determined by means of the Clauser (1954) method. This method, commonly employed by boundary layer analysts, requires the assumption of an overlap region in the side-wall boundary layer and further, that this region is governed by the log law (2.4). Another method available is the Preston tube which was previously introduced to determine wall shear stress around the perimeter of the channel. The Preston tube method does not rely on the log law, however it does assume the law of the wall (2.1) holds. Both methods give very good agreement and tables of U_τ may be found in Appendix D. In summary of the apparently fully developed flow calculations: it was observed that the Clauser determined U_τ at the centre of the side-wall was, on average, $85.0 \pm 1\%$ of the channel bed centre friction velocity (as determined from the pressure drop relation, 2.24). In fact, this was true for all stations except the clearly underdeveloped station, $L/h = 50$, and the fraction had no significant Reynolds number dependence. For the underdeveloped station, the ratio of the two friction velocities dropped to 0.825 at the lower Reynolds numbers and 0.81 for the highest. The invariance (with Re) and magnitude of the friction velocity ratio is consistent with the carefully measured side-wall shear stress measurements presented in section §4.1.3.

Again it may be useful to plot inner flow scaled profiles of a given Reynolds number

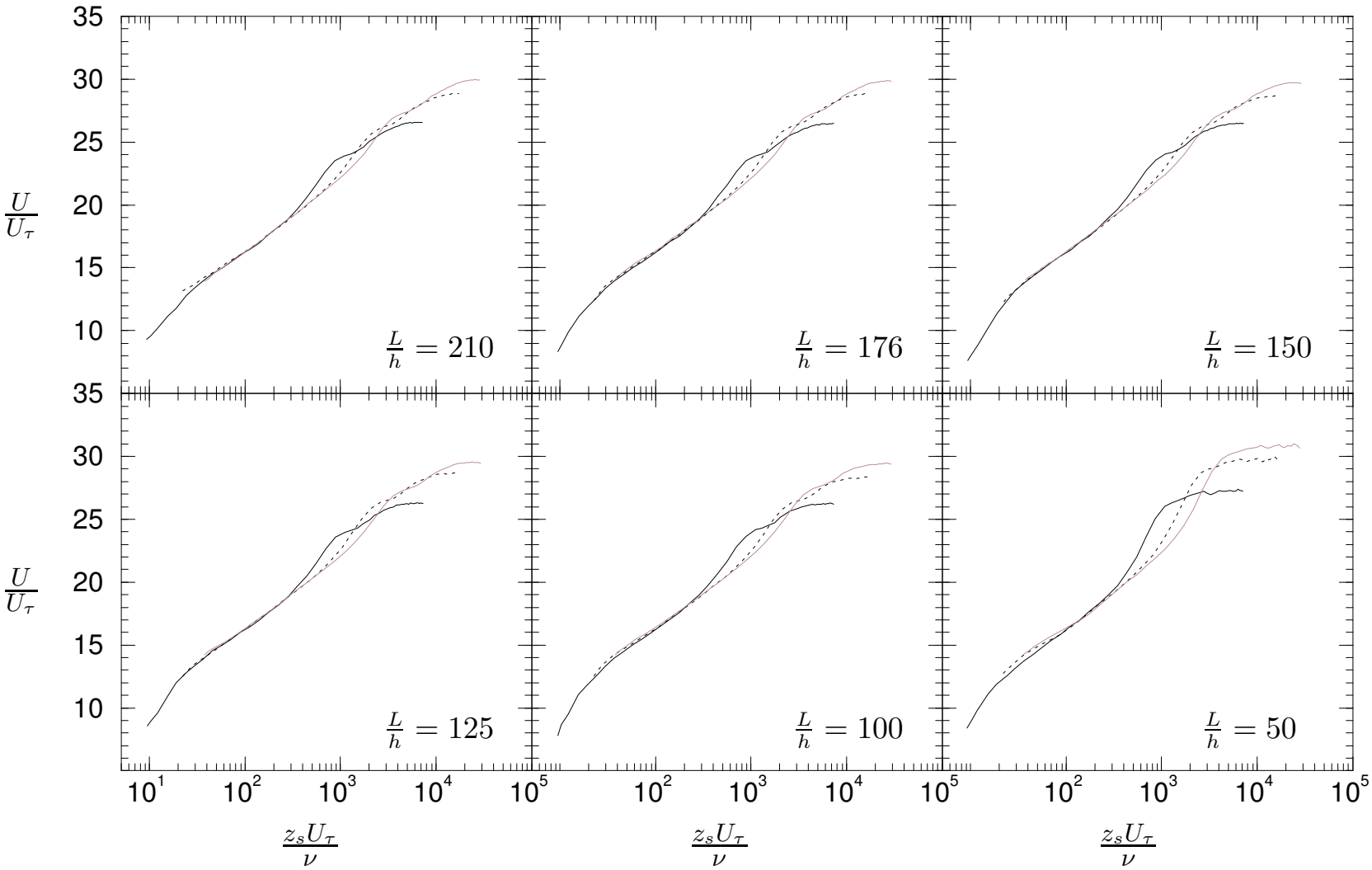

Figure 4.10: Side-wall velocity profiles with inner flow scaling at three Reynolds numbers: $Re = 40 \times 10^3$, ——— ; $Re = 106 \times 10^3$, - - - - ; $Re = 186 \times 10^3$, ——— .

at all streamwise locations together. Such plots are displayed in the subplots of figure 4.11. Aside from the now expected underdeveloped flow behaviour at $L/h = 50$, it is clear that the apparently fully developed flow measurements collapse well past the overlap region, even approaching the limit of the so-called side-wall boundary layer. This gives confidence that the Clauser (1954) method is useful near the side-walls because, for equivalent Re, inappropriate determination of the velocity scale U_τ would result in incomplete collapse of the data outside of the overlap region. It follows that the law of the wall is upheld in the complex, highly three-dimensional turbulent flow at the side-walls. Furthermore, while the scaled profiles are identical for each streamwise location where $L/h \geqslant 100$, the U_τ values also display no systematic relationship with L/h. For developing flow it would be expected that the Clauser determined local U_τ values would increase with streamwise location. This appears to contradict the earlier data analysis that concluded the side-wall flow remains under weak development possibly as far as $L/h = 150$. However, there are two possible explanations for this contradiction of which the latter is most important:

i. The Clauser determination of U_τ not only requires the assumption of the log law, but also a curve-fit to a limited amount of data (only four points at the lowest Re).

ii. The differences between developing flow profiles seen in figure 4.9 were very small and only noticeable due to the amplification of the subplots in this figure. Such small differences closer to the side-wall may be masked by measurement inaccuracies combined with processing of the data.

In summary, the side-wall affected flow has been shown to asymptotically approach full development, although there is barely a noticeable change in this flow region for $L/h \geqslant 150$. However, the effect of development on the flow very near to the side-wall appears to be negligible. While these observations are interesting, the true relevance of this finding to the central flow development will only be understood when the channel bed-wall-normal distributions of velocity are presented in the following section.

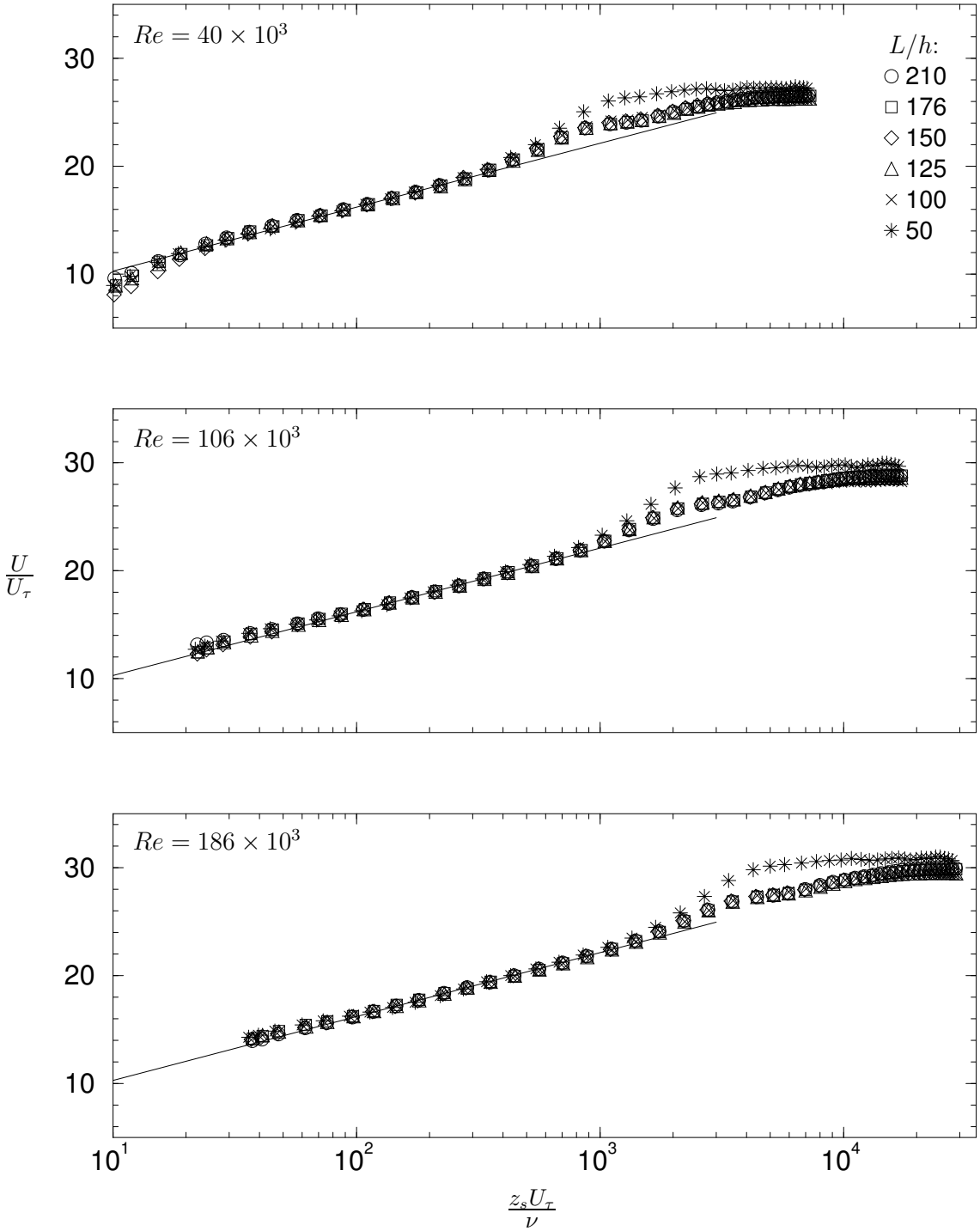

Figure 4.11: Inner flow scaled side-wall velocity profiles at all measuring stations at the Reynolds number indicated. The solid line represents the log law with constants $\kappa = 0.39$ and $A = 4.4$.

4.3 Central flow development

As stated in the introductory remarks of this chapter, there are a number of issues in duct flow that remain poorly understood. The development of the flow with distance from the inlet, x, is perhaps the best example. In the literature there are a number of sources describing efforts to *check* that the flow is fully developed. Many of these references compare profiles of turbulence statistics at two streamwise stations for this purpose. However, the author holds the view that there exists no reliable, comprehensive study of duct flow development length; that is, there is no study comparing turbulence statistics at a number of streamwise stations with the aim of determining the point of full development. Following on from the side-wall flow analysis of the previous section, velocity profiles at the channel bed centre at various streamwise stations will be presented and analysed in detail here.

Velocity profiles were measured with a pitot tube with $d_p = 1mm$ at streamwise locations of $L/h = 70, 94, 128, 148, 176$ and 205. All profiles have the MacMillan shear and wall proximity corrections applied. The turbulence correction (2.47) was not applied to any data due to the uncertainty of the turbulence intensity behaviour with streamwise location. It should be noted that the corrections applied in addition to that for shear should not affect the ensuing analysis. As discussed earlier in this chapter, the relationship between pressure gradient and wall shear stress given by equation (2.24) is valid for two-dimensional channel flow. However, the pressure gradient is only constant for fully developed flow so that (2.24) is only practical for fully developed flow. Thus, it is to be expected that τ_w calculated using dp/dx measured in the fully developed flow will eventually represent the local τ_w incorrectly as the streamwise station approaches the inlet. When this occurs (i.e., when the flow is underdeveloped) an alternative method of determining τ_w, and hence U_τ, will be required. The Clauser (1954) method will again be employed for this purpose. This method is not ideal since it effectively forces the inner flow scaled data to fit onto the log law (2.4) with predetermined constants, κ and A. This procedure *may* modify profiles in such a way that changes in the velocity profile due to development — which are of primary interest — are skewed or even masked. Such an effect would be most pronounced at low Reynolds numbers due to the reduced size of the overlap

region, as discussed in the previous section. However, it will be clearly shown in this section that systematic trends in the scaled data are undeniable. Moreover, conclusions drawn from such trends are independent of any random error introduced by the Clauser calculation of U_τ.

Figure 4.12 presents inner flow scaled velocity profiles at each of the six streamwise stations studied. At each station three profiles are plotted, corresponding to the $Re = 40, 105$ and 185×10^3 flows. For all profiles, the friction velocity was calculated from pressure gradient — which is not expected to be the correct scale for all profiles as discussed. It is somewhat surprising then, that at every station, Reynolds number similarity is exhibited in the inner flow region. This gives an early indication that the development length will have little dependence on Reynolds number (for the Re range studied here). An overview of all profiles given in figure 4.12 reveals that there are differences between profiles at different stations. An example is a very slight increase in wake strength as the inlet is approached.

To more clearly illustrate changes in profiles with streamwise station, figure 4.13 is given. The three sub-plots of this figure display profiles at all streamwise stations for a given Reynolds number. Note that the individual profiles of figure 4.13 are identical to those of figure 4.12 — only their arrangement has been altered. The most striking feature of the behaviour of velocity profiles with streamwise distance is now obvious. Figure 4.13 plainly shows that the dominant difference between profiles is a vertical shift, $\Delta U/U_\tau$, which remains close to constant for a given profile at higher Re. Upon discovery, this feature was very surprising because it is commonly thought that a change in the outer flow region of the profile would be the first indication of underdeveloped flow. The vertical shift (at higher Re) may be thought of as analagous to the characteristic wall roughness effect (see Hama, 1954 or Clauser, 1954). Adopting the common definition of roughness effect, the parameter $\Delta U/U_\tau$ is defined by the additional term in the log law:

$$\frac{U}{U_\tau} = \frac{1}{\kappa} \ln \left(\frac{y U_\tau}{\nu} \right) + A + \frac{\Delta U}{U_\tau}. \tag{4.4}$$

For the apparently fully developed profiles measured at $L/h = 205$ (with shear and wall corrections, but no turbulence correction), the constants found to fit the data in the overlap region were: $\kappa = 0.395$ and $A = 4.65$. It will be assumed that κ is

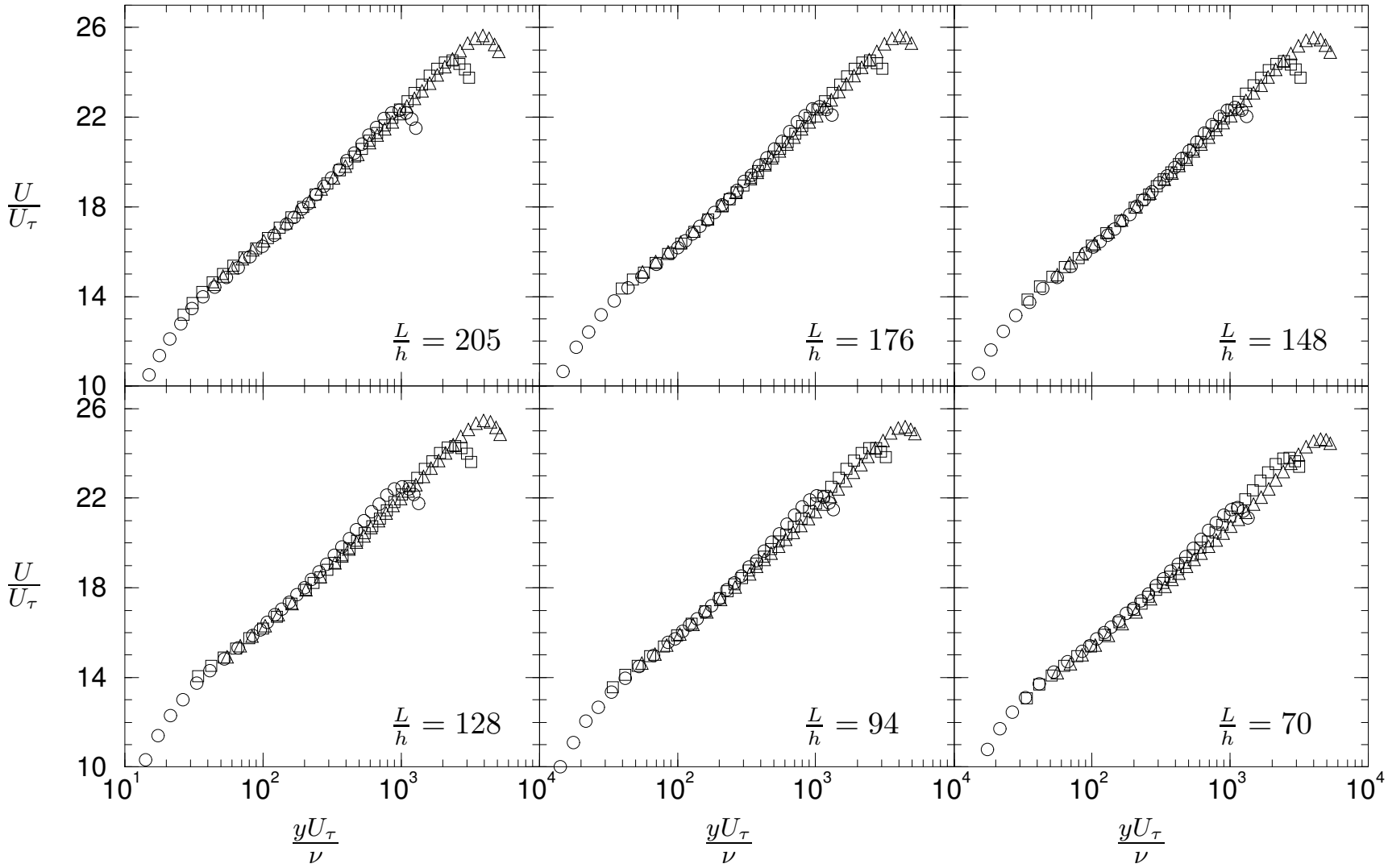

Figure 4.12: Inner flow scaled mean velocity profiles at each streamwise location. ∘ , $Re = 40 \times 10^3$; △ , $Re = 105 \times 10^3$; ▫ , $Re = 185 \times 10^3$.

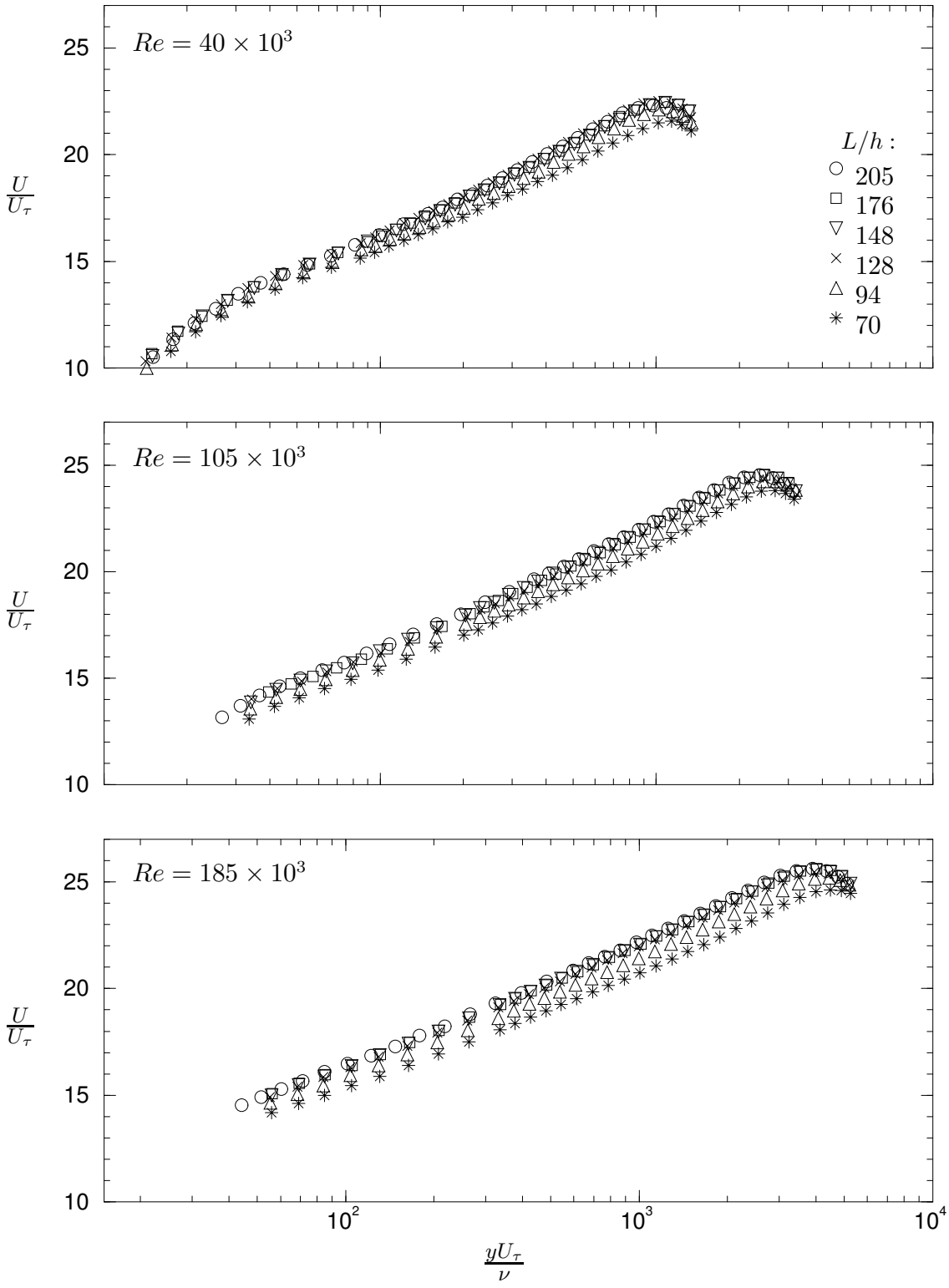

Figure 4.13: Inner flow scaled velocity profiles for each Re at all streamwise stations.

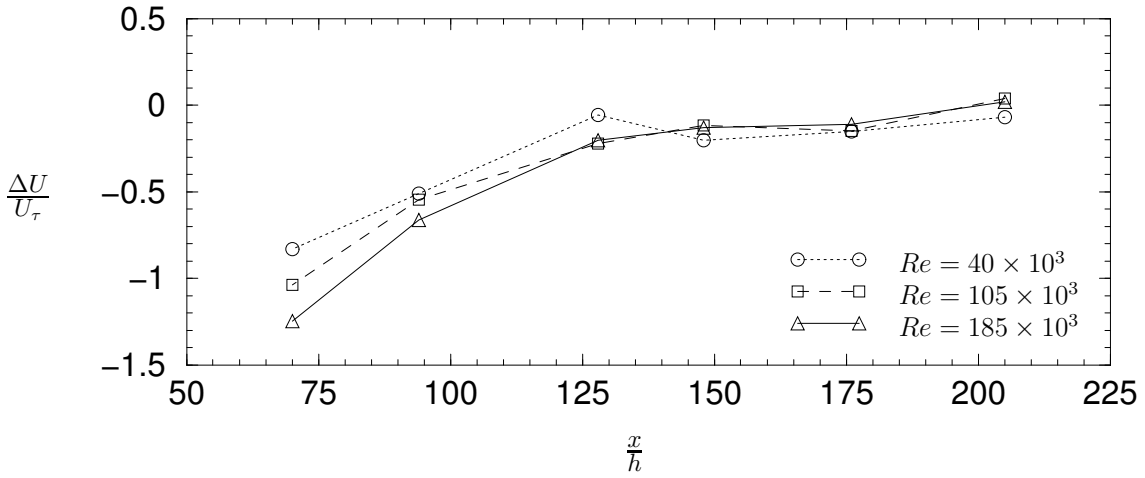

Figure 4.14: The behaviour of the shift in velocity profiles with streamwise distance.

constant for the underdeveloped flow profiles. Constancy in κ does not appear to be an unreasonable assumption from observation of figure 4.13. Thus, the vertical shift in velocity may be determined by a curve-fit of (4.4) to the data in the overlap region.

For each Reynolds number, $\Delta U/U_\tau$ is presented as a function of streamwise station in figure 4.14. It is observed from this figure that the vertical shifting first occurs at around $94h$ from the inlet. Acknowledging the streamwise resolution of the profiles, the point of full development is no further downstream than $148h$. It is suggested that fully developed flow should exist close to $L/h = 128h$, while it is certain that the flow is underdeveloped at $L = 94h$. Additionally, the streamwise development of the profiles does vary with Reynolds number, although this variation appears to be rather weak. The Re dependence is to be expected since the channel flow begins its development by the merging of two boundary layers and the growth of these layers will be Reynolds number dependent. Although the observed Re dependence must influence the flow development length in some way, the streamwise spacing of the data presented here appears to be insufficient to resolve this issue.

At this point, the effect of flow underdevelopment has most clearly appeared as a shift in scaled velocity; the *reason* for the shift is now explained. After merging of the top and bottom wall boundary layers, it would be expected that two flow regions will be present:

i) The flow near the wall which is 'well-behaved' (i.e., behaves the same as the fully developed flow) and includes the inner flow region and a portion of the outer flow region.

ii) In the vicinity of the centreline, where the edges of two boundary layers merge, the flow will be intermittent and unpredictable. This *developing core* region must diminish in size with streamwise location if fully developed flow is to exist. The developing core flow should not influence the 'well-behaved' region, except that a change in boundary conditions (namely, U_τ) would be expected.

The data shown in figures 4.12 & 4.13 appear to show that only the region nearer the wall exists, even at $70h$ from the inlet. However, closer scrutiny of the data reveals that for the two streamwise stations nearest the inlet, there is a change in the flow near the centreline. Careful analysis of the raw data reveals that the maximum velocity occurs *before* the centreline is reached, for $L/h = 70$ and 94. It is very difficult to see this effect in the velocity profiles of figure 4.12 because the velocity gradient near the centreline is very weak. The shift in maximum velocity indicates that the developing core region is very small in size relative to h even at $L/h = 70$. Due to poor spatial resolution of the data near the centreline, the developing core cannot be accurately determined; a rough estimate lies between 0.05–$0.1h$ at the most upstream station. It should be recognised that, if a developing core region exists, the channel half-height is no longer the most appropriate outer flow length scale. Note, however, that any modification of the outer flow length scale for the measurements presented here will have only minor impact due to the small size of the developing core.

Although the developing core region is very small, its impact on the boundary condition, U_τ, is not. In fact, the change in U_τ with streamwise station is responsible for the profile shifting observed in figure 4.13. Thus, the vertical shift parameter, $\Delta U/U_\tau$, is not strictly correct; that is, the profiles are not truly *shifted* vertically, rather they are *scaled* as the flow develops. The shift parameter remains a useful analysis tool, since there is no reliable method of measuring skin friction of the developing flow. Nevertheless, it would be useful to have an estimate of skin friction in order to more appropriately scale the velocity profiles. Hence, the Clauser method

is employed (as suggested earlier) to determine friction velocity.

Assuming the log law with constants $\kappa = 0.395$ and $A = 4.65$, which were determined from the fully developed flow, U_τ was calculated for each profile. Rescaling the data forces almost complete collapse of the inner flow scaled profiles for all stations at a given Re as shown in figure 4.15. However, for the two stations closest to the inlet, the developing core appears more clearly at higher Re. This behaviour was originally mistaken for Re variation. After realising the Re was well-matched for all profiles (in a given sub-plot of figure 4.15), the conclusion was drawn that there is a noticeable change in the wake with development length. It should be noted that this change remains relatively small, given the streamwise spacing of the measurements. Due to the observed wake changes, the rescaled velocity defect profiles should exhibit poor collapse for the two higher Re. Figure 4.16 shows these defect profiles with U_{max} replacing U_{CL} as the reference velocity. This is necessary due to the aforementioned shift of maximum velocity away from the channel centreline when the flow is underdeveloped. The outer flow length scale, Δ, was chosen as the wall-distance corresponding to $U = U_{max}$. Figure 4.16 shows excellent collapse at low Re as expected, while for the two higher Re flows, changes in the profiles are noticeable at the most upstream station, $L/h = 70$. These trends are reasonably consistent with the inner flow scaled profiles, although almost no outer flow variation is observed for any Re for $L/h \geqslant 94$.

Figures 4.15 & 4.16 highlight the small size of the wake change, even while the flow is not fully developed. This finding may provide some insight into the claims of early flow development by authors such as Abell (1974) ($\sim 80D$ for pipe flow). The well-known pipe flow study by Nikuradse (1932) is another example, claiming full development of the mean flow by $40D$. In Abell's case, measurements at two stations approximately $10D$ apart were used for comparison. Measurements shown in this thesis are at stations separated by no less than $20h$. Figure 4.13 clearly shows that even with the larger spacing, there is little difference between any two stations taken in isolation; two stations $10h$ apart would be close to indistinguishable. Futhermore, Abell (1974) used the Clauser method to determine friction velocity — a practice that masks the noticeable development effects observed in figure 4.13, while the

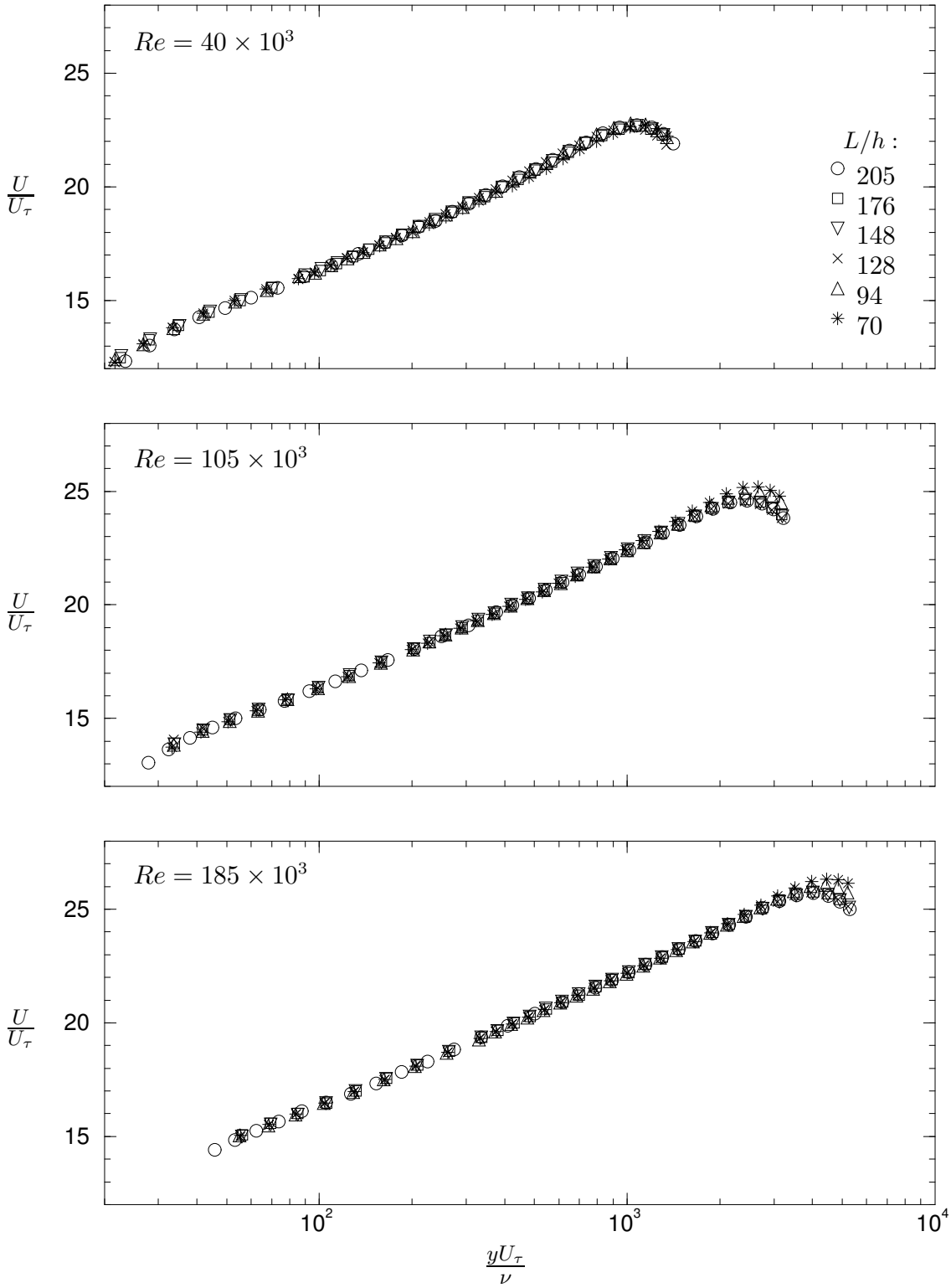

Figure 4.15: Rescaled mean velocity profiles at all streamwise locations for each Re. The friction velocity, U_τ, has been determined using the Clauser (1954) method.

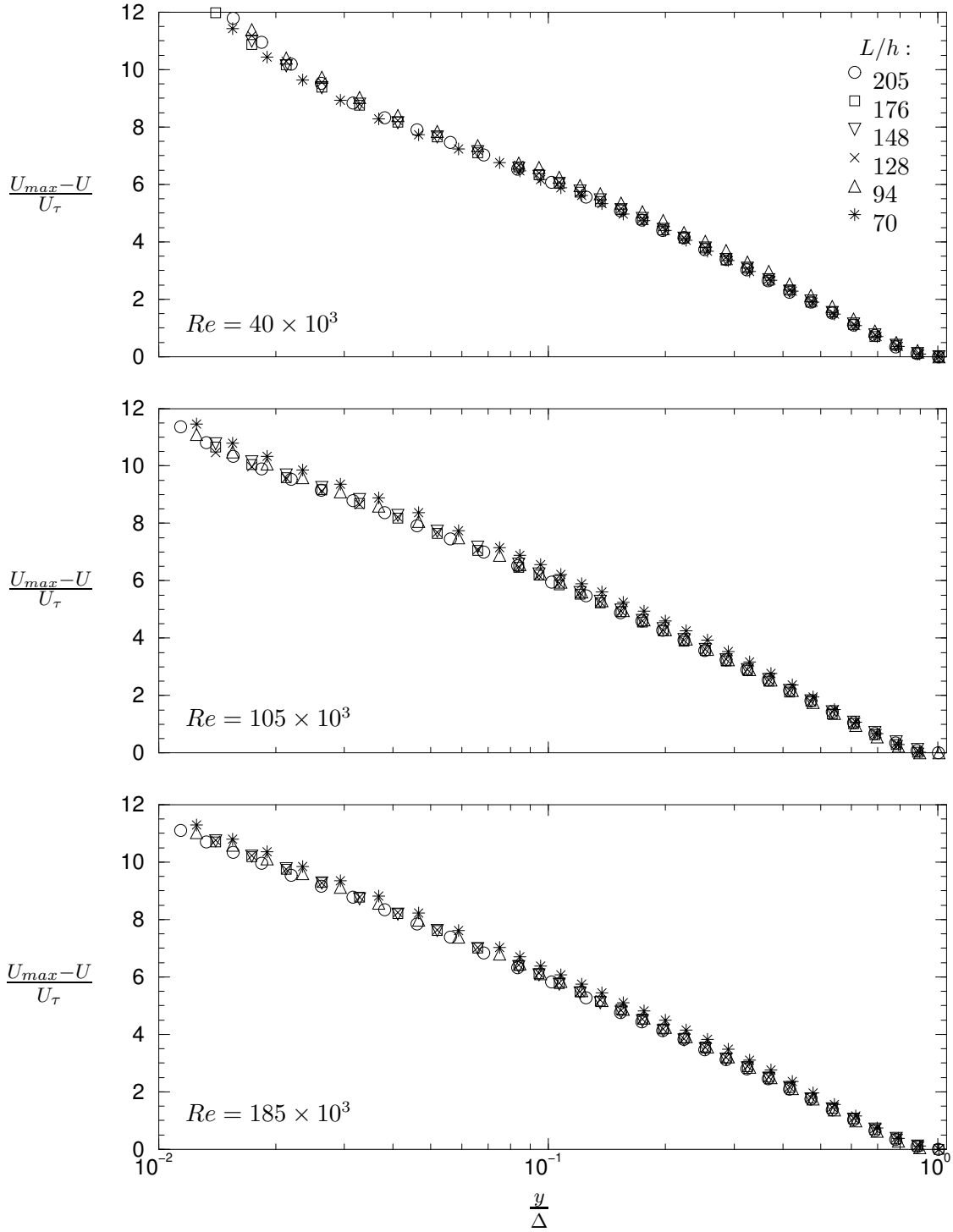

Figure 4.16: Outer flow scaled velocity defect plots at all stations for a given Re. Note that U_{max} is the maximum velocity of a profile and Δ is the wall-distance corresponding to U_{max}.

friction velocity would remain within the error bounds of the Clauser method. Thus, the comparison of two streamwise stations is unlikely to give an accurate account of the flow development (especially if the stations are too close together). Further, for small ducts (i.e., $h < 100mm$), the small size of the developing core observed in this study may be immeasurable for $L/h \gtrsim 100$ using common measurement techniques. These issues should be taken into account by the researcher when analysing the relevant literature.

Some final notes on channel flow development

The above arguments have shown some clear trends concerning flow development, however the following considerations must be noted:

i) The results are specific to high aspect ratio channels with uniform flow at the inlet and with tripped perimeter boundary layers to introduce turbulence immediately.

ii) Only a small Re range has been studied as the facility permits. Extrapolation to higher Re should be carried out with caution.

iii) Only mean velocity measurements have been recorded. Higher-order turbulence statistics would be very helpful in providing more details of the developing core region. Unfortunately, it was beyond the scope of this project to complete these measurements.

iv) On the streamwise resolution of the measurements: even if more profiles were recorded to improve spatial resolution, conclusions drawn are likely to be inconsequential. The reason for this relates back to the motivation for a development length study, which was to provide a *guide* for construction of new facilities or to aid analysis and evaluation of published data.

Finally, it is recalled that the side-wall flow development study concluded that beyond $150h$, the flow is arguably fully developed near the channel sides. Further, the side-wall velocity profiles changed only a very small amount downstream of $L/h = 100$. It has since been observed that these changes have no effect on the

central flow. It is therefore tentatively suggested that the point of full flow development for channel flow is approximately $130h$ for the Re range studied here. It is certain, however, that flows with less than $100h$ development will not reach a fully developed state.

Chapter 5

Mean flow results

It was previously stated that there is no shortage of rectangular duct flow studies in the literature. A similar observation may be made concerning pipe flow and, more specifically, mean flow measurements are among the most common presented. Such data is, in general, measured with erroneous pitot tubes and furthermore, careful analysis of the literature reveals that many experiments suffer from hinderances such as insufficient flow development, low spatial resolution or invalid assumptions about flow conditions (usually based on geometrical properties alone). Unfortunately, the author has found the latter experimental practice to occur with disturbing frequency. It is therefore clear to the author that new, more accurate experimental mean flow data will not only be a useful addition to that currently available, but an important reference in the ongoing debate over mean flow scaling laws (see §2.1).

In the following chapter, mean flow results from both pipe and channel facilities of this investigation will be presented. Details given in Chapter 3 establish that the accuracy of experimental techniques was of the highest degree and that construction of the facilities involved was performed with utmost care. The results include a detailed analysis and comparison of pitot tube and hot-wire measured mean streamwise velocity profiles in fully developed flow. The chapter will conclude with a discussion of the previously unexplained differences between mean velocity profiles in circular pipe and channel flows.

5.1 Pipe flow

Mean streamwise velocity profiles (hereafter referred to as simply *velocity profiles*) in the Reynolds number range 40×10^3 – 133×10^3 were measured in the pipe flow facility. The results will be presented and discussed in this section and judgements of the applicability of pitot tube corrections will be made based on comparison with hot-wire measurements.

5.1.1 Inner flow scaling

Firstly, pitot tube measured velocity profiles were recorded and the results are shown in figure 5.1 with inner flow scaling. Both the MacMillan and turbulence intensity corrections have been applied to the data. Secondly, records of hot-wire measured velocity profiles were made and the inner flow scaled results are presented in figure 5.2. No corrections are applied to the hot-wire data, which displays almost identical characteristics to the corrected pitot tube data. Using either measurement technique, the data clearly exhibit excellent collapse for all Reynolds numbers up to the inner flow region limit ($y \approx 0.15R$). This expected result validates the assumption required to arrive at Prandtl's law of the wall (2.1), namely that large scale geometry has no influence on the flow in the immediate vicinity of the wall.

Included in figures 5.1 and 5.2 are the logarithmic laws (2.4) with appropriate constants. The following values were determined from a least squares error fit to all data in the overlap region ($100\nu/U_\tau < y < 0.15R$[†]): $\kappa = 0.386$ and $A = 4.21$ for pitot tube measurements; $\kappa = 0.384$ and $A = 4.33$ for hot-wire measurements. These constants should be universal across all wall-bounded shear flows and many researchers have adopted the classical values suggested by Coles (1962). Recently, however, there has been considerable debate over the validity of Coles' values. Table 5.1 lists a selection of universal constant values from various recent studies along with the classical values. This table could be extended to include the results of many other experimental programs, however, such collections already exist and may be found, for example, in Zanoun *et al.* (2002), Zanoun *et al.* (2003) or Dean (1978).

[†] The effect of varying these overlap region limits will be discussed shortly in §5.4.

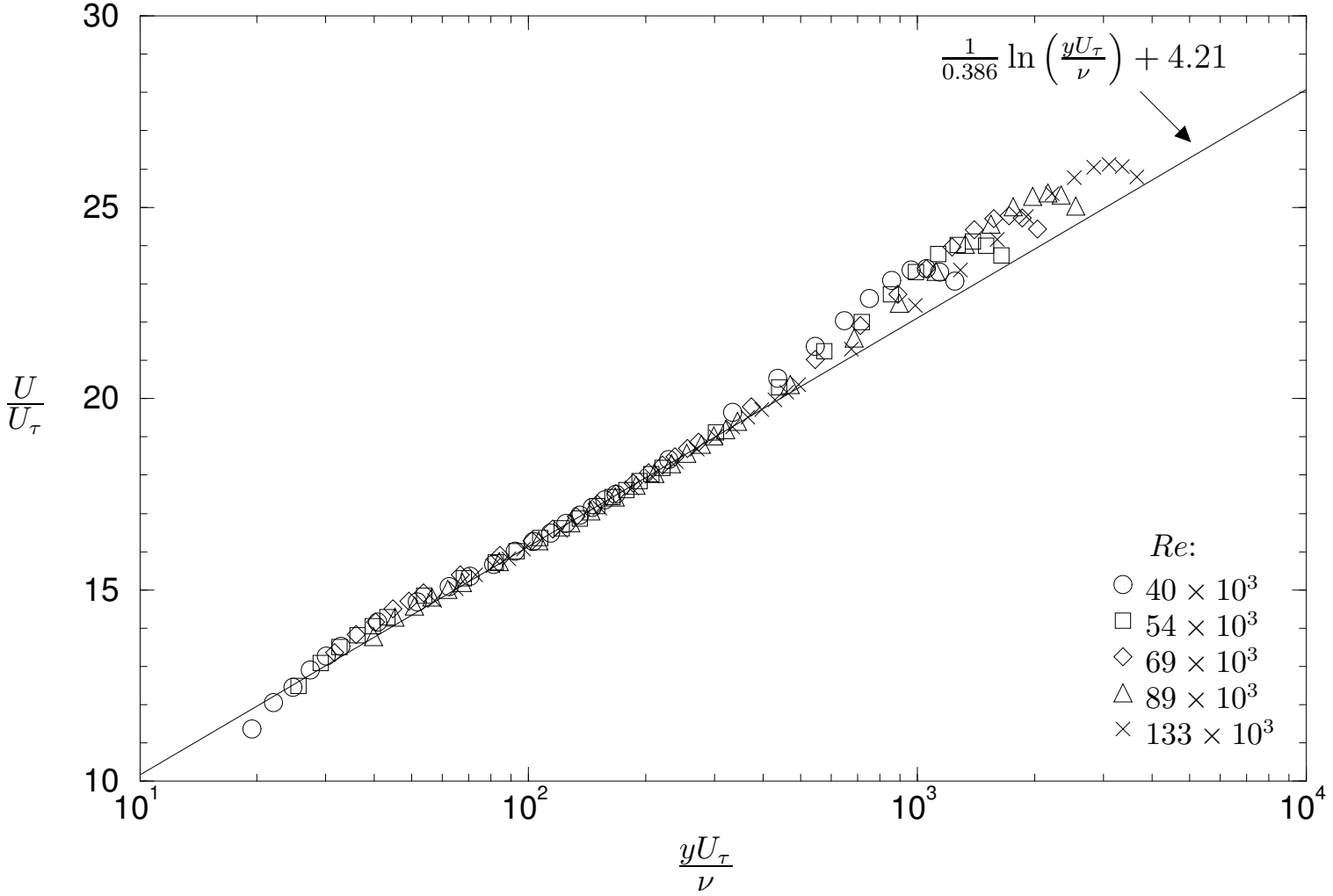

Figure 5.1: Pipe flow: mean velocity profiles measured with a pitot tube; inner flow scaling applied.

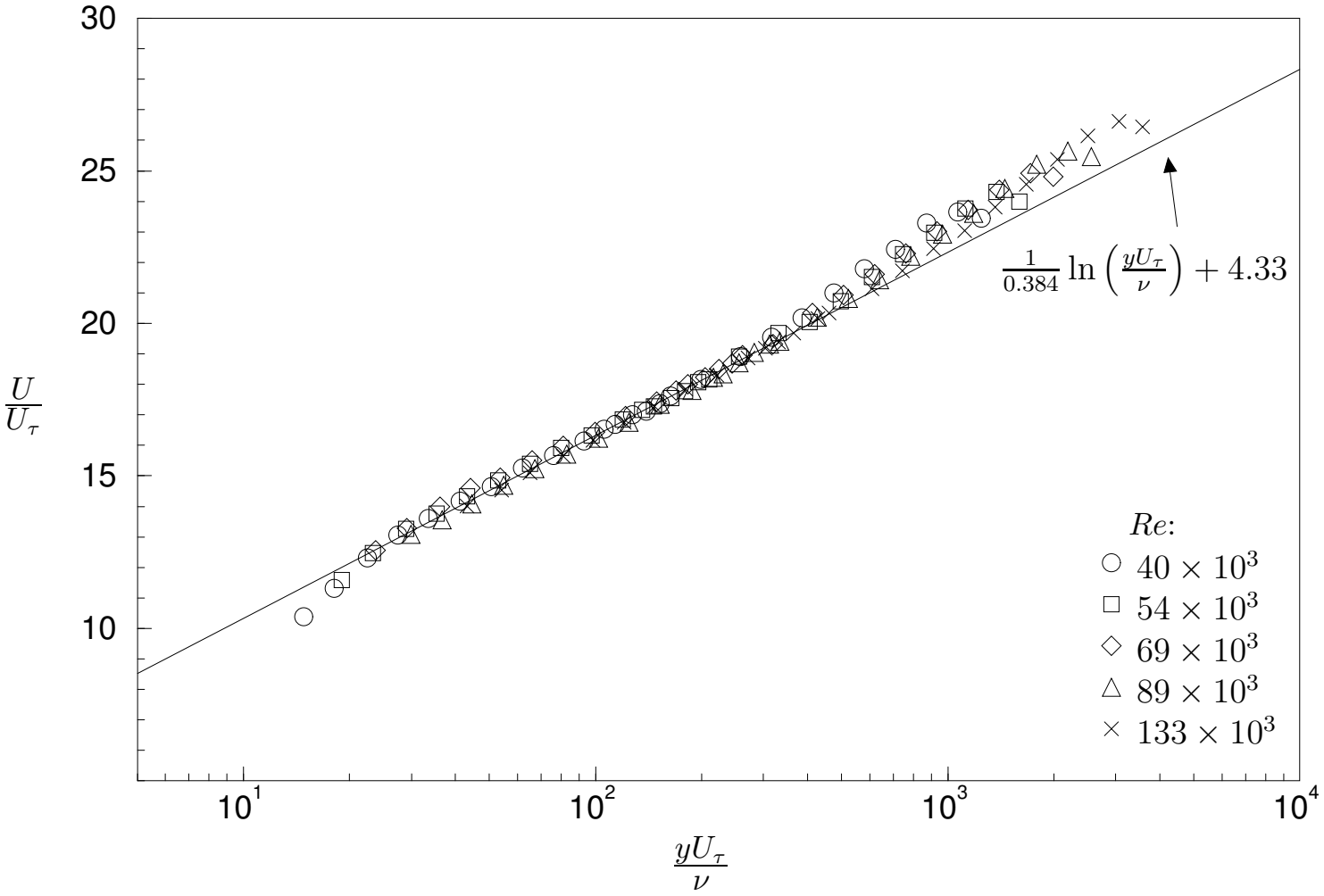

Figure 5.2: Pipe flow: mean velocity profiles measured with a hot-wire; inner flow scaling applied.

	κ	A
Coles (1962)	0.410	5.00
Zanoun *et al.* (2003)	0.370	3.71
Zagarola & Smits (1998)	0.436	6.13
Perry *et al.* (2001)	0.390	4.42

Table 5.1: Recently published values of the universal constants κ and A.

The universal constant values given in table 5.1 are intended to indicate the extremes encountered in the recent literature. Zanoun *et al.* (2003) and Zagarola & Smits (1998) clearly give two very different sets of universal constants, emphasising the need for clarification of these properties of the velocity profiles. While the pipe flow data of Zagarola & Smits (1998) are at extraordinarily high Reynolds numbers, measurements were taken with a pitot tube and therefore require correction. A reanalysis of the data presented in Zagarola & Smits (1998) by Perry *et al.* (2001) produced almost identical constants to those found from the pitot tube measured pipe flow data of this study. This reanalysis simply involved application of the MacMillan and turbulence intensity corrections to the raw pitot tube results of Zagarola & Smits (1998). Zanoun *et al.* (2003) experimented with a similar channel flow apparatus ($Re = 10^4 - 10^5$) to that of this thesis to determine their remarkably low values of κ and A. The working section length of Zanoun's study ($L/h \approx 105$) is probably insufficient for fully developed flow based on the conclusions of Chapter 4. Furthermore, it was shown in the previous chapter, that low values of log law constants are consistent with underdeveloped flow.

Support for the present pipe flow universal constant values is readily available and examples known to the author are listed in table 5.2. Österlund *et al.* (2000b) examined extensive hot-wire data extracted from two boundary layer tunnels in the Reynolds number (based on momentum thickness) range, $Re_\theta = 2,500 - 27,000$. Note that Österlund *et al.* (2000b) uses the direct method of oil-film interferometry to determine skin friction. Hellstedt (2003) also determined constants from a boundary layer flow, however, this special flow satisfied the Rotta (1962) equilibrium conditions which allowed the calculation of skin friction from a momentum balance.

	κ	A
Pipe flow — pitot	0.386	4.21
Pipe flow — hot-wire	0.384	4.33
Perry *et al.* (2001)	0.390	4.42
Hellstedt (2003)	0.390	4.10
Österlund *et al.* (2000b)	0.384	4.10

Table 5.2: Support for the universal constants of the pipe flow study.

Log law or power law?

An issue that has received much attention in the recent literature is the appropriate scaling law for the overlap region of the inner flow scaled velocity profile. Traditionally, the log law (2.4) is the chosen form. As detailed in §2.1, however, there has been a recent resurgence in support for the power law (2.6).

The applicability of a scaling law can be judged by plotting two diagnostic functions, Θ and Γ. These are defined as

$$\Theta = \left(y^+ \frac{dU^+}{dy^+} \right)^{-1}$$

and,

$$\Gamma = \frac{y^+}{U^+} \frac{dU^+}{dy^+}$$

respectively. Both of the above are derived by differentiating the appropriate scaling law. It can be shown that if the logarithmic scaling is appropriate, Θ should be invariant with y^+ in the overlap region. Further, Θ must be equal to κ in this region. Alternatively, Γ will be invariant with y^+ if the power law is the appropriate description of the velocity profile. Also, Γ will be the index, β, of the power law which may or may not be independent of Reynolds number. Unfortunately, both diagnostic functions require differentiation of the data which is often an inaccurate procedure. The most accurate method found (that which gave the least scatter) was a second-order finite difference scheme. The scheme first fits a parabola to three data points y^+_{i-1}, y^+_i and y^+_{i+1}. It can then be shown that the first derivative of the fitted parabola at y^+_i is given by:

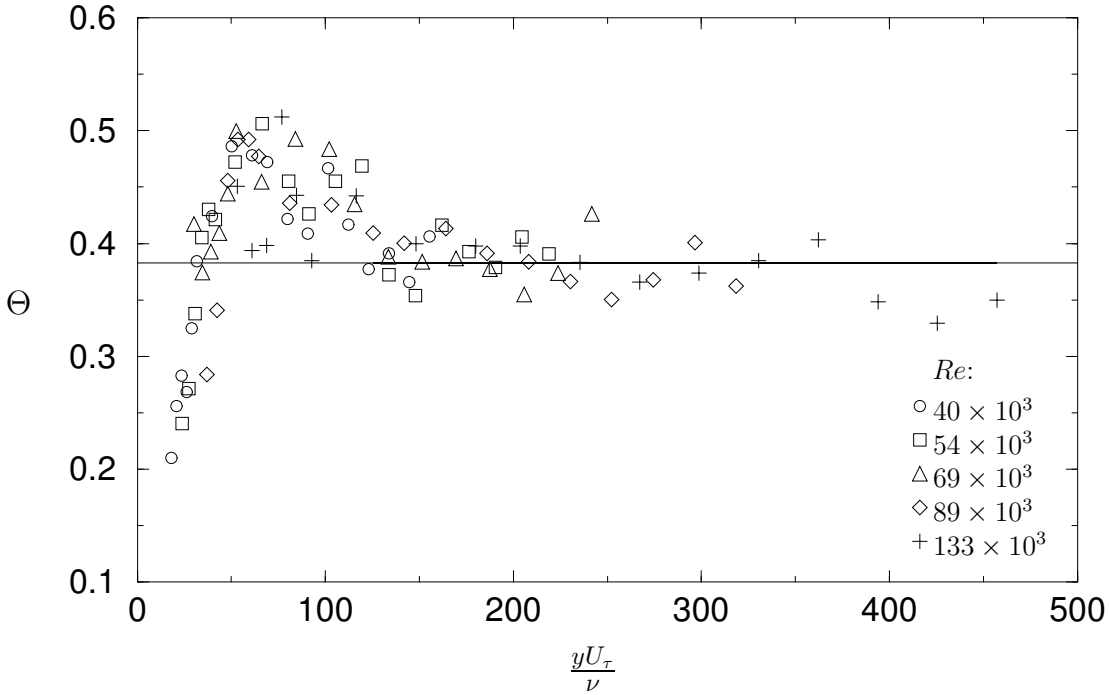

Figure 5.3: Wall-normal distribution of the diagnostic function, Θ, in the inner flow region. The horizontal solid line represents $\Theta = 0.384$.

$$\left(\frac{dU^+}{dy^+}\right)_i = \frac{U^+_{i+1}(\Delta y^+_i)^2 - U^+_{i-1}(\Delta y^+_{i+1})^2 + U^+_i[(\Delta y^+_{i+1})^2 - (\Delta y^+_i)^2]}{\Delta y^+_i \Delta y^+_{i+1}(\Delta y^+_i + \Delta y^+_{i+1})} \tag{5.1}$$

Since y-coordinates are spaced logarithmically, for increased accuracy the algorithm (5.1) was applied to data sets of $(\ln(y^+), U^+)$, which are linearly spaced in $\ln(y^+)$.

Figure 5.3 presents the distribution of Θ for fully corrected pitot tube measured data. Only data in the inner flow region is included in this figure, i.e., $y < 0.15R$ data. It is clear that for $y^+ \gtrsim 120$ a region of constant Θ exists and an average of the data in this region returns the value $\Theta = 0.384$. The reader will recall the almost identical value of $\kappa = 0.386$ found from the least squares error curve fit.

The distribution of the Γ diagnostic function is presented in figure 5.4. Once again, the data displayed was measured with a pitot tube and has the MacMillan and turbulence intensity corrections applied. Note that it is $1/\Gamma$ which is plotted here since $1/\Gamma$ will be seven if the data collapse on to the Blasius $1/7^{th}$ power law† . The distribution appears to have a constant range for $y^+ > 100$, suggesting the power

† The power law with exponent $\beta = 1/7$ can be derived from the Blasius friction factor formula (see Appendix B); hence, this velocity law is referred to as the *Blasius* power law.

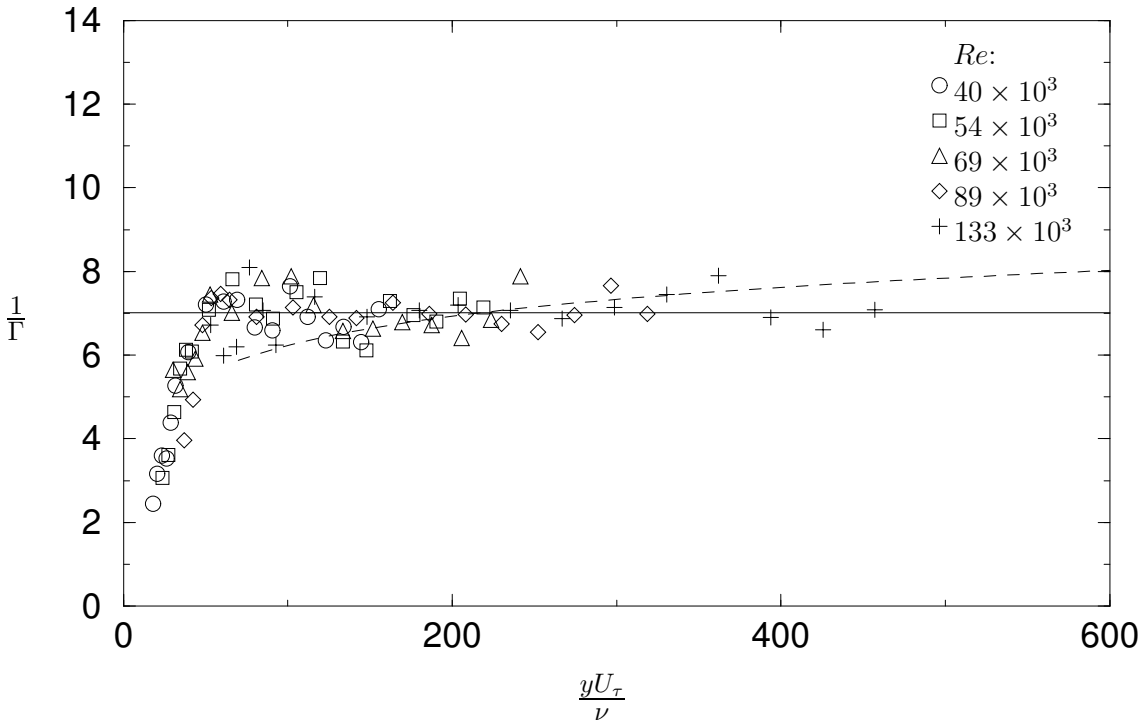

Figure 5.4: Wall-normal distribution of the diagnostic function, Γ, in the inner flow region. The horizontal solid line represents $1/\Gamma = 7.019$. The broken line is the log law with $\kappa = 0.386$, $A = 4.21$.

law scaling is no less appropriate than the log law. Further, the data do not display any notable Reynolds number dependence, although the small Reynolds number range shown may be the reason. Taking an average of the data for $y^+ > 100$ reveals $1/\Gamma = 1/\beta = 7.019 \approx 7$ in accordance with the Blasius profile. Returning to the inner flow scaled velocity profiles, a power law curve fit to all data in the overlap region gives the constants $\alpha = 8.337$ and $1/\beta = 6.926$. This power law is shown plotted over the velocity profiles in figure 5.5. Also plotted in this figure is the power law with constants $\alpha = 8.700$ and $\beta = 1/7.299$, found by Zagarola (1996) to fit the Superpipe data for $50\nu/U_\tau < y < 0.1R$. Figure 5.5 clearly shows Zagarola's power law lies above the pipe flow data of this thesis, even deep into the overlap region.

The applicability of the $1/7^{th}$ power law to the velocity profiles observed here is in apparent contradiction to the recent analyses of Österlund *et al.* (2000b), Hellstedt (2003), Jones *et al.* (2001b) and Zanoun *et al.* (2002). All these references show a clear slope in the Γ function, while Θ remains undeniably constant in the overlap region, thus indicating the log law is the suitable scaling. An explanation for the

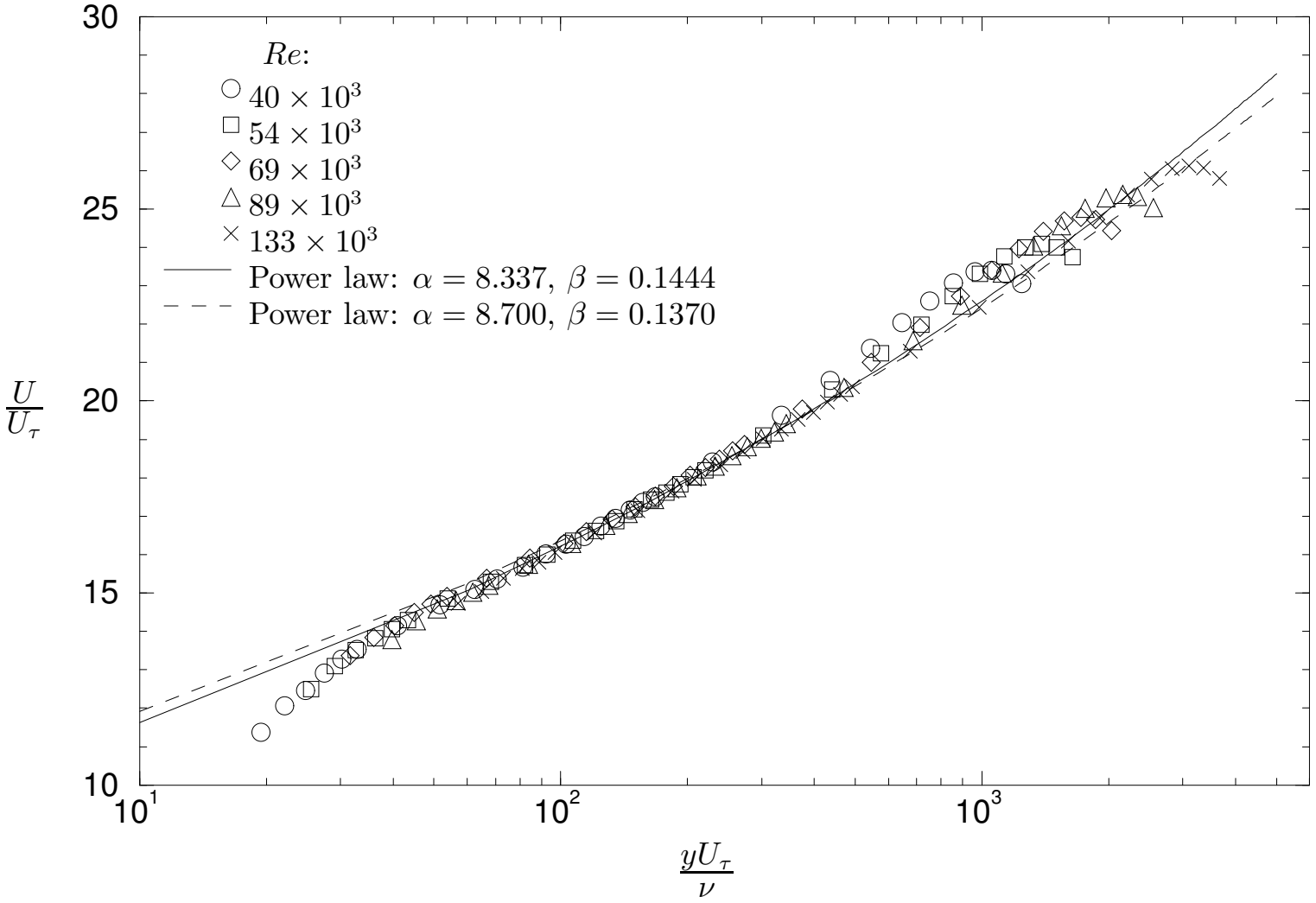

Figure 5.5: Pipe flow: Mean velocity profiles measured with a pitot tube; inner flow scaling applied. Power laws overlaid: —— Fitted to data, ---- Zagarola (1996) fitted to low Re Superpipe data.

invariance of both Γ and Θ is possibly poor spatial resolution; that is, more closely spaced data would allow a more accurate derivative calculation. Noting this possibility, however, a closer look at figure 5.4 could arguably reveal a slight positive slope in $1/\Gamma$ which is further highlighted by the dashed log law ($\kappa = 0.385$, A = 4.23). Moreover, the power law overlaid in figure 5.5 does appear to cross through the data somewhat; the curve does not collapse the data over the entire overlap region as opposed to the excellent collapse of the log law (see figure 5.1).

At this point it is interesting to note that the power law curves upward as the wall is approached. This curvature coincides with the 'kick-up' of the data from the logarithmic law at $y^+ \approx 50$. This 'kick-up' was identified by Jones *et al.* (2001a) as an error in pitot tube measurement (based on comparison with hot-wire data) which is relieved, but not removed, by appropriate corrections to the data. This finding will be confirmed later in this section, however, it is obvious from figure 5.5 that the presence of the 'kick-up' favours the power law curve fit. Furthermore, if the 'kick-up' is indeed amplified by — or even a complete figment of — pitot tube error, then the existence, or at least the true form, of the power law is highly dependent on pitot tube corrections. Thus the issue of corrections becomes evermore significant and further investigation on this topic will be detailed in subsequent paragraphs of this section.

In summary, it does appear that no definite conclusions can be drawn concerning the correct scaling based only on the diagnostic functions calculated from the pipe flow data. Recent publications, the slight slope observed in Γ, invariance of Θ and relatively less impressive collapse of the power law to the data, however, all suggest that there is no significant evidence to discount the classical logarithmic law as the correct scaling for the overlap region of inner flow scaled velocity profiles.

5.1.2 Outer flow scaling

Velocity defect profiles measured with a pitot tube and scaled with outer flow variables are presented in figure 5.6. Both MacMillan and turbulence corrections have been applied to the data. Similar profiles measured with a hot-wire without correc-

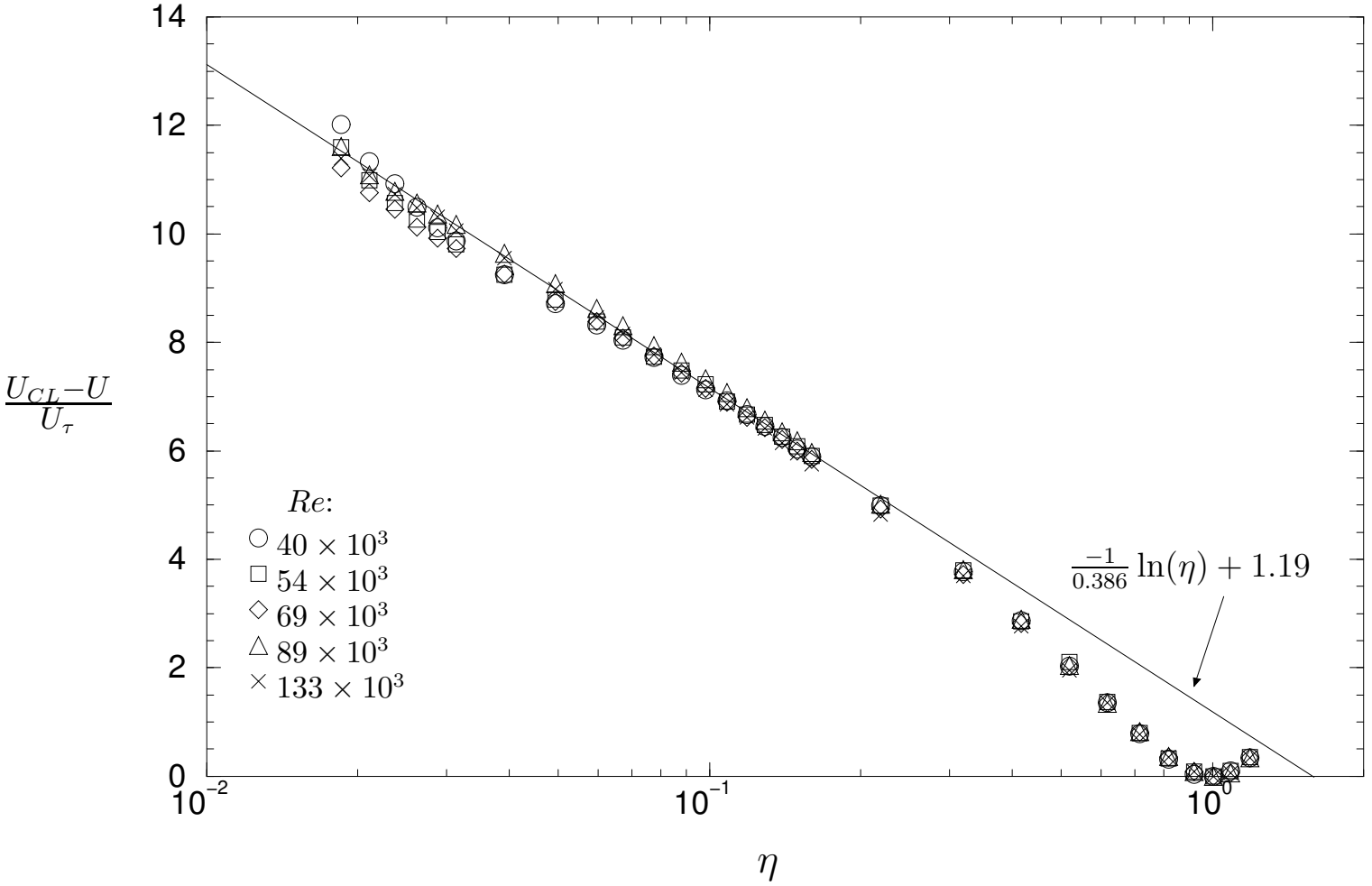

Figure 5.6: Pipe flow: velocity defect profiles measured with a pitot tube; outer flow scaling applied.

tion are presented in figure 5.7. Once again the expected trends are observed; good collapse of the data is evident down to the outer flow region limit of $y \approx 100\nu/U_\tau$. No noticeable Reynolds number dependence of the data in the overlap region is found. Thus the data is in agreement with the Townsend (1956) Reynolds number similarity hypothesis which states that viscosity has no effect on mean relative motions in the outer flow region (except that viscosity may alter the friction velocity, U_τ). Additionally, von Kármán's velocity defect law (2.2) is also supported by the data.

Included in figures 5.6 and 5.7 is the logarithmic velocity defect law (2.5). The constant B was again determined from least squares error curve fits to all data lying in the overlap region. For the pitot tube data, $B = 1.19$ was found to best fit the data, while for the hot-wire data, $B = 1.27$. As with the mean velocity profiles presented in the previous section, differences in logarithmic law constants fitted to hot-wire and pitot tube data are small. Due to the non-universality of the constant B, there is much less reliable data available to compare values of B with than there is for the inner flow scaled logarithmic law. An example is $B = 1.51$ for the Superpipe data of Zagarola (1996). It should be noted that applying the MacMillan shear correction and turbulence correction to the profiles of Zagarola (1996) would reduce this value.

5.1.3 Comparison with Henbest (1983)

Since the pitot tube measurements of the current study had been previously acquired by Henbest (1983), comparison of the two studies should reveal only minor discrepancies. Figure 5.8a presents the velocity profiles for all Reynolds numbers plotted with those of Henbest (1983) over a similar Re range. The differences between the data sets are far from minor and are disturbingly consistent. It is clear that the wake components of the Henbest velocity profiles are much weaker than the author's. Reasons for this anomaly are unclear, although the author is confident that the data of the current study are accurate. This is because, apart from the careful techniques employed and repeated measurement of all profiles, the wake components of the author's data agree very well with the Superpipe data as shown

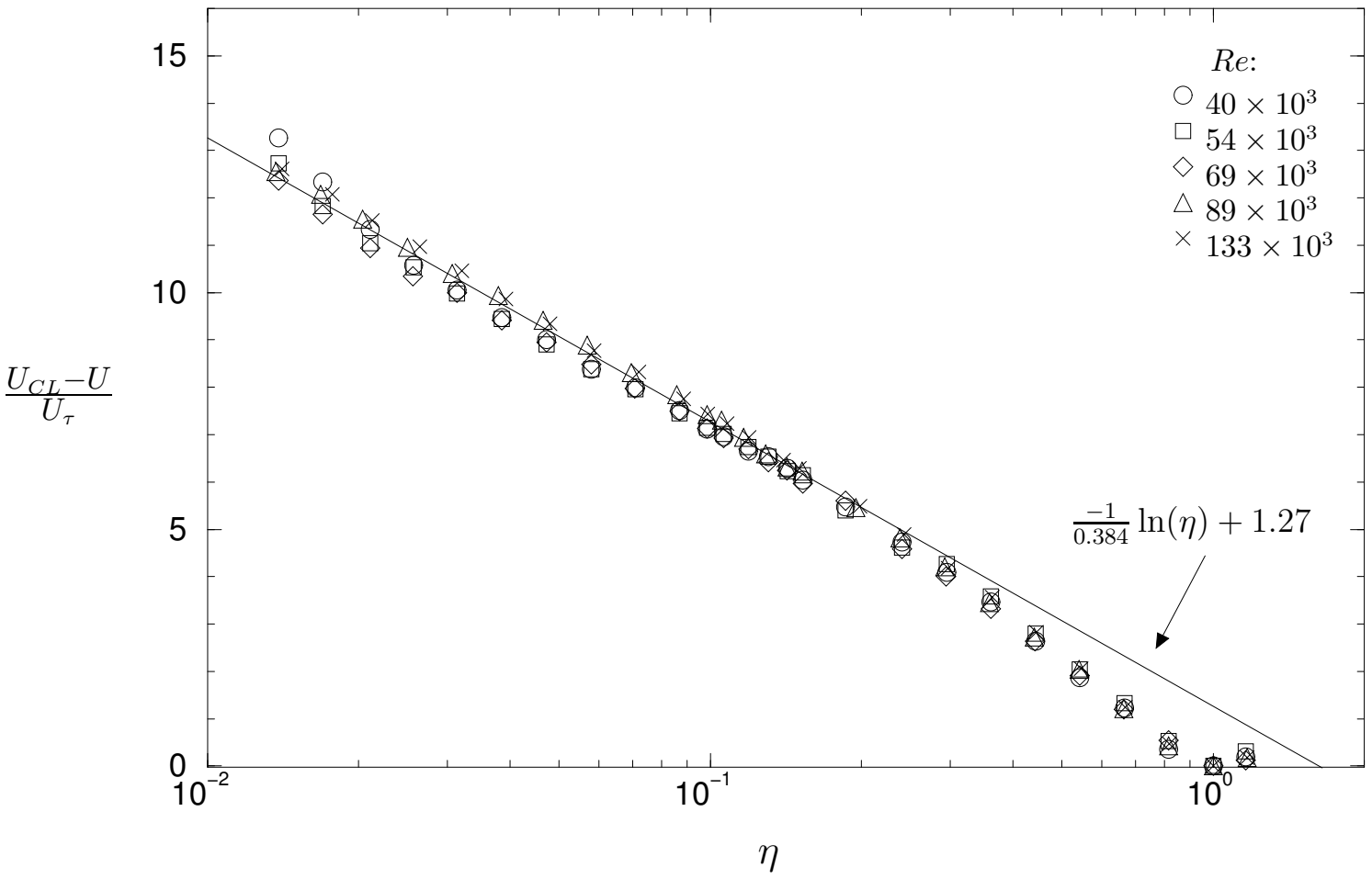

Figure 5.7: Pipe flow: velocity defect profiles measured with a hot-wire; outer flow scaling applied.

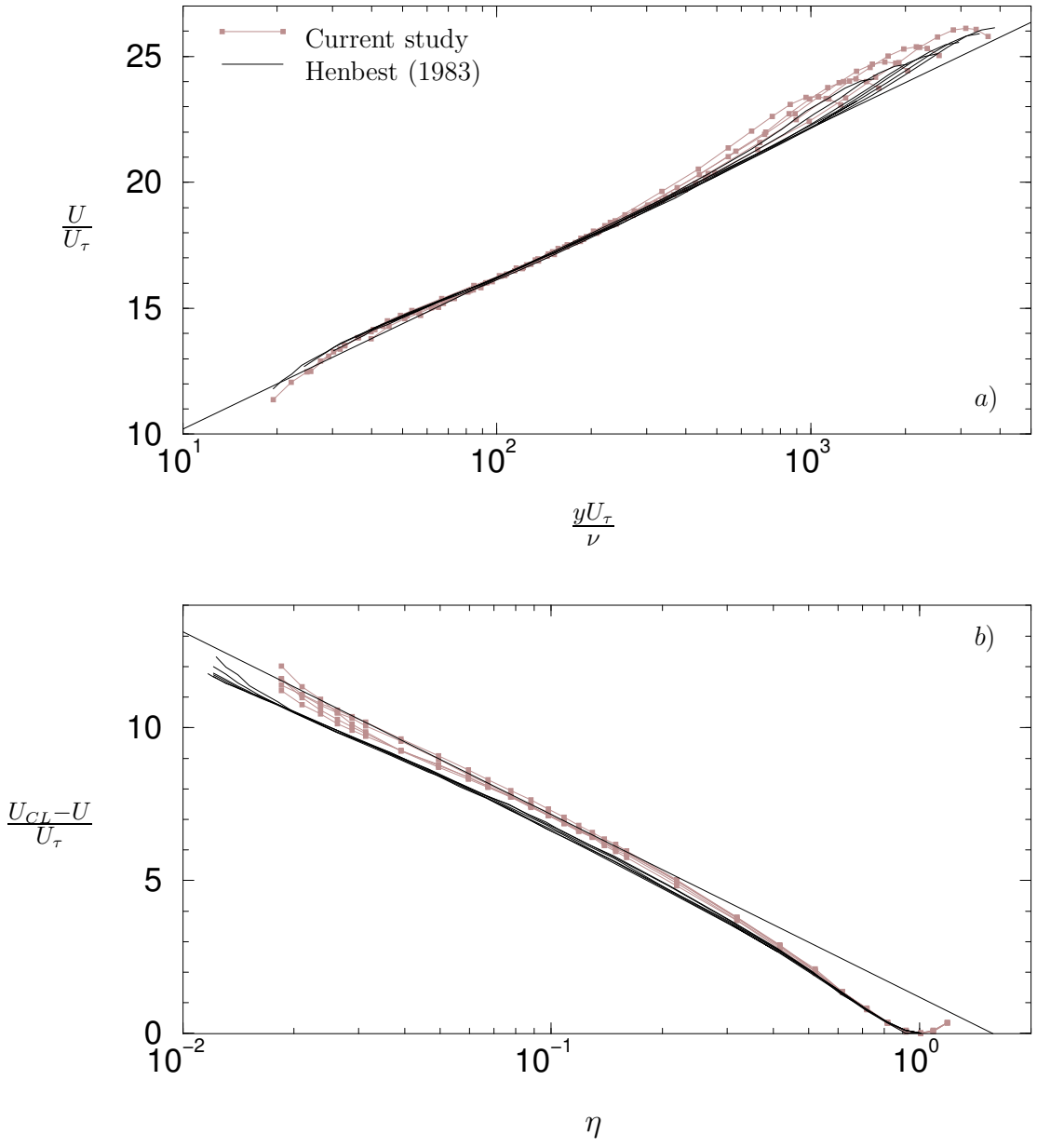

Figure 5.8: Comparison of the author's pipe flow mean velocity data with that of Henbest (1983).

in figure 5.9. Although the outer flow regions are in disagreement, figure 5.8a shows that the two data sets compare favourably in the inner flow region. This suggests that a velocity defect plot may be useful. Defect plots are shown in figure 5.8b which clearly illustrates the large differences between the results. A rough estimate of the log law constant, B, gives $B = 0.825$ for the Henbest data — over 30% lower than that of the author's data.

The evidence presented here leaves no option but to conclude that the mean flow data of Henbest (1983) are erroneous in the outer flow region. Since the pipe flow facility used in this project was virtually unchanged from that used by Henbest (1983), flow quality issues are unlikely to be responsible for the discrepancies revealed. Thus it is most likely that pitot tube measurement error has occurred, the source of which will remain a mystery.

5.1.4 A comparison of pitot tube with hot-wire mean flow data

All pitot tube data presented above has been corrected for shear and turbulence effects. While the correction for shear is commonly employed and validated by recent experimental data (see McKeon *et. al.*, 2003), the turbulence correction does not enjoy such popularity. As discussed in §2.7.2, however, a turbulence correction must be applied. In this section the applicability of the chosen corrections will be judged based on a comparison with hot-wire data. This does not suggest that hot-wire data is free from error or that it is a true reference. In the absence of more accurate reference data, however, hot-wire data is used here.

Before comparison of pitot tube with hot-wire measured velocity profiles, an illustration of the importance of corrections may be useful. Presented in figure 5.9a are two pairs of pitot tube measured velocity profiles without correction and with inner flow scaling. Each pair consists of a pipe flow profile from this thesis and a profile from the Princeton University Superpipe (obtained from the thesis of Zagarola, 1996). The similarities are obvious, however the reader should note that the pitot tube diameters of the two studies are quite different. The data in this thesis was

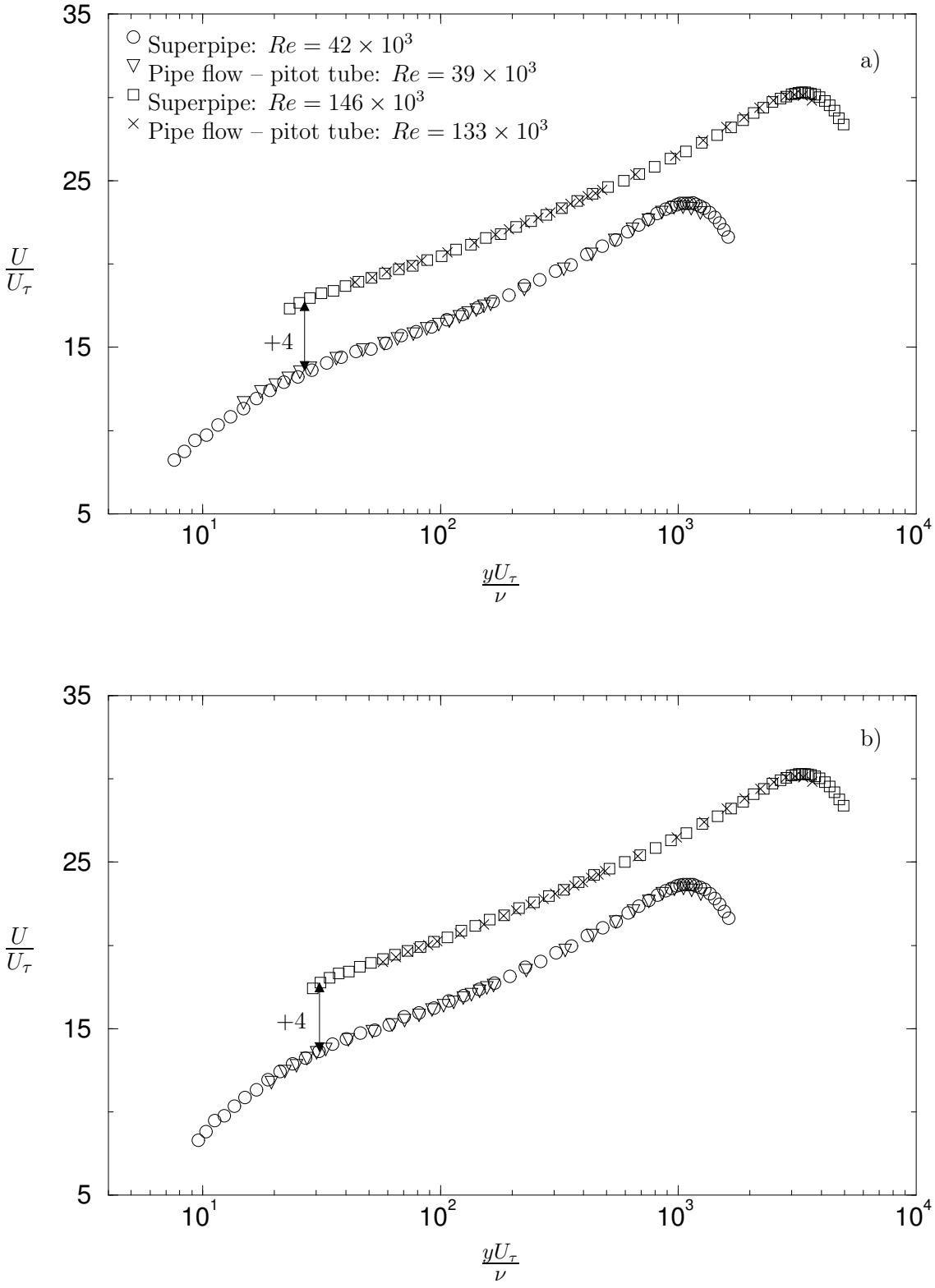

Figure 5.9: Comparison of selected Superpipe data with the author's pipe flow data: a) Uncorrected pitot data; b) MacMillan shear and wall proximity corrections applied to all data. Note that profiles pairs have been manually spaced by 4 ordinate units for clarity.

taken with a $d_p = 1.44mm$ tube, while a $d_p = 0.9mm$ tube was employed for the Superpipe data. For this reason, figure 5.9b is given, which has the MacMillan shear and wall proximity corrections applied to each data set. The resultant profiles are virtually indistinguishable. The analysis of the Superpipe data by Zagarola & Smits (1998) using the Chue (1975) shear correction, however, gives significantly different results to those found from the current pipe flow study (see table 5.1). This clearly implies that the issue of pitot tube corrections is of utmost importance, especially in the recent mean flow scaling debates appearing in the literature.

As previously stated, all pitot tube data presented in §5.1.1 has MacMillan's shear and wall proximity correction applied, combined with a turbulence correction based on hot-wire measured turbulence intensity profiles (these profiles are presented in Chapter 6). To clearly understand the effect of these corrections and observe the agreement with hot-wire measurements, figure 5.10 is provided. This figure includes uncorrected pitot tube, fully corrected pitot tube and hot-wire measured velocity profiles with inner flow scaling applied. Note that only the $Re = 40 \times 10^3$ profiles are vertically unchanged; each of the remaining Reynolds number profiles have been manually spaced by two ordinate units. The first impressions of figure 5.10 are that the corrected data are very close to the hot-wire data, certainly relative to the original, erroneous data. The effects of the corrections clearly extend into the overlap region of the profile which again highlights the importance of corrections to scaling law conclusions. Further analysis of the data shows that only the highest Reynolds number corrected pitot profile seems significantly deviant from the hot-wire data. This inconsistency may be explained by a small error in either U_τ or calibration for the hot-wire measured profile since the data appear to be shifted over the entire y^+ range, not simply in the corrected region. Observing the entire range of profile sets should, however, convince the reader that the corrections applied significantly improve the pitot tube measurements relative to hot-wire measured profiles.

Due to the small observable differences between profiles, figure 5.10 is only truly useful for superficial judgement of the corrections. In order to fully understand and appreciate the effect of the pitot tube corrections, the deviation from the log law (2.4) is calculated, amplifying the trends in the data. The deviation function is

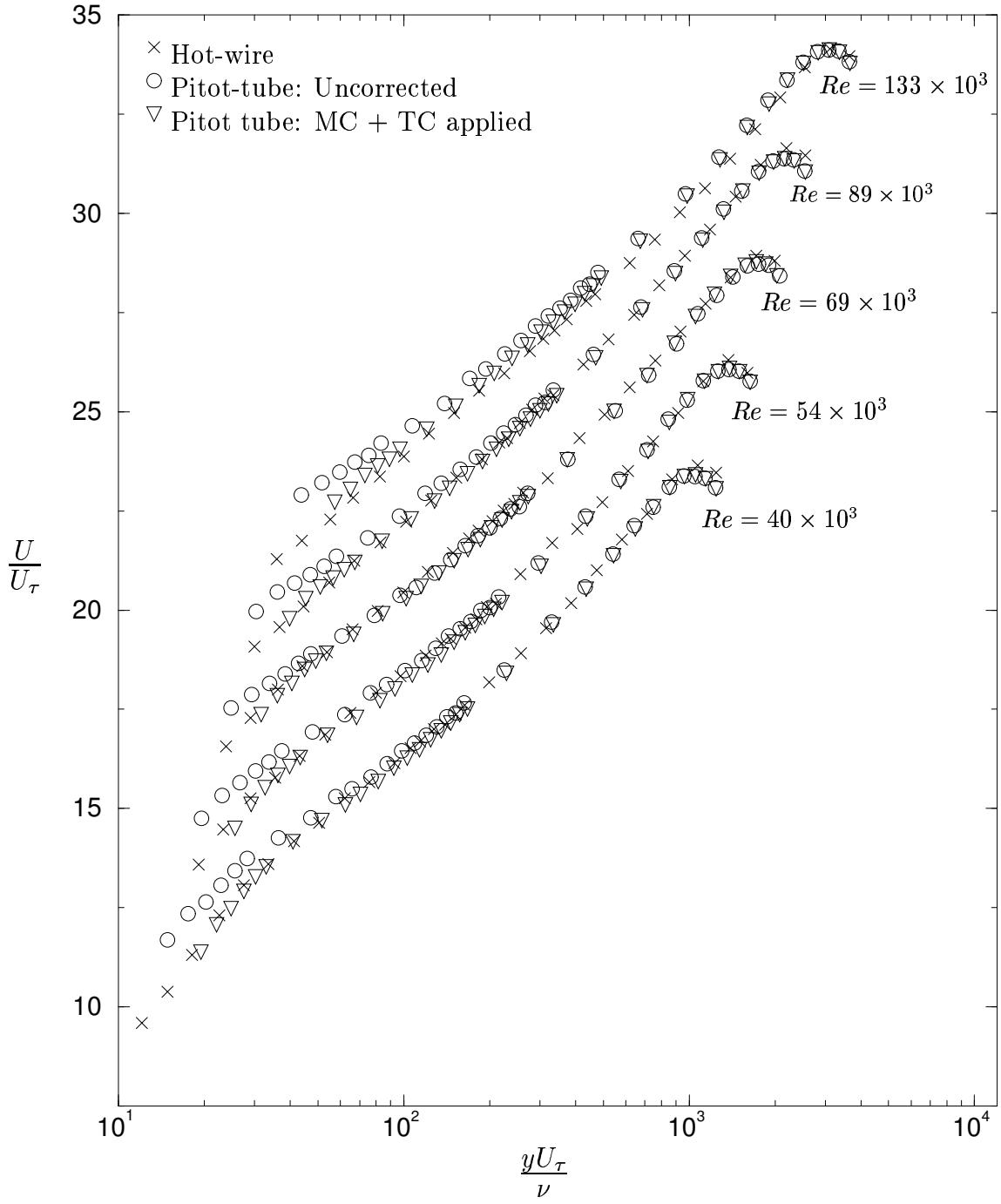

Figure 5.10: The effect of pitot tube corrections and comparison with hot-wire data. Velocity profiles are scaled with near wall variables and manually spaced by 2 ordinate units.

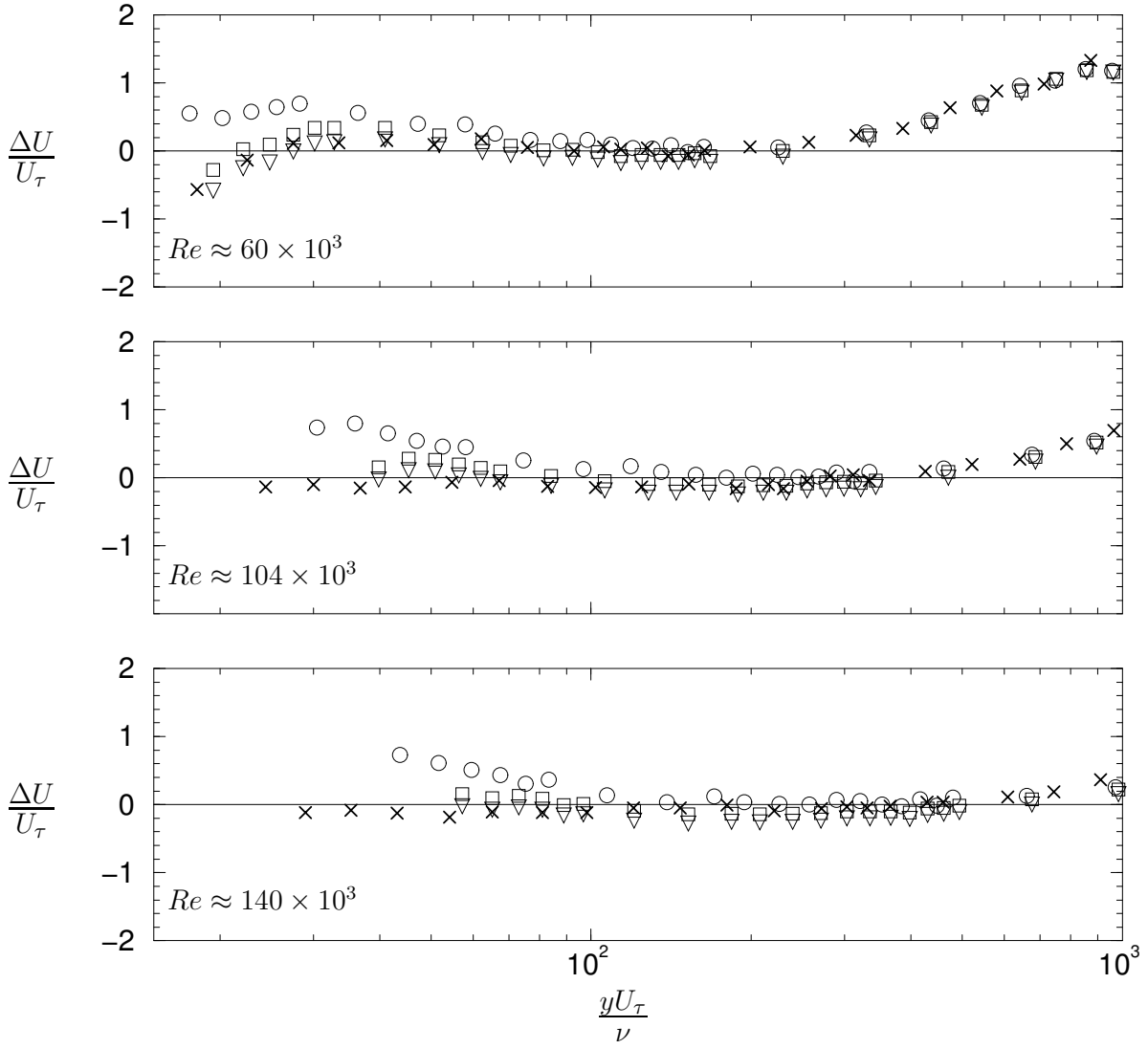

Figure 5.11: The deviation of velocity profiles from the log law. Four data sets are presented in each subplot: ∘ , uncorrected pitot tube, ▫ MacMillan corrected pitot tube, ▽, fully corrected pitot tube and × hot-wire measurements.

defined as:

$$\frac{\Delta U}{U_\tau} = \frac{U}{U_\tau} - \frac{1}{\kappa} \ln\left(\frac{yU_\tau}{\nu}\right) - A, \tag{5.2}$$

where constants employed in this analysis are $\kappa = 0.384$ and $A = 4.33$ (as determined from hot-wire velocity profiles). The deviation function is plotted in figure 5.11 for the $Re = 60, 104, 140 \times 10^3$ cases. Each subplot in the figure includes four data sets: data with no corrections, data with the MacMillan shear and wall proximity corrections applied, fully corrected data and hot-wire measurements. Thus, the effect of each correction is more clearly observed, with the final result lying satisfactorily close to the hot-wire measurement in all cases. In fact, for the two lower

Reynolds number subplots, the corrected pitot data is in almost complete agreement with hot-wire measurements, with only minimal over-correction in the overlap region (less than 0.6% of the scaled mean velocity). For the highest Reynolds number deviation data, the over-correction in the overlap region appears much larger (approximately 1.0% of the mean) which may be explained by a combination of error in U_τ ($\pm 0.5\%$ at most) and other minor experimental errors. This seems plausible as the pitot data lies a small, though consistent, amount lower than the hot-wire data across the entire range of y^+.

Another interesting aspect of the inset of figure 5.11 is the 'kick-up' or deviation from the log law for $30 \lesssim y^+ \lesssim 100$. It is clear that the 'kick-up' is significantly reduced by corrections to the data and that the hot-wire data exhibits only a small kick-up from the log law. Now, if the overlap region is assumed to extend down to $y^+ = 50$ and described by a power law (Zagarola & Smits, 1998), then constants determined from a curve fit to the data will depend heavily on the pitot tube corrections applied. More importantly, the power law curve fit shown in figure 5.5 will provide a better fit to the data if that data is under-corrected; that is, if the kick-up is not reduced appropriately. This point is perhaps best illustrated in figure 5.12 where the log law with MacMillan shear correction *subtracted* is plotted against the power law. Note that the constants in both the power and log laws are those fitted to the corrected pitot tube data and the MacMillan correction is determined using $d_p = 1.44mm$ and flow properties from the $Re = 69 \times 10^3$ case. This graph indicates that without the dominant correction (shear correction), the log law is shifted into agreement with the power law for low y^+. Thus one must remain sceptical of a claimed power law fit to any pitot tube data until serious consideration is given to the corrections applied.

In summary, the MacMillan (1956) corrections and additional turbulence correction applied to the pipe flow pitot tube measurements presented here, produce results in excellent agreement with hot-wire measured data. It is acknowledged that the MacMillan shear correction is strictly incorrect close to the centreline where there is very low shear, although this error is deemed negligible (less than 0.4% in y^+ at the centreline). Moreover, in the region of most interest, the overlap region, the corrections perform satisfactorily.

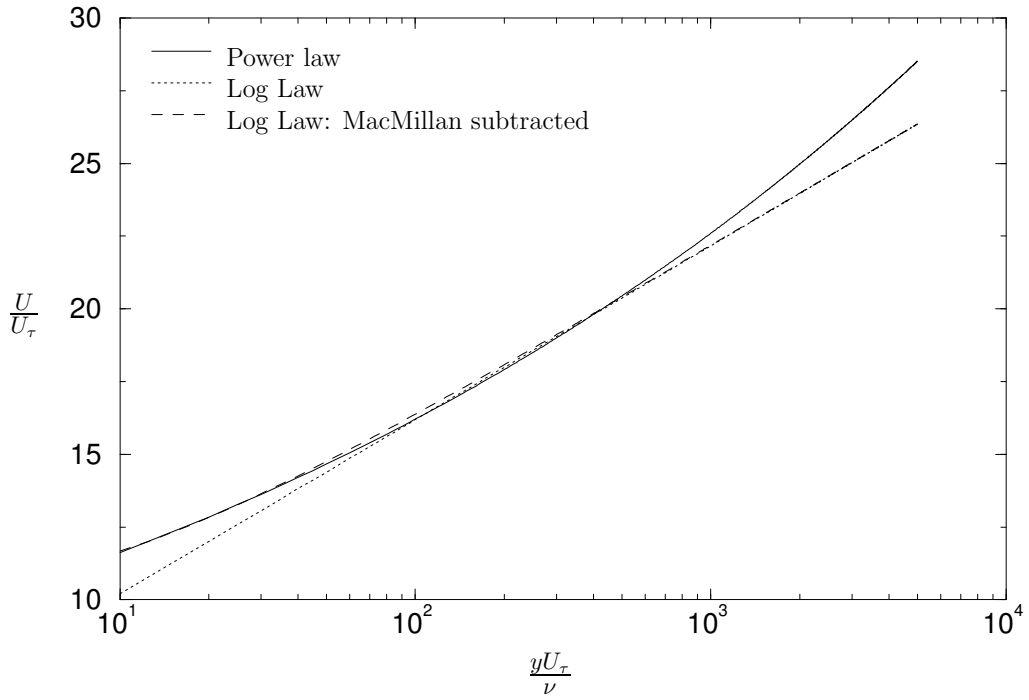

Figure 5.12: Comparison of the log law, power law and log law with MacMillan's correction for shear subtracted. Constants in the log and power laws were determined from corrected pitot tube profiles. Note the similarity of the laws in the overlap region.

5.2 Channel flow

Channel flow velocity profiles measured with both pitot tubes and hot-wires are presented in this section. Similar analyses to those of the pipe flow data will be repeated here. Since much more data was recorded in the channel facility, however, the mean flow analysis presented will be limited to allow deeper analysis of other flow quantities in subsequent chapters.

5.2.1 Inner flow scaling

Mean velocity profiles scaled with inner flow variables and measured with pitot tubes are shown in figure 5.13; hot-wire measurements are given in figure 5.14. The pitot tube data has the MacMillan and turbulence intensity corrections applied. As with the pipe flow results, excellent collapse in the inner flow region is evident for all Reynolds numbers, regardless of measurement technique.

Both figures 5.13 & 5.14 have log laws overlaid with constants determined from a

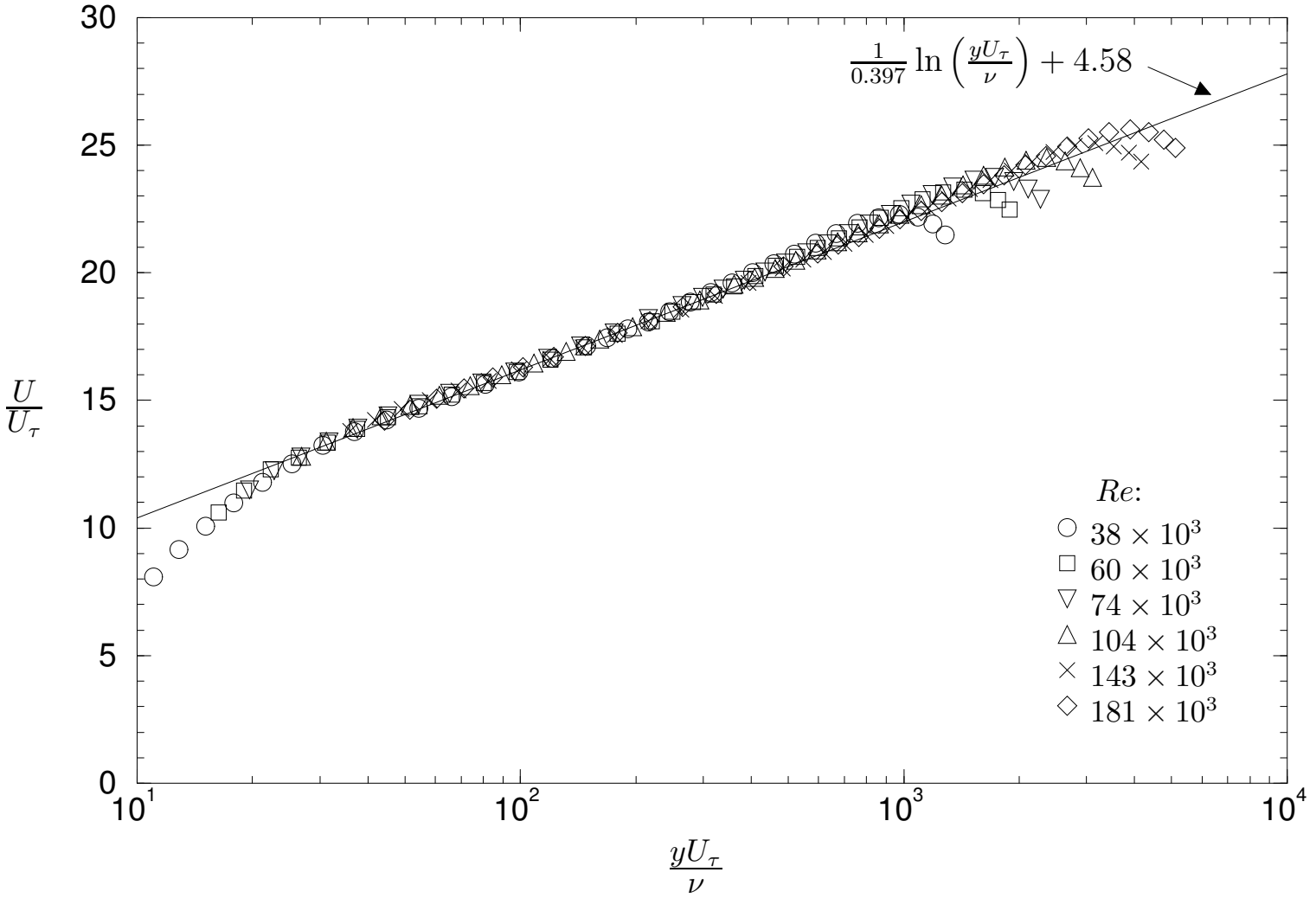

Figure 5.13: Channel flow: mean velocity profiles measured with a pitot tube; inner flow scaling applied.

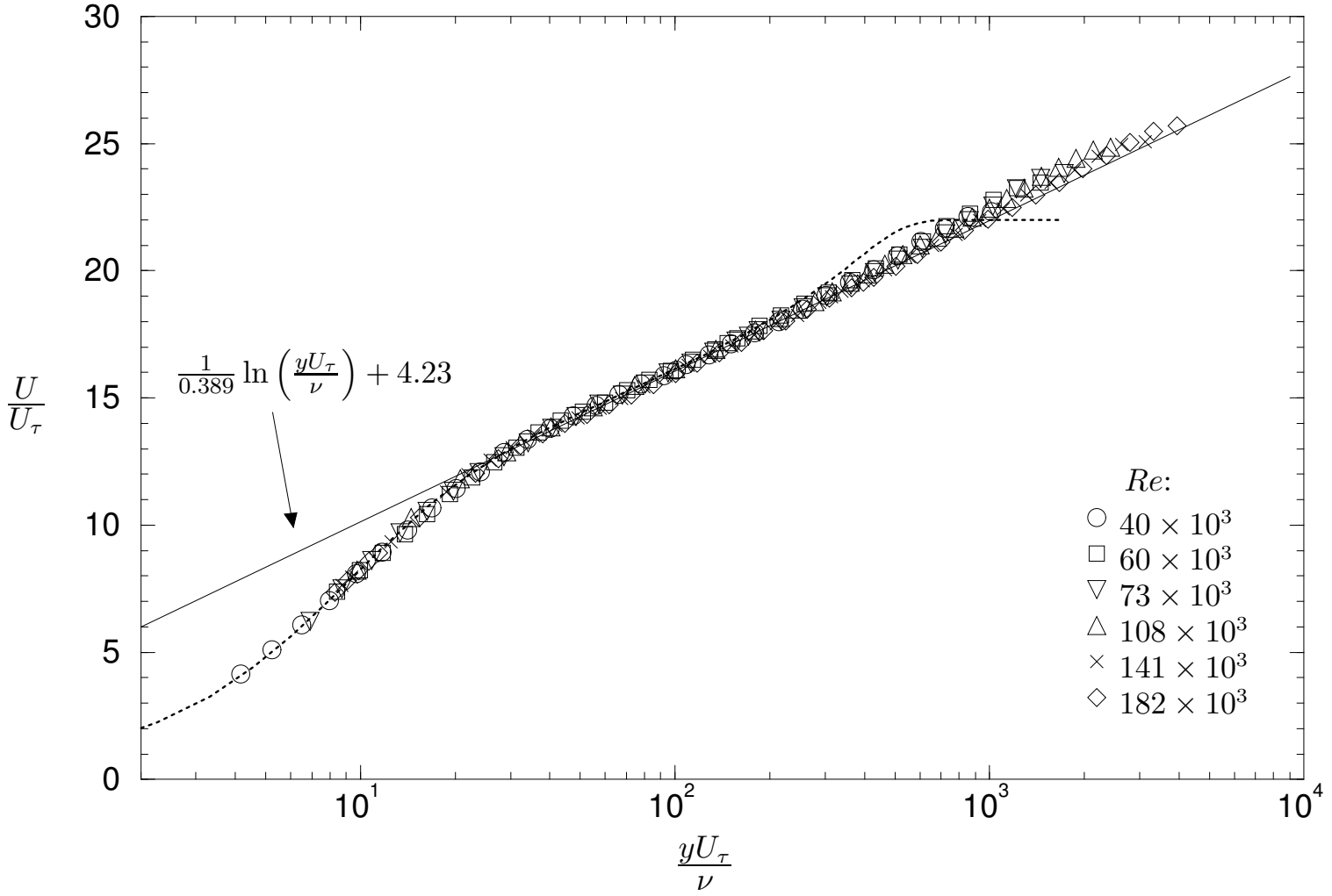

Figure 5.14: Channel flow: mean velocity profiles measured with a hot-wire; inner flow scaling applied. Note the excellent agreement with the DNS boundary layer data of Spalart (1990), ····· , in the inner flow region.

least squares error fit to all data in the overlap region. For the pitot tube data, $\kappa = 0.397$ and $A = 4.58$ were found and for the hot-wire measurements, $\kappa = 0.389$ and $A = 4.23$. These values are in excellent agreement with the pipe flow results as well as those of various other studies listed in table 5.2. The most interesting characteristic of the channel flow profiles is the weak deviation from the log law in the outer flow region. The weakness of the channel flow wake will be further discussed later in this section and in §5.5; the observation is first highlighted here since it is most obvious in the inner flow scaled velocity profiles.

5.2.2 Outer flow scaling

Figure 5.15 displays velocity defect data measured with a pitot tube, scaled with outer flow variables and fully corrected for shear, wall proximity and turbulence effects. Figure 5.16 also presents velocity defect data, in this case measured using hot-wire anemometry. Again there is excellent collapse observed in the outer region with no significant Reynolds number dependence of the data in the overlap region. In fact, the data show even less scatter in the overlap region than the pipe flow data (figures 5.6 & 5.7).

The applicable logarithmic laws are overlaid on the data in both figures 5.15 & 5.16. The constants found from least squares error fits to all data in the overlap region are: $B = 0.238$ for pitot tube measurements and $B = 0.327$ for hot-wire measurements. As stated previously, the deviation from the log law is much weaker than for pipe flow. This is reiterated in figure 5.16 and is the reason for the low value of B found (relative to the pipe flow value, $B \approx 1.2$). This weak deviation gives the appearance of an extended overlap region beyond $y = 0.15h$, perhaps up to $y \approx 0.25h$. In their rectangular duct flow facility, Zanoun *et al.* (2003) cite a similar significant extension of the overlap region; up to $0.75h$ at the highest Reynolds number studied ($K_\tau \approx 5000$). This finding is not consistent with the data presented in figure 5.16 where the first sign of deviation from the log law is clearly apparent around $y^+ = 0.25h$.

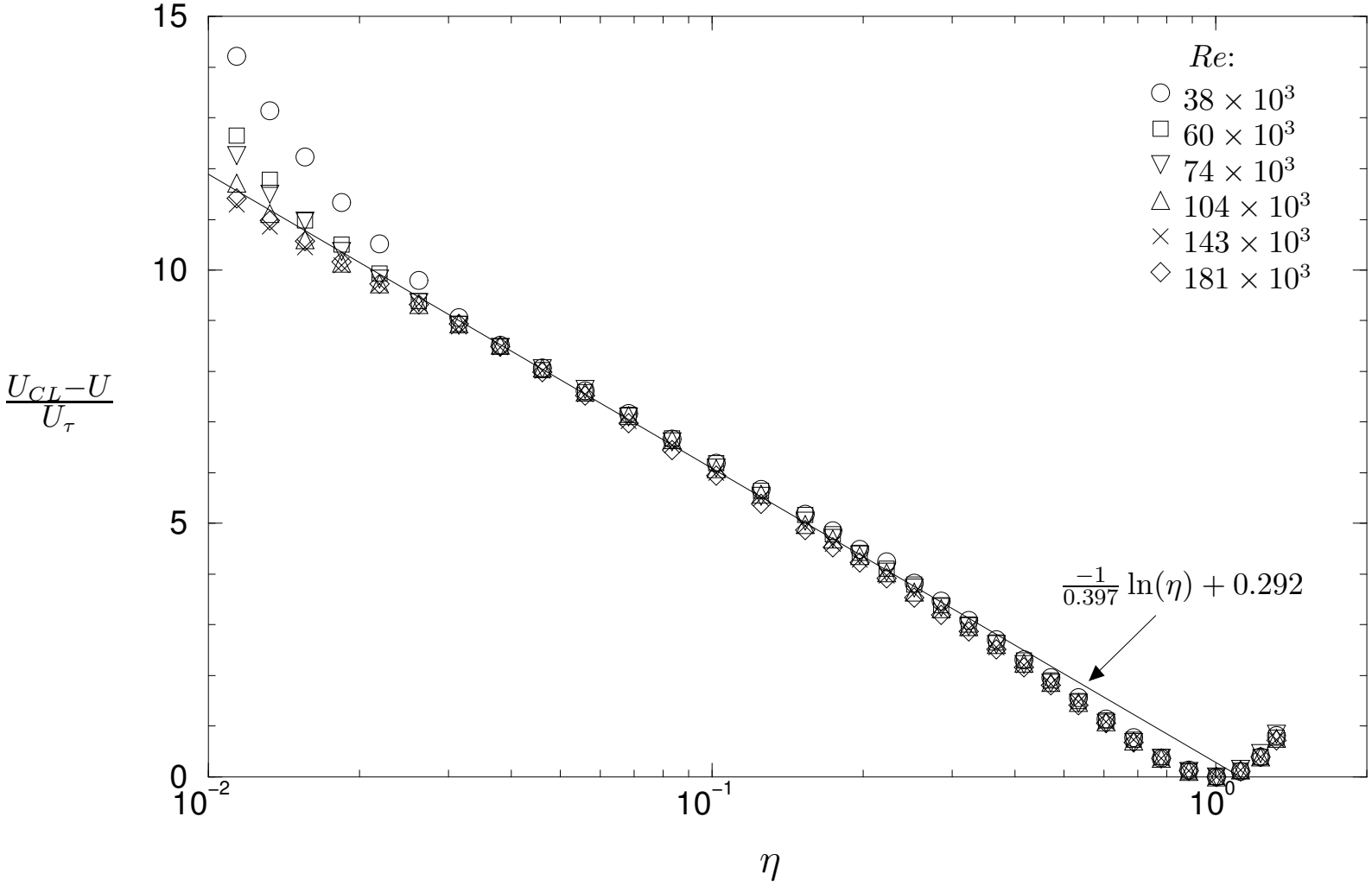

Figure 5.15: Channel flow: mean velocity profiles measured with a pitot tube; outer flow scaling applied.

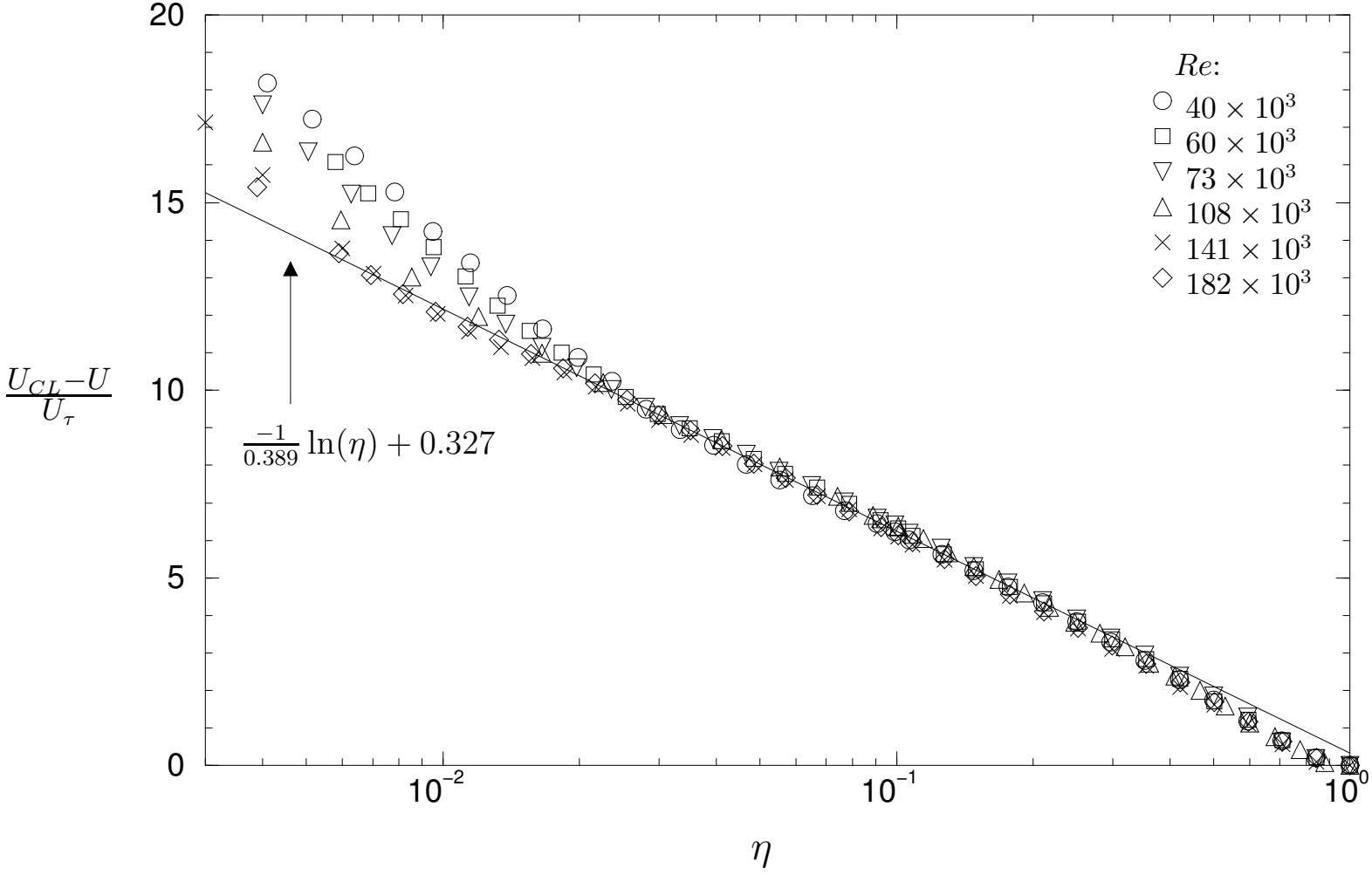

Figure 5.16: Channel flow: mean velocity profiles measured with a hot-wire; inner flow scaling applied.

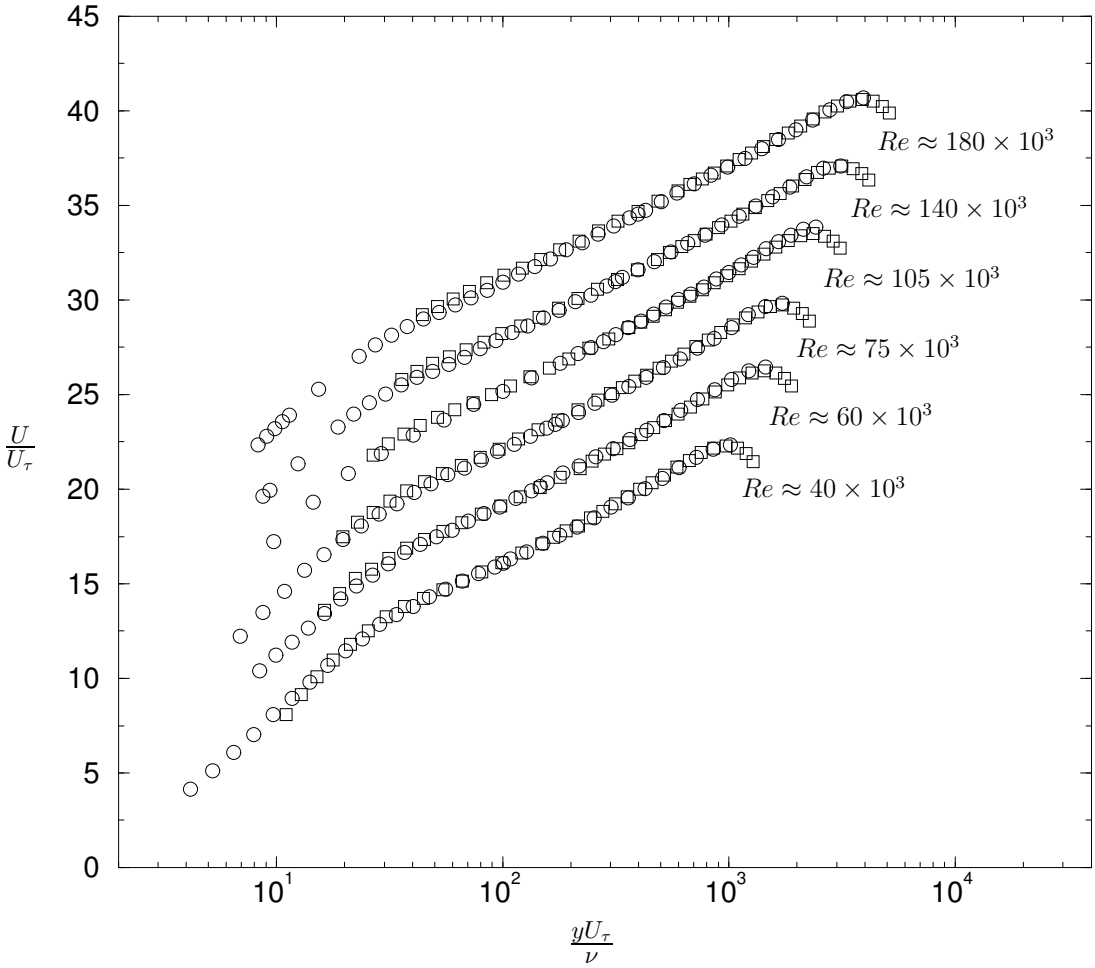

Figure 5.17: Comparison of fully corrected pitot tube, ▫, with hot-wire data, ○, measured in the channel. Inner flow scaling has been applied and profiles are manually spaced by 3 ordinate units.

5.2.3 Comparisons of pitot tube with hot-wire measurements

A brief comparison of pitot tube and hot-wire measured velocity profiles is presented here. Figure 5.17 displays both fully corrected pitot tube data and hot-wire measured profiles with inner flow scaling across the Reynolds number range. Note that the profiles have been manually spaced by 3 ordinate units for clarity, with only the $Re \approx 40 \times 10^3$ profile unchanged.

The agreement in the overlap region between the two measurement techniques is excellent with the slight exception of the highest Reynolds number profile. Since the turbulence correction is determined from hot-wire measured turbulence inten-

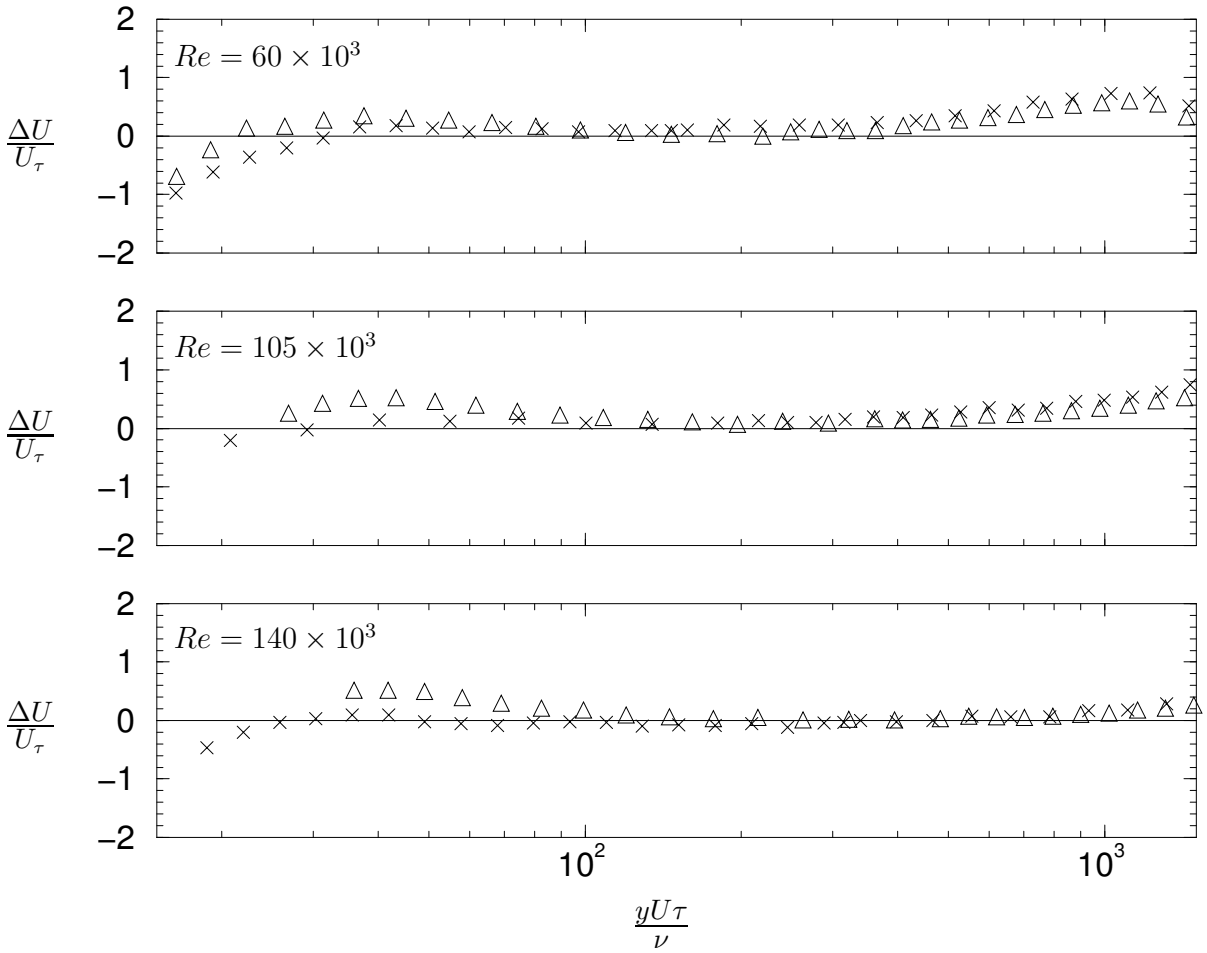

Figure 5.18: Deviation of channel flow velocity profiles from the log law for selected Reynolds numbers. Hot-wire, ×; pitot tube, △ .

sity which is known to be attenuated at high Reynolds numbers, it is possible that excessive attenuation of $\overline{u'^2}$ is the reason. Closer to the wall there appears to be a larger 'kick-up' from the log law in the pitot tube data. This is consistent with the findings of Jones *et al.* (2001a), while inconsistent with the pipe flow results reviewed earlier. To further analyse this effect, the deviation from the log law is plotted for three Reynolds numbers across the range in figure 5.18. The deviation was defined previously by equation (5.2). For the lowest Reynolds number, there appears to be little difference in the profiles, while the kick-up is clear for the higher Reynolds numbers. A plausible explanation may be that the MacMillan or turbulence correction is insufficient, particularly as Reynolds number increases, although this would be inconsistent with both the pipe flow results and the results of McKeon *et al.* (2003a) who studied a large Re range. Unfortunately, no other propositions for the cause of the kick-up present themselves at this stage (this was acknowledged

also by Jones *et al.*, 2001a) and further investigation may be justified. It is clear, however, that the kick-up will not significantly affect conclusions drawn in this thesis since data in the overlap region remains uncontaminated. This point is perhaps best illustrated by the similarities in log law constants found for hot-wire and pitot tube profiles.

5.3 Analytical forms of the mean velocity profile

A variety of analytical formulations postulated to describe the mean velocity profile in part or as a whole were introduced in §2.3. Firstly, three formulations of the sublayer and overlap region profile were given by Reichardt (1951), Spalding (1961) and Nickels (2001). In figure 5.19 these formulations are compared with hot-wire measured velocity profiles in the channel. The first two sub-plots of this figure indicate that the Reichardt and Nickels curves provide a very good description of the sublayer. For the Nickels formulation the value of $a_0 = 0.0857$ was used (as suggested by Nickels, 2001, based on zero pressure gradient boundary layer data only) which appears to give a slightly better fit between y^+ of 10 to 20 compared with Reichardt. The third sub-plot of figure 5.19 indicates that Spalding's curve (2.20) does not provide such a close fit to the data. Neither in the overlap region (when $\kappa = 0.389$ and $A = 4.23$ are used in equation 2.20) or the sublayer region does the data follow the curve. If one compares the log law with Spalding's formula (see figure 5.20), it is observed that the formula overshoots the log law and then asymptotes back to it; not until $y^+ \approx 10^3$ are the two curves effectively colinear. Based on the plots shown in figure 5.19, the Nickels (2001) formulation gives the best fit to the measurements near to the wall.

For the outer flow, the formulation of Jones *et al.* (2001a), given by (2.17):

$$U^+ = \frac{1}{\kappa}\ln(y^+) + A - \frac{1}{3\kappa}\eta^3 + \frac{2\Pi}{\kappa}\eta^2(3-2\eta),$$

was introduced in §2.3. By evaluating (2.17) at the duct centreline and subtracting (2.17) from the result, the velocity defect form is found:

$$U_{CL} - U^+ = -\frac{1}{\kappa}\ln(\eta) + \frac{1}{3\kappa}(\eta^3 - 1) + \frac{2\Pi}{\kappa} - \frac{2\Pi}{\kappa}\eta^2(3-2\eta). \qquad (5.3)$$

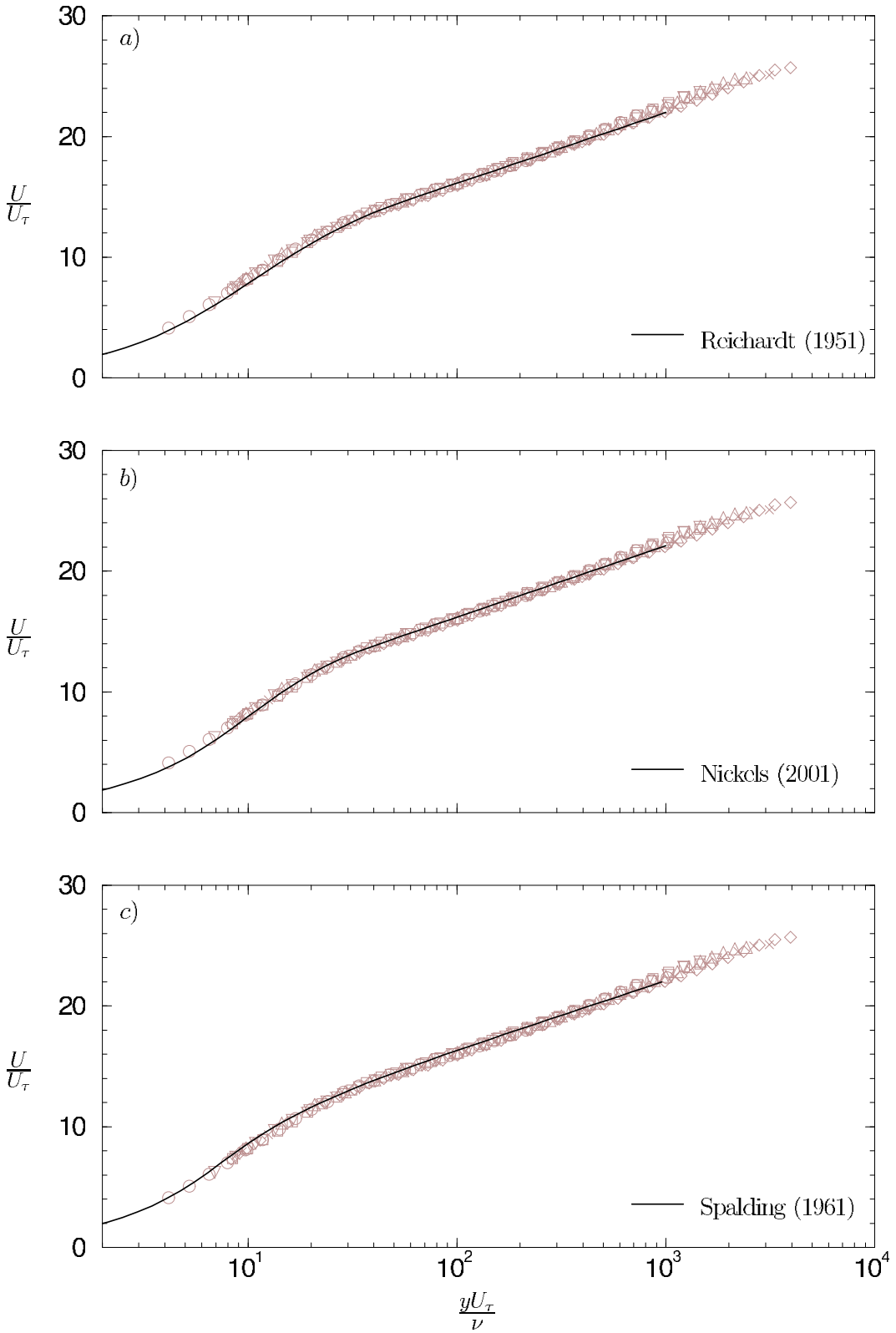

Figure 5.19: Comparisons between channel flow measurements and the formulations of Reichardt (1951), Nickels (2001) and Spalding (1961). Symbols of the measured data are the same as those in figure 5.14. Where appropriate, $\kappa = 0.389$ and $A = 4.23$.

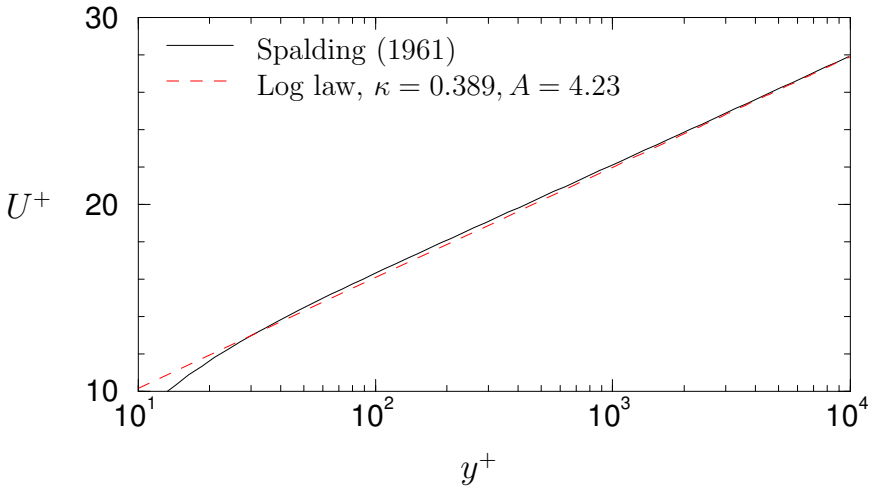

Figure 5.20: The Spalding (1961) inner flow velocity profile formula compared to the log law (2.4).

In figure 5.21 equation (5.3) is compared with channel and pipe flow velocity defect data. A least squares error fit to the data gave $\Pi = 0.250$ for channel flow and $\Pi = 0.454$ for pipe flow. For both cases the data collapse extremely well on to (5.3) indicating that Jones' law of the wall, law of the wake formulation gives an excellent description of the outer flow region.

Nickels (2001) also proposes an outer flow function which strictly applies only to boundary layer flows:

$$U^+ = \frac{1}{6\kappa} \ln \left(\frac{1 + (0.66 a_0 y^+)^6}{1 + \eta^6} \right) + a_2 (1 - e^{-2(\eta^2 + \eta^6)}). \tag{5.4}$$

The first term in the above equation is essentially the log law with a 'built-in' corner function so that the term asymptotes to a constant at the edge of the layer. For large y^+ and small η the first term is identical to the log law (2.4). The second term is the wake component which Nickels (2001) concedes may not provide much improvement on Jones' law of the wake (2.16). a_2 is a wake strength parameter similar to Coles' wake factor, Π_c. Out of interest the above formulation was also compared to the channel flow data. As explained above for the Jones' formulation, a velocity defect expression can be found from (5.4):

$$U_{CL} - U^+ = \frac{1}{6\kappa} \ln \left(\frac{1 + \eta^6}{2\eta^6} \right) + a_2 (e^{-2(\eta^2 + \eta^6)} - e^{-4}). \tag{5.5}$$

This equation also has a free parameter, a_2, which was found to be $a_2 = 0.604$ for the channel flow data. Figure 5.22 displays the channel flow velocity defect with

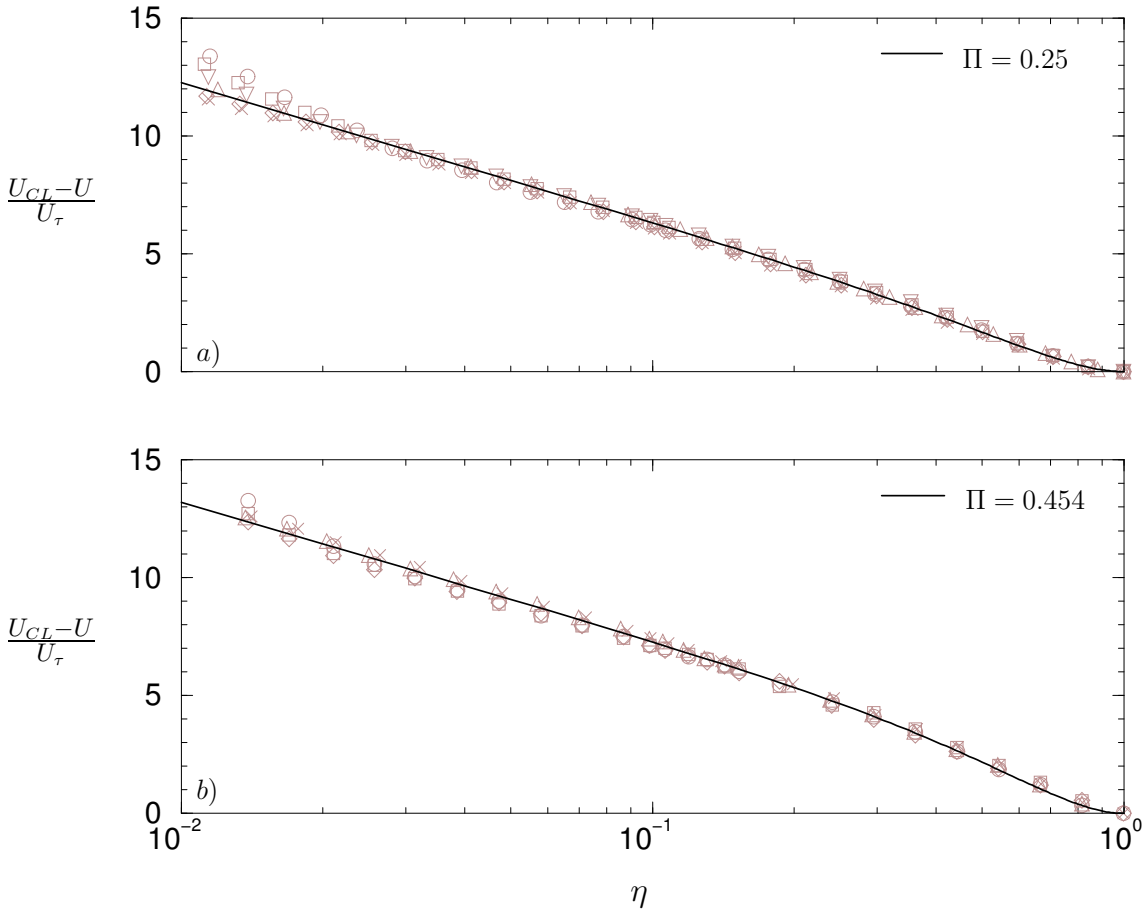

Figure 5.21: Velocity defect plots from the channel (a) and pipe flow (b) facilities with the Jones *et al.* (2001a) velocity defect formulation (5.3) overlaid. Symbols are those used in figure 5.16 for channel flow and figure 5.7 for pipe flow.

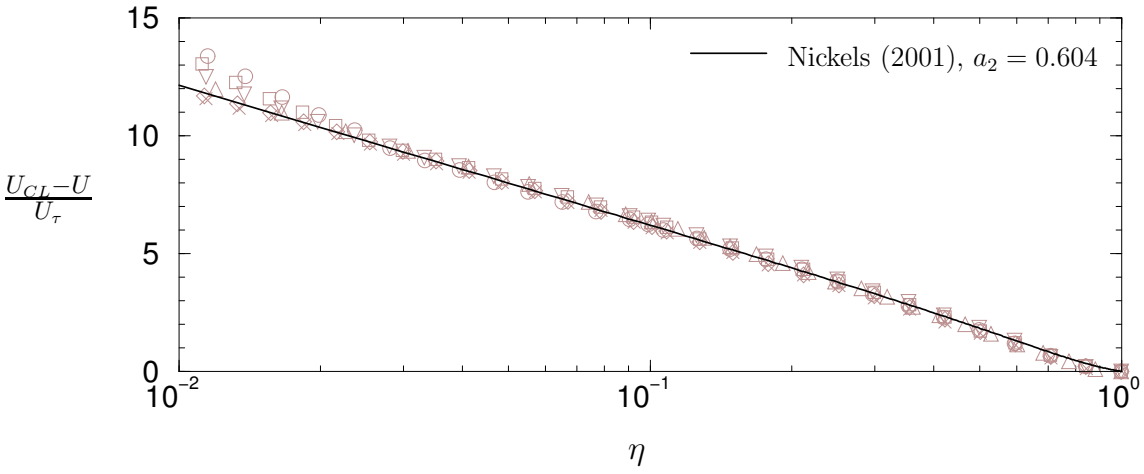

Figure 5.22: Velocity defect plots from the channel compared with Nickels (2001) velocity defect formulation (5.5). Symbols are those used in figure 5.16.

(5.5) overlaid for comparison. It is observed that the fit is reasonable, but clearly not as good as the Jones *et al.* (2001a) formula. Now, combining all expressions given by Nickels (2001) provides a description of the *complete* mean velocity profile; the applicability of this formulation for the inner flow region has already been established. Figure 5.23 illustrates the overall goodness of fit of the full Nickels formula by comparison with all inner flow scaled velocity profiles of channel flow. Thus, the Nickels velocity profile remains an attractive tool for further analytical work. Through private communication, it is understood that a new outer flow function tailored to duct flows has been formulated by Nickels, although it is yet appear in the literature.

5.4 Effects of redefining the overlap region

The discussions of results in §5.1.1 and §5.2.1 included the fitting of the log law (2.4) to the inner-flow scaled mean velocity profiles of both pipe and channel flows. This theoretical log law (2.4) is only expected to describe the profile in the overlap region as discussed in Chapter 2. The boundaries of the overlap region are not well defined in the literature and were assumed to be $y^+ = 100$ and $\eta = 0.15$ in earlier discussions. Here, a brief statistical analysis of the effects of varying the overlap region limits is presented. This analysis was conducted by simply fixing the upper limit of the overlap region ($\eta = 0.15$) and varying the lower limit, then fixing the

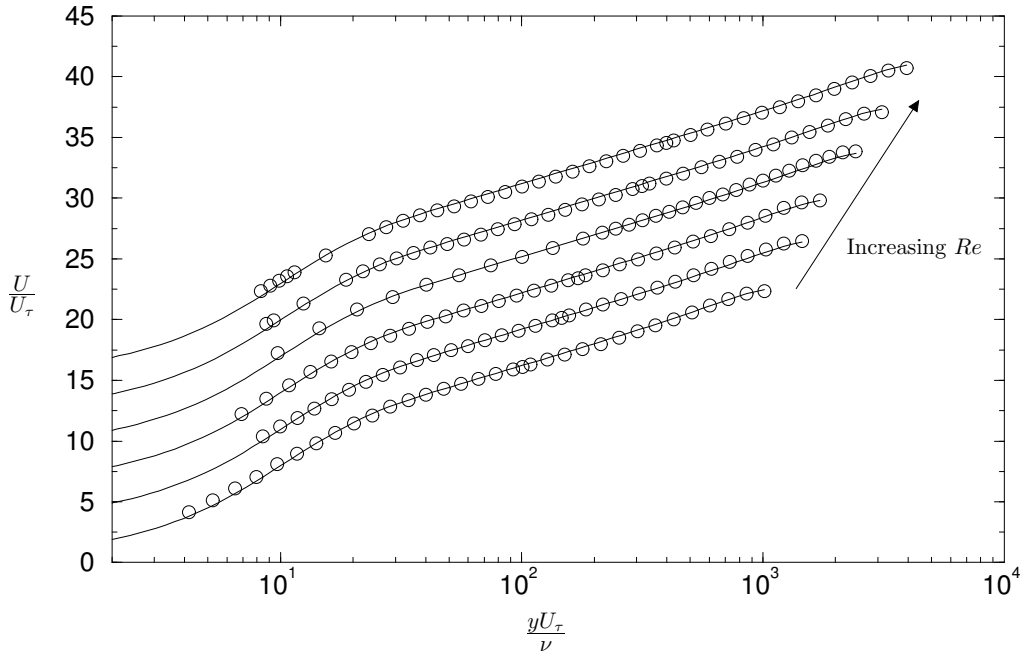

Figure 5.23: The full Nickels (2001) velocity profile formulation plotted with mean velocity profiles from the channel flow facility for $Re = 40, 60, 75, 105, 140, 180 \times 10^3$. Solid lines represent the Nickels formulation with $a_0 = 0.0857$ and $a_2 = 0.604$; the scaled velocity data are shown as circles. The profiles have been manually separated by 4 ordinate units.

lower limit at $y^+ = 100$ and varying the upper limit. Some other combinations of boundaries were experimented with and these are included in Appendix G. For each of the overlap regions chosen a least squares error curve-fit to equation (2.4) was performed to determine the constants κ and A.

The results of the overlap region analysis for pipe flow are tabulated in tables 5.3 & 5.4. The first block in each table suggests that varying the lower boundary from $y^+ = 70$ – 120 has very little effect on the resultant curve-fit. Note that at $y^+ = 70$ – 90 the pitot tube profiles kick-up from those measured with a hot-wire; therefore, the first three rows of table 5.3 may be influenced by pitot measurement error.

For a comparison of two given sets of log law constants (i.e., any two rows in the tables 5.3 – 5.6), the maximum percentage difference between the log laws was calculated over the range $y^+ = 100$ – 1000. From varying the lower limit of the overlap region from $y^+ = 100$ – 200 for the pitot tube measured data, the maximum difference in log laws was 0.14%. For the hot-wire measured data, the maximum

y^+	η	κ	A	# Obs.
70	0.15	0.392	4.45	58
80	0.15	0.391	4.40	56
90	0.15	0.387	4.27	50
100	0.15	0.386	4.21	47
110	0.15	0.383	4.11	43
120	0.15	0.381	4.05	41
150	0.15	0.381	4.04	31
175	0.15	0.379	3.97	25
200	0.15	0.383	4.10	20
100	0.10	0.400	4.65	22
100	0.11	0.396	4.53	27
100	0.12	0.392	4.43	32
100	0.13	0.390	4.37	37
100	0.14	0.388	4.28	42
100	0.15	0.386	4.21	47
100	0.16	0.383	4.13	52

Table 5.3: Pitot tube measurements in pipe flow: the effect of overlap region limit variation on the empircally derived log law constants. The right hand column contains the number of experimental observations lying in the specified overlap region.

difference in log laws was 0.23% when the lower limit was varied from $y^+ = 70 - 120$. Increasing the lower limit beyond $y^+ = 120$ results in significantly decreasing κ and A. This decreasing trend is likely attributable to the lack of data at high Reynolds numbers and the spatial resolution of the velocity profiles (there are less hot-wire data points than pitot tube); that is, the trend may be a result of experimental limitations rather than a property of the true velocity profiles. It is interesting to note that the channel flow results given in tables 5.5 & 5.6 show similar trends. In fact, any variation on the lower limit of the overlap region for hot-wire measured channel flow profiles had little effect on the resultant log law — even up to $y^+ = 200$.

The second (lower) blocks of data in tables 5.3 & 5.4 contain the results of fixing

y^+	η	κ	A	# Obs.
70	0.15	0.389	4.48	45
80	0.15	0.386	4.38	43
90	0.15	0.386	4.40	40
100	0.15	0.384	4.33	36
110	0.15	0.386	4.38	34
120	0.15	0.384	4.30	32
150	0.15	0.379	4.13	23
175	0.15	0.378	4.08	19
200	0.15	0.374	3.93	14
100	0.10	0.393	4.62	17
100	0.11	0.394	4.66	22
100	0.12	0.392	4.59	27
100	0.13	0.391	4.54	28
100	0.14	0.389	4.48	31
100	0.15	0.383	4.28	41
100	0.16	0.371	3.86	52

Table 5.4: Hot-wire measurements in pipe flow: the effect of overlap region limit variation on the empircally derived log law constants.

the lower limit of the overlap region and varying the upper limit from $\eta = 0.10$ – 0.16. Beyond $\eta = 0.16$ the wake peel off is visibly evident in the velocity profiles (see figure 5.1). As the overlap region is extended, the most obvious trend in the data is the consistent decrease in both κ and A. For the pitot measured data, the kick-up in velocity profiles may still influence the data at $y^+ = 100$. With only a small overlap region (i.e., an upper limit of $\eta = 0.10$ or 0.11) the log law constants found may be influenced by this pitot error. As the overlap region is extended, the data points in the pitot error affected region become less significant to the curve-fit. Since the kick-up tends to flatten the velocity profile, one would expect higher values of κ and A. This explanation is supported by the fact that the hot-wire measured data analysis (table 5.4) does not show such a decreasing trend as the overlap region limit extends to $\eta = 0.12$. However, extending the upper limit from $\eta = 0.13$ to

y^+	η	κ	A	# Obs.
70	0.15	0.404	4.83	42
80	0.15	0.400	4.71	39
90	0.15	0.396	4.57	34
100	0.15	0.397	4.58	30
120	0.15	0.392	4.43	25
150	0.15	0.391	4.39	18
175	0.15	0.390	4.34	17
200	0.15	0.391	4.39	12
100	0.10	0.406	4.86	19
100	0.12	0.400	4.70	24
100	0.14	0.397	4.58	30
100	0.15	0.397	4.58	30
100	0.16	0.393	4.47	36
100	0.18	0.391	4.38	42
100	0.20	0.390	4.35	48
100	0.25	0.389	4.31	54
100	0.30	0.386	4.21	66
100	0.35	0.384	4.16	72
100	0.40	0.382	4.10	78

Table 5.5: Pitot tube measurements in channel flow: the effect of overlap region limits on the empirically derived log law constants.

0.16 still results in a consistent decrease in the constants. It seems to the author that this trend can only indicate that there is a consistent curvature in the velocity profiles plotted on semi-logarithmic axes. That is, the velocity profiles do not behave *precisely* logarithmically between $\eta = 0.10$ – 0.16; although it must be noted that the deviation from the log law is certainly only slight, as only a small decrease in constants is observed. Unfortunately, the Reynolds numbers of this study and the data resolution prohibit the analysis of overlap regions with upper limits of less than $\eta = 0.10$ (with fixed lower limit of $y^+ = 100$). However, Appendix G includes analyses of overlap regions with lower limit of $y^+ = 80$ and upper limit varying

y^+	η	κ	A	# Obs.
70	0.15	0.391	4.31	61
80	0.15	0.390	4.26	56
90	0.15	0.390	4.26	53
100	0.15	0.389	4.23	49
120	0.15	0.390	4.25	41
150	0.15	0.390	4.28	34
175	0.15	0.394	4.44	28
200	0.15	0.395	4.45	23
100	0.10	0.397	4.45	27
100	0.12	0.394	4.38	37
100	0.14	0.392	4.32	43
100	0.15	0.389	4.23	49
100	0.16	0.389	4.23	49
100	0.18	0.386	4.13	55
100	0.20	0.384	4.07	56
100	0.25	0.380	3.92	65
100	0.30	0.378	3.88	74
100	0.35	0.377	3.84	75
100	0.40	0.375	3.77	81

Table 5.6: Hot-wire measurements in channel flow: the effect of overlap region limit variation on the empirically derived log law constants.

from $\eta = 0.07$ – 0.13. The data do not exhibit the same decreasing trend in log law constants and $\kappa = 0.392 \pm 0.002$, $A = 4.58 \pm 0.07$ were found. This suggests an upper limit of $\eta = 0.13$ may be more appropriate than 0.15. Returning to table 5.4, it is observed that similar values of $\kappa = 0.391$ and $A = 4.54$ result when the overlap region is defined by $100\nu/U_\tau < y < 0.13R$.

The upper limit variation analysis for channel flow also gave similar results to that of pipe flow. For the channel flow case, the upper limit was varied from $\eta = 0.10$ to 0.40 and the results are included in the second blocks of tables 5.5 & 5.6. This increased

upper limit range was analysed because channel flow velocity profiles visually appear to behave logarithmically over a large wall-distance range. From the tables above and from closer inspection of the mean velocity data, the overlap region does not extend beyond $\eta \approx 0.18$. As with the pipe flow analysis there is a clear trend of decreasing log law constants with increasing size of the overlap region. Reducing the upper limit below $\eta = 0.10$ did not improve the consistency of the constants, contradictory to the pipe flow case. However it should be noted that, although the log law constants do vary, the maximum percentage difference in log laws is only 0.42% (at $y^+ = 1000$ for the pitot tube measurements) when the overlap region limit is varied from $\eta = 0.12$ – 0.18. This small difference indicates that the data closely obey a logarithmic law, but to extrapolate the results to higher Reynolds numbers is only speculative. At the lowest Re of the present study, an overlap region of $100\nu/U_\tau < y < 0.15h/2$ spans less than 50 y^+ units which is plainly insufficient. It is suggested that an overlap region size of no less than one decade in y^+ (1000 y^+ units) would be required to confidently determine log law constants for higher Re. Thus it would appear that no definite overlap region limits can be proposed from the channel flow analysis presented here — higher Re measurements are necessary to confidently address this problem.

5.5 Comparison of pipe and channel flow results

The similarities between pipe and channel flows have been clearly stated so far: invariance with streamwise location for fully developed flow, wall shear stress dependence on pressure gradient and Reynolds number independent inner flow behaviour of the mean velocity profiles. The differences between pipe and channel flow, however, receive far less attention in the literature. In this section, mean profiles from both facilities will be compared and an attempt to explain the differences will be made.

5.5.1 Inner flow region

Figure 5.24 presents the first comparison between pipe and channel flow velocity profiles. In this figure, all pipe and channel velocity profiles scaled with inner flow variables and measured with pitot tubes are presented. The agreement between the two data sets in the inner flow region is excellent. The inset plot displays the deviation of the data from the log law with constants determined from the channel flow data: $\kappa = 0.393$, $A = 4.46$. The kick-up from the log law in the inner flow region appears similar in magnitude for both pipe and channel measurements. Earlier the issue of channel flow velocity profiles measured with a pitot tube showing greater kick-up than hot-wire data was discussed. This phenomenon was not observed in hot-wire measurements, however. The collapse of the data in figure 5.24 implies that the hot-wire data may be in error for one of the pipe or channel flow investigations. Figure 5.25, displaying the deviation of hot-wire data for both facilities, confirms this suspicion. In this figure, deviation from the log law fitted to channel flow hot-wire data is plotted. For comparison, the discrepancy between log laws fitted to pipe and channel flows is plotted as a broken line. It is obvious that the pipe flow data sit well above that of the channel flow. Furthermore, a closer analysis reveals the low Reynolds number pipe flow data (that is, the data sitting above the broken line in the vicinity of $y^+ = 50$) display marginally more kick-up than any of the channel flow data presented. The only explanation for this observation that the author can provide is that the hot-wire anemometry system used responded poorly to high frequency velocity fluctuations. This would result in an over-reading of the mean and an under-reading of turbulence intensity. It must be conceded, however, that no more solid reasoning for the hot-wire discrepancy can be provided at this time.

With regard to observations in comparisons of the inner flow region data, it is clear that pipe and channel flow pitot tube data are in excellent agreement and this data lies between the hot-wire measurements from each facility within experimental error ($\pm 1\%$). Hot-wire measurements from the two facilities, however, differ excessively. For the following reasons it is concluded that the channel flow hot-wire measurements and pitot tube measurements in both facilities are acceptable and of the highest

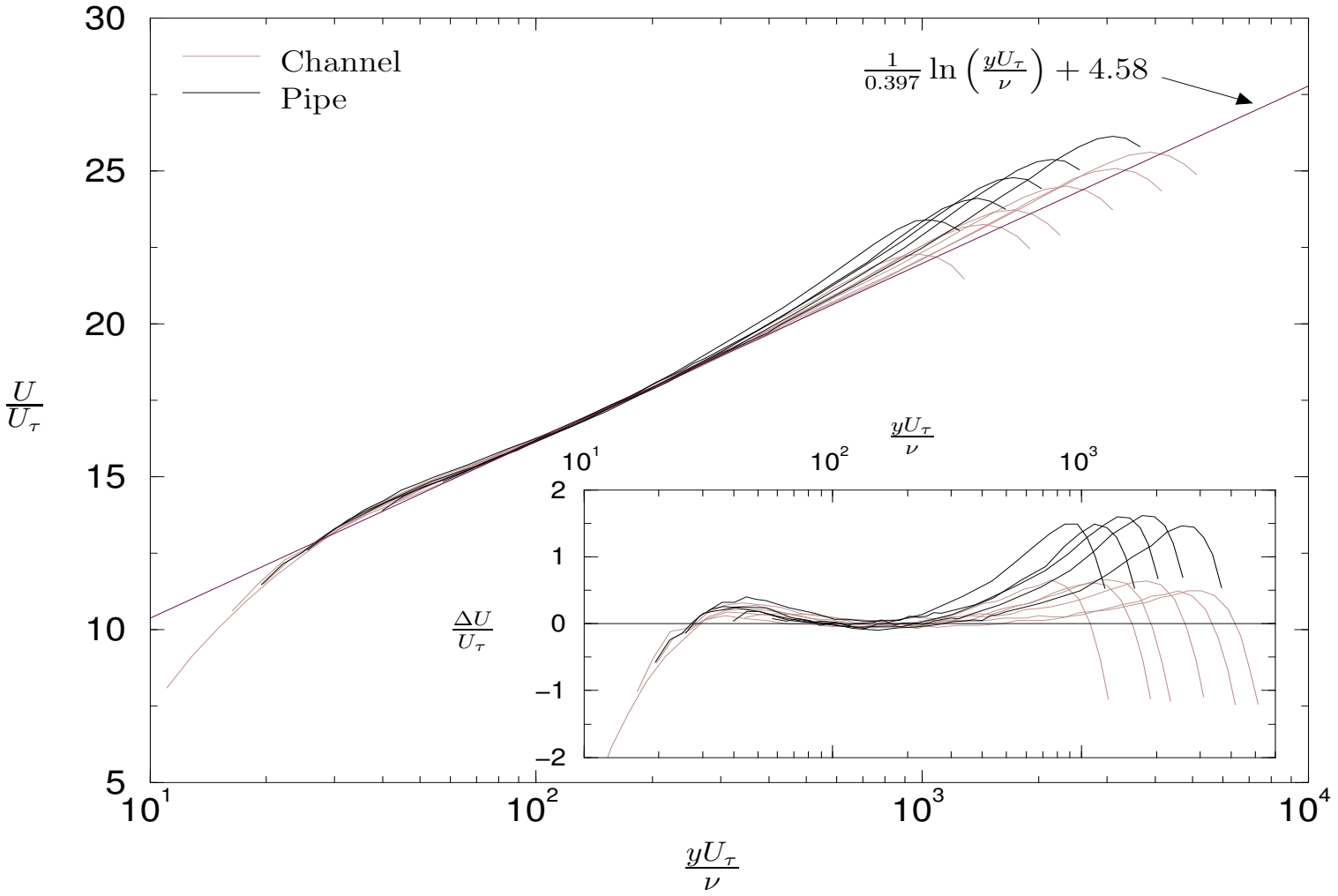

Figure 5.24: Comparison of pipe and channel inner flow scaled velocity profiles measured with pitot tubes. The inset plot displays the deviation of both data sets from the log law fitted to channel flow data. All data has been fully corrected.

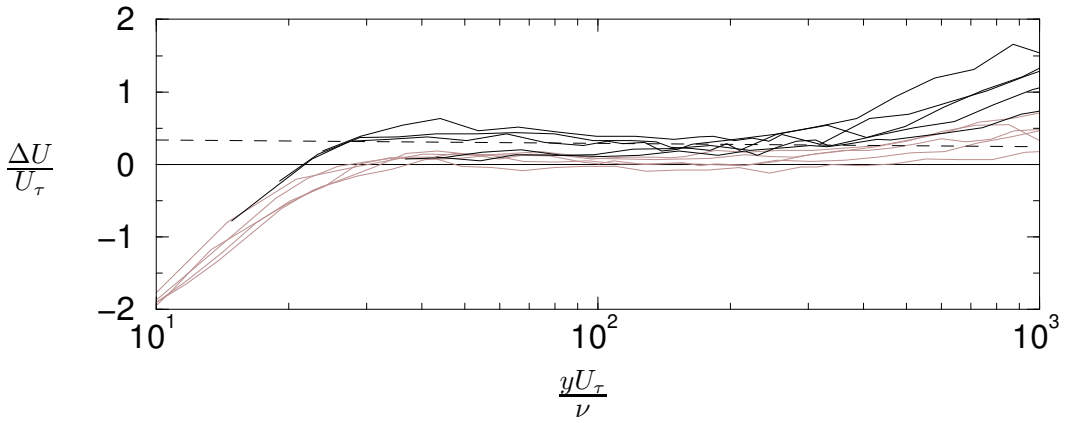

Figure 5.25: Comparison of pipe and channel hot-wire measurements. Deviation from the log law fitted to channel flow data is plotted. Symbols as in fig. 5.24. Also included is the deviation of the log law found for pipe flow data from that fitted to channel data, ---- .

accuracy: i) the channel flow hot-wire data agree well with Jones *et al.* (2001a) and Österlund *et al.* (2000a) in that almost no kick-up from the log law is evident, ii) only low Re pipe flow hot-wire data disagree with channel flow data, and iii) the author's experience with the difficulties of hot-wire anemometry was significantly more advanced during channel flow experiments.

5.5.2 Outer flow region

Observing the outer flow region of the pipe and channel velocity profiles reveals the most significant difference between the two flows. Figure 5.24 shows that the wake in the pipe flow is much larger than that of the channel flow for all Reynolds numbers. A comparison with zero-pressure-gradient boundary layer profiles indicates that the boundary layer has a stronger wake than both pipe and channel flows (see figure 5.26). These observations have been made in the literature by Wei & Willmarth (1989) and Zanoun *et al.* (2002). While it is expected that the boundary layer flow will have the strongest wake due to the absence of restrictive walls, this same reasoning would lead to the expectation that the channel flow wake would be similar to, if not larger than, that in the pipe. This is because, of the three flows, a circular pipe provides the greatest boundary imposed restriction on the flow. Neither reference given above offers an explanation for the undeniable weakness of the

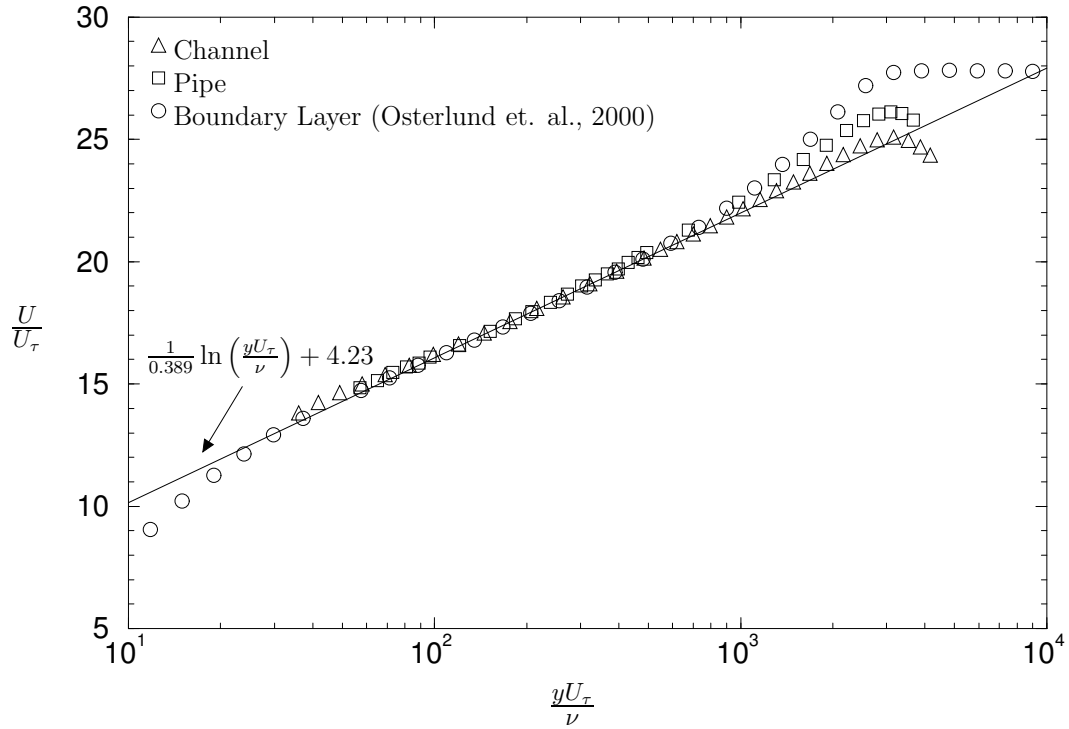

Figure 5.26: Comparison of pipe, channel and boundary layer measurements. Boundary layer data is from Österlund *et al.* (2000b) and all three flows had $K_\tau \approx 3200$.

channel flow wake; in fact, Zanoun *et al.* (2002) concludes:

> "[The wake] of the channel is significantly smaller than that for the pipe flow. This result is counter-intuitive, especially when the results from these two flows are compared to the case of the boundary layer..."

It is postulated here that a possible explanation may be found by a comparison of the turbulence structure of the pipe and channel flows. In analysing the structure, the attached eddy model of Perry & Chong (1982), discussed earlier in Chapter 2, will be employed.

5.5.3 A physical description of the mean flow behaviour

In §2.9.1 the concept of attached eddies and some postulated shapes were introduced. The two most common characteristic eddy shapes used in the literature are the $\wedge$- and the $\sqcap$-eddy. In the following paragraphs, models incorporating both of these eddy types will be used to help explain the wake behaviour of turbulent flows.

Perry & Chong (1982) have shown that the magnitude of the mean spanwise (or 'azimuthal' for pipe flow) vorticity contribution from each hierarchy of eddies, ξ_H, is given by:

$$\xi_H = \frac{U_\tau}{\delta} f\left(\frac{y}{\delta}\right), \tag{5.6}$$

where δ is the hierarchy scale. Integrating across all scales and including the p.d.f. of hierarchy scales, gives the mean vorticity magnitude (ξ) at a given wall-distance, y:

$$\xi(y) = \frac{dU}{dy} = \int_{\delta_1}^{\Delta_E} \frac{U_\tau}{\delta} f\left(\frac{y}{\delta}\right) p_H(\delta) d(\delta). \tag{5.7}$$

In §2.9.1 the transformation $\lambda = \ln(\delta/y)$ was introduced to aid integration across the scales. By applying this transformation here, the following relationships are found:

$$\frac{y}{\delta} = e^{-\lambda}; \qquad h(\lambda) = f\left(\frac{y}{\delta}\right); \qquad \frac{dU_D^+}{d\lambda_E} = \frac{y}{U_\tau}\frac{dU}{dy}; \qquad p_H(\lambda) = \frac{M}{\delta} W(\lambda - \lambda_E),$$

where U_D^+ is the scaled velocity defect, $U_{CL}^+ - U^+$. Substituting these relationships into (5.7) gives a gradient of velocity defect,

$$\frac{dU_D^+}{d\lambda_E} = M \int_{\lambda_1}^{\lambda'_E} h(\lambda) e^{-\lambda} W(\lambda - \lambda_E) d\lambda, \tag{5.8}$$

where λ'_E is an intermediate variable with range $0 \rightarrow \lambda_E$. Thus, $dU_D^+/d\lambda_E$ is a function of λ'_E. Integrating (5.8) gives the velocity defect,

$$U_D^+ = M \int_0^{\lambda_E} \int_{\lambda_1}^{\lambda'_E} h(\lambda) e^{-\lambda} W(\lambda - \lambda_E) d\lambda d\lambda'_E. \tag{5.9}$$

To make any further progress, the functional forms of $h(\lambda)$ and $W(\lambda - \lambda_E)$ are required. §2.9.1 explains that W is a weighting function which may be adjusted to account for the wake of the velocity profile. Since the large scale geometry of the flow has not entered the argument so far, W will be left unexplained at this point. $h(\lambda) = f(y/\delta)$ relates to the vorticity distribution around a single eddy. Examples of this function for the $\wedge$- and $\sqcap$-eddy are given in figure 5.27. For the $\sqcap$-eddy all spanwise vorticity is confined to the 'horizontal' vortex rod at the top of the eddy (which has been projected onto the $y - z$ plane in the figure). In the case of the $\wedge$-eddy, the vorticity is distributed evenly with non-dimensional wall-distance, y/δ. Hence, $f(y/\delta)$ is a dirac delta function (at $y = \delta$) for the $\sqcap$-eddy, and unity for $y = 0$ to $y = \delta$ for the $\sqcap$-eddy. Transforming $f(y/\delta)$ to $h(\lambda)$ and multiplying by $e^{-\lambda}$

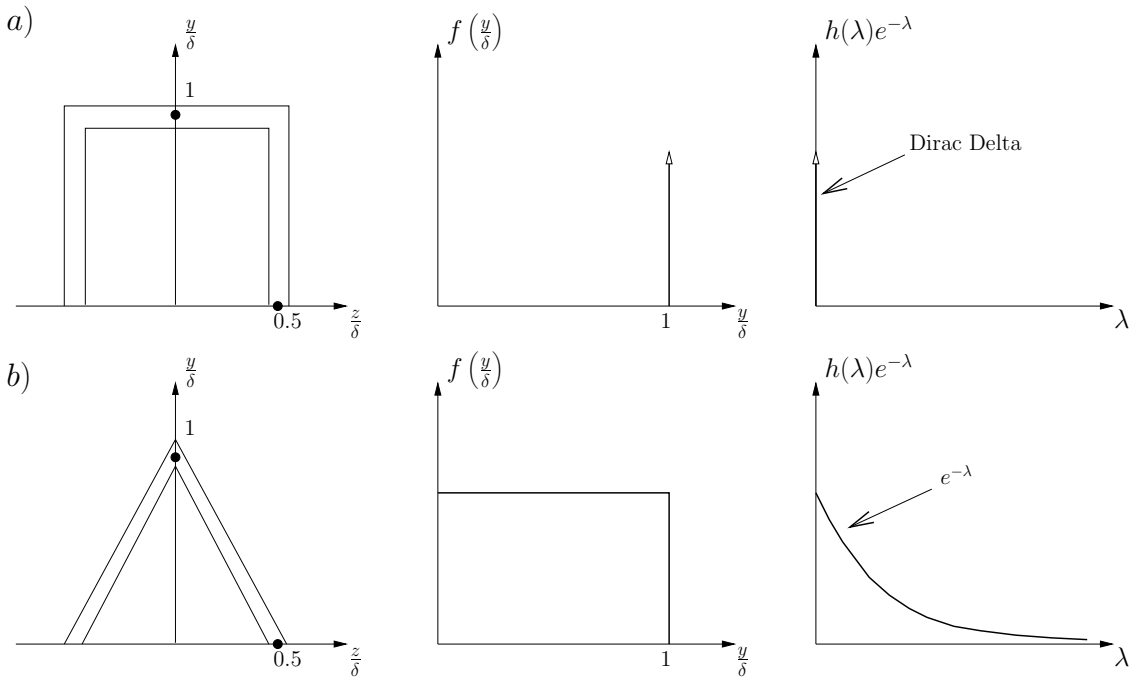

Figure 5.27: Sketches of two eddy shapes and their $h(\lambda)e^{-\lambda}$ distributions: a) $\sqcap$-eddy and, b) $\wedge$-eddy.

gives the forms shown in figure 5.27. These distributions are very important as they make the critical connection between the mean flow and eddy shape.

At this stage, there is enough information to calculate U_D^+ from (5.9) if it is assumed that $W = 1$. That is, the p.d.f. of hierarchy scales is a -1 power law. However, Perry *et al.* (1986) have shown that no eddy shape will provide the desired wake behaviour if the p.d.f. is of this form† . Interestingly, it was found that all eddy shapes studied gave the correct scaling in the overlap region, even with $W = 1$. It was concluded by Perry *et al.* (1986) that a modification to the p.d.f. was necessary to account for the outer flow deviation from the log law. Therefore, since the problem of interest is the anomalous difference between pipe and channel outer flow behaviour, the form of W is of most interest here. Note that only the two eddy shapes shown in figure 5.27 will be considered in this analysis.

Returning to equation (5.8), it is seen that this equation is simply a convolution of two functions: $h(\lambda)e^{-\lambda}$ and $W(\lambda)$. Therefore, if the analytical form of $dU_D^+/d\lambda_E$

† There *was* one eddy shape that was postulated by Perry *et al.* (1986) which gives the correct wake. The eddy was of a "bow-legged, parabolic" shape, however, it was discarded by the authors as an unrealistic shape.

is known, a deconvolution of (5.8) will return $W(\lambda)$ since $h(\lambda)e^{-\lambda}$ is known and dependent only on eddy geometry. Analytical forms of the outer flow velocity profile were introduced in §2.3. Recalling the Jones *et al.* (2001a) formulation in velocity defect form (5.3):

$$U_D^+ = -\frac{1}{\kappa}\ln(\eta) + \frac{1}{3\kappa}(\eta^3 - 1) + \frac{2\Pi}{\kappa} - \frac{2\Pi}{\kappa}\eta^2(3 - 2\eta).$$

If Δ_E is the largest length scale in the flow, then $\eta = y/\Delta_E = e^{-\lambda_E}$. Substituting this into (5.10) and differentiating with respect to λ_E gives

$$\frac{dU_D^+}{d\lambda_E} = \frac{1}{\kappa} - \frac{1}{\kappa}(1 - 2\Pi)e^{-3\lambda_E} + \frac{12\Pi}{\kappa}e^{-2\lambda_E}. \tag{5.10}$$

Note the presence of Π, the wake strength parameter, which depends on large scale geometry and pressure gradient. All that remains now is to deconvolve (5.8) for each eddy shape. Such a mathematical procedure is made possible by a Laplace transformation of the convolution.

Let $\mathcal{L}\{X(\lambda)\} = \Lambda(s)$ and $\mathcal{L}\{h(\lambda)e^{-\lambda}\} = \Sigma(s)$ represent the Laplace transforms of $X(\lambda)$ (an arbitrary function) and $h(\lambda)e^{-\lambda}$ respectively. It is well-known, then, that the Laplace transform of the convolution is given by:

$$\mathcal{L}\left\{M\int_{-\infty}^{\infty} h(\lambda)e^{-\lambda}X(\lambda_E - \lambda)d\lambda\right\} = M\Sigma(s)\Lambda(s). \tag{5.11}$$

If the substitution $X(\lambda) = W(-\lambda)$ is made, then (5.11) becomes the Laplace transform of (5.8) so that

$$\mathcal{L}\left\{\frac{dU_D^+}{d\lambda_E}\right\} = M\Sigma(s)\Lambda(s). \tag{5.12}$$

Note that the convolution integration limits of (5.11) are $\pm\infty$ which is not a cause for concern since $W(\lambda - \lambda_E) = 0$ outside the range of integration in (5.8); that is, (5.12) holds even with this change of integration limits.

From the distributions of $h(\lambda)e^{-\lambda}$ shown in figure 5.27, it can easily be shown that $\Sigma(s) = 1$ for the $\sqcap$-eddy and $\Sigma(s) = 1/(s + 1)$ for the $\wedge$-eddy. By substituting these and the Laplace transform of (5.10) into (5.12), $\Lambda(s)$ for each eddy shape may be determined. The inverse Laplace transform of the $\Lambda(s)$ functions gives, for the $\sqcap$-eddy,

$$W(\lambda - \lambda_E) = 1 - (1 + 12\Pi)e^{3(\lambda - \lambda_E)} + 12\Pi e^{2(\lambda - \lambda_E)}; \tag{5.13}$$

and for the $\wedge$-eddy,

$$W(\lambda - \lambda_E) = 1 + 2(1 + 12\Pi)e^{3(\lambda-\lambda_E)} - 12\Pi e^{2(\lambda-\lambda_E)}. \tag{5.14}$$

The above equations may be rewritten in terms of $\delta/\Delta_E = e^{(\lambda-\lambda_E)}$ and substituted into the p.d.f. equation (2.51) to obtain the final result:

$$\frac{p_H(\delta)}{M_d} = \frac{\Delta_E}{\delta} - \frac{\delta}{\Delta_E}\left[(1 + 12\Pi)\frac{\delta}{\Delta_E} - 12\Pi\right], \tag{5.15}$$

$$\frac{p_H(\delta)}{M_d} = \frac{\Delta_E}{\delta} + \frac{\delta}{\Delta_E}\left[2(1 + 12\Pi)\frac{\delta}{\Delta_E} - 12\Pi\right] \tag{5.16}$$

for the $\sqcap$- and $\wedge$-eddies respectively. Note that $M_d = M/\Delta_E$. Both of these functions are plotted in figure 5.28 for various wake strengths, Π. Figure 5.28a presents p.d.f.'s for the $\wedge$-eddy model and figure 5.28b displays those for the $\sqcap$-eddy model. The heavy broken line in each figure represents the inverse power law p.d.f. (i.e., the $W = 1$ case). Until this point these graphs are merely the end result of mathematical manipulation. The real interest, however, is in their physical interpretation.

It should be remembered that the eddy shape is representative only. By this it is meant that individual eddies in the flow need not have the exact geometrical features of the proposed eddy shapes, rather, the real and representative eddies will, on average, bear the same statistical properties. Thus, the choice of representative eddy shape is of little consequence to the model, provided W is chosen correctly. However, the resultant p.d.f.'s of figure 5.28 obviously depend on eddy shape and these should be somewhat physically justifiable. At first glance it would seem that the p.d.f. of $\sqcap$-eddy hierarchies has the more logical behaviour as wake strength is increased. Certainly for boundary layer flow it would be expected that the p.d.f. should diminish smoothly to zero as hierarchy scale is increased to its maximum, Δ_E. In fact, this eddy shape is preferred in the recent literature; Marusic (1991), Uddin (1994), Nickels & Marusic (2001) and Marusic (2001) are examples. It could be argued further that the representative eddies in a channel flow should not differ from those of constant pressure boundary layer flow. This is because the channel flow is formed from two adjacent, developing boundary layers. The only significance of this to the current argument is that it suggests the hierarchies of eddies exisiting in channel and boundary layer flows should behave similarly (although the channel flow hierarchy p.d.f. should not reach zero at $y = \Delta_E = h/2$).

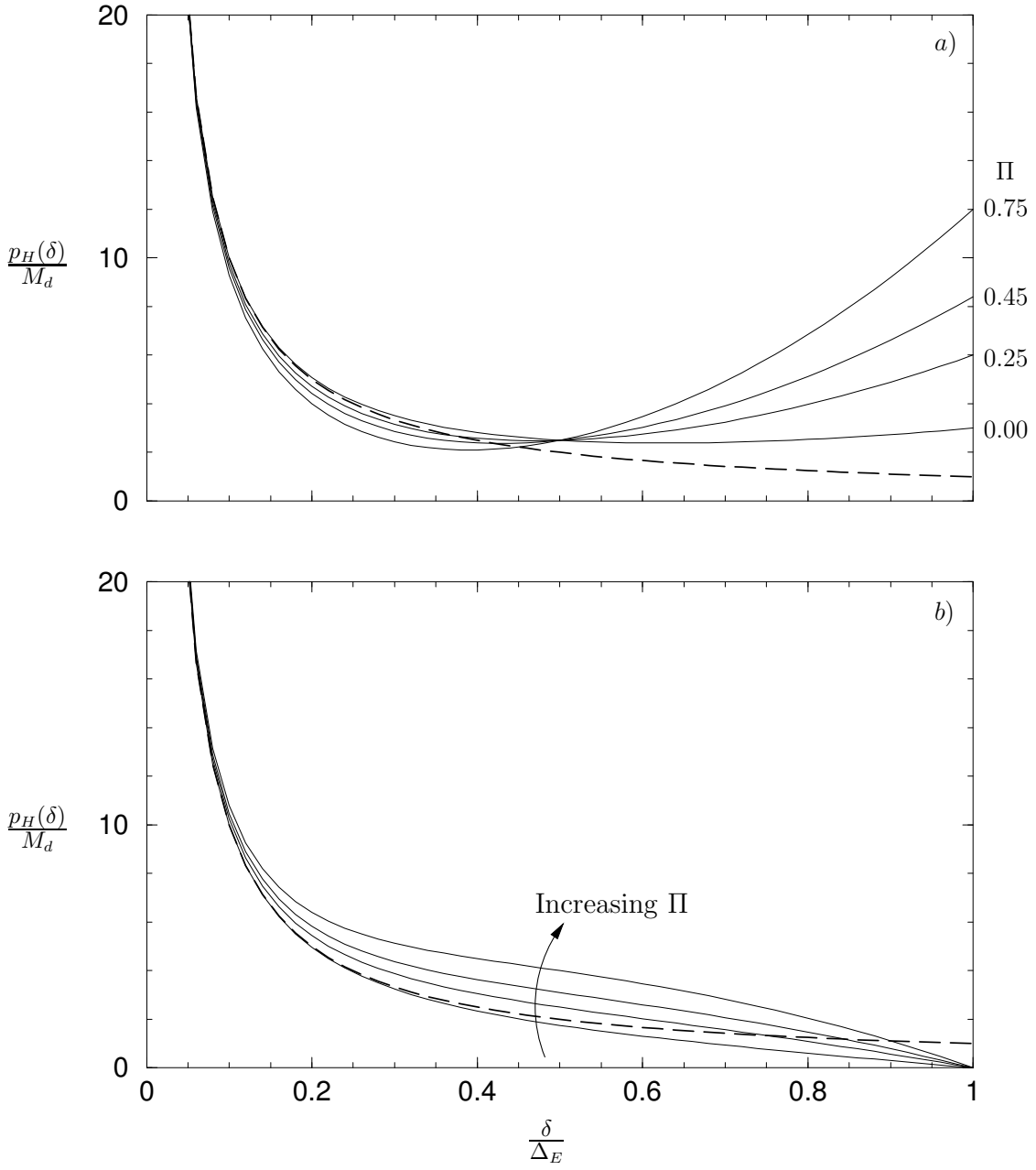

Figure 5.28: p.d.f.'s of attached eddy hierarchy scales modified in order to give the desired wake behaviour of the mean flow. a) $\wedge$-eddy; b) $\sqcap$-eddy. The heavy dashed line represents the weightless p.d.f., $p_H = M/\delta$.

In pipe flow, the $\sqcap$-eddy would seem an odd choice due to the axis-symmetry of the flow; the $\wedge$-eddy model appears to more naturally adhere to the large scale geometry of a pipe as illustrated in figure 5.29. The figure presents idealised hierarchies of attached $\wedge$-eddies in a pipe, in a similar way to figure 2.6 which applied to a plane wall-bounded flow. The figure illustrates a major difference between pipe and plane wall-bounded flows with regard to the attached eddy model: as the hierarchy scale increases in the pipe, the characteristic eddies are increasingly angled toward each other. Therefore, as the pipe centreline is approached, the assumption that contributions to the azimuthal vorticity come only from those hierarchies of eddies originating from *one* wall location is invalid. That is, equation (5.7) needs to be modified to include the vorticity contributions from neighbouring hierarchies. Such a modification would only add another weighting function to equation (5.8) and would therefore be embedded in the weighting function, W, determined for pipe flow in equation (5.13). Thus, the p.d.f. of scales given in figure 5.28a may be interpreted as the p.d.f. not of scales *existing*, but of scales *contributing* to the mean azimuthal vorticity, ξ. Figure 5.28a then suggests that as the length scale increases beyond $0.5\Delta_E = 0.5R$, the probability of hierarchies contributing to ξ increases. The interesting point is that this behaviour is physically consistent with the diminishing proximity of neighbouring hierarchies as scale increases (as clearly illustrated by figure 5.29).

The above arguments are summarised as follows: it is obvious from figure 5.29 that many more attached structures will contribute to the mean flow than in the centre of a channel flow, regardless of characteristic eddy shape. This is due to the presence of a wall at any distance R (pipe radius) from the centre of the pipe; conversely, in a channel there are only two wall locations at a distance $h/2$ (channel half-height) from the centreline. While the arguments provided above may be conceivable, the reader is reminded that the attached eddy hypothesis at the foundation of these arguments *is* still an hypothesis at this point in time. Further discussion of evidence in support of the attached eddy model will be provided in the following chapters.

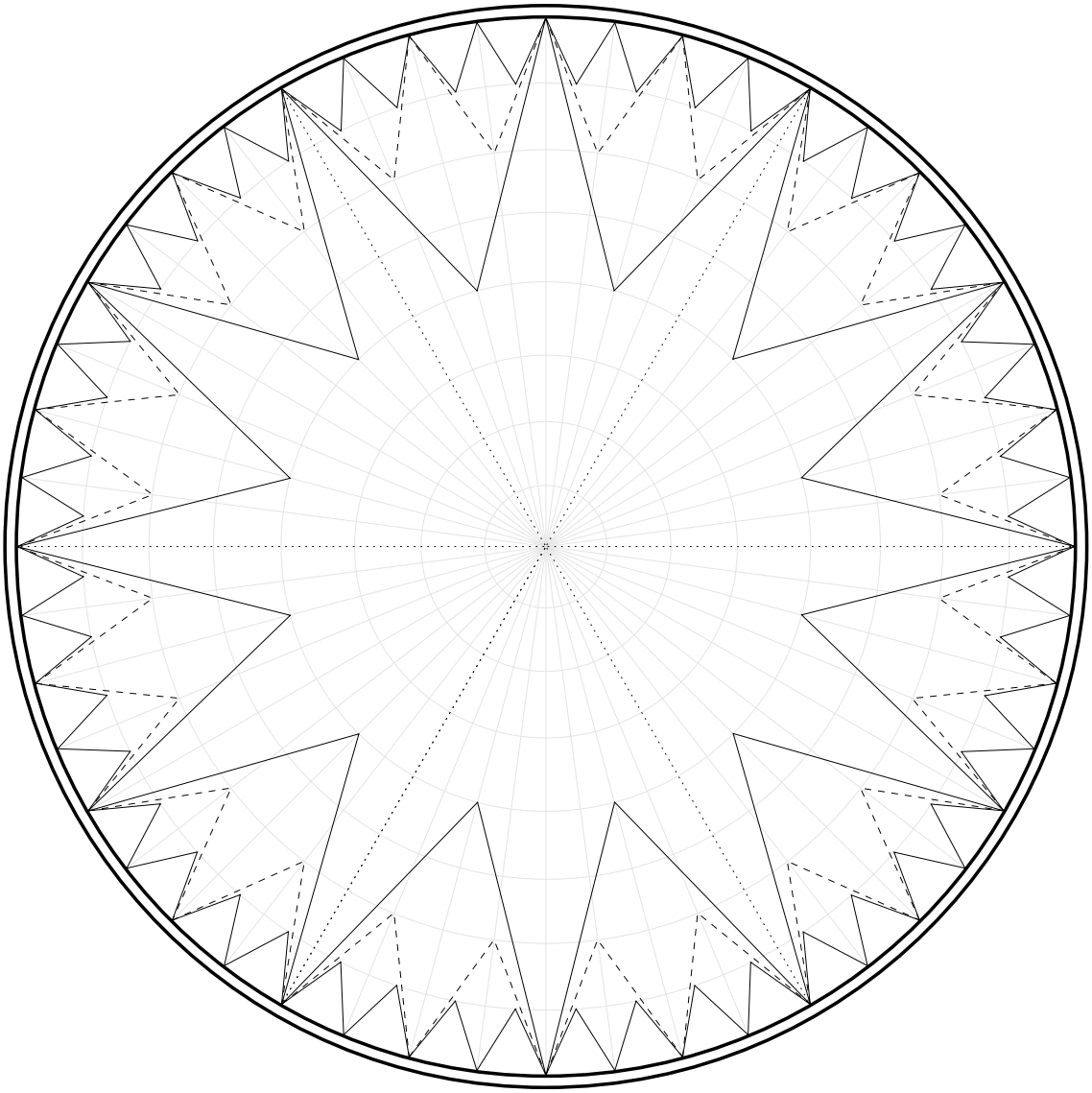

Figure 5.29: Hierarchies of attached $\wedge$-eddies in a circular pipe cross-section. Note that the dotted lines represent hierarchies of length scale equal to the pipe radius. Grey lines are gridlines only.

Chapter 6

Second-order turbulence statistics

Measurement of higher-order turbulence statistics was made possible mid-way through the 20^{th} Century by the introduction of the hot-wire anemometer. The technique remains popular today, even with the rapid progress of Laser Doppler Velocimetry (LDV) and Particle Image Velocimetry (PIV). The latter technique is now almost universally employed for water flows, while hot-wire methods are common for experimentation with gas flows.

All who have experimented with hot-wires are aware of the various issues that affect its performance. For example, calibration drift, ambient temperature change, dust and external electronic noise. Most of these problems can be removed through careful experimentation, however, the limitation of spatial resolution of the anemometer cannot. While the resolution issue has always been known, the full extent of its effects in high Reynolds number turbulence has only recently been revealed. Nonetheless, hot-wire anemometry remains a relatively cost-effective and convenient technique for the difficult measurement of turbulence in air flow.

In this chapter, wall-normal distributions of streamwise turbulence intensity, $\overline{u'^2}$, are presented for both pipe and channel flows. Measurements were taken with a normal hot-wire probe. For channel flow only, the remaining turbulence intensities, $\overline{v'^2}$ and $\overline{w'^2}$, and the measureable Reynolds stresses, $\overline{u'v'}$ and $\overline{u'w'}$, were measured with a X-wire and are also presented here.

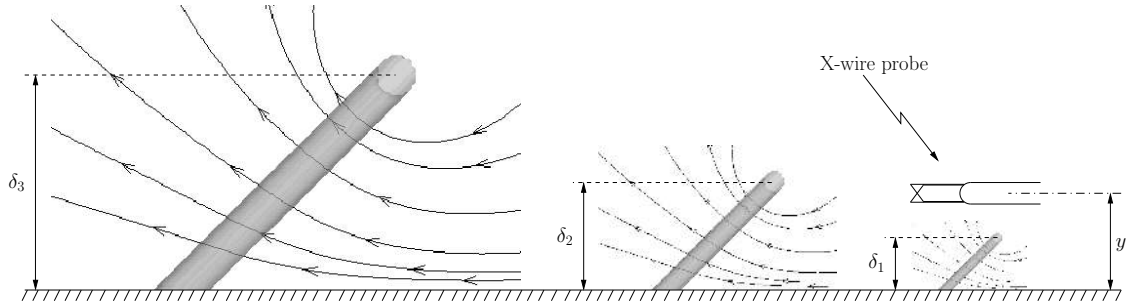

Figure 6.1: Attached eddies of three scales, δ_1, δ_2 and δ_3, passing by a stationary X-wire probe. Solid lines represent instantaneous streamlines. The probe is located at a wall-distance, y, such that $\delta_1 < y < \delta_2$.

6.1 The role of attached eddies

Before the presentation of results, a brief discussion of the physical expectations of the turbulence measurements is provided here. Figure 6.1 displays three attached eddies of varying scale moving from left to right as part of a turbulent flow field. Some† instantaneous streamlines are shown as calculated from the Biot-Savart law (for a $\sqcap$-eddy). Also shown is a stationary X-wire probe, the response of which will be affected in a different way by each eddy:

1. Firstly, the probe will have negligible response to the smallest eddy, which has length scale $\delta = \delta_1$. It was shown in Chapter 2 (see the vector field plotted in figure 2.8) that the velocity induced by an eddy rapidly diminishes with wall-distance for $y > \delta$. Thus, it is safe to assume that *all* eddies of length scale $\delta < \mathcal{O}(y)$ make no contribution to the turbulent velocity felt by a X-wire at y.

2. As the second eddy shown in figure 6.1 passes the probe, relatively high velocities in all directions will be induced. That is, eddies of scale $\delta = \mathcal{O}(y)$ will significantly contribute to all turbulence intensities, $\overline{u'^2}$, $\overline{v'^2}$ and $\overline{w'^2}$. Obviously, then, these eddies will also make contributions to the Reynolds shear stress, $\overline{u'v'}$.

3. The third eddy, having length scale $\delta = \delta_3 > \mathcal{O}(y)$, will also contribute strongly

† Only six streamlines have been plotted for clarity.

to the velocity field seen by the X-wire. However, only significant contributions will be made to $\overline{u'^2}$ and $\overline{w'^2}$. This is because of the boundary condition forcing wall-normal velocity, v, to diminish at the wall, combined with the fact that y/δ decreases as δ increases. The velocity vector field of figure 2.8 shows the effect of this boundary condition; that is, the vectors have negligible v component as the wall is approached. Thus, eddies of scale much larger than the probe wall-distance will not contribute to Reynolds shear stress; they are referred to as "inactive" motions by Townsend (1976). Finally, it should be noted that the usual no-slip boundary condition is not imposed in the attached eddy model. That is, slip at the wall is permitted by the presence of the thin viscous sublayer at the base of the eddies. Therefore, eddies of increasing scale will indefinitely contribute to the streamwise and spanwise components of velocity.

With this physical understanding, it should now be possible to more meaningfully analyse the measured data.

6.2 Streamwise turbulence intensity

Turbulence intensity, $\overline{u'^2}$, was calculated from data collected during the recording of a mean velocity profile using a normal hot-wire. That is, mean velocity profiles presented in Chapter 5 and the turbulence intensity profiles displayed in this section were measured simultaneously. The $\overline{u'^2}$ profiles are plotted in figures 6.2 – 6.5.

6.2.1 Inner flow scaling

For pipe flow, figure 6.2 displays the inner flow scaled $\overline{u'^2}$ profiles. Analysis of this figure reveals that the expected peak in turbulence intensity at $y^+ \approx 15$ is not visible due to a lack of data close to the wall. The reason for this is that data for $y^+ < 50$ were not required to meet the aims of the pipe flow study. Moreover, the absence of measurements in this region give the false impression that some Reynolds number similarity exists in the profiles for $y^+ \lesssim 40$. No similarity is expected in this region

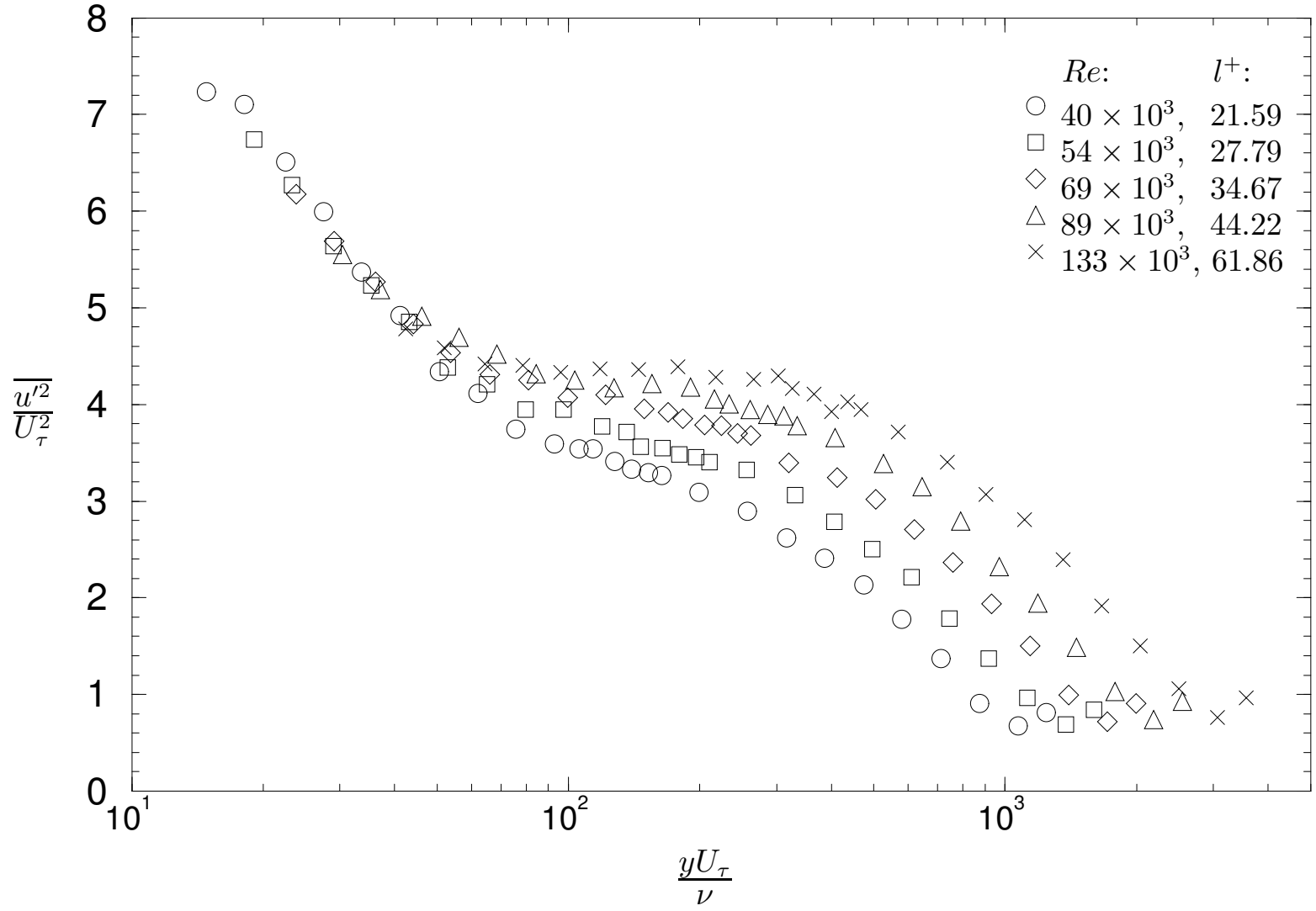

Figure 6.2: Pipe flow: streamwise turbulence intensity profiles with inner flow scaling.

as explained below.

Reynolds number similarity implies that, at a given y^+, the scaled streamwise turbulence intensity is invariant with Re. Now, as Re increases, U_τ/ν increases so that y must decrease if y^+ is fixed. Similarly, the smallest eddy height also decreases, since the smallest eddies scale as $\delta_1^+ = \mathcal{O}(100)$. Thus, the *range* of eddy length scales increases with increasing Re. Recalling the third point of discussion in §6.1: eddies indefinitely larger than the probe wall-distance contribute to the $\overline{u'^2}$ measurement. Therefore, if the probe wall-distance is decreased to keep y^+ constant as Re increases, an increased number of eddies with scale $\delta > \mathcal{O}(y)$ will exist and make contributions to $\overline{u'^2}$. The result is an increased $\overline{u'^2}/U_\tau^2$ at a given y^+.

Obviously, the above argument applies for $y^+ > 100$ only; application below this wall-distance should be invalid due to the lower limit of eddy length scale ($\delta^+ = 100$). Marusic, Uddin & Perry (1997) propose that, although a physical interpretation of the sublayer flow is unavailable, it is most likely that no Reynolds number similarity would exist in this region if there is no similarity at its edge (i.e., at $y^+ \approx 100$). Further, it is conjectured by Perry & Chong (1982) that the eddies form and begin to take shape in the sublayer. Hence, the argument given above may be of some relevance in the sublayer — assuming the range of structure scales roughly increases with increasing Re, as occurs further from the wall.

Figure 6.2 confirms the main points of the above discussion for $y^+ > 100$: there is clearly no similarity and the turbulence intensity increases with increasing Re. The inner flow scaled $\overline{u'^2}$ measurements in the channel, shown in figure 6.3, display similar trends to pipe flow data. The major difference between the two flows is simply that measurements were recorded much closer to the wall for the channel flow case. Hence, the dissimilarity in profiles below $y^+ = 100$ is clear. The expected trend of increased $\overline{u'^2}$ with increasing Re, however, is not realised in this region. In fact, the magnitude of the peak in turbulence intensity (at $y^+ \approx 15$) decreases markedly as Re increases. This behaviour is attributed to insufficient spatial resolution of the hot-wire. The spatial resolution effect may be characterised, at least in part, by the non-dimensional variable l^+, where l is the length of the exposed platinum hot-wire

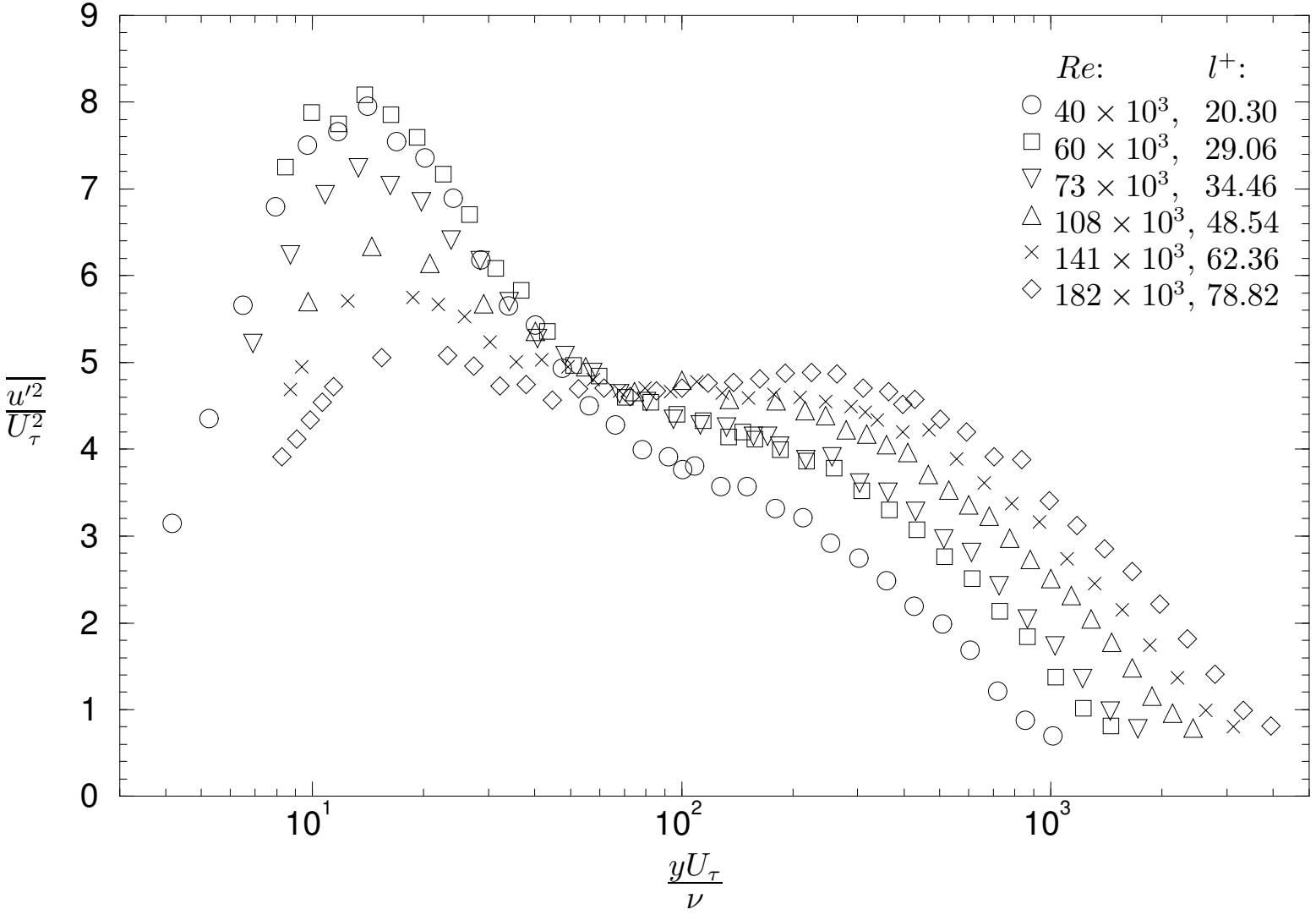

Figure 6.3: Channel flow: streamwise turbulence intensity profiles with inner flow scaling.

filament. This length was maintained at $1mm$† for all measurements presented in this thesis.

In both figures 6.2 & 6.3, the value of l^+ for each profile is included in the figure legend. The studies of Ligrani & Bradshaw (1987) and Hites (1997) suggest that measurements made with a wire length of $l^+ \gtrsim 30$ will be significantly affected by spatial resolution effects. Furthermore, preliminary studies in the high Reynolds number boundary layer wind tunnel at Melbourne (unpublished) agree with this criteria. Inspection of the profiles with low l^+ shown in figure 6.3, reveals that there is a slight increase in peak turbulence intensity as Re increases, as expected. The increase is small, although notable, and is consistent throughout the inner flow region. For larger wire lengths — that is, for $l^+ > 30$ — the data exhibit increasing attenuation. Thus, the data appears to agree with the observations of the aforementioned references. Note, however, that without a set of measurements made with much smaller wires, it is not possible to make any conclusions about l^+ effects here.

A closer look at the highest Re profile reveals that the attenuation in $\overline{u'^2}$ begins to occur as far as $y^+ = 300$ from the wall. Further evidence of such attenuation is available in the literature, Morrison *et al.* (2004) and Henbest (1983) are examples. The reason for this attenuation is not understood at this time. It would be expected that attenuation would start at non-dimensional wall distances of the order l^+, which is only 78.82 at the highest Re of this study. Two possible explanations for the extended attenuation are postulated here:

1. Conduction losses from the exposed wire to the silver 'stubs' attached to the hot-wire prongs. This would result in a non-uniform temperature distribution across the exposed hot-wire and would be more severe with increased velocity. Once again, no definite conclusions can be drawn without varying wire length.

2. Very long (in the streamwise sense) structures exist in the flow, which are smaller (in the spanwise sense) than the wire length. These structures would

† In hindsight, experimentation with smaller wire lengths (and therefore, smaller wire diameters) would have been very informative.

pass by only a portion of the wire, so that the velocity fluctuations measured are attenuated, while the streamwise wavenumber remains high. To verify this possibility would be rather difficult since extremely highly resolved, three-dimensional measurements in high Reynolds number flows would be required. Of the techniques available at this time, only stereoscopic PIV technology is potentially capable of such measurements. However, the required resolution is not possible with current technology.

6.2.2 Outer flow scaling

Shifting attention to the outer flow region, it would be expected that outer flow similarity should be observed based on the discussion of §6.1. This is also a requirement of Townsend's Reynolds number similarity hypothesis. Figure 6.4 displays the outer flow scaled turbulence intensity profiles for pipe flow. It is immediately evident that there is poor collapse in the outer region at low Re, even for $\eta > 0.15$. The extent of this dissimilarity is somewhat surprising, although it appears as a low Reynolds number effect only. Further evidence of the low Re shift is observed in the channel flow $\overline{u'^2}$ measurements, shown with outer flow scaling in figure 6.5. Upon consultation of the literature, it was found that the low Re effect on $\overline{u'^2}$ is not unique to this investigation; Henbest (1983), McLean (1990)† and Morrison *et al.* (2004) present outer flow scaled data showing similar behaviour.

For higher Re, turbulence intensity profiles do show similarity in the outer region and follow the same trends found in the data presented by Marusic *et al.* (1997). This reference clearly shows that the extent of similarity depends on Re. Unfortunately, the Re range studied here is insufficient for the data to noticeably display such a feature (more data points in the outer flow region would also be required). However, in general agreement with the lower Re data of Marusic *et al.* (1997), the scaled turbulence intensity exhibits similarity for $\eta \gtrsim 0.15$, while $\overline{u'^2}/U_\tau^2$ increases with increasing Re at $\eta \approx 0.1$.

† The turbulent boundary layer measurements of McLean (1990) are also plotted in figure 5 of Marusic *et al.* (1997).

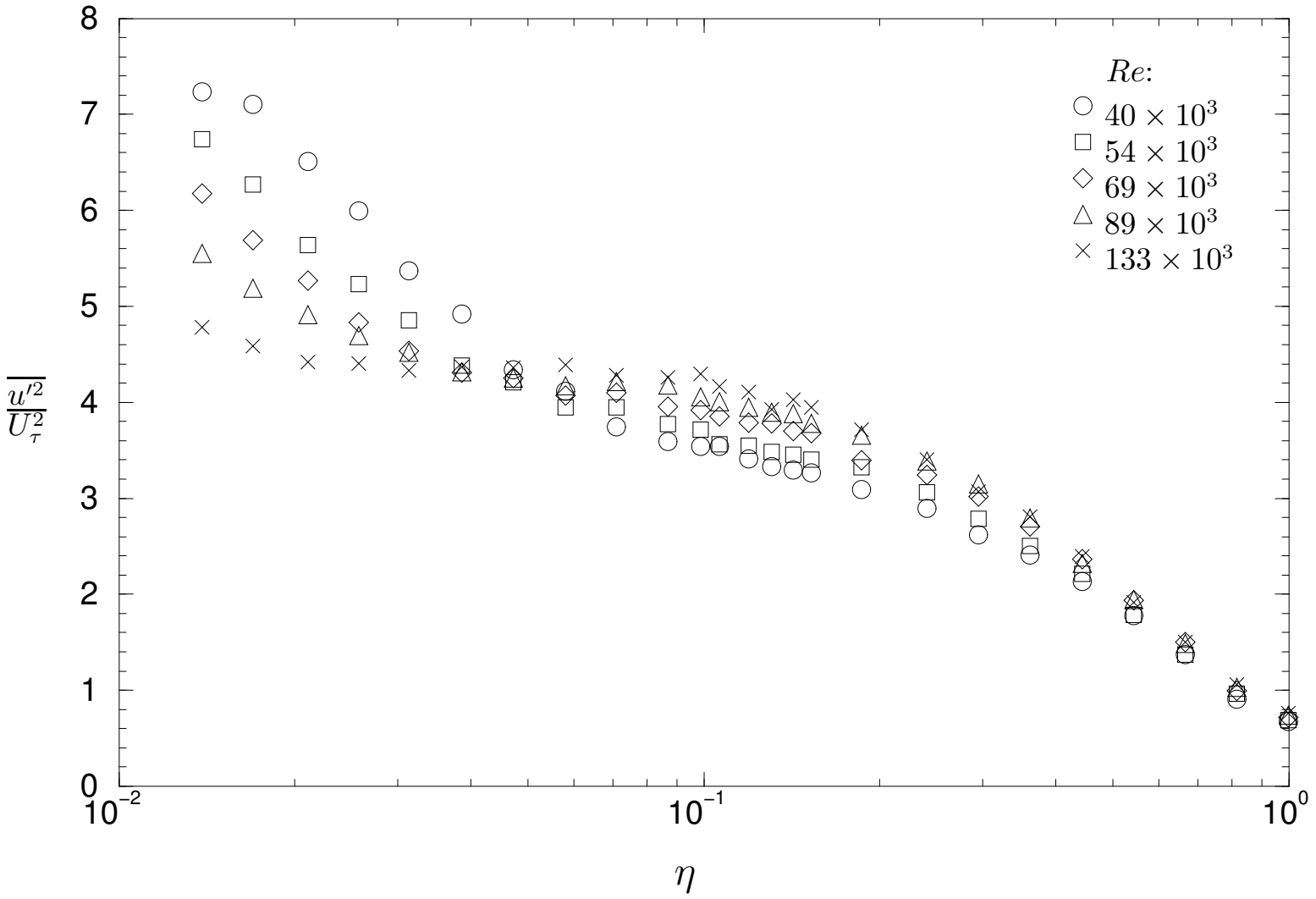

Figure 6.4: Pipe flow: streamwise turbulence intensity profiles with outer flow scaling.

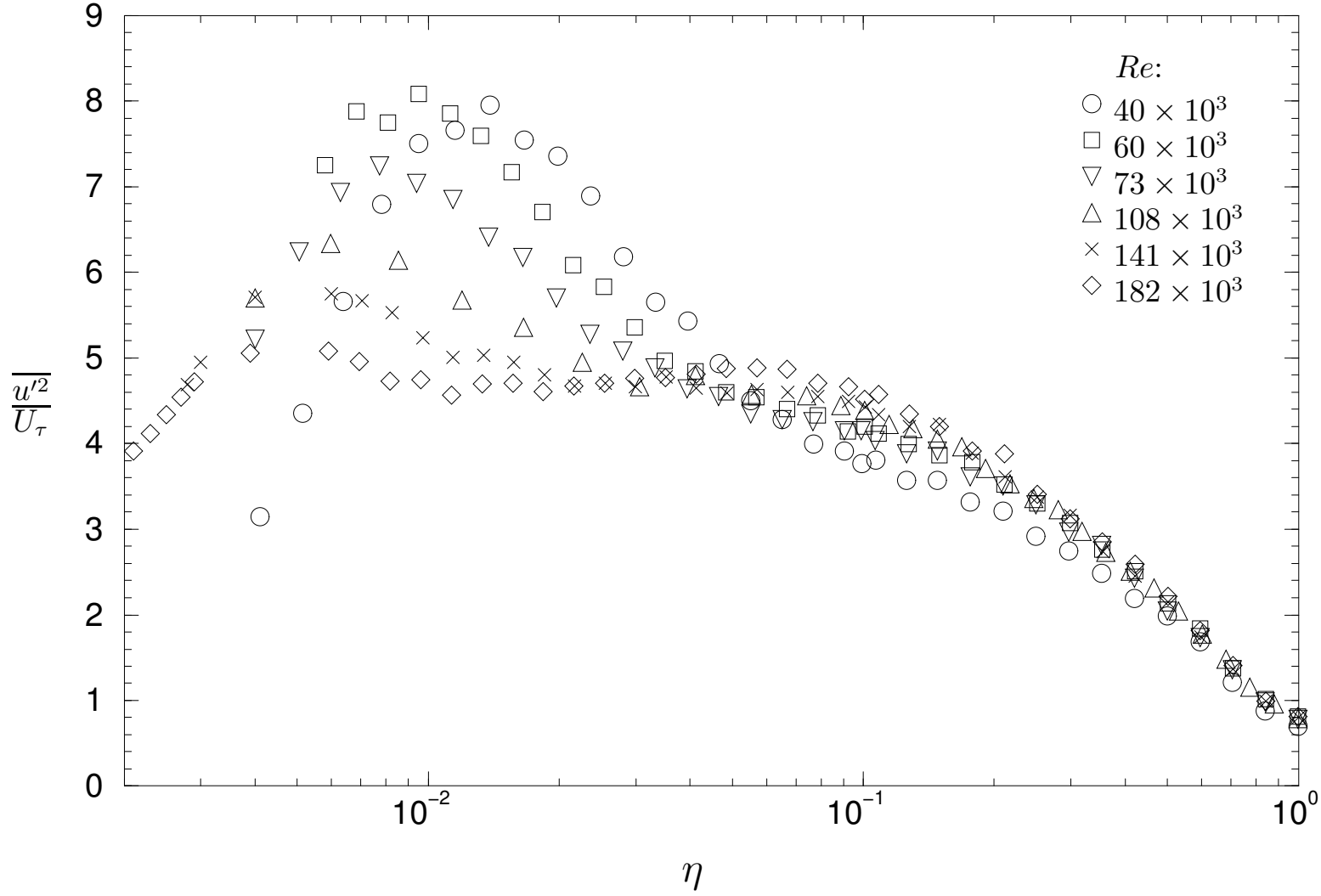

Figure 6.5: Channel flow: streamwise turbulence intensity profiles with outer flow scaling.

6.2.3 Streamwise turbulence intensity formulation

In Chapter 2, during the introduction of the attached eddy hypothesis, a formulation for streamwise turbulence intensity in the turbulent wall region was discussed. The attached eddy model and the contributions of each eddy, discussed in §6.1 above, can be shown to predict

$$\frac{\overline{u'^2}}{U_\tau^2} = B_1 - A_1 \ln[\eta] - V(y^+), \tag{6.1}$$

where A_1 is a universal constant and B_1 depends only on large scale geometry. The last term is an isotropic viscous correction term and more details of its origin are given in Perry & Li (1990). This formulation, applicable to the turbulent wall region only, was extended to the entire outer flow region by Marusic *et al.* (1997). Their new $\overline{u'^2}$ formulation is given by

$$\frac{\overline{u'^2}}{U_\tau^2} = B_1[\Pi_c] - A_1 \ln[\eta] - V_g[y^+, \eta] - W_g[\eta]. \tag{6.2}$$

V_g is an extended viscous correction term which includes the function $V(y^+)$ and should be universal. The exact form of V_g is rather complicated and is not repeated here; it can be found in Marusic *et al.* (1997). W_g is an outer flow function which depends on large scale geometry, similar to the wake component of the law of the wall, law of the wake (2.14). It was defined by Marusic *et al.* (1997) as

$$W_g[\eta] = B_1\eta^2(3 - 2\eta) - A_1\eta^2(1 - \eta)(1 - 2\eta). \tag{6.3}$$

This function was chosen to give the correct boundary conditions for the streamwise turbulence intensity of a boundary layer. For duct flows, the Dirichlet boundary condition, $\overline{u'^2} = 0$ at $\eta = 1$, is invalid since the flow is turbulent at all wall-distances. Thus, the form of W_g should be

$$W_g[\eta] = (B_1 - B_d)\eta^2(3 - 2\eta) - A_1\eta^2(1 - \eta)(1 - 2\eta), \tag{6.4}$$

where,

$$B_d = \left.\frac{\overline{u'^2}}{U_\tau^2}\right|_{\eta=1} \approx \begin{cases} 0.8 & \text{for channel flow,} \\ 0.7 & \text{for pipe flow.} \end{cases}$$

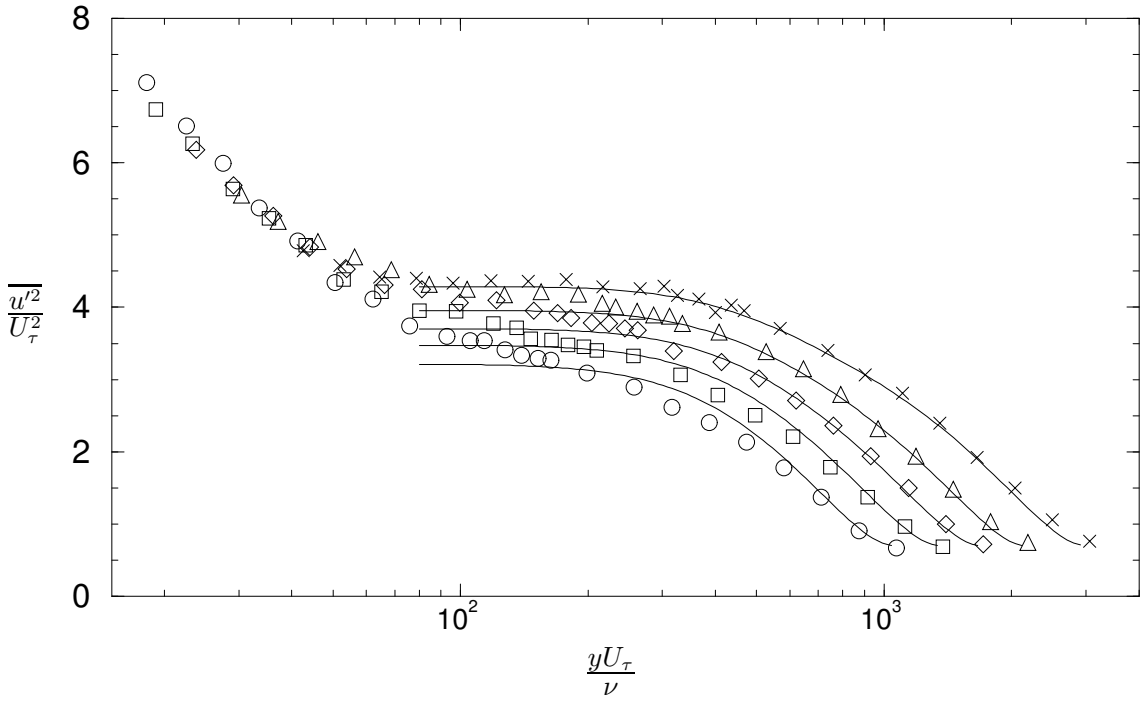

Figure 6.6: Pipe flow: $\overline{u'^2}$ formulation with inner scaling.

The values of B_d were estimated from the data presented in this thesis. Note that B_d should not be Re dependent, only large scale dependent. From the discussion of §5.5, it might be expected that B_d should be higher for pipe flow than for channel flow due to the larger probability of eddies existing at the pipe centreline. No reasons to explain why this is not observed were found, although further work on the attached eddy hypothesis (beyond that discussed in §5.5) may help resolve this anomaly. The second important difference in the $\overline{u'^2}$ prediction, is that the form for B_1 proposed by Hafez (1991),

$$B_1[\Pi] = 0.41 + 3.66\Pi_c - 0.76\Pi_c^2, \tag{6.5}$$

is also invalid for duct flows. It was found that setting $B_1 = 2.20$ for channel flow, and $B_1 = 2.25$ for pipe flow gave best results.

Figures 6.6 & 6.7 show the formulation (6.2) plotted over the measured data with inner flow scaling. For the pipe flow case, all constants and functions used are those suggested by Marusic *et al.* (1997) — apart from B_1, of course. In the channel flow case, setting $A_1 = 1.03$ did not give such a good fit to the data. It was found that a value of $A_1 = 1.10$ provided a much better result (this is the value used in figure 6.7). The fit to the data of the funtional form is undoubtedly excellent for all

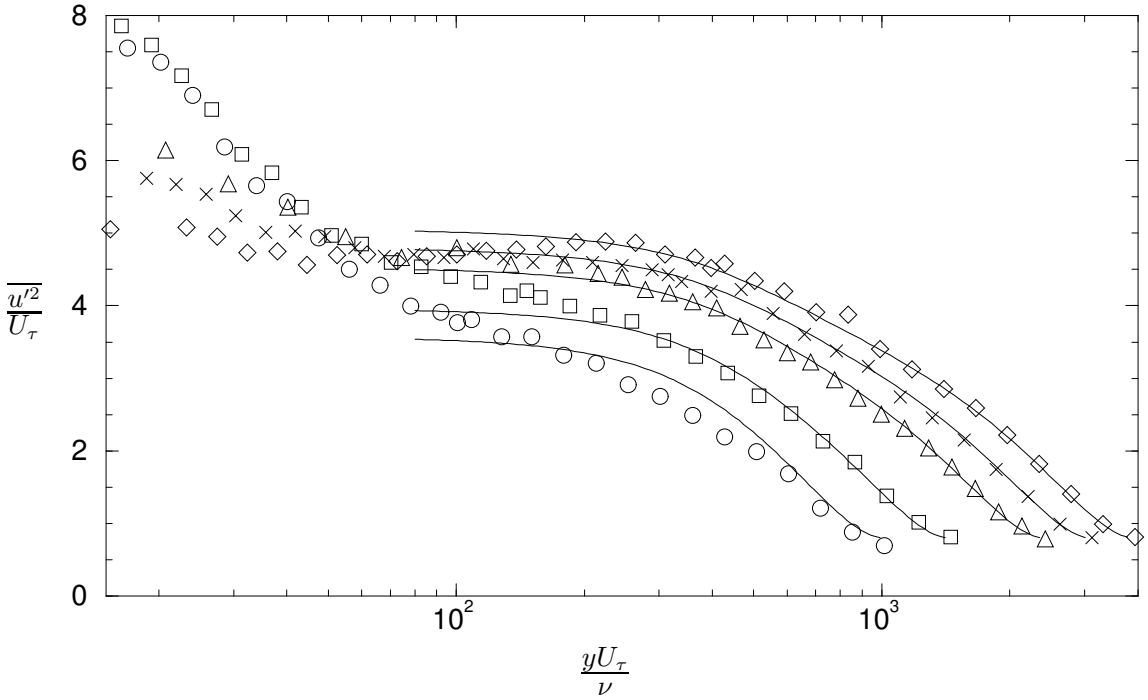

Figure 6.7: Channel flow: $\overline{u'^2}$ formulation plotted over the data with inner scaling.

higher Re. Finally, figure 6.8 is provided which displays the same data as figure 6.7 but with outer flow scaling. This plot clearly shows the outer flow similarity and the increased extent of this similarity with increasing Re.

The observed collapse of the data onto the $\overline{u'^2}$ formulation of Marusic *et al.* (1997) provides support not only for the functional form in itself, but also for the attached eddy hypothesis, on which the formulation relies heavily. There are also a number of other assumptions, beyond the scope of this thesis (see Marusic *et al.*, 1997), concerning the physical behaviour of the flow that are validated by the observations of this section.

6.3 Reynolds shear stress

Measurement of the spanwise and normalwise velocity components was achieved using a X-wire as mentioned eariler. The spatial resolution issues discussed above will certainly apply to each wire of the X-wire. Unfortunately for X-wire measurements, there is a further resolution issue due to the spacing between the two wires. For all experiments conducted, the spacing was very close to $1mm$. The effect of these

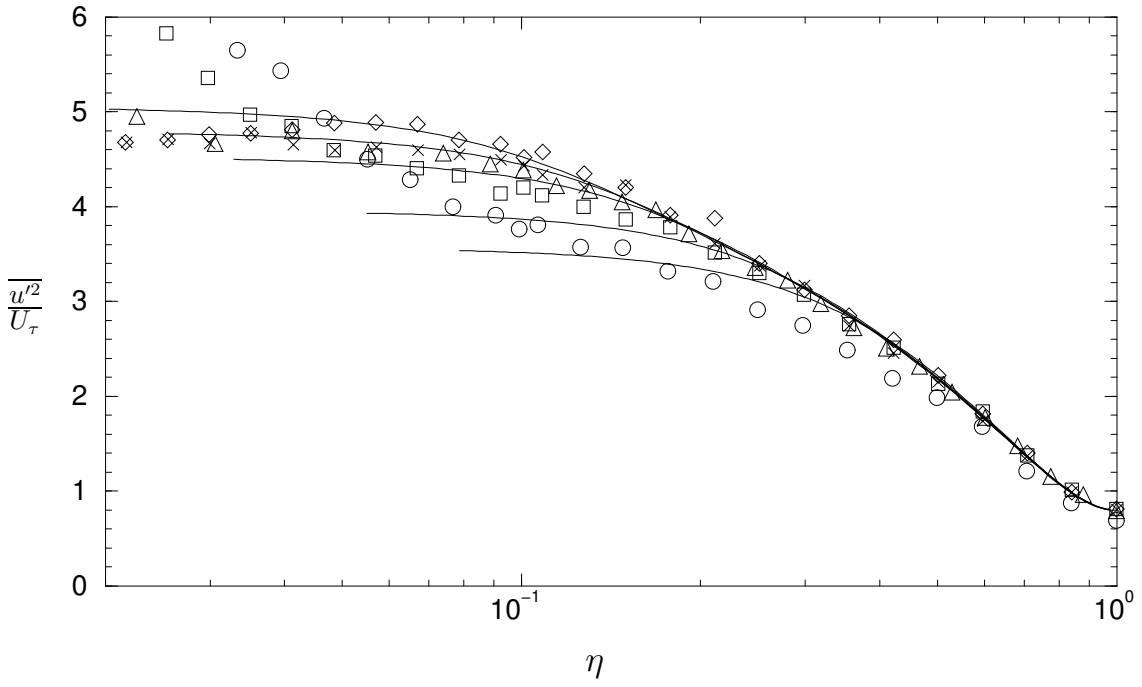

Figure 6.8: Channel flow: $\overline{u'^2}$ formulation plotted over the data with outer scaling.

inevitable errors will be more severe closer to the wall. To obtain an idea of how the X-wire error might behave, it may be useful to plot the correlation of streamwise and spanwise velocity, $\overline{u'w'}/U_\tau^2$. This quantity should, of course, be equal to zero throughout the nominally two-dimensional flow. Figure 6.9 displays the wall-normal variation of $\overline{u'w'}$ with outer flow scaling. The scatter near the wall is clearly evident and reaches a maximum of ± 0.1 ordinate units.

Now, the significant Reynolds shear stress component, $\overline{u'v'}$, has the simple form given by (2.54) for duct flows:

$$-\frac{\overline{u'v'}}{U_\tau^2} = -\eta + 1 - \frac{dU^+}{dy^+}.$$

This equation is found directly from the Navier-Stokes equations by assuming that the flow is fully developed (i.e., all streamwise derivatives are zero). With the expected, and therefore accepted, level of scatter near the wall in mind, the Reynolds stress measurements are presented in figure 6.10 with outer flow scaling. The figure shows that the data follow the expected trends reasonably well. In comparison, the equivalent data of Laufer (1950) and Henbest (1983) display significantly larger deviations from (2.54). In the light of these studies, the measurements shown here appear to be very accurate.

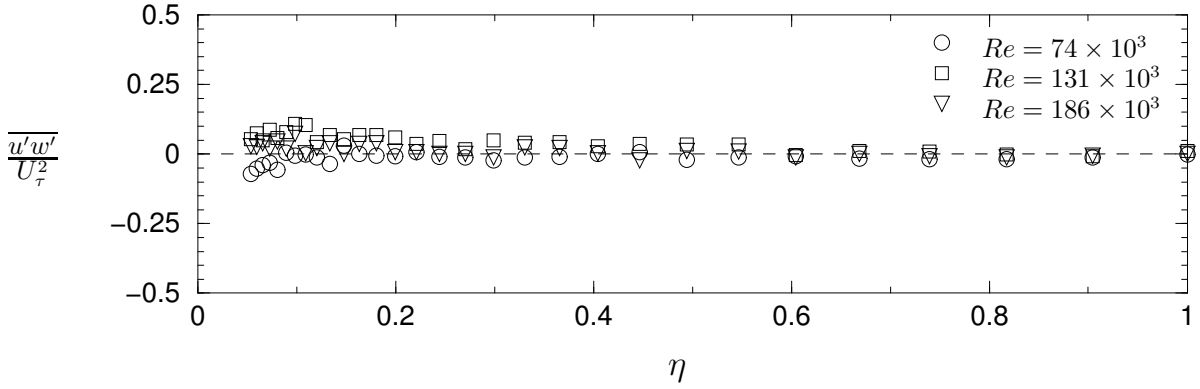

Figure 6.9: Wall-normal distribution of the Reynolds shear stress, $\overline{u'w'}$, with outer flow scaling.

Also included in figure 6.10 are plots of the theoretical stress distribution (2.54) for each profile. The stress distribution is not universal due to the viscous velocity gradient term which will, of course, vary with Karman number. This term was computed by taking the derivative of the mean velocity formulations of: Reichardt (1951) for the sublayer, given by equation (2.19) with $\kappa = 0.39$ and $A = 4.4$; Jones *et al.* (2001a) for the outer flow region, given by equation (2.17) with $\Pi = 0.25$. Figure 6.10 illustrates that the viscous term is almost negligible for most of the flow, even down to the lowest wall-distances at which measurements were taken. It is suggested that the deviation from the theoretical curve near the wall is possibly due to the aforementioned, unavoidable spatial resolution effects.

6.4 Spanwise and normalwise measurements

In a similar manner to the analysis of streamwise turbulence intensity, the forms of the remaining intensities in the turbulent wall region are predicted, by Perry & Li (1990), as

$$\frac{\overline{w'^2}}{U_\tau^2} = B_2 - A_2 \ln[\eta] - V(y^+), \tag{6.6}$$

$$\frac{\overline{v'^2}}{U_\tau^2} = A_3 - V(y^+). \tag{6.7}$$

It is noted that the $\overline{w'^2}$ prediction is identical in form to that for $\overline{u'^2}$ given by equation (6.1). This is expected based on the discussion of the contributions of each eddy

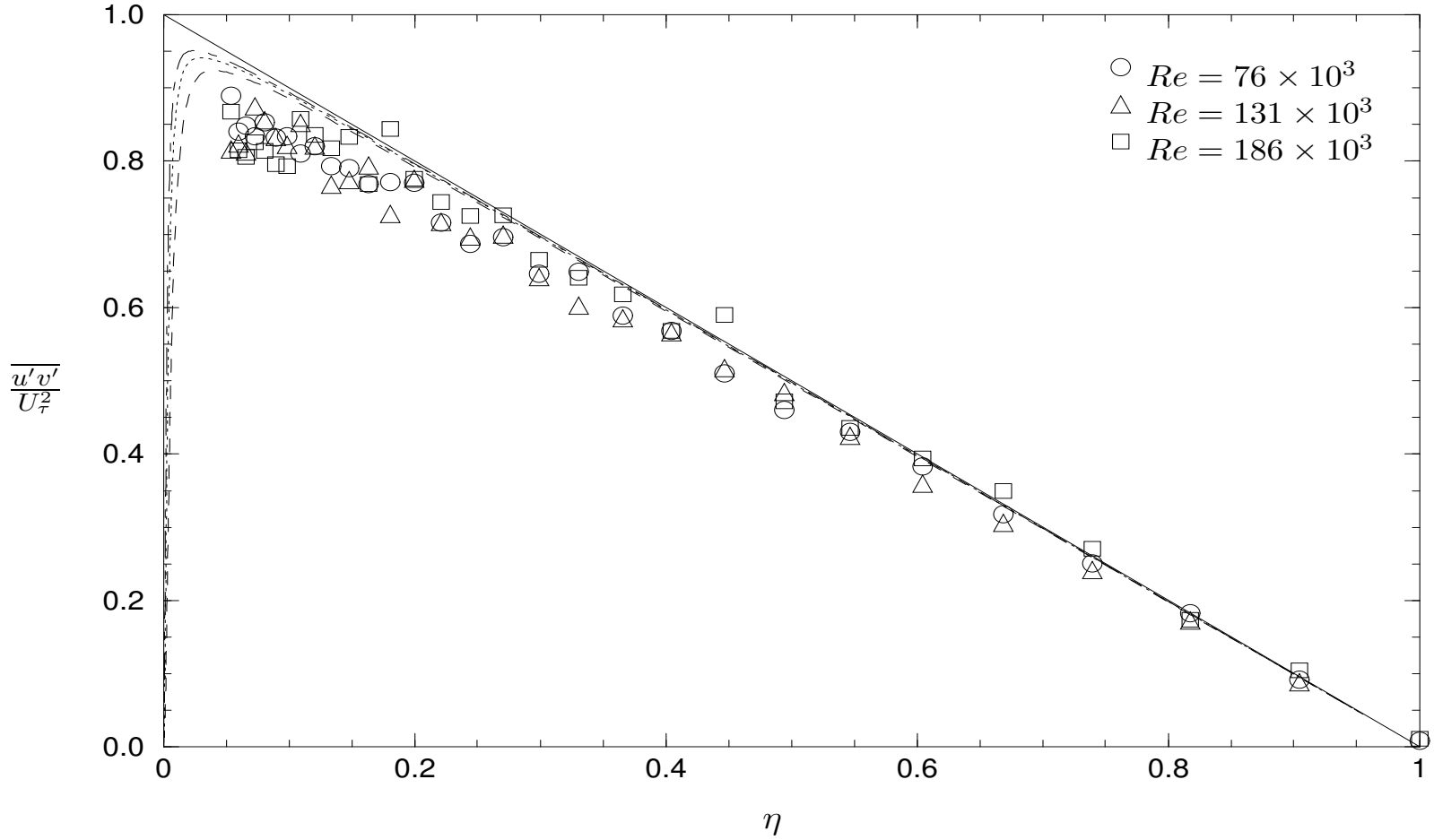

Figure 6.10: Wall-normal distribution of Reynolds stress, $\overline{u'v'}$, with outer flow scaling. The broken lines correspond to equation (2.54) with: ---- , $K_\tau = 1770$; ····· , $K_\tau = 2908$; —·— , $K_\tau = 4159$. These Karman numbers correspond to the flow Reynolds numbers of each profile.

in §6.1. The discussion points out that the same eddies contributing to $\overline{u'^2}$ also contribute to $\overline{w'^2}$. The wall-normal turbulence intensity, however, is expected to behave differently since eddies much larger than the probe wall-distance make no significant contribution to this statistic (see §6.4.2).

The last term in all of the turbulence intensity formulations is the isotropic viscous correction term, $V(y^+)$. Since it is related to the isotropic, Kolmogorov scale motions, $V(y^+)$ is the same in each equation. This viscous correction is required since the predicted intensity functions are only truly applicable for infinite Reynolds number. That is, by subtracting $V(y^+)$, contributions from very high wavenumber motions that do not exist at finite Re are removed. The fact that $V(y^+)$ requires the knowledge of the high wavenumber contributions presents a problem, since measurements in this range are difficult to obtain (recall the aforementioned spatial and temporal resolution issues). From empirical formulations for the streamwise velocity spectrum, Marusic *et al.* (1997) propose†

$$V(y^+) = 4.63 \left[1 - \left(\frac{yU_\tau}{\nu} \right)^{-0.9} \right] \left(\frac{yU_\tau}{\nu} \right)^{-\frac{1}{2}}, \tag{6.8}$$

which will be employed here.

6.4.1 Spanwise turbulence intensity

The spanwise turbulence intensity profiles are presented in figure 6.11 with outer flow scaling on semi-logarithmic axes. The first of the sub-plots of this figure indicates a roughly logarithmic trend in the data for all Re when η is small. This is in agreement with the predicted form of $\overline{w'^2}$ (6.6) in the turbulent wall region. The second sub-plot, figure 6.11b, displays equation (6.6) with the universal constant, $A_2 = 0.475$ suggested by Perry & Li (1990), and $B_2 = 1.00$ (chosen by the author). For the low Re measurements, the agreement appears reasonably good. However, Perry & Li (1990) state that the value of A_2 is not well-known and not necessarily 0.475. In fact, from their review of existing boundary layer and DNS data, Perry & Li (1990) state that A_2 should be "about 0.5". Figure 6.11c displays curves of equation (6.6)

† This reference mistakenly quotes a coefficient of 5.58 in equation (6.8).

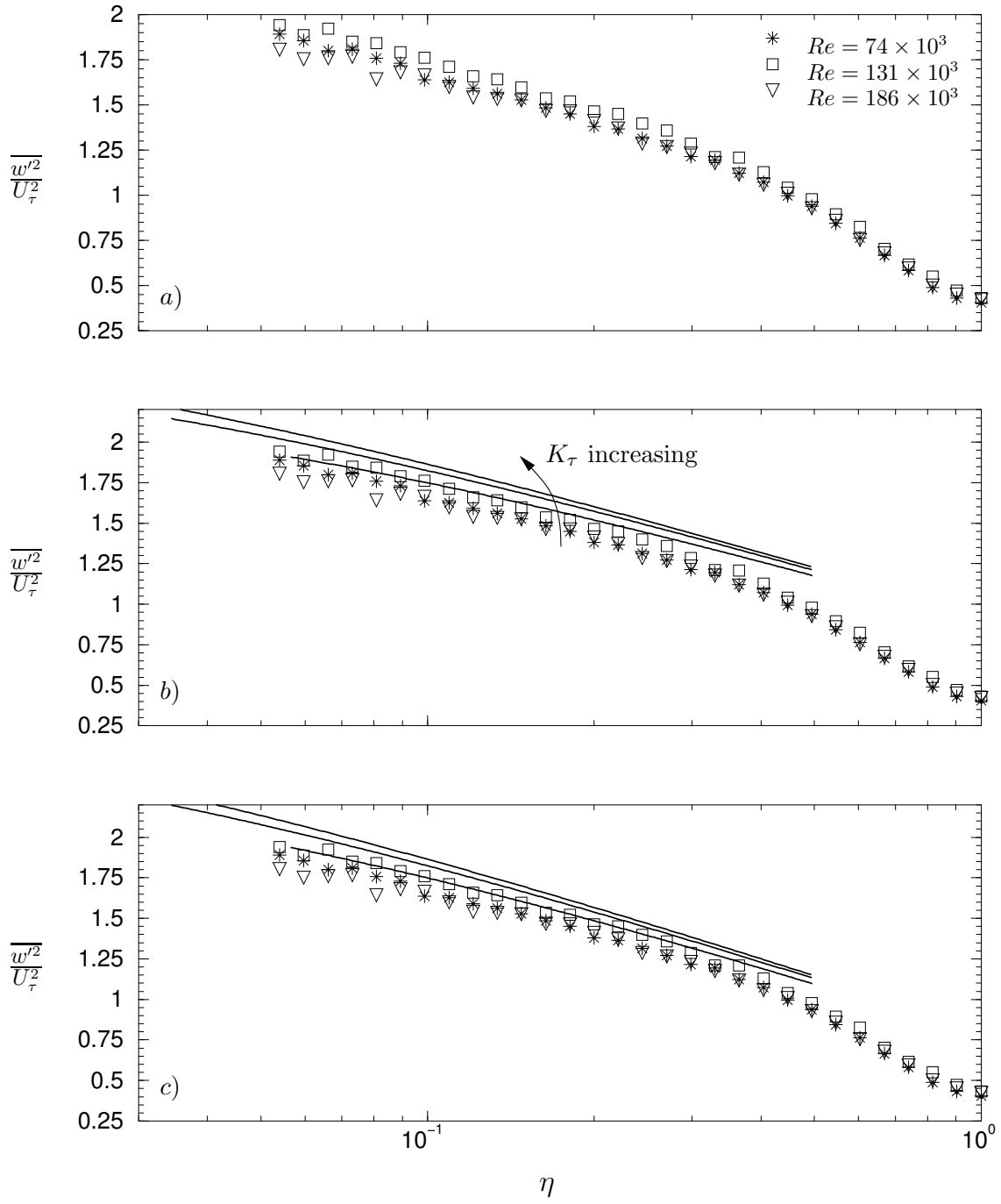

Figure 6.11: a) Wall-normal distribution of spanwise turbulence intensity, $\overline{w'^2}$, with outer flow scaling. The remaining sub-plots feature equation (6.6) overlaid for $K_\tau = 1767, 2904$ and 4011. The constants used in each figure are: b) $A_2 = 0.475$ and $B_2 = 1.00$; c) $A_2 = 0.525$ and $B_2 = 0.885$.

with new constants found to best fit the lowest Re data. The constants found are $A_2 = 0.525$ and $B_2 = 0.885$. Clearly, the fit to the low Re measurements is excellent. It is also clear that improved resolution of the higher Re measurements is needed to permit more extensive conclusions concerning the chosen constants.

6.4.2 Wall-normal turbulence intensity

The normalwise turbulence intensity is displayed in the sub-plots of figure 6.12. The data shown appear to approach a reasonably constant level in the turbulent wall region as the wall is approached. Figure 6.12a also includes three heavy lines representing the predicted intensity (6.7) at the appropriate Karman number (the viscous correction term is Karman number dependent). The constant A_3 in (6.7) is given the value used by Perry & Li (1990) of $A_3 = 1.60$. The predicted curves lie well above the experimental data; even the trends of the predictions and the data are in disagreement. It is unlikely that spatial resolution effects explain such differences. On returning to the calculation of equation (6.7), it was found that Perry & Li (1990) deliberately neglected an extra term. That is, the prediction for $\overline{v'^2}$ should be

$$\frac{\overline{v'^2}}{U_\tau^2} = A_3 - f[\eta] - V(y^+), \tag{6.9}$$

as recognised by Hafez (1991). Now, the new term has the property that $f[\eta] \to 0$ as $\eta \to 0$ and it is dependent on large scale geometry. Perry & Li (1990) assume that $\eta < 0.15$ is sufficiently small to neglect f. A Taylor series expansion of f about $\eta = 0$ reveals that f is a linear function for small η and the predicted turbulence intensity becomes

$$\frac{\overline{v'^2}}{U_\tau^2} = A_3 - B_3[\Pi_c]\eta - V(y^+). \tag{6.10}$$

Hafez (1991) gives a convenient formulation for $B_3[\Pi_c]$, based on his favorable and zero pressure gradient boundary layer measurements:

$$B_3 = 4.134 - 9.651\Pi_c + 8.229\Pi_c^2. \tag{6.11}$$

This gives $B_3 = 3.386$ for channel flow where $\Pi_c \approx 0.083$ ($\Pi = 0.25$). It should be noted that Hafez (1991) found $A_3 = 1.781$ was required if the above formulation for B_3 was employed.

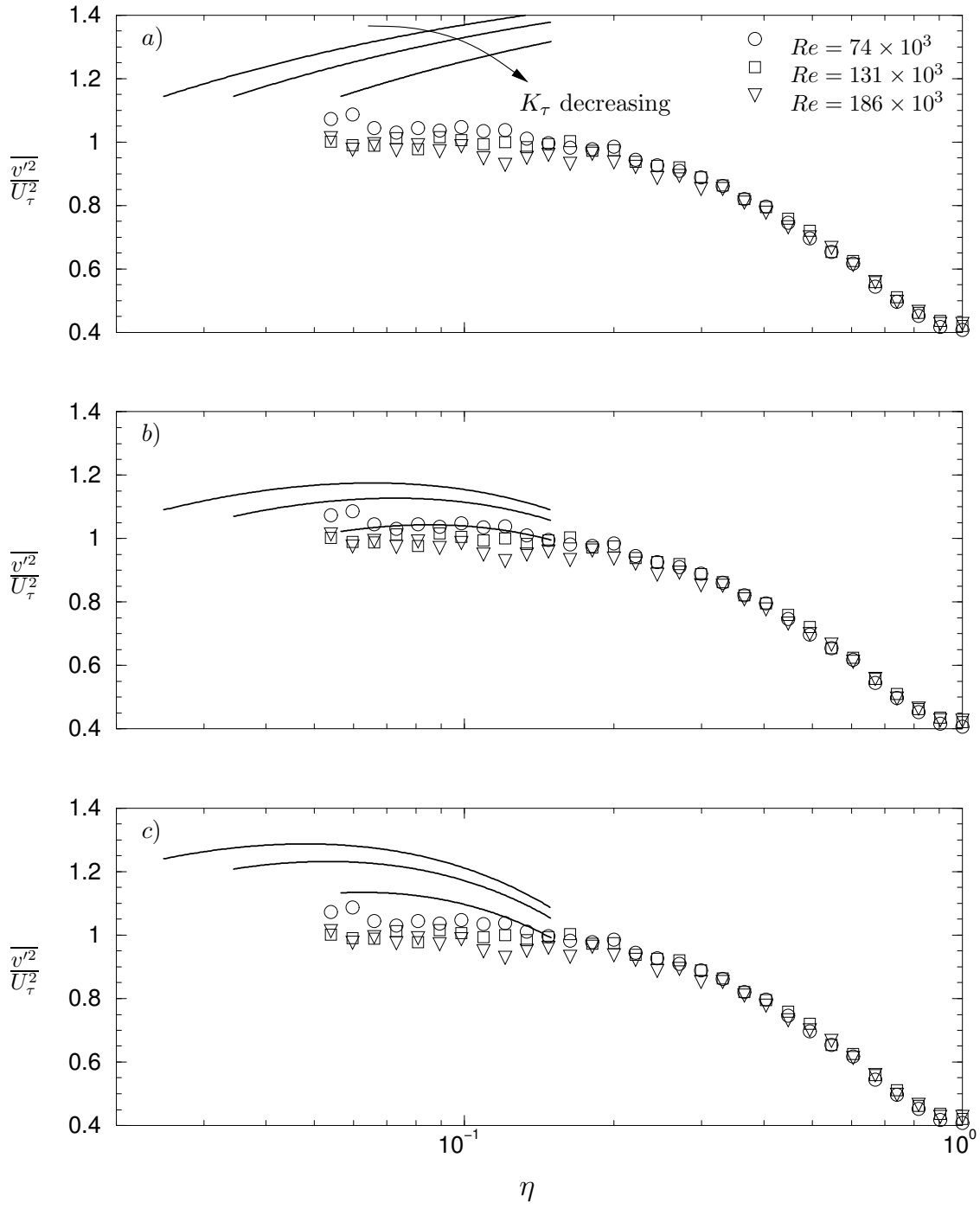

Figure 6.12: Wall-normal distribution of normalwise turbulence intensity, $\overline{v'^2}$. Each sub-plot includes equation (6.10) overlaid for $K_\tau = 1767, 2904$ and 4011. The constants used in each figure are: a) $A_3 = 1.60$ and $B_3 = 0.00$ as suggested by Perry & Li (1990); b) $A_3 = 1.60$ and $B_3 = 2.15$; c) $A_3 = 1.781$ and $B_3 = 3.386$.

Figures 6.12b & 6.12c display the modified $\overline{v'^2}$ prediction (6.10). In figure 6.12c, the curves plotted correspond to those with constants, $B_3 = 3.386$ and $A_3 = 1.781$ (as suggested by Hafez, 1991). The fit to the data is a clear improvement on the Perry & Li (1990) equation and it is possible that spatial resolution effects could account for the near-wall peel off of the data. However, it was noted in §6.2.3 above, that the large scale dependent constant B_1 for channel flow in the $\overline{u'^2}$ prediction (6.1) did not follow the form found for boundary layers. This gives rise to the possibility of equation (6.11) also being inappropriate for channel flow. For this reason, figure 6.12b is provided which displays equation (6.10) with the universal constant of Perry & Li (1990), $A_3 = 1.60$ and $B_3 = 2.15$. The latter constant was simply chosen to fit the lowest Re curve; this assumes spatial resolution effects are small for the lowest Re. It is suggested that this assumption is most likely inaccurate so that a slightly smaller value of B_3 is probably more correct. Nevertheless, the *trends* in the data are best accounted for by the modified $\overline{v'^2}$ prediction shown in figure 6.12b with $A_3 = 1.60$ and $B_3 = 2.15$.

Finally, it is interesting to note the similarities between the measurements presented in figure 6.12 and those of the pipe flow study by Henbest (1983). Both sets of measurements are qualitatively identical in that they have almost constant levels ($\overline{v'^2} \approx U_\tau^2$) near the wall. The only discrepancy of note is the behaviour near the duct centreline. It was postulated in §5.5.2 that a greater number of eddies contribute to the outer flow region of a pipe than a channel flow. This gives a possible reason for the higher $\overline{v'^2}$ in the vicinity of the centerline of Henbest's pipe. That is, more eddies possibly contribute to $\overline{v'^2}$ near the centreline of a pipe than a channel flow.

Chapter 7

Auto-correlation

Of all the analyses of wall-bounded turbulence data presented in the literature to date, the auto-correlation coefficient appears to be one of the simplest measurements that is frequently overlooked. Indeed, the author himself (perhaps influenced by the lack of published data) anticipated little success before the analysis presented in this chapter was conducted. The reason for the apparent lack of interest in auto-correlation could be that its behaviour has, in the past, been difficult to interpret. Recent DNS and PIV studies, however, have provided new information concerning cohesive features of wall-bounded shear layers. It will be shown here that the auto-correlation coefficients can provide useful information about the streamwise cohesion of structures in the flow. Measurements at different wall-normal coordinates shed light on how cohesive features of the flow vary through the shear layer. Additionally, it is well-documented (see Hinze, 1959) that the taylor microscale, λ, and integral length scale, $\mathcal{L}$, can be computed from the auto-correlation coefficient.

The frozen turbulence hypothesis of Taylor (1938) will be invoked in this chapter to convert auto-correlations from the temporal to the spatial domain. As previously stated, the convection velocity required for Taylor's hypothesis is assumed to be $U_c = 0.82U_{CL}$ in this thesis, after Uddin (1994). Due to the implication of Sternberg (1967) that the convection velocity should be a characteristic velocity of the shear layer, it might be expected that $U_c = U_b$. Figure 7.1 shows that the bulk and centreline velocities in the channel share a strong linear relationship, with

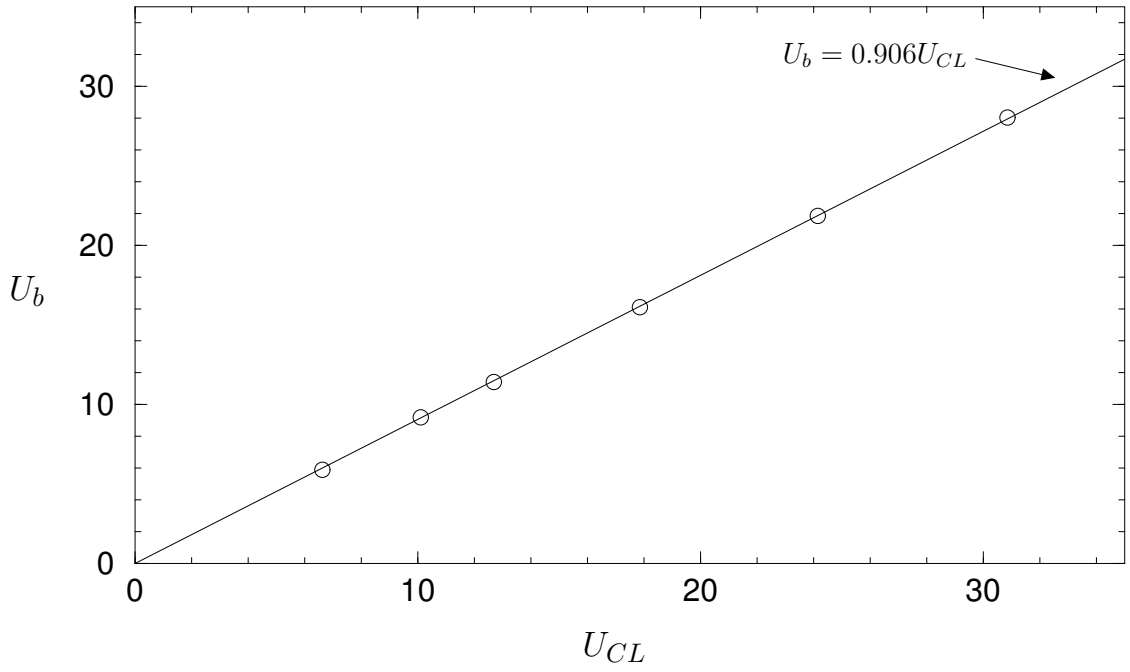

Figure 7.1: Variation of bulk velocity with centreline velocity. Note that the units of both axes are ms^{-1}.

$U_b = 0.906U_{CL}$. Based on the literature review presented in §2.10 it would appear that a convection velocity of the magnitude of U_b would be too large for boundary layer flows. It could be argued that this value is appropriate for fully developed duct flows; however, the important point here is that a constant convection velocity is employed as opposed to a velocity variant with y. Whether this constant is U_b or $0.82U_{CL}$ is of little consequence as evidenced by the following discussion of results.

7.1 Auto-correlation measurements

The auto-correlation coefficient, $R_{11}(x_0)$, defined by equation (2.56) with application of Taylor's hypothesis, was computed for 12 levels of $\eta = 2y/h$ at three Re spanning the possible range. The results are plotted in figure 7.2 which consists of three sub-plots; each plot contains correlation curves at only four η values (levels) for clarity. Note that results are shown only for the intermediate Reynolds number (105×10^3) for brevity. Coefficients for higher and lower Re are reserved for Appendix H. In regard to the omitted data, it is sufficient to note that the general behaviour of $R_{11}(x_0)$ is similar for all Re; the extent of this similarity will be discussed later in this section.

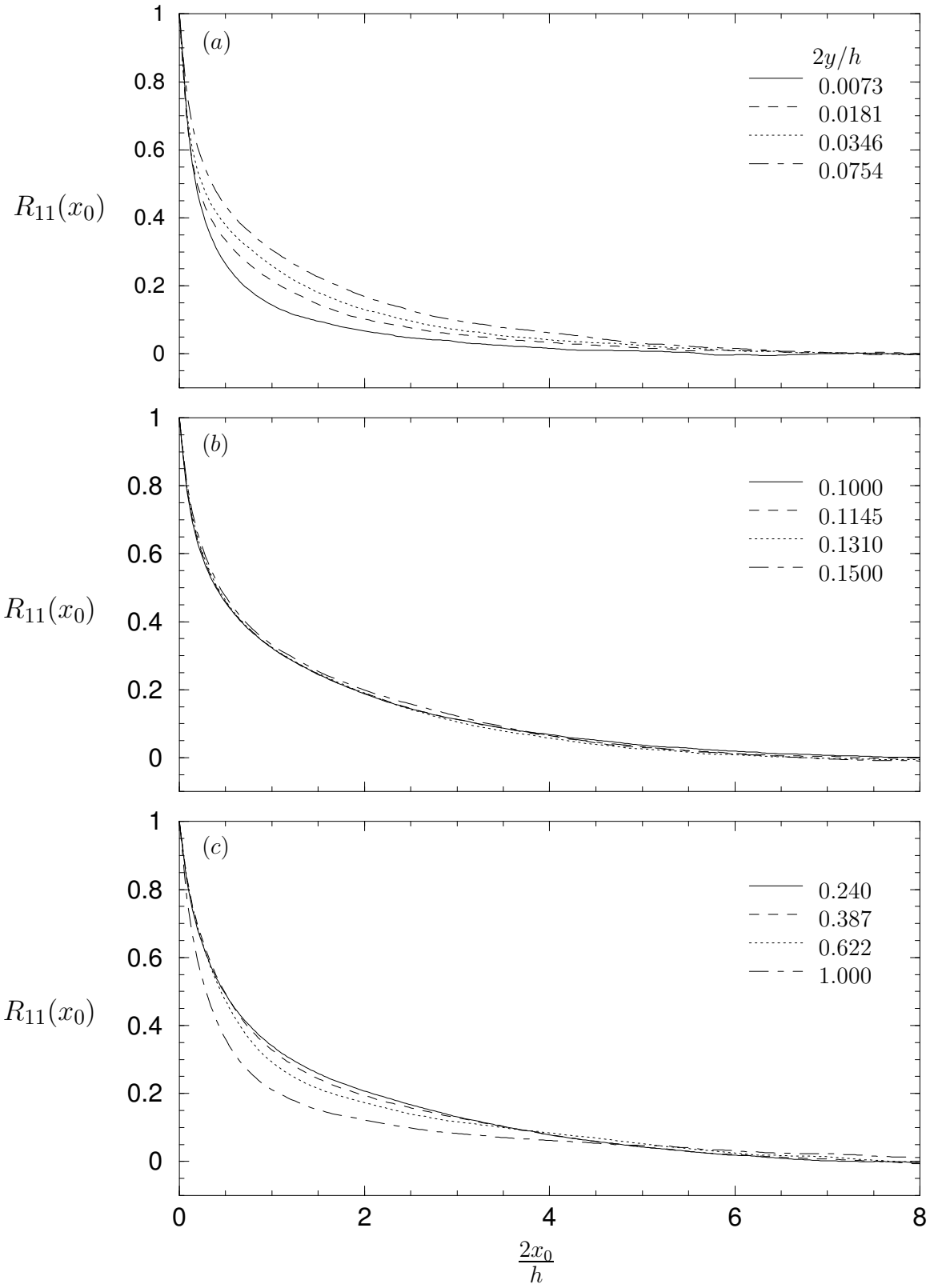

Figure 7.2: Channel flow auto-correlation coefficient at 12 wall-normal levels for $Re = 105 \times 10^3$. Similar plots for other Reynolds numbers are included in Appendix H.

Figure 7.2a displays the expected trends in R_{11} as η increases. Very close to the wall, the correlation decays relatively rapidly with increasing separation x_0. The rate of decay is seen to decrease as the probe traverses through the viscous sublayer ($\eta = 0.0073$ and 0.0754 correspond to $y^+ = 18$ and 181 respectively). This trend indicates that the characteristic size of the largest cohesive structures in the flow increases with distance from the wall. This is not unexpected and is consistent with the attached eddy hypothesis (i.e., sizes of the dominant eddies scale with distance from the wall). For comparison with attached eddy hypothesis predictions, figure 7.3 is included. This figure was taken from Uddin (1994) as there was insufficient time for the author to complete the difficult task of generating his own attached eddy model data. Uddin (1994) computed the auto-correlation profiles using simple Π-eddies inclined at 45^o with core radius, $r_0 = 0.05\delta$. Note that Δ is the largest eddy size and should be interpreted as the channel half-height, $h/2$, where channel flow is concerned.

Returning to figure 7.2 and examining 7.2b reveals that the correlation decay with x_0 does not change as the probe is traversed through the overlap region ($\eta = 0.10$ and 0.15 correspond to $y^+ = 240$ and 361 respectively). This is inconsistent with the attached eddy model, as seen in 7.3b, which shows slower decay of R_{11} curves up to $y/\delta \approx 0.5$); nevertheless it is an interesting result, although the trend is exaggerated due to non-uniform spacing between levels[†] . Finally, figure 7.2c shows that the rate of decay of correlation coefficient begins to increase around $\eta = 0.24$ and this trend continues up to the channel centreline. Interestingly, the correlation never descends below zero. Figure 7.3c shows that negative correlation is predicted near $y/\Delta \approx 1$. However, Uddin's predictions were made for boundary layer flow where the turbulence intensity tends to zero toward the edge of the layer. In this case it is expected that there will be negative correlations as the free stream is approached and experimental data given in Uddin (1994) confirms this[‡] . In a channel flow, as the centreline is approached, the streamwise normal stress does not tend to zero owing

[†] The spacing between levels was kept the same as that employed for spectral measurements where the overlap region was of particular interest.

[‡] Velocity fluctuations are extremely weak near the edge of a boundary layer meaning correlations calculated in this region cannot be considered highly accurate.

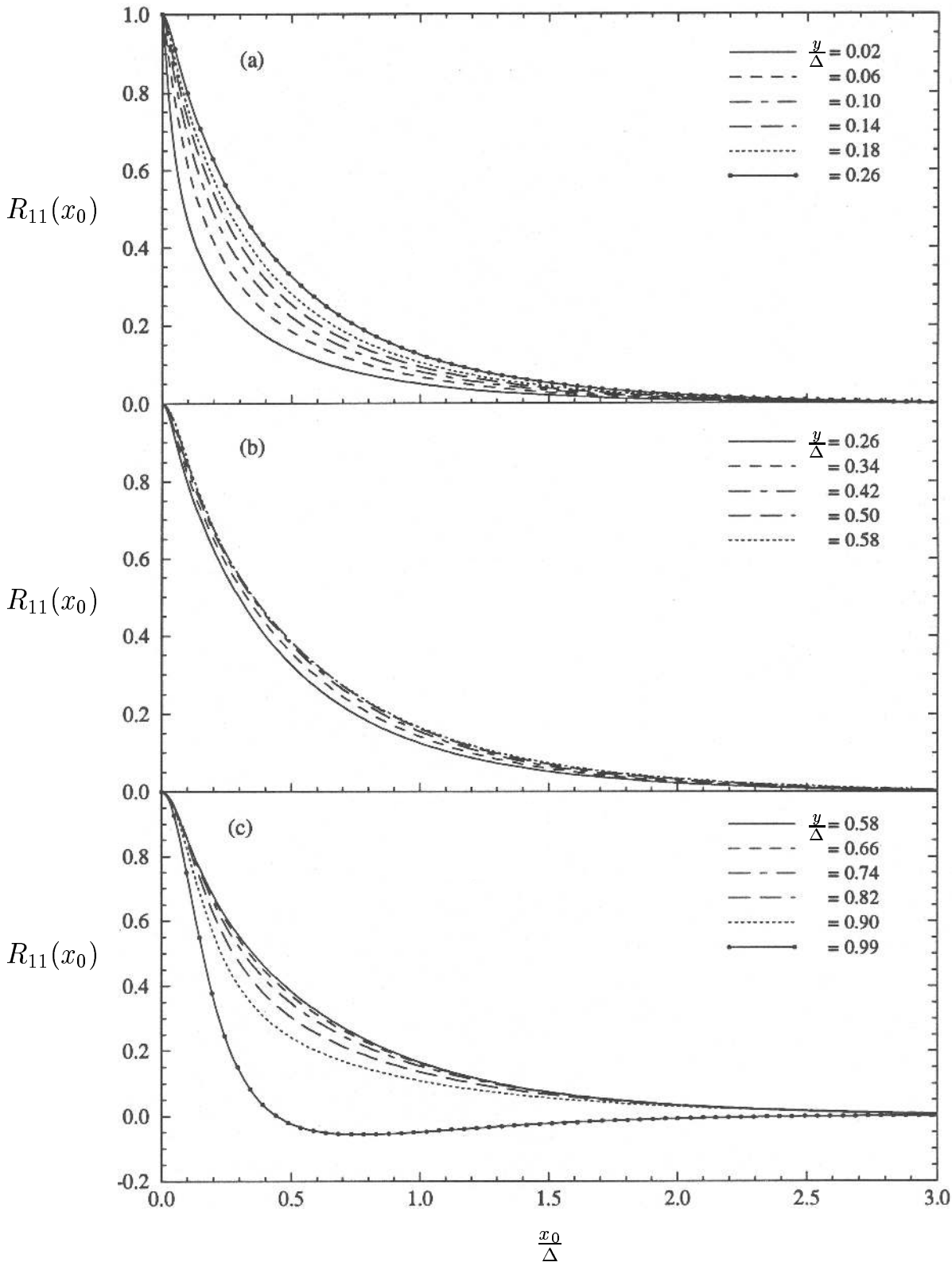

Figure 7.3: Attached eddy hypothesis predictions of auto-correlation coefficient at various levels throughout a turbulent boundary layer. The plot is taken directly from the thesis of Uddin (1994). Δ is the boundary layer thickness.

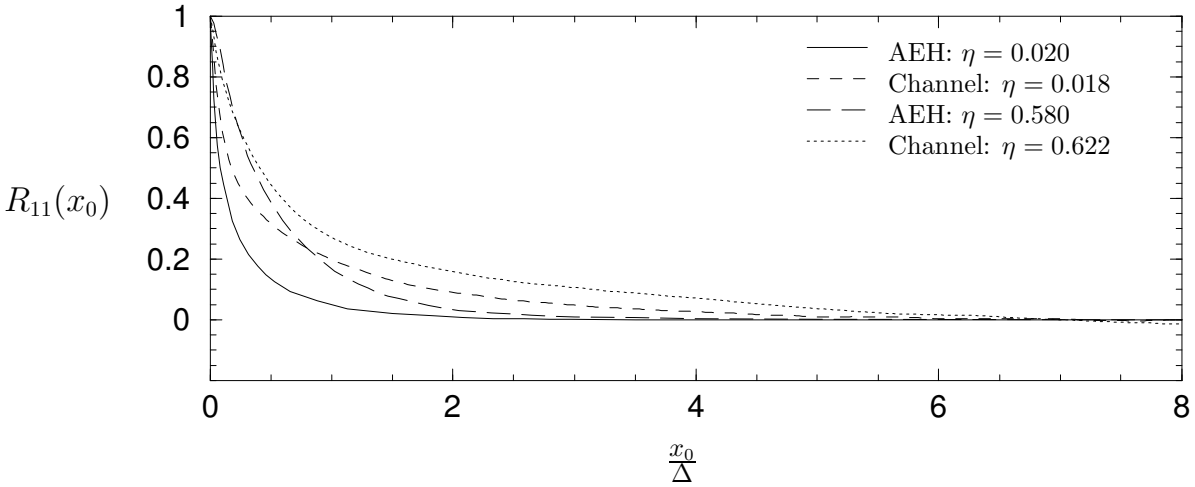

Figure 7.4: Attached eddy hypothesis (AEH) predictions of auto-correlation coefficient compared with channel flow data. The AEH data are taken from Uddin (1994). Note that η is: $2y/h$ for channel flow; y/Δ_E in the AEH.

to the centreline presence of eddies 'attached' to the channel ceiling. Moreover, it can be shown through the attached eddy hypothesis that negative correlation is impossible in fully developed duct flows due to the meeting of eddies from the ceiling and floor (bed) of the channel.

A quick glance at figures 7.2 and 7.3 might give the overall impression that the attached eddy model and the experimental data agree reasonably well. However, plotting the predictions together with the data indicates very poor quantitative agreement. Figure 7.4 presents measured auto-correlation coefficients for two channel levels compared with the attached eddy model predictions given by Uddin (1994) at similar levels. Both near the wall and near the centreline, the predicted auto-correlation is far less for large separations than the experimental data. Note that this is not the same trend observed in boundary layer flows. Data provided in Uddin (1994) displays similarly poor agreement with predictions near the wall, while quite good agreement is found away from the wall (i.e., $y/\Delta > 0.3$).

Keeping the disagreement with the attached eddy model in mind, further observation of figure 7.2a reveals that the correlation of velocity does not become negligible until separations of approximately 4-6 channel half-heights. This presents an anomoly since the characteristic heights of the largest eddies in the flow cannot exceed the channel half-height. So either the eddy inclination angle is extremely small (i.e.,

much less than the commonly postulated 45^o, which was used in Uddin's model) or there is some streamwise coherency between individual eddies. The former is inconceivable given the measurements of Uddin (1994) who shows the eddy inclination angle *is* smaller than 45^o near the wall, but not nearly small enough to explain the trends of figure 7.2a. The suggestion of streamwise coherency of eddies is much more plausible and warrants further discussion here.

Recent experimental (Adrian *et al.*, 2000) and numerical studies (Zhou *et al.*, 1999) have confirmed the existence of spatially coherent 'packets' of vortex structures in wall-bounded shear flows. Marusic, who most recently developed the attached eddy model (see Marusic & Perry, 1995), took note of these studies and incorporated their findings into the model. Marusic (2001) shows that the attached eddy model gives very good quantitative predictions of the near wall correlation when coherent streamwise packets of eddies are substituted for the assumed random distribution of individual eddies. This encouraging result gives further support to the attached eddy hypothesis, however, extended analysis seems to be required to explain the channel flow correlation behaviour in the outer flow region.

In this new attached eddy model, Marusic (2001) reverts to the assumption of randomly distributed eddies for those *large* eddies with length scale exceeding 0.35Δ. This assumption concerning large scale behaviour is supported by measurements of Adrian *et al.* (2000) and Ganapathisubramani *et al.* (2003). These references show that coherent packets of eddies break down beyond the near-wall region of a boundary layer. In the case of channel flow, however, it would appear from the auto-correlation measurements of figure 7.2, that considerable spatial coherency persists much further into the shear layer. That is, packets with much larger eddies than 0.3Δ may exist in a channel flow. While it is observed that beyond the overlap region the extent of coherency (i.e., the characteristic streamwise length of the largest packets) certainly ceases to increase, the correlation curves in this region decay much more slowly than those of a turbulent boundary layer. Furthermore, the decay to negligible correlation occurs at separations of over 4–5 channel half-heights until $\eta = 0.622$. This would suggest that coherent packets of eddies exist well into the outer flow region for channel flow. Incorporating this finding into the modified

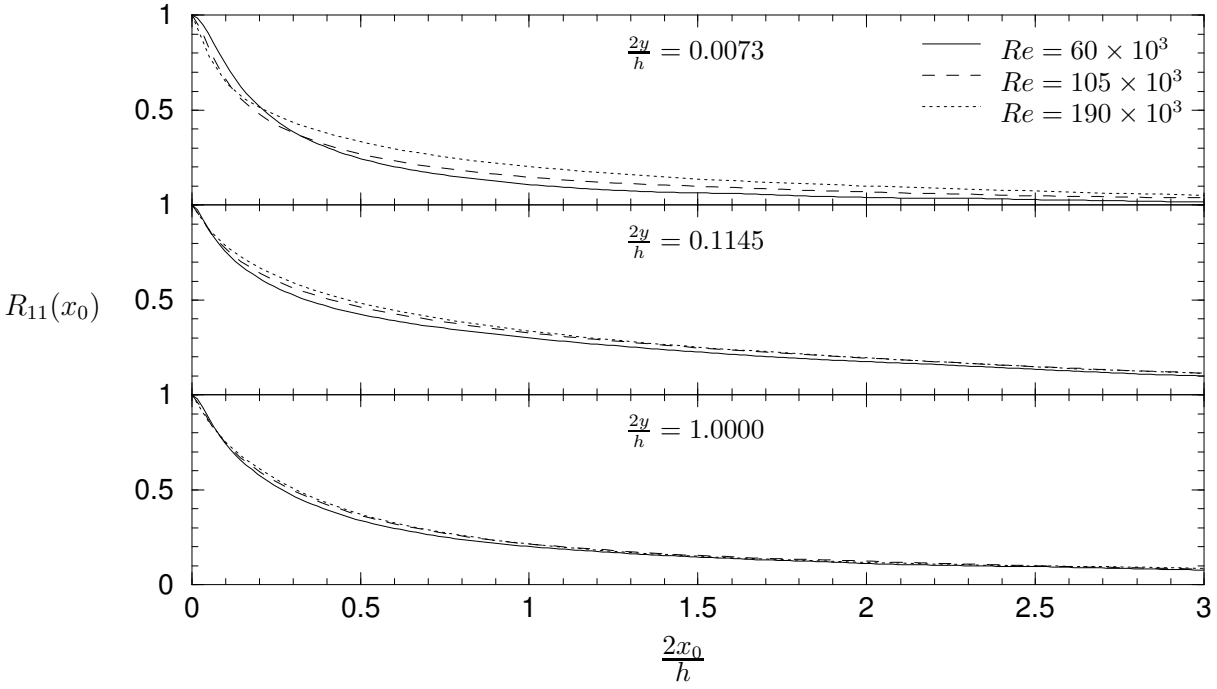

Figure 7.5: The variation of auto-correlation with Reynolds number.

attached eddy model of Marusic (2001) would be an interesting exercise, although it was unfortunately beyond the scope of this thesis. The author expects that the results would give much better agreement with experimental data presented in figure 7.2, as compared with the model results of Uddin (1994). Moreover, it would further establish the attached eddy model as a useful model for turbulent duct flows as well as boundary layers.

7.2 Reynolds number and other effects

The auto-correlation plots for all Re are included in Appendix H. However, figure 7.5 is included here to exemplify the effect of Reynolds number. Three sub-plots, each at different levels in the channel, are presented in this figure. The sub-plots contain $R_{11}(x_0)$ curves at each of the three Re flow cases considered. For all levels the $Re = 60 \times 10^3$ correlation distributions lie below those of the higher Re cases. The two higher Re cases collapse very well at higher levels, while some difference between the two exists very close to the wall. Although there are noticeable differences over the Reynolds number range, the arguments of the preceding subsection (where only the $Re = 105 \times 10^3$ case was considered) remain valid. Furthermore, the arguments

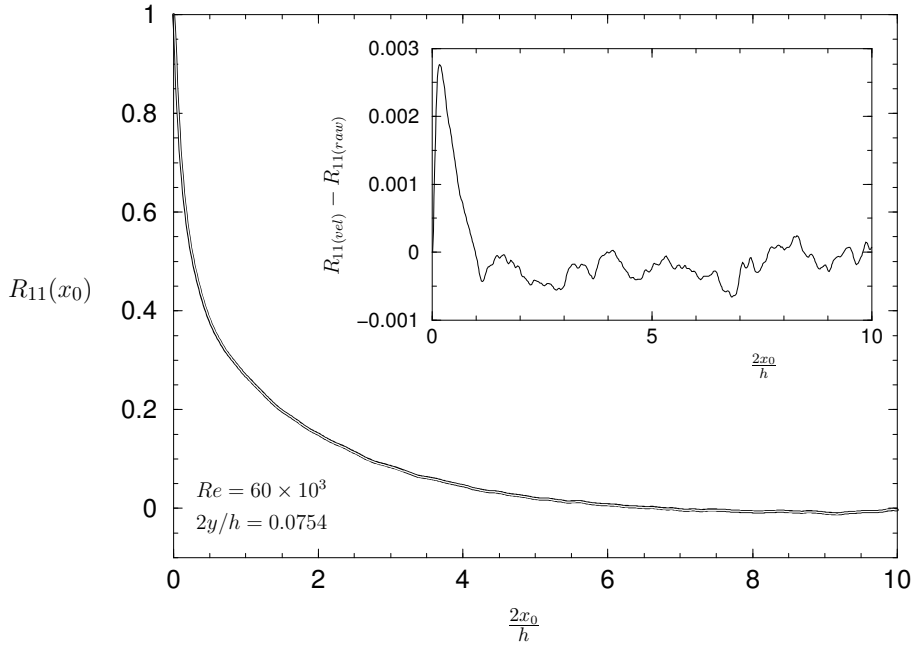

Figure 7.6: Comparison of the auto-correlation of streamwise velocity and raw hot-wire voltage. The latter is plotted in white as it overlaps the correlation of velocity. The inset plot displays the difference between the two curves.

should be consistent throughout and beyond the Reynolds number range.

7.2.1 Experimental and data processing considerations

A common assumption in experimental turbulence measurements employing hot-wire anemometry, is that the auto-correlation of raw hot-wire voltage is equivalent, within acceptable margins, to the correlation of velocity. Li (1989) has shown that differences between the spectrum of streamwise velocity and that of raw hot-wire voltage are negligible. It is therefore to be expected that the auto-correlation (which forms a fourier transform pair with the spectra) should follow the same trend. Since the required data is at hand, a more thorough check on this assumption is found in figure 7.6. Here the auto-correlation of the raw voltage is plotted in white over that of the velocity, since the two curves are virtually indistinguishable. Only auto-correlation at one level (where the turbulence level is relatively high) for one Re is required as the assumption of linearity is in question; the validity of this assumption should not depend on Re or position in the flow. The inset plot of figure 7.6 more clearly illustrates the minute differences between the two correlations.

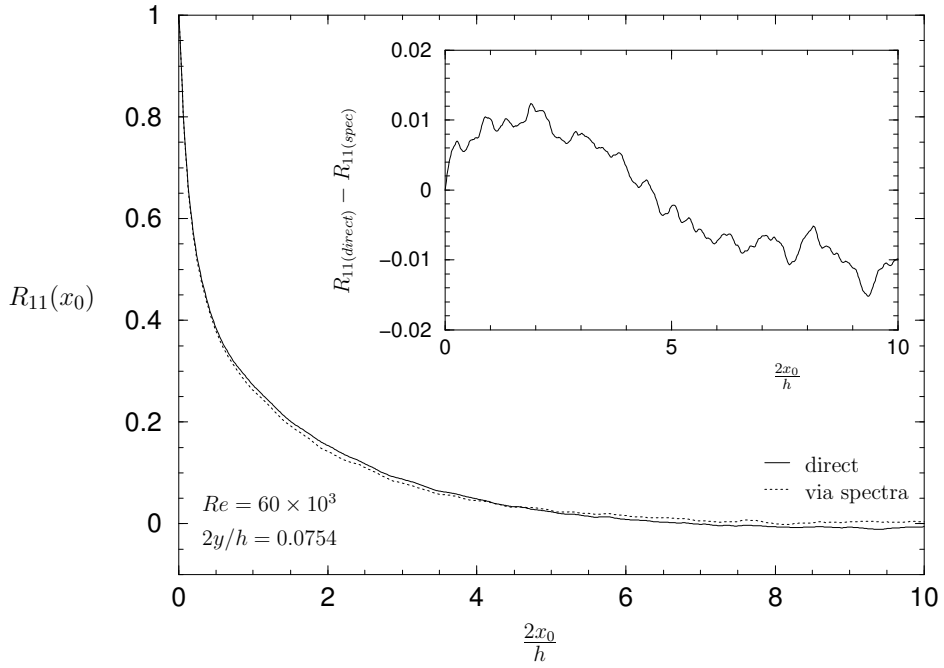

Figure 7.7: Comparison of the auto-correlation of streamwise velocity calculated directly and via spectra. The inset plot displays the difference between the two curves.

Another point of interest to the author was the difference between calculating auto-correlation by the direct method (as applied here) and that obtained from the inverse fourier transform of the streamwise velocity spectra. Uddin (1994) employs the latter method even though it is more complicated and requires more computational steps than the former. Auto-correlations calculated by both methods are shown in figure 7.7. The differences between the two are reasonably large, although the arguments of the preceding section would not be affected by these small differences. The author sees no reason why the auto-correlation calculated through direct multiplication of velocities should not be used; taking the inverse FFT of spectra serves only to introduce error as illustrated in figure 7.7.

7.3 The integral length scale

According to Hinze (1959), the integral time scale, $\mathcal{T}$, "may be considered to be a rough measure of the longest connection in the turbulent behaviour of $u_1(t)$ (streamwise velocity)". Introducing Taylor's frozen turbulence hypothesis, this time scale is easily converted to the integral length scale, $\mathcal{L}$. This length scale may also be

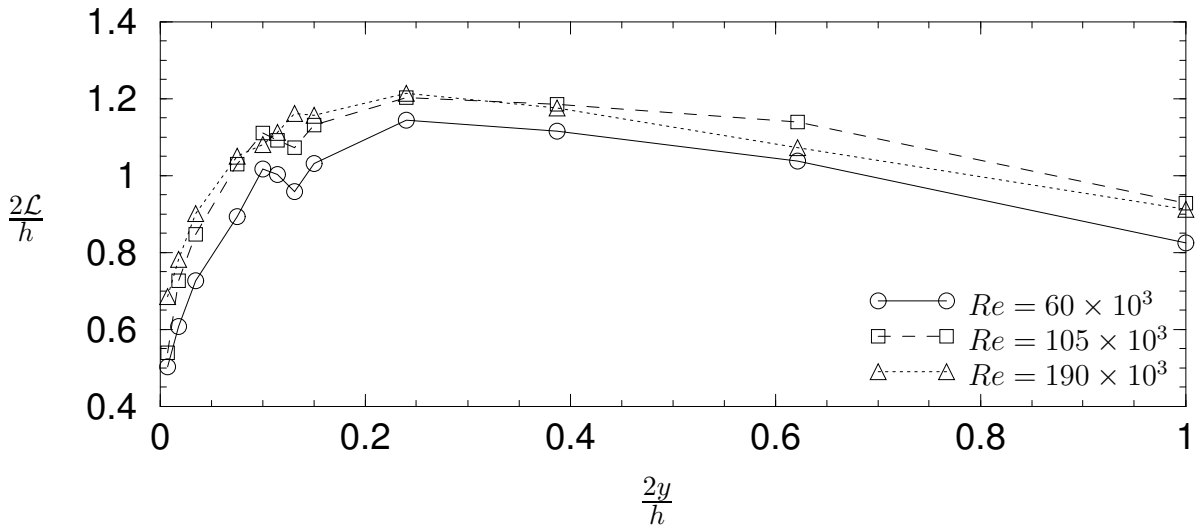

Figure 7.8: The variation of non-dimensionalised integral length scale, $\mathcal{L}$ with non-dimensional wall-distance.

simply defined as the integral of the spatial auto-correlation, that is,

$$\mathcal{L} = \int R_{11}(x_0)dx_0. \tag{7.1}$$

It is emphasised that this length scale is only regarded as an estimate and will clearly be affected by the assumption of Taylor's hypothesis and the selection of convection velocity. Figure 7.8 displays the variation of $\mathcal{L}$ with wall distance (both axes are non-dimensionalised with channel half-height) at three Re. The trends in $\mathcal{L}$ are consistent across the Re range, while the two higher Re curves are of similar magnitude, which is higher than that at the lowest Re. This is not surprising since the same Re trends were observed in the auto-correlation coefficients shown in figure 7.5. The magnitudes of $\mathcal{L}$, however, are somewhat confusing. Marusic (2001) successfully used coherent packets of vortices of streamwise length up to 6.7Δ (equivalent to $6.7h/2$) in his modified attached eddy model; the maximum $\mathcal{L}$ in figure 7.8 is no greater than $1.2h/2$. Now since the modified attached eddy model of Marusic (2001) is shown to predict the auto-correlation coefficient very well in the near-wall region, the large difference between the known largest streamwise length scale and $\mathcal{L}$ must be explained.

The author suggests that the integral length scale is not a physical measure of the largest streamwise length scale in the flow. Just which physical length scale it does represent will be postulated shortly. Figure 7.9 illustrates the definition

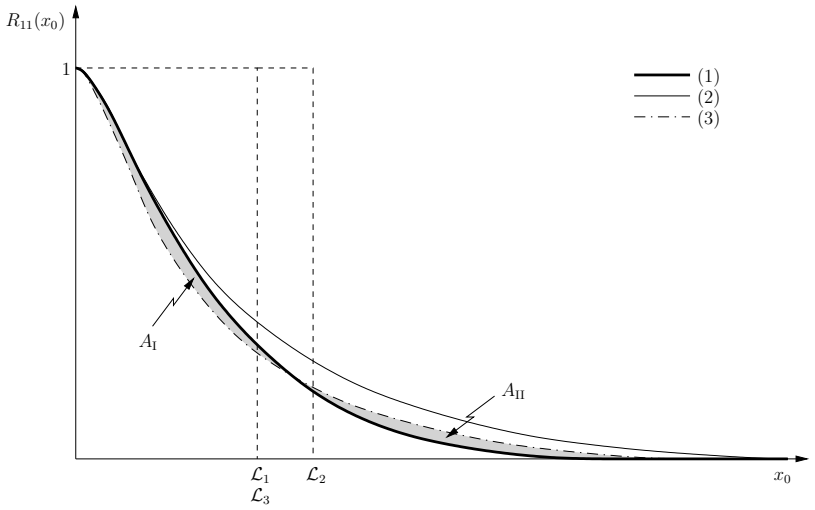

Figure 7.9: An illustration of possible auto-correlation coefficient curves of three different hypothetical flows. Note that $A_{\mathrm{I}} = A_{\mathrm{II}}$.

of the integral length scale for three hypothetical flows. The figure shows that $\mathcal{L}$ is defined such that the area of the rectangle enclosed by the lines $x_0 = \mathcal{L}$ and $R_{11}(x_0) = 1$ is equal to the area under the $R_{11}(x_0)$ curve. The correlation curves for flow cases (1) and (2) (analogous to, say, levels $\eta = 0.0073$ and 0.15) show that slower decay of the correlation curve generally results in an increase in $\mathcal{L}$ (provided the correlation curves for small x_0 are similar). Now consider a flow case where the correlation drops off quickly for small x_0 then decays slowly to zero (flow case 3 in figure 7.9). In comparison with flow case (2): if $A_{\mathrm{I}} = A_{\mathrm{II}}$ then $\mathcal{L}_2 = \mathcal{L}_3$. So, although the largest length scale in the flow has obviously changed, the integral length scales are the same. $\mathcal{L}$ is therefore *not necessarily* indicative of the largest scales in the flow. However, returning to figure 7.2: it is observed that, in general, the auto-correlation curves behave more like flow cases (1) and (2) than (2) and (3). Therefore for wall-bounded turbulent flows, as stated above, $\mathcal{L}$ is generally larger when correlation curves decay less rapidly with x_0. Thus, the behaviour of $\mathcal{L}$ through the channel shown in figure 7.8, while quantitatively irrelevant, qualitatively reflects the behaviour of the largest streamwise coherent structures.

This last statement means that the integral length scale distribution could be used as a guide to the length scales of the eddy packets required for a successful attached eddy simulation. Figure 7.8 indicates that longer streamwise packets are required

as the largest eddy height increases until this height reaches $\approx 0.3\Delta$ as noted in the literature (assuming the characteristic height of the eddies scales with wall distance). Interestingly, this height is about the same as the edge of the overlap region observed in the mean velocity profiles; this suggests a likely relationship between packet existence and logarithmic velocity scaling. For larger scales, however, the required packet size ($\sim \mathcal{L}$) is almost stagnant, decreasing only slightly. This implies that packets do breakdown slightly in the outer region, though not enough to reintroduce the assumption of a random distribution of single eddies. In the turbulent boundary layer, much more rapid decrease in $\mathcal{L}$ is observed as the edge of the layer is approached. Thus, the earlier findings have been confirmed by the distribution of $\mathcal{L}$.

7.4 The Taylor microscale

The Taylor microscale, λ is a rather peculiar length scale in turbulence. It cannot be related to any structures in the flow. Its only use appears to be in isotropic turbulence where it is used to determine the viscous dissipation rate, ϵ; that is,

$$\epsilon = 15\nu\frac{\overline{u^2}}{\lambda^2}. \tag{7.2}$$

In wall-bounded turbulence this equation gives an *estimate* of the dissipation rate since the flow is not truly isotropic; although, for the finer scales, the assumption is arguably permissible. Regardless of its lack of physical relevance, λ is a length scale which is commonly quoted. In this section, λ will not be calculated, rather, some of the limitations of calculating this length scale for wall-bounded turbulent flows are discussed.

The definition of λ is

$$\frac{\overline{u^2}}{\lambda^2} = \overline{\left(\frac{\partial u}{\partial x}\right)^2}. \tag{7.3}$$

To calculate λ directly from this equation first requires calculation of the derivative of velocity with respect to time (for fixed anemometer measurements), then invoking Taylor's hypothesis to determine the spatial velocity gradient. This presents a potential problem for high Reynolds number turbulence research. In high Re

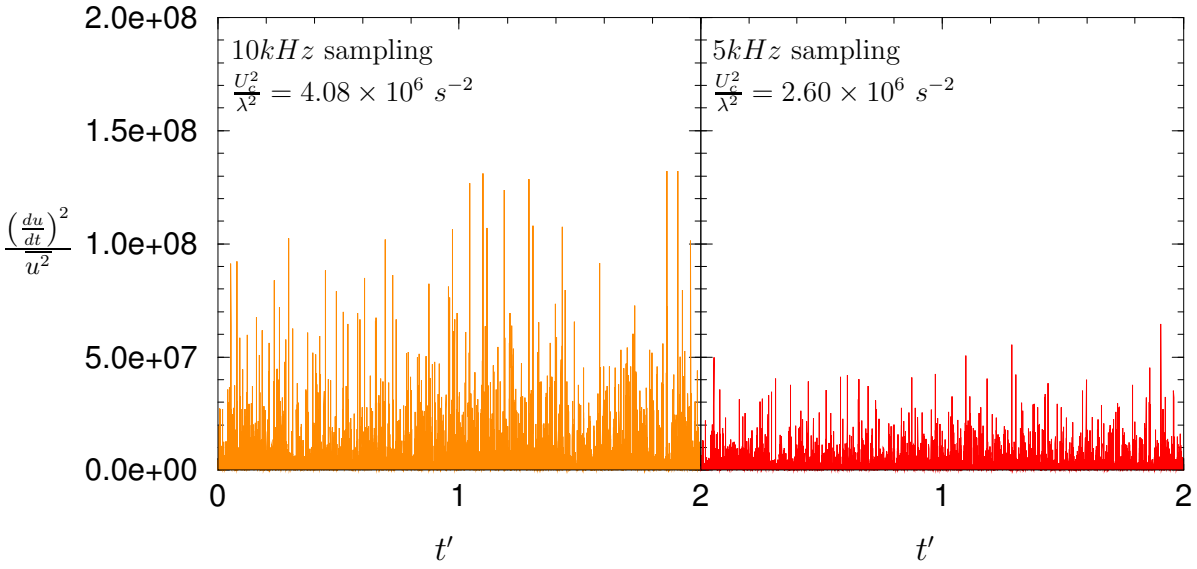

Figure 7.10: Normalised temporal streamwise velocity gradient for high and low sampling rates. U_c^2/λ^2 value given in each plot is the time-average of the normalised gradient.

laboratory facilities, the smallest scales are typically beyond the spatial resolution of the anemometer. Moreover, the highest scale frequencies are often beyond either the maximum sampling frequency or the maximum frequency response of the anemometer (i.e., inadequate temporal resolution). With current technology, temporal resolution should be a rare problem, although it should be noted that these problems would have existed even until the late 20^{th} century. If contributions from *all* the scales are not included, the numerical derivative of velocity at a given point in space/time will be spurious. In fact, it can be shown that the mean gradient of an insufficiently resolved fluctuating velocity trace will always be less than the true value.

The effect of inadequate temporal resolution on the square of the velocity gradient can be easily observed. A velocity trace sampled at $10kHz$ (primarily used to determine auto-correlation coefficient; $Re = 60 \times 10^3$) is used as an example. The velocity trace sampled at $5kHz$ is obtained by simpling dropping every second data point. For the two resulting data sets, the normalised square of the velocity gradient may be calculated. The results are shown in figure 7.10. It should be noted that even the higher sampling rate is insufficient to resolve the flow at this Re so that the two plots of figure 7.10 compare velocity gradients of two unresolved velocity traces. The plots clearly indicate the large attenuation of velocity gradient with

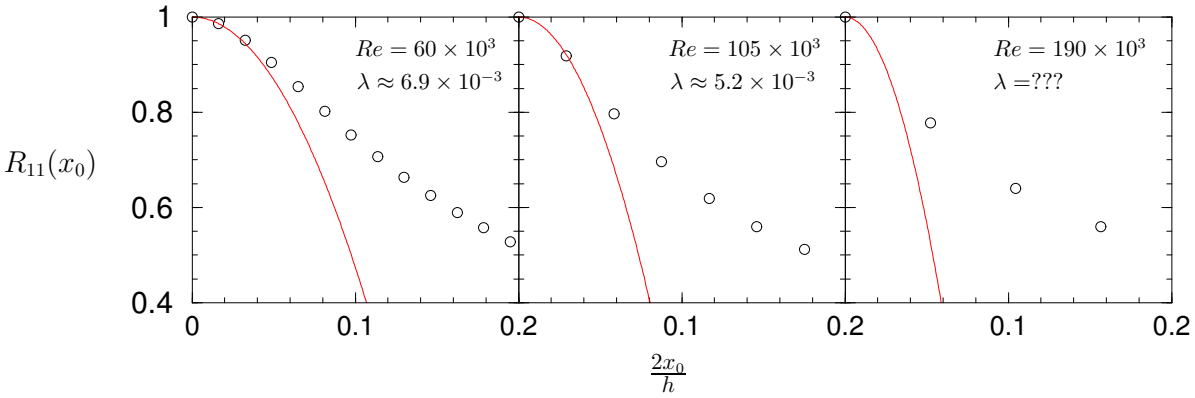

Figure 7.11: Auto-correlation coefficient curves in the vicinity of $2x_0/h = 0$; all curves are at $\eta = 0.0073$ and the units of λ are metres; solid lines are parabolas fitted to points near the origin as described by equation (7.4).

reduced temporal resolution. The plots also include values of the mean normalised gradient (equivalent to U_c^2/λ^2) illustrating the effect of poor resolution on λ. These mean values show that more poorly resolved data results in a higher estimate of the microscale.

A second method commonly used to determine λ originates from a Taylor series expansion of the auto-correlation, $R_{11}(x_0)$ about $x_0 = 0$. It can be shown that

$$R_{11}(x_0) \approx 1 - \frac{x_0^2}{\lambda^2}. \tag{7.4}$$

Therefore a quadratic curve fit to data near $x_0 = 0$ estimates λ. This method is acceptable on the proviso of high temporal resolution. Just how high the sampling rate needs to be is illustrated in figure 7.11. The subplots of figure 7.11 present the auto-correlation coefficient curves in the range $2x_0/h = 0$ – 0.2 for three Re (note that the curves shown are all at the level $\eta = 0.0073$). The temporal resolution is almost acceptable for the lowest Re case only. Clearly, the sampling rates for the higher Re cases are too low and would need to be raised by a factor of at least 3-5 in order to fit equation (7.4) to the data.

It is therefore concluded that any attempt to meaningfully determine λ, and hence ϵ using equation (7.2), is prohibited in this study by lack of temporal resolution. Moreover, for typical laboratory Reynolds numbers, a sampling rate of 10kHz has been shown to under-resolve the streamwise velocity for the purposes of equations (7.3) and (7.4). As suggested earlier, the required sampling rates are commonly

achievable with current data acquisition technology; however, since most turbulence statistics do not require such high sampling rates for convergence, it is common practice to temporally resolve only a limited range of scales. The aim of this short discussion is to highlight the need for greater temporal resolution *if* the Taylor microscale, or indeed any quantity derived from the velocity gradient, is required. Since the author sees no reason that the microscale should contribute to the aims of this thesis, the repeated measurement of velocity traces at higher sampling rates was not deemed appropriate.

Chapter 8

Conclusions

Revisiting the history of duct flow measurements has revealed that many issues are yet to be resolved. It is also evident that progress in fluid mechanics has been relatively slow compared with many other engineering disciplines. With rapidly advancing measurement technology and computational power, however, accurate experimental studies, such as those presented in this thesis, will hopefully increase the rate of progress in this exciting science.

Perhaps one of the most significant outcomes of this project will eventually prove to be the construction of a new experimental apparatus at Melbourne: the fully developed, turbulent channel flow facility. The channel was designed with careful thought, consultation with experts in the field and model testing. Construction was carried out with utmost care and accuracy. Further, many tests were conducted to ensure requirements such as two-dimensionality and uniform flow at the inlet were met. It is hoped that the channel will become a source of further significant contributions to fluid mechanics beyond those made during this investigation.

Measurement of the turbulence statistics in duct flows is a challenging task which needs ongoing development at this stage. The hot-wire anemometer has proven to be a very useful instrument, despite its limitations and difficulties. One of the problems with hot-wire anemometry is the effect of ambient temperature change. This was a significant problem during pipe flow measurements that was eliminated (for the channel study) by the construction of a temperature controlled calibration

tunnel. This facility is another which will hopefully be of use to future workers at the Walter Bassett Aerodynamics Laboratory.

The experimental practice of matching a X-wire through sinusoidal shaking of the probe has previously been accomplished through an electronic matching circuit and a trial-and-error procedure. The matching circuit has been replaced with computer software developed during this investigation. The software eliminates a potentially problematic device from the apparatus, giving one less element to check in the inevitable event of X-wire complications. Moreover, the software gives non-subjective, *optimal* matching.

Before construction of the channel, an existing pipe flow apparatus at Melbourne was studied. Hot-wire and pitot tube measured mean velocity profiles were recorded and compared. It was found that the pitot corrections of MacMillan (1954) and a turbulence intensity correction gave good agreement with the hot-wire data. Further, it was shown from first principles that the turbulence intensity correction *must* be applied to the pitot tube data. From the corrected pitot tube measurements, the law of the wall, law of the wake for the pipe flow was found to be

$$\frac{U}{U_\tau} = \frac{1}{0.386}\ln\left(\frac{yU_\tau}{\nu}\right) + 4.21 - \frac{1}{3\kappa}\eta^3 + \frac{0.908}{\kappa}\eta^2(3-2\eta).$$

A constant cause of concern with the study of nominally two-dimensional channel flow is the effect of the side-walls on the central flow. To alleviate these concerns, extensive spanwise measurements were taken from the side-wall to the central (2-D) flow in the channel. The wall shear stress distributions showed no Reynolds number dependence on the channel bed, while on the side-wall, wall shear stress increased with increasing Re. These measurements give an indication of the extent of two-dimensional flow and help to understand how the flow changes through the channel cross-section. Streamwise velocity profiles, measured normal to the side-walls, were also recorded. The results again provide evidence that rectangular ducts of $A_s > 7.0$ should have a region of two-dimensional flow. Furthermore, the profiles show that the law of the wall applies normal to the centre of the side-wall, even though the surrounding flow is highly three-dimensional.

The development of the flow in the vicinity of the side-walls was also measured

by recording side-wall velocity profiles at various streamwise stations. These were required to settle the debate over whether or not the side-wall affected flow increasingly protudes into the two-dimensional central flow with streamwise distance. The inner flow scaled profiles show little significant change for $L/h \geqslant 100$; the velocity defect plots indicate that the side-wall flow exhibits a very small region that continues to develop until the last measuring station. However, it is clear that the side-wall affected flow reaches a maximum protrusion of approximately $2.9h$ normal to the side-wall (24% of the channel width) for all Reynolds numbers; that is, the side-wall affected flow does not grow indefinitely with streamwise distance.

The above results gave an early indication of full flow development well before the channel exit, although it was known that central flow measurements were needed. During analysis of velocity profiles recorded in the central flow at various streamwise stations, an interesting result was found. The first sign of underdeveloped flow was a seemingly vertical shift in the inner flow scaled profiles, where the velocity scale, U_τ, was taken as the fully developed value. It was found that the shift was the result of changes in local skin friction due to underdevelopment of the flow. By analysing the shift in velocity profiles, it was concluded that flow development in the channel centre was only complete for $L/h \geqslant 130$. This casts doubt on a number of studies claiming full flow development with lengths much less than $130h$. More importantly, this gives a guide for future experimentalists and computationalists as to the length of duct required.

With full flow development at the centre of the channel bed ensured, all measureable turbulence statistics were recorded at the most downstream station, $L/h = 205$. Mean streamwise velocity profiles displayed the well-known channel flow behaviour; that is, the law of the wall applies in the inner flow region, while the channel flow wake is very weak, rising only marginally above the log law. The law of the wall, law of the wake found to effectively describe the mean velocity data, at all Reynolds numbers, for $y^+ \geqslant 100$ was

$$\frac{U}{U_\tau} = \frac{1}{0.389}\ln\left(\frac{yU_\tau}{\nu}\right) + 4.23 - \frac{1}{3\kappa}\eta^3 + \frac{1}{2\kappa}\eta^2(3-2\eta).$$

Comparing this formulation with that of the pipe flow reveals only one significant difference: a difference in the wake parameter, Π, where $\Pi = 0.250$ for channel flow

and 0.454 for pipe flow. A possible reason for this observation was suggested, which essentially postulates that there is a higher probability of large scale attached eddies contributing to the mean flow in a pipe than a channel. To the author's knowledge, this is the first attempt at a physical explanation of the differences between fully developed pipe and channel flow.

Streamwise turbulence intensity measurements were also recorded in both pipe and channel flow. The results show the expected behaviour with no Reynolds number similarity in the inner flow region. Measurements in both facilities show excellent collapse onto the analytical formulation derived from the attached eddy hypothesis. This formulation has previously only been verified for boundary layer flows. It was extended here to duct flows by the addition of a constant to the outer flow term, $W_g[\eta]$, given by

$$W_g[\eta] = (B_1 - B_d)\eta^2(3 - 2\eta) - A_1\eta^2(1 - \eta)(1 - 2\eta),$$

where B_d is the normalised turbulence intensity at the centreline. For pipe flow, the constants found to fit the data were $A_1 = 1.03$, $B_1 = 2.25$ and $B_d = 0.70$; while for channel flow, $A_1 = 1.10$, $B_1 = 2.20$ and $B_d = 0.80$. Spanwise and normalwise turbulence intensity measurements in the channel also displayed good agreement with the attached eddy model predictions. Best fit to the data was given by the following equations for spanwise and normalwise turbulence intensities respectively:

$$\frac{\overline{v'^2}}{U_\tau} = 0.885 - 0.525\ln[\eta] - V(y^+)$$

and

$$\frac{\overline{v'^2}}{U_\tau} = 1.600 - 2.150\eta - V(y^+),$$

Once again, this is the first time these results have been applied to turbulent channel flow. The agreement of all turbulence intensity formulations with the data provides encouraging support for Townsend's attached eddy hypothesis in duct flows.

Auto-correlation measurements, which the author believes could reveal more information about the flow than previously thought, were recorded at three Reynolds numbers across the possible range. It has recently become generally accepted that

cohesive 'packets' of structures exist close to the wall in turbulent boundary layers. Auto-correlation coefficients confirm that this phenomenon also occurs in channel flow. Further, it appears that the breakdown of these long structures occurs at much larger length scales in a channel than in a boundary layer. This behaviour is confirmed by the distribution of the integral length scale, $\mathcal{L}$, which decreases at a relatively slow rate with increasing wall-distance (beyond the turbulent wall region).

Finally, while there remains much to be discovered before the science of wall-bounded turbulence is well-understood, it is hoped that the work presented here has made some progress toward achieving that goal. A brief outline of the activities that the author foresees as important steps toward a better understanding is presented in the following section.

8.1 Further work

- With respect to measurements near the side-walls of a channel, it would be interesting to know the effect of increased wall shear stress on the side-walls. At this time, it is not understood how this would affect the channel bed centre wall shear stress. Such a study could be conducted by adhering sandpaper to the channel side-walls and re-measuring perimetric wall shear stress distributions. The results would be useful to further the current understanding of side-wall effects on the central flow.

- In the present investigation, flow development has only been studied with pitot tubes measuring mean streamwise velocity. For a definitive value of the development length, hot-wire measurements of higher-order turbulence statistics are required.

- It is not known if the channel flow development results apply to pipe flow also. The long pipe flow facility available at Melbourne would be an ideal apparatus in which to study pipe flow development.

- As suggested in Chapter 6, a repeat of hot-wire measurements at the most downstream measuring location using wires with smaller length is required. Spatial resolution effects were found to have contaminated the author's data

very close to the wall at higher Re. A correction for such effects — or even simply a better understanding of these effects — would be invaluable.

- Further application of the attached eddy model to channel flow is needed. Unfortunately, there was insufficient time to complete this work during the current investigation. It is postulated that adding the 'packet' phenomenon to the model (see Marusic, 2001) could show better agreement between the predicted auto-correlation and the measured data of Chapter 7.

- Finally, a study of wall roughness effects in the channel should be carried out. As stated earlier, the channel was constructed with the intention of studying roughness effects. Roughness effects present a great challenge to the experimentalist and the facility now available provides the simplest possible geometry in which to conduct this study. It is now feasible to investigate a large number of roughness geometries and distributions within a relatively short time frame.

References

Abell, C. J. (1974). *Scaling Laws for Pipe Flow Turbulence*. PhD thesis. University of Melbourne.

Adrian, R. J., Meinhart, C. D., & Tomkins, C. D. (2000). Vortex organization in the outer region of the turbulent boundary layer. *J. Fluid Mech.* **422**, 1–54.

Barenblatt, G. I. (1993). Scaling laws for fully developed turbulent shear flows. Part 1. Basic hypotheses and analysis. *J. Fluid Mech.* **248**, 513–520.

Barenblatt, G. I., Chorin, A. J., & Protoskishin, V. M. (2000). A note on the intermediate region in turbulent boundary layers. *Phys. Fluids* **12**, 2159–2161.

Blasius, H. (1911). Das ähnlichkeitsgesetz bei rebungsvorgängen. *Physikalische Zeitschrift* **12**, 1175–1177. Or refer to H. Schlicting, *Boundary layer theory*, 560–566, McGraw-Hill, 1968.

Chue, S. H. (1975). Pressure probes for fluid measurement. *Prog. Aerospace Sci.* **16**, 147–223.

Clauser, F. H. (1954). Turbulent boundary layers in adverse pressure gradients. *J. Aero. Sci.* **21**, 91–108.

Coleman, H. W., Hodge, B. K., & Taylor, R. P. (1984). A re-evaluation of Schlichting's surface roughness experiment. *J. Fluids Engineering* **106**, 60–65.

Coles, D. E. (1956). The law of the wake in the turbulent boundary layer. *J. Fluid Mech.* **1**, 191–226.

Coles, D. E. (1962). The turbulent boundary-layer in compressible fluid. Technical report R-403-PR. The RAND Corporation, Santa Monica, CA.

Coles, D. E. (1968). The young person's guide to the data. In *Proc. Computation of turbulent boundary layers*. Vol II AFOSR-IFP-Stanford conference.

Cornish, R. J. (1928). Flow in a pipe of rectangular cross section. *Proc. of the Royal Soc.* **120**, 691–700.

Davies, S. J. & White, C. M. (1928). An experimental study of the flow of water of pipes of rectangular section. *Proc. Royal Soc.* pp. 92–107.

Dean, R. B. (1978). Reynolds number dependence of skin friction and other bulk flow variables in two-dimensional rectangular duct flow. *J. Fluids Engineering* **100**, 215–223.

Favre, A. J., Gaviglio, J. J., & Dumas, R. J. (1958). Further space-time correlations of velocity in a turbulent boundary layer. *J. Fluid Mech.* **3**, 344–356.

Franklin, R. E. & Wallace, J. M. (1970). Absolute measurements of static-hole error using flush transducers. *J. Fluid Mech.* **42**, 33–48.

Ganapathisubramani, B., Longmire, E. K., & Marusic, I. (2003). Characteristics of vortex packets in turbulent boundary layers. *J. Fluid Mech.* **478**, 35–46.

George, W. K., Castillo, L., & Knecht, P. (1993). The zero pressure-gradient turbulent boundary layer. In *Reynolds Symposium on Turbulence*. Asilomar, CA.

Gessner, F. B. & Jones, J. B. (1965). On some aspects of fully-developed turbulent flow in rectangular channels. *J. Fluid Mech.* **23**, 689–713.

Goldstein, S. (1936). A note on the measurement of total head and static pressure in a turbulent stream. *Proc. of the Royal Soc. of London* **155**, 570–575.

Hafez, S. H. M. (1991). *The structure of accelerated turbulent boundary layers*. PhD thesis. University of Melbourne.

Hama, F. R. (1954). Boundary layer characteristics for smooth and rough surfaces. *Trans. Soc. Naval Arch. Mar. Engrs* **62**.

Hartnett, J. P., Koh, J. C. Y., & McComas, S. T. (1962). A comparison of predicted and measured friction factors for turbulent flow through rectangular ducts. *J. Heat Transfer* **84**, 82–88.

Head, M. R. & Bandyopadhyay, P. (1981). New aspects of turbulent structure. *J. Fluid Mech.* **107**, 297–337.

Hellstedt, A. K. (2003). *Streamwise Evolution of Turbulent Boundary Layers towards Equilibrium Conditions*. PhD thesis. University of Melbourne.

Henbest, S. (1983). *The structure of turbulent pipe flow*. PhD thesis. University of Melbourne.

Hinze, J. O. (1959). *Turbulence*. McGraw-Hill.

Hites, M. H. (1997). *Scaling of high-Reynolds number turbulent boundary layers in the National Diagnostic Facility*. PhD thesis. Illinois Institute of Technology.

Hussein, A. K. M. F., Jeong, J., & Kim, J. (1987). Structure of turbulent shear flows. In *Proc. 1987 Summer Program, Centre for Turbulence Research*. Stanford University.

Jones, M. B. (1998). *Evolution and structure of sink flow turbulent boundary layers*. PhD thesis. The University of Melbourne.

Jones, M. B., Marusic, I., & Perry, A. E. (2001a). Streamwise evolution and structure of sink-flow turbulent boundary layers. *J. Fluid Mech.* **428**, 1–27.

Jones, M. B., Nishizawa, N., & Chong, M. S. (2001b). Experimental study of high Reynolds number turbulent boundary layers — mean flow scaling. In *Proc. 14th Australasian Fluid Mech. Conf.* Adelaide University, Adelaide, Aust.

Jones, O. C. (1976). An improvement in the calculation of turbulent friction in rectangular ducts. *J. Fluids Engineering* pp. 173–181.

von Kármán, T. (1930). Mechanische ahnlichkeit und turbulenz. Technical report Nachr. Ges. Wiss. Gottingen.

Kim, J. & Hussein, F. (1993). Propagation velocity of perturbations in turbulent channel flow. *Phys. Fluids A* **5**, 695–706.

Kim, J., Moin, P., & Moser, R. (1987). Turbulence statistics in fully developed channel flow at low Reynolds number. *J. Fluid Mech.* **177**, 133–166.

Kline, S., Reynolds, W., Shrub, F., & Rundstadler, P. (1967). The structure of turbulent boundary layers. *J. Fluid Mech.* **30**, 741–773.

Knight, D. W. & Patel, H. S. (1985). Boundary shear in smooth rectangular ducts. *J. Hydraulic Engineering* **111** (1).

Kuroda, A., Kasagi, N., & Hirata, M. (1993). A direct numerical simulation of turbulent plane Couette-Poiseuille flows: effect of near stream on the near wall turbulence structures. In *TSF 9*. Kyoto, Japan.

Laufer, J. (1950). Investigation of turbulent flow in a two-dimensional channel. Technical Report 2123 N. A. C. A.

Leutheusser, H. J. (1963). Turbulent flow in rectangular ducts. *Proc. of A. S. C. E. (Hydraulics Div.)* pp. 1–19.

Li, J. D. (1989). *The turbulence structure of wall shear flow*. PhD thesis. The University of Melbourne.

Ligrani, P. M. & Bradshaw, S. (1987). Spatial resolution and measurement of turbulence in the viscous sublayer using subminiature hot-wire probes. *Experiments in Fluids* **5**, 407–417.

Liu, Z. C. & Adrian, R. (1999). Evidence for hairpin packet structure in DNS channel flow. In *Proc. Turb. Shear Flow Phen. 1*. Santa Barbara, U.S.A.

MacMillan, F. A. (1954). Viscous effects on pitot-tubes at low speeds. *J. R. Aero. Soc.* **58**, 570.

MacMillan, F. A. (1956). Experiments on pitot-tubes in shear flow. Technical Report 3028 A. R. C.: R. & M.

Marusic, I. (1991). *The structure of zero- and adverse-pressure-gradient turbulent boundary layers.* PhD thesis. The University of Melbourne.

Marusic, I. (2001). On the role of large-scale structures in wall turbulence. *Phys. Fluids* **13**, 735–743.

Marusic, I. & Perry, A. E. (1995). A wall-wake model for the turbulence structure of boundary layers. Part 2. Further experimental support. *J. Fluid Mech.* **298**, 389–407.

Marusic, I., Uddin, A. K. M., & Perry, A. E. (1997). Similarity law for the streamwise turbulence intensity in zero-pressure gradient turbulent boundary layers. *Phys. Fluids* **9**, 3718–3726.

McKeon, B. J. (2003). *High Reynolds Number Turbulent Pipe Flow.* PhD thesis. Princeton University.

McKeon, B. J., Li, J., Jiang, W., Morrison, J. F., & Smits, A. J. (2003a). Pitot probe corrections in fully developed turbulent pipe flow. *Meas. Sci. Tech.* **14**, 1449–1458.

McKeon, B. J., Morrison, J. F., Jiang, W., Li, J., & Smits, A. J. (2003b). Revised log law constants for fully-develped turbulent pipe flow. In *Reynolds Number Scaling in Turbulent Pipe Flow: Proc. IUTAM Symp.* (ed. A. J. smits).

McKeon, B. J. & Smits, A. J. (2002). Static pressure correction in high Reynolds number fully developed turbulent pipe flow. *Meas. Sci Ṫech.* **13**, 1608–1614.

McLean, I. R. (1990). *The near wall eddy structure in an equilibrium boundary layer.* PhD thesis. University of Southern California.

Millikan, C. B. (1938). A critical discussion of turbulent flows in channels and circular tubes. In *Proc. 5th Int. Congress of Appl. Mech.* pp. 386–392. Cambridge, Mass.

Moin, P. & Kim, J. (1982). Numerical investigation of turbulent channel flow. *J. Fluid Mech.* **119**, 341–377.

Morrison, J. F., McKeon, B. J., Jiang, W., & Smits, A. J. (2004). Scaling of the streamwise velocity component in turbulent pipe flow. *J. Fluid Mech.* **508**, 99–131.

Nickels, T. B. (2001). The mean velocity profile for wall-bounded flows at low Reynolds number. In *14th Australasian Fluid Mechanics Conference*. Adelaide University, Adelaide, Aust.

Nickels, T. B. & Marusic, I. (2001). On the different contributions of coherent structures to the spectra of a turbulent round jet and a turbulent boundary layer. *J. Fluid Mech.* **448**, 367–385.

Nickels, T. B. & Perry, A. E. (1996). An experimental and theoretical study of the turbulent coflowing jet. *J. Fluid Mech.* **309**, 157–182.

Nikuradse, J. (1932). Gesetzmassigkeiten der turbulenten stromung in glatten rohren. *Forsch. Auf Dem Gebiet des Ingenieurwesens* **3**, 1–36.

Nikuradse, J. (1933). Stromungsgesetze in rauhen rohren. *Forsch. Arb. Ing. Wes.* **361**.

Österlund, J. M. (1999). *Experimental studies of zero pressure-gradient turbulent boundary-layer flow*. PhD thesis. Department of Mechanics, Royal Institute of Tech. Stockholm, Sweden.

Österlund, J. M., Johansson, A. V., & Nagib, H. M. (2000a). Comment on "A note on the intermediate region in turbulent boundary layers" [Phys. Fluids 12, 2159 (2000)]. *Phys. Fluids* **12** (9), 2360–2363.

Österlund, J. M., Nagib, A. V. J. H. M., & Hites, M. H. (2000b). A note on the overlap region in turbulent boundary layers. *Phys. Fluids* **12** (1), 1–4.

Panton, R. L. (2002). Evaluation of the Barenblatt-Chorin-Protostokishin power law for turbulent boundary layers. *Phys. Fluids* **14**, 1806–1808.

Patel, V. C. (1965). Calibration of the Preston tube and limitations on its use in pressure gradients. *J. Fluid Mech.* **23**, 185–208.

Perry, A. E. (1982). *Hot-wire Anemometry.* Clarendon Press Oxford.

Perry, A. E. & Abell, C. J. (1975). Scaling laws for pipe-flow turbulence. *J. Fluid Mech.* **67**, 257–271.

Perry, A. E. & Abell, C. J. (1977). Asymptotic similarity of turbulence structures in smooth- and rough-walled pipes. *J. Fluid Mech.* **79**, 785–799.

Perry, A. E. & Chong, M. S. (1982). On the mechanism of wall turbulence. *J. Fluid Mech.* **119**, 173–217.

Perry, A. E., Hafez, S., & Chong, M. S. (2001). A possible reinterpretation of the Princeton Superpipe data. *J. Fluid Mech.* **439**, 395–401.

Perry, A. E., Henbest, S., & Chong, M. S. (1986). A theoretical and experimental study of wall turbulence. *J. Fluid Mech.* **165**, 163–199.

Perry, A. E. & Li, J. D. (1990). Experimental support for the attached-eddy hypothesis in zero-pressure-gradient turbulent boundary layers. *J. Fluid Mech.* **218**, 405–438.

Perry, A. E., Lim, K. L., & Henbest, S. M. (1987). An experimental study of the turbulence structure in smooth- and rough-wall boundary layers. *J. Fluid Mech.* **177**, 437–466.

Perry, A. E. & Marusic, I. (1995). A wall-wake model for the turbulence structure of boundary layers. Part 1. Extension of the attached eddy hypothesis. *J. Fluid Mech.* **298**, 361–388.

Prandtl, L. (1925). Uber die ausgebildete turbulenz. *ZAMM* **5**, 136–139.

Prandtl, L. (1935). *From* Durand, W. F.*: Aerodynamic Theory, Vol. III.* Publisher Unknown.

Reichardt, H. (1951). Vollständige darstellung der turbulenten geschwindigkeitsverteilung in glatten leitungen. *Z. angew. Math. Mech.* **31**, 208–219.

Reynolds, O. (1883). An experimental investigation of the circumstances which determine whether the motion of water shall be direct or sinuous, and of the law of resistance in parallel channels. *Royal Soc., Phil. Trans.* pp. 935–982.

Reynolds, O. (1894). On the dynamical theory of incompressible viscous fluids and the determination of the criterion. *Royal Soc., Phil. Trans.* pp. 123–164.

Robinson, S. K. (1991). Coherent motions in the boundary layer. *Annu. Rev. Fluid Mech.* **23**, 601–639.

Rotta, J. C. (1962). Turbulent boundary layers in incompressible flow. *Prog. Aero. Sci.* **2**, 1–219.

Rouse, H. & Ince, S. (1957). *History of Hydraulics.* Iowa City: Iowa Institue of Hydraulic Research.

Saddoughi, S. G. (1988). *Experimental studies of the effects of streamline divergence on developing turbulent boundary layers.* PhD thesis. The University of Melbourne.

Schlichting, H. (1936). Experimental investigation of the problem of surface roughness. Technical Report 823 N. A. C. A.

Schlichting, H. (1979). *Boundary Layer Theory.* New York: McGraw-Hill 7th edition.

Shaw, R. (1960). The influence of hole dimensions on static pressure measurements. *J. Fluid Mech.* **7**, 550–564.

Spalart, P. R. (1990). Direct simulation of a turbulent boundary layer up to $R_\theta = 1410$. *J. Fluid Mech.* **187**, 61–98.

Spalding, D. B. (1961). A single formula for the "law of the wall". *J. Applied Mechanics* pp. 455–457.

Sternberg, J. (1967). On the interpretation of space-time correlation measurements in shear flow. *Phys. Fluids* **10**, S146–S152.

Tanner, L. H. & Blows, L. G. (1976). A study of the motion of oil films on surfaces in air flow, with application to the measurement of skin friction. *J. Physics E: Scientific Instruments* **9**, 194–202.

Taylor, G. I. (1938). The spectrum of turbulence. *Proceedings of the Royal Society* **A164**, 476–490.

Townsend, A. A. (1956). *The structure of turbulent shear flow*. Cambridge University Press. 1^{st} edition.

Townsend, A. A. (1976). *The structure of turbulent shear flow*. Cambridge University Press. 2^{nd} edition.

Uddin, A. K. M. (1994). *The structure of a turbulent boundary layer*. PhD thesis. The University of Melbourne.

Wei, T. & Willmarth, W. W. (1989). Reynolds number effects on the structures of a turbulent channel flow. *J. Fluid Mech.* **204**, 57–95.

Young, A. D. & Maas, J. N. (1936). The behaviour of a pitot-tube in a transverse total-pressure gradient. Technical Report 1770 A. R. C.: R. & M.

Zagarola, M. V. (1996). *Mean flow scaling in turbulent pipe flow*. PhD thesis. Princeton University.

Zagarola, M. V. & Smits, A. J. (1998). Mean-flow scaling of turbulent pipe flow. *J. Fluid Mech.* **373**, 33–79.

Zanoun, E.-S., Durst, F., & Nagib, H. (2003). Evaluating the law of the wall in two-dimensional fully developed turbulent channel flows. *Phys. Fluids* **15** (10).

Zanoun, E.-S., Nagib, H., Durst, F., & Monkewitz, P. (2002). Higher Reynolds number channel data and their comparison to recent asymptotic theory (invited). In *40th AIAA Aerospace Sciences Meeting*. Hilton, Reno, NV.

Zhou, J., Adrian, R. J., Balachandar, S., & Kendall, T. M. (1999). Mechanisms for generating coherent packets of hairpin vortices. *J. Fluid Mech.* **387**, 353–396.

Appendix A

Derivation of Prandtl's smooth wall resistance formula

The Darcy friction factor was defined in Chapter 2 for pipe flow as

$$\lambda_p = \frac{4\tau_w}{\frac{1}{2}\rho U_b^2} = 8\left(\frac{U_\tau}{U_b}\right)^2.$$

In channel flow, the centreline skin friction was defined as

$$C_f = \frac{\tau_w}{\frac{1}{2}\rho U_b^2} = 2\left(\frac{U_\tau}{U_b}\right)^2.$$

Thus, the analytical forms of λ_p and C_f can be found from the calculation of U_b/U_τ.

First, take the log law (2.4),

$$\frac{U}{U_\tau} = \frac{1}{\kappa}\ln\left(\frac{yU_\tau}{\nu}\right) + A,$$

which holds for all wall-bounded turbulent flows. Rewriting this log law with outer flow scaled wall-distance:

$$\frac{U}{U_\tau}(\eta) = \frac{1}{\kappa}\ln\left(\eta K_\tau\right) + A. \tag{A.1}$$

Recall that $K_\tau = \Delta U_\tau/\nu$ is the Karman number; Δ is the largest scale in the flow.

Integration over the cross-section provides the definition of non-dimensional bulk velocity:

$$\frac{U_b}{U_\tau} = \frac{1}{A_x}\iint_S \frac{U}{U_\tau} dS, \tag{A.2}$$

where A_x is the cross-sectional area. At this point the derivations for pipe and channel flow deviate.

A.1 Pipe flow

Using polar coordinates, (A.2) becomes

$$\frac{U_b}{U_\tau} = \frac{1}{\pi R^2}\int_0^{2\pi}\int_0^R \frac{U}{U_\tau} r dr d\theta. \tag{A.3}$$

Now r is a radial coordinate measured from the pipe centreline. The relationship between η and r/R is

$$\frac{R-y}{R} = \frac{r}{R} = 1-\eta; \qquad \frac{d}{d\eta}\left(\frac{r}{R}\right) = -1.$$

Substituting this into (A.3) and assuming the flow is axis-symmetric (i.e., independent of θ):

$$\begin{aligned}
\frac{U_b}{U_\tau} &= 2\int_1^0 [\eta-1]\frac{U}{U_\tau}(\eta)d\eta && \text{(A.4)}\\
&= 2\int_1^0 [\eta-1]\left[\frac{1}{\kappa}\ln(\eta K_\tau) + A\right]d\eta \\
&= 2\int_1^0 [\eta-1]\left[\frac{1}{\kappa}\ln(\eta) + \frac{1}{\kappa}\ln(K_\tau) + A\right]d\eta && \text{(A.5)}\\
&= \frac{2}{\kappa}\int_1^0 [\eta-1]\ln(\eta)d\eta + \left(\frac{2}{\kappa}\ln(K_\tau) + 2A\right)\int_1^0 [\eta-1]d\eta.
\end{aligned}$$

The first term must be integrated by parts, while the value of the integral in the second term is simply $-1/2$. The result is

$$\frac{U_b}{U_\tau} = -\frac{3}{2\kappa} + \frac{1}{\kappa}\ln(K_\tau) + A.$$

Since $K_\tau = RU_\tau/\nu$ and $Re = 2RU_b/\nu$,

$$\begin{aligned}
\frac{U_b}{U_\tau} &= \frac{1}{\kappa}\ln\left(\frac{Re}{2}\frac{U_\tau}{U_b}\right) - \frac{3}{2\kappa} + A. \\
\sqrt{\frac{8}{\lambda_p}} &= \frac{1}{\kappa}\ln\left(\frac{Re}{2}\sqrt{\frac{\lambda_p}{8}}\right) - \frac{3}{2\kappa} + A. && \text{(A.6)}
\end{aligned}$$

With some trivial algebra, the final result is achieved:

$$\sqrt{\frac{1}{\lambda_p}} = C_1\log_{10}\left(Re\sqrt{\lambda_p}\right) + C_2,$$

where

$$C_1 = \frac{\ln 10}{\sqrt{8}\kappa}; \quad C_2 = \frac{1}{\sqrt{8}}\left[A - \frac{3}{2\kappa} - \frac{1}{\kappa}\ln\left(2\sqrt{8}\right)\right].$$

A.2 Channel flow

Assuming infinite aspect ratio (i.e., flow between parallel plates), (A.2) becomes

$$\frac{U_b}{U_\tau} = \frac{2}{h}\int_0^{h/2} \frac{U}{U_\tau} dy. \tag{A.7}$$

Substituting $\eta = 2y/h$ gives the very simple equation

$$\begin{aligned} \frac{U_b}{U_\tau} &= \int_0^1 \frac{U}{U_\tau}(\eta) d\eta \\ &= \int_0^1 \left[\frac{1}{\kappa}\ln(\eta K_\tau) + A\right] d\eta \\ &= \int_0^1 \frac{1}{\kappa}\ln(\eta) d\eta + \left(\frac{1}{\kappa}\ln(K_\tau) + A\right)\int_0^1 d\eta. \end{aligned} \tag{A.8}$$

Integration by parts gives:

$$\begin{aligned} \frac{U_b}{U_\tau} &= -\frac{1}{\kappa} + \frac{1}{\kappa}\ln(K_\tau) + A \\ &= \frac{1}{\kappa}\ln\left(Re\frac{U_\tau}{U_b}\right) + A - \frac{1}{\kappa}, \end{aligned}$$

and noting that $K_\tau = hU_\tau/2\nu$ and $Re = hU_b/\nu$,

$$\begin{aligned} \frac{U_b}{U_\tau} &= \frac{1}{\kappa}\ln\left(\frac{Re}{2}\frac{U_\tau}{U_b}\right) + A - \frac{1}{\kappa} \\ \sqrt{\frac{2}{C_f}} &= \frac{1}{\kappa}\ln\left(\frac{Re}{2}\sqrt{\frac{C_f}{2}}\right) + A - \frac{1}{\kappa}. \end{aligned}$$

Further trivial algebra leads to the final result:

$$\sqrt{\frac{1}{C_f}} = C_3 \log_{10}\left(Re\sqrt{C_f}\right) + C_4,$$

where

$$C_3 = \frac{\ln 10}{\sqrt{2}\kappa}; \qquad C_4 = \frac{1}{\sqrt{2}}\left[A - \frac{1}{\kappa} - \frac{1}{\kappa}\ln(2\sqrt{2})\right].$$

Appendix B

The Blasius' power laws

Blasius (1911) found the following empirical power law fitted the available pipe flow resistance data quite well:

$$\lambda_p = 0.3164 Re^{-\frac{1}{4}}. \tag{B.1}$$

This relationship is commonly referred to as the *Blasius resistance law* for smooth pipes. It can be shown that this resistance law implies a power law in the mean velocity distribution. That is,

$$\frac{U}{U_\tau} = \alpha (y^+)^\beta.$$

It will be shown here that the Blasius resistance law (B.1) stipulates the constant values of $\alpha = 8.562$ and $\beta = 1/7$.

From Appendix A it is known that the non-dimensional bulk velocity in a pipe flow is given by

$$\frac{U_b}{U_\tau} = 2 \int_1^0 [\eta - 1] \frac{U}{U_\tau} d\eta.$$

Substituting in the assumed mean velocity power law and integrating;

$$\begin{aligned} \frac{U_b}{U_\tau} &= 2 \int_1^0 [\eta - 1] \alpha (y^+)^\beta d\eta \\ &= 2\alpha \int_1^0 [\eta - 1] (\eta K_\tau)^\beta d\eta \\ &= 2\alpha K_\tau^\beta \int_1^0 [\eta^{\beta+1} - \eta^\beta] d\eta \\ &= 2\alpha K_\tau^\beta \left[\frac{1}{\beta + 1} - \frac{1}{\beta + 2} \right]. \end{aligned} \tag{B.2}$$

Returning to the Blasius resistance law (B.1):

$$\begin{aligned}
\frac{1}{\lambda_p} = \frac{1}{8}\left(\frac{U_b}{U_\tau}\right)^2 &= 3.1606 Re^{\frac{1}{4}} \\
\frac{1}{8}\left(\frac{U_b}{U_\tau}\right)^2 &= 3.1606 (K_\tau)^{\frac{1}{4}} \left(2\frac{U_b}{U_\tau}\right)^{\frac{1}{4}} \\
\left(\frac{U_b}{U_\tau}\right)^{\frac{7}{4}} &= 8 \cdot 2^{\frac{1}{4}} \cdot 3.1606 (K_\tau)^{\frac{1}{4}} \\
\left(\frac{U_b}{U_\tau}\right) &= 6.9926 (K_\tau)^{\frac{1}{7}}
\end{aligned}$$

Substituting for U_b/U_τ given by (B.2) then gives:

$$2\alpha K_\tau^\beta \left[\frac{1}{\beta+1} - \frac{1}{\beta+2}\right] = 6.9926 (K_\tau)^{\frac{1}{7}}.$$

Equating coefficients and exponents achieves the desired result:

$$\beta = \frac{1}{7}; \qquad 2\alpha \left[\frac{1}{\beta+1} - \frac{1}{\beta+2}\right] = 6.9926 \quad \rightarrow \quad \alpha = 8.5623.$$

Appendix C

The MacMillan wall proximity correction

$\frac{y}{d_p}$	$\frac{\Delta U}{U}$	$\frac{y}{d_p}$	$\frac{\Delta U}{U}$
0.5000	1.5000e-02	0.8874	3.9872e-03
0.5135	1.4003e-02	0.9949	2.9742e-03
0.5242	1.3017e-02	1.0971	2.1945e-03
0.5431	1.1980e-02	1.1993	1.5446e-03
0.5619	1.0994e-02	1.2966	1.0762e-03
0.5834	9.9824e-03	1.3982	6.5967e-04
0.6130	8.9706e-03	1.4950	3.9878e-04
0.6426	8.0107e-03	1.5972	2.4154e-04
0.6830	6.9987e-03	1.6993	1.3615e-04
0.7000	6.6679e-03	1.7773	8.3026e-05
0.7368	5.9864e-03	1.8983	2.9201e-05
0.7960	5.0519e-03	2.0000	0.0000e-00

Table C.1: Tabulated data of the MacMillan (1956) wall proximity correction. ΔU is the correction to be applied to the measured velocity, U.

Appendix D

Convergence test

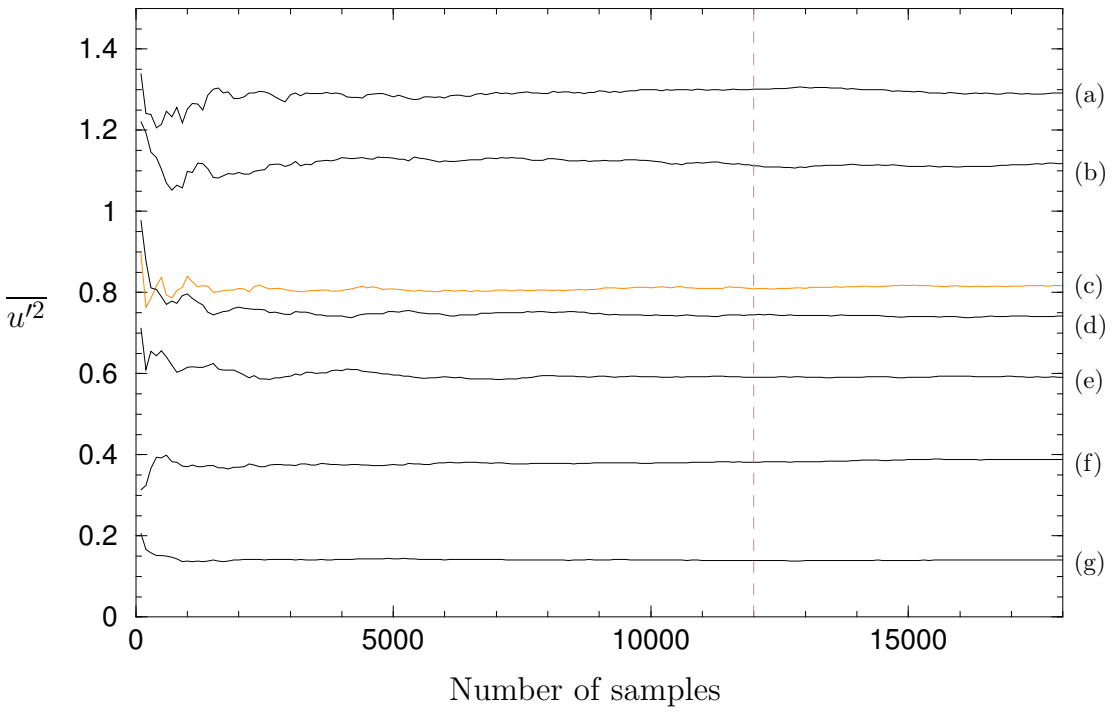

Figure D.1: Running average of turbulence intensity measured with a hot-wire at $Re = 64 \times 10^3$. The broken line indicates the number of samples acquired for final results. The sample frequency was $200Hz$. Averages are plotted for $y/h =$: a) 0.0030; b) 0.0093; c) 0.0380; d) 0.0748; e) 0.1412; f) 0.2657; g) 0.5000.

Appendix E

Convergence test

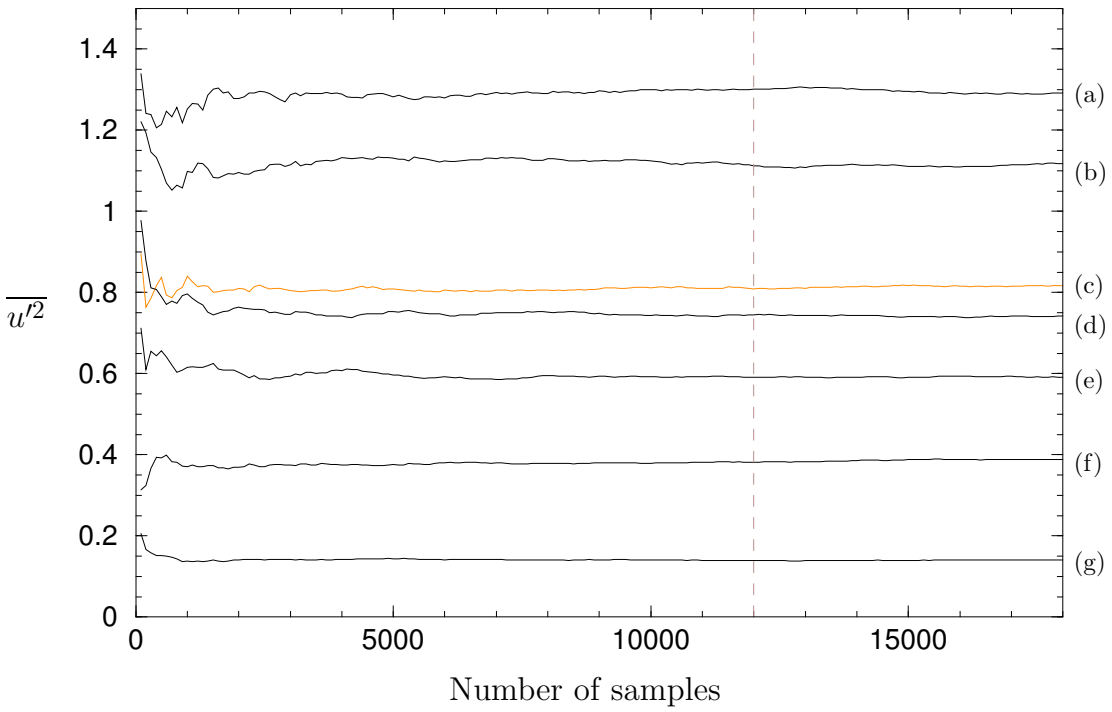

Figure E.1: Running average of turbulence intensity measured with a hot-wire at $Re = 64 \times 10^3$. The broken line indicates the number of samples acquired for final results. The sample frequency was $200Hz$. Averages are plotted for $y/h =$: a) 0.0030; b) 0.0093; c) 0.0380; d) 0.0748; e) 0.1412; f) 0.2657; g) 0.5000.

Appendix F

Matching circuit behaviour

The mathematical description of the matching box function was given by equations (3.1) & (3.2):

$$\begin{aligned} E_u &= K_1(E_1 - E_{A1}) + K_2K_2'(E_2 - E_{A2}) \qquad \text{(F.1)} \\ E_v &= K_1(E_1 - E_{A1}) - K_2K_2''(E_2 - E_{A2}). \end{aligned}$$

By sinusoidally shaking the X-wire in the horizontal direction, the constant K_2'' can be adjusted (through an amplifier) until $E_v < 0.05E_u$. In practice, it is commonly observed that when matching occurs, the resultant signals, E_u and E_v, are out of phase by 90^o. The reason for this can be explained mathematically as shown in this appendix.

Firstly, rewrite the above equations as

$$E_u = K_1E_1^* + K_3E_2^* \qquad \text{(F.2)}$$

$$E_v = K_1E_1^* - K_4E_2^*. \qquad \text{(F.3)}$$

For horizontal shaking, the outputs from the hot-wire circuits of each wire, E_1^* and E_2^*, should be in phase. However, in reality, there will be a slight phase lag between the two outputs. Thus, the HWA outputs will be assumed to be of the form

$$E_1^* = A_1\sin(\omega t) = |E_1 - E_{A1}|\sin(\omega t) \qquad \text{(F.4)}$$

$$E_2^* = B_1\sin(\omega t + \phi) = |E_2 - E_{A2}|\sin(\omega t + \phi), \qquad \text{(F.5)}$$

where ω is the frequency of shaking, A_1 and B_1 are the amplitudes of each output and ϕ is the phase lag. Note that the mean output voltages are irrelevant to the matching process, so they are set to zero here. Also, the amplitudes A_1 and B_1 should be very similar if the HWA circuits are of the same design and construction. Substituting these forms into equations (F.3) & (F.3) gives

$$\begin{aligned} E_u &= K_1 A_1 \sin(\omega t) + K_3 B_1 \sin(\omega t + \phi), \\ E_v &= K_1 A_1 \sin(\omega t) - K_4 B_1 \sin(\omega t + \phi). \end{aligned}$$

Including the double angle trigonometric identity, $\sin(\omega t) = \sin(\omega t)\cos(\phi) + \sin(\phi)\cos(\omega t)$ with $\cos\phi \approx 1$,

$$E_u = (K_1 A_1 + K_3 B_1)\sin(\omega t) + K_3 B_1 \sin\phi \cos(\omega t), \tag{F.6}$$

$$E_v = (K_1 A_1 - K_3 B_1)\sin(\omega t) - K_3 B_1 \sin\phi \cos(\omega t). \tag{F.7}$$

Now, it can be shown that

$$G\sin t + H\cos t = R\cos(t - \alpha),$$

where $R = \sqrt{G^2 + H^2}$ and $\tan(\alpha) = G/H$. Applying this relationship to equations (F.7) & (F.7),

$$\begin{aligned} E_u &= \sqrt{(K_1 A_1 + K_3 B_1)^2 + (K_3 B_1)^2 \sin^2\phi}\cos(\omega t - \alpha_u), \\ E_v &= \sqrt{(K_1 A_1 - K_4 B_1)^2 + (K_4 B_1)^2 \sin^2\phi}\cos(\omega t - \alpha_v). \end{aligned}$$

If ϕ is small, then $\sin^2\phi \approx 0$ so that

$$\begin{aligned} E_u &= \sqrt{(K_1 A_1 + K_3 B_1)^2}\cos(\omega t - \alpha_u) \\ E_v &= \sqrt{(K_1 A_1 - K_4 B_1)^2}\cos(\omega t - \alpha_v), \end{aligned}$$

where,

$$\tan\alpha_u = \frac{K_1 A_1 + K_3 B_1}{K_3 B_1 \sin\phi}; \quad \tan\alpha_v = \frac{K_1 A_1 - K_4 B_1}{K_4 B_1 \sin\phi}.$$

Since the aim of the matching circuit is to minimise the amplitude of E_v during horizontal shaking, it is clear that $K_4 B_1$ should be set as close as possible to $K_1 A_1$. That is, the X-wire will be matched when

$$K_4 = \frac{A_1}{B_1} K_1 = \frac{|E_1 - E_{A1}|}{|E_2 - E_{A2}|} K_1, \tag{F.8}$$

or alternatively,

$$K_2'' = \frac{A_1}{B_1}\frac{K_1}{K_2}. \tag{F.9}$$

Now, if the wires are matched and ϕ is very small, then it can be seen that the phases of E_u and E_v will be

$$\alpha_u \to \frac{\pi}{2}; \quad \alpha_v \to 0. \tag{F.10}$$

Thus, the matching X-wire outputs, E_u and E_v are out of phase by 90^o.

In the case of vertical shaking, where E_u should be minimised, the analysis is identical that given above, with one major difference: during vertical shaking the two X-wire outputs are out of phase by approximately 180^o. Hence, simply letting $\phi = \pi + \phi_v$ in (F.5) & (F.5) gives

$$\begin{aligned} E_1^* &= A_2 \sin(\omega t) = |E_1 - E_{A1}| \sin(\omega t) \\ E_2^* &= -B_2 \sin(\omega t + \phi) = -|E_2 - E_{A2}| \sin(\omega t + \phi). \end{aligned}$$

Performing the same analysis as given above delivers the result that matching is achieved when

$$K_3 = \frac{A_2}{B_2}K_1 = \frac{|E_1 - E_{A1}|}{|E_2 - E_{A2}|}K_1, \tag{F.11}$$

or alternatively,

$$K_2' = \frac{A_2}{B_2}\frac{K_1}{K_2}. \tag{F.12}$$

Once again it can be shown that the two outputs, E_u and E_v will be out of phase by 90^o when matched.

Finally, if the two HWA circuits behave similarly, then $A_1 \approx B_1$. Also, if the shaking amplitude is the same in both directions, $A_1 \approx B_1 \approx A_2 \approx B_2$. Therefore, in practice, matching should be achieved when $K_2K_2'' \approx K_1 \approx K_2K_2'$; that is, the gains K_2'' and K_2' should always be of similar magnitude. Further, K_1 is an arbitrary constant and may be set to unity so that $K_2K_2'' \approx K_2K_2' \approx 1$ should provide the desired result. It should be noted that this analysis does not suggest that K_2'', K_2' *must* be set to the values given, rather, it is intended to give an approximate indication of the expected gains which should successfully match a X-wire.

Appendix G

Extended overlap region analysis

y^+	η	κ	A	# Obs.
120	0.10	0.390	4.31	17
120	0.11	0.388	4.25	21
120	0.12	0.386	4.21	26
120	0.13	0.385	4.18	31
120	0.14	0.383	4.11	36
120	0.15	0.381	4.05	41
120	0.16	0.379	3.98	46
150	0.10	0.391	4.36	11
150	0.11	0.389	4.29	14
150	0.12	0.387	4.23	18
150	0.13	0.386	4.20	22
150	0.14	0.382	4.08	26
150	0.15	0.381	4.04	31
150	0.16	0.379	3.95	36

Table G.1: Pitot tube measurements in pipe flow: the effect of varying overlap region limits on the empircally derived log law constants.

y^+	η	κ	A	# Obs.
80	0.07	0.393	4.55	11
80	0.08	0.394	4.63	14
80	0.09	0.395	4.65	19
80	0.10	0.392	4.59	24
80	0.11	0.393	4.60	29
80	0.12	0.391	4.56	34
80	0.13	0.390	4.52	35
80	0.14	0.389	4.49	38
120	0.10	0.396	4.71	14
120	0.11	0.396	4.72	18
120	0.12	0.394	4.64	23
100	0.13	0.392	4.58	24
120	0.14	0.389	4.49	27
120	0.15	0.384	4.30	32
120	0.16	0.382	4.24	37
150	0.10	0.389	4.46	8
150	0.11	0.396	4.70	11
150	0.12	0.390	4.52	15
150	0.13	0.388	4.44	16
150	0.14	0.386	4.38	18
150	0.15	0.379	4.13	23
150	0.16	0.378	4.09	28

Table G.2: Hot-wire measurements in pipe flow: the effect of varying overlap region limits on the empircally derived log law constants.

y^+	η	κ	A	# Obs.
120	0.10	0.400	4.67	14
120	0.12	0.395	4.53	19
120	0.15	0.392	4.43	25
120	0.17	0.389	4.32	31
120	0.20	0.387	4.23	43
120	0.25	0.386	4.21	49
120	0.30	0.383	4.12	61
120	0.35	0.382	4.07	67
120	0.40	0.380	4.01	73
150	0.10	0.392	4.39	9
150	0.12	0.393	4.46	13
150	0.15	0.391	4.39	18
150	0.17	0.388	4.28	23
150	0.20	0.386	4.19	35
150	0.25	0.385	4.17	41
150	0.30	0.383	4.08	53
150	0.35	0.381	4.04	59
150	0.40	0.380	3.98	65

Table G.3: Pitot tube measurements in channel flow: the effect of varying overlap region limits on the empircally derived log law constants.

y^+	η	κ	A	# Obs.
80	0.07	0.407	4.75	18
80	0.08	0.403	4.65	26
80	0.09	0.400	4.54	27
80	0.10	0.399	4.52	34
80	0.11	0.396	4.45	43
80	0.12	0.395	4.41	44
80	0.13	0.394	4.39	49
80	0.14	0.392	4.35	50
80	0.15	0.390	4.26	56
120	0.10	0.397	4.45	20
120	0.12	0.395	4.42	29
120	0.15	0.390	4.25	41
120	0.17	0.387	4.18	42
120	0.20	0.384	4.06	48
120	0.25	0.379	3.88	57
120	0.30	0.378	3.84	66
120	0.35	0.376	3.79	67
120	0.40	0.374	3.72	73
150	0.10	0.394	4.35	15
150	0.12	0.394	4.38	23
150	0.15	0.390	4.28	34
150	0.17	0.388	4.19	35
150	0.20	0.384	4.05	41
150	0.25	0.378	3.83	50
150	0.30	0.377	3.82	59
150	0.35	0.375	3.76	60
150	0.40	0.373	3.68	66

Table G.4: Hot-wire measurements in channel flow: the effect of varying overlap region limits on the empircally derived log law constants.

Appendix H

Additional auto-correlation data

Auto-correlation coefficient plots left out of Chapter 7 for brevity are presented in this Appendix. In Chapter 7 only the auto-correlation curves for the $Re = 105 \times 10^3$ case were included. Here data for all three Reynolds numbers, $Re = 60, 105, 190 \times 10^3$ are displayed (the $Re = 105 \times 10^3$ case is repeated for completeness).

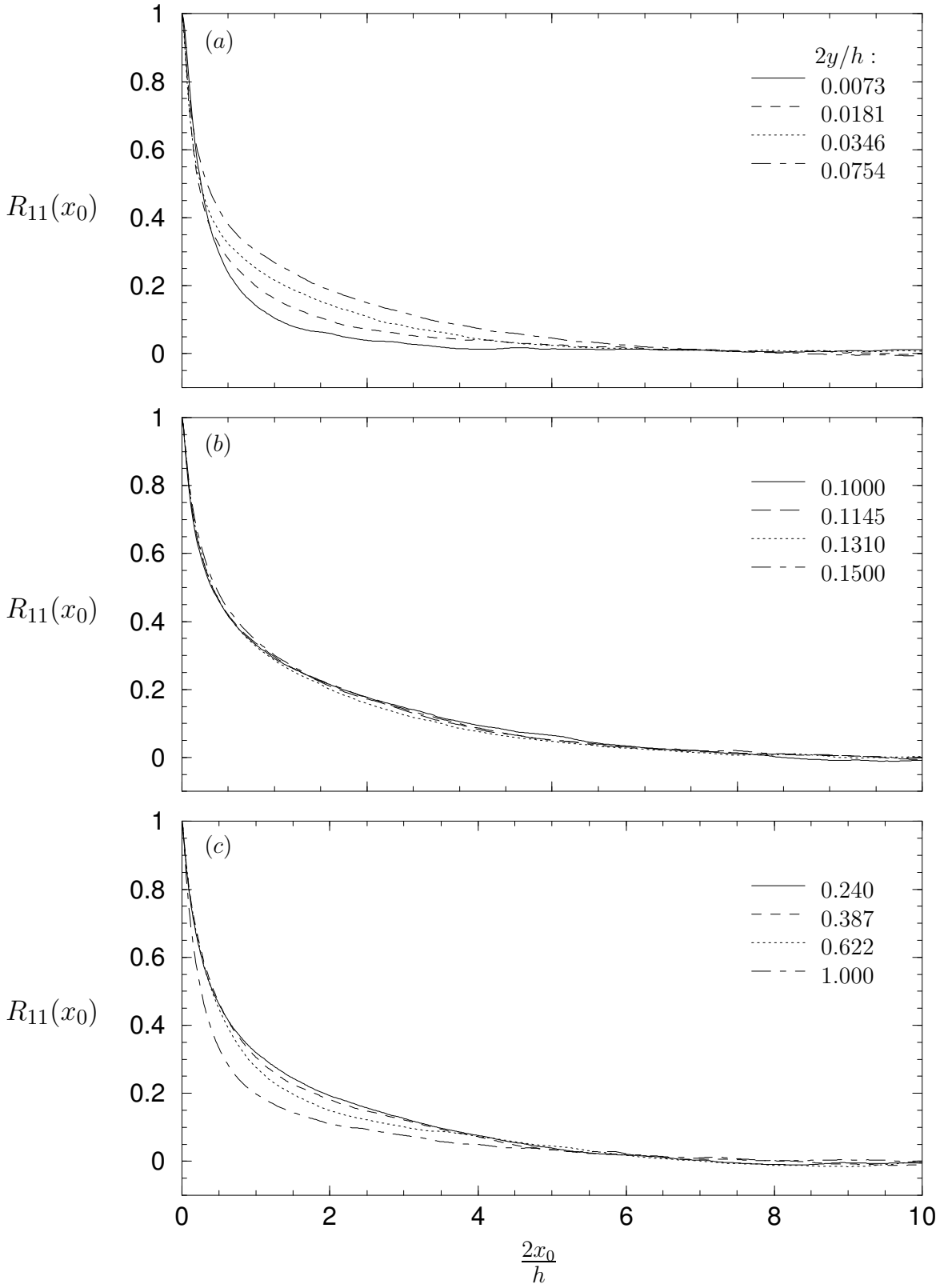

Figure H.1: Channel flow auto-correlation coefficient at 12 wall-normal levels for $Re = 60 \times 10^3$.

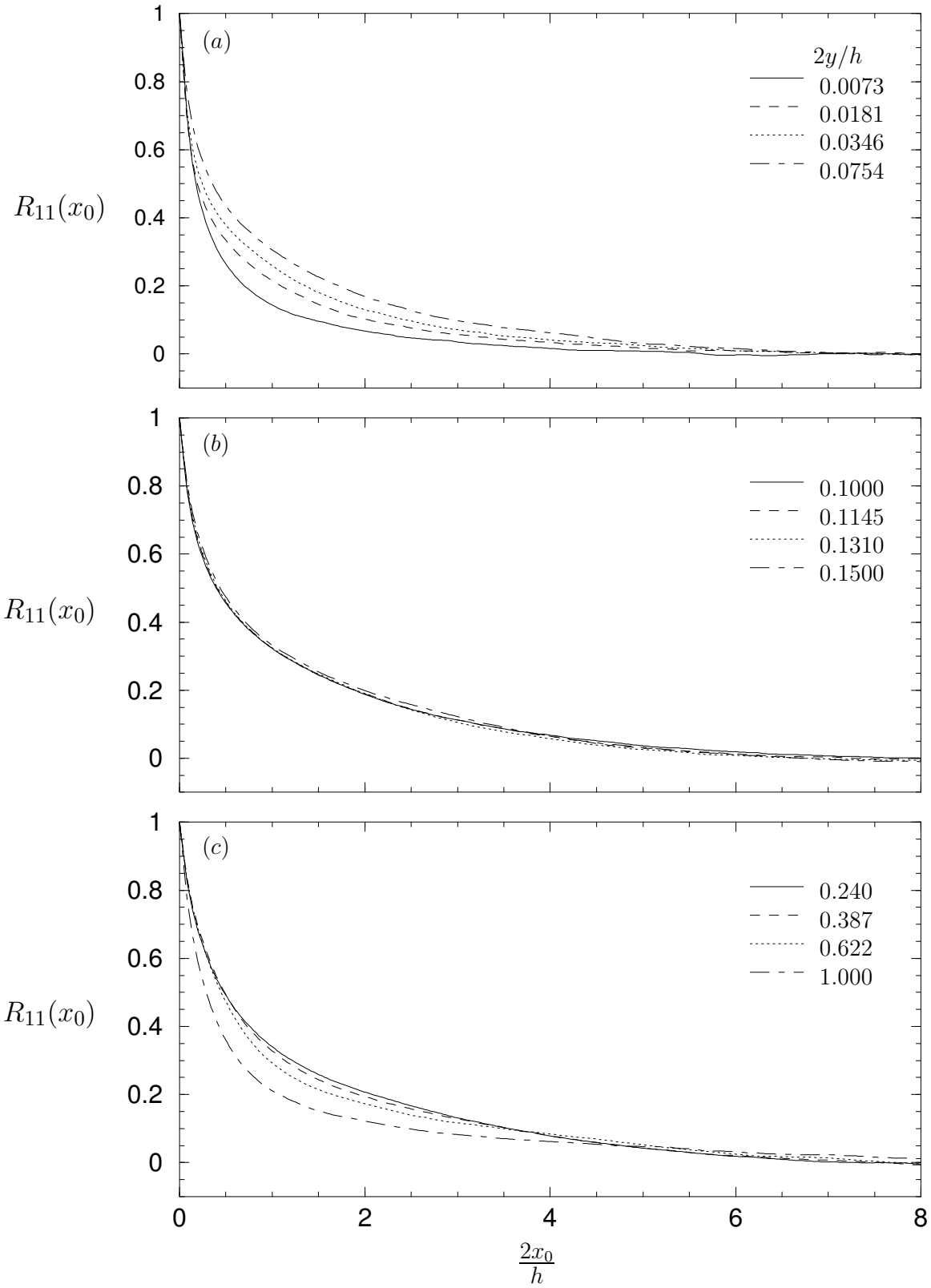

Figure H.2: Channel flow auto-correlation coefficient at 12 wall-normal levels for $Re = 105 \times 10^3$.

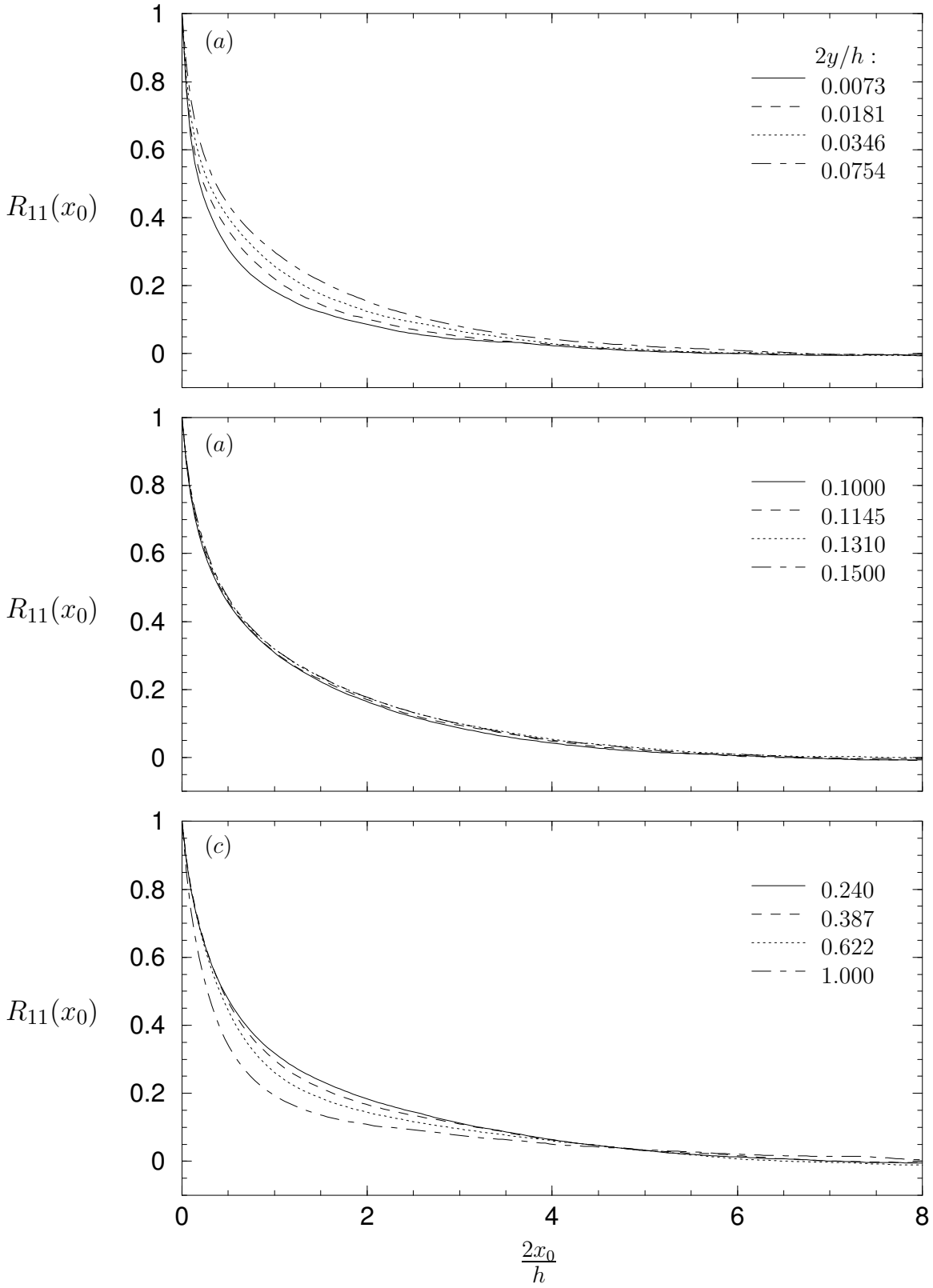

Figure H.3: Channel flow auto-correlation coefficient at 12 wall-normal levels for $Re = 190 \times 10^3$.